

**The Role of Macrophages in the Sequestration of Drug and
Formation of Insoluble Drug Aggregates**

By

Phillip Rzczycki

A dissertation submitted in partial fulfillment
of the requirements for the degree of
Doctor of Philosophy
(Pharmaceutical Sciences)
In The University of Michigan
2018

Doctoral Committee:

Professor Gustavo R. Rosania, Chair
Associate Professor Wei Cheng
Assistant Professor James Moon
Associate Professor Haoxing Xu

Phillip M. Rzezycki

pmrzec@umich.edu

ORCID iD: [0000-0002-2149-2249](https://orcid.org/0000-0002-2149-2249)

To taking the stairs

Acknowledgements

Firstly, I would like to thank my adviser Dr. Gus Rosania for his support and guidance throughout my time working on my Ph.D. He provided me invaluable insight into how to become a better scientist, writer, and most importantly of all, thinker. I would also like to thank my committee members, Dr. Wei Cheng, Dr. James Moon, and Dr. Haoxing Xu for their insightful comments and suggestions throughout the course of performing the research in my dissertation work. I also would like to thank Dr. Kathleen Stringer for her support and valuable comments throughout my research.

I am also happy to thank all members of the Rosania lab, past and present. The work performed by previous students, in particular Jason Baik, established the direction that I would take my project. Rahul Keswani and Gi Sang Yoon taught me many of the techniques that I used throughout my research work, and were incredibly patient with the many mistakes that I made on the way. I would also like to thank the current members in our lab, Tehetina Woldemichael, Misha Murashov, and Vernon LaLone for their support and advice at our many lab meetings.

I would like to thank my friends for their friendship and support throughout graduate school. Without them, I would not have been able to make it to this point. From tailgating and watching Michigan football games, struggling at intramural sports, to going to see concerts, my friends have helped me get through the highs and lows of graduate school. I want to give a special thanks to Ryan Clauson, Emily Morin, and Nick Waltz for their great friendship.

Finally, I would like to thank my family for their unwavering belief in me throughout graduate school. Without them, I would not have been able to make it to this point. I owe all of my success in my academic career to them.

Table of Contents

Dedication	ii
Acknowledgements	iii
List of Figures.....	vi
List of Tables	x
List of Appendices.....	xii
Abstract.....	xiii
Chapter 1 Introduction	1
Chapter 2 A Role for Low Density Lipoprotein Receptor-Related Protein 1 in the Cellular Uptake of Tissue Plasminogen Activator in the Lungs	28
Chapter 3 Massive Bioaccumulation and Self-Assembly of Phenazine Compounds in Live Cells	55
Chapter 4 Clofazimine Biocrystal Accumulation in Macrophages Upregulates Interleukin 1 Receptor Antagonist Production to Induce a Systemic Anti-Inflammatory State	87
Chapter 5 Elasticity in Macrophage-Synthesized Biocrystals	113
Chapter 6 Detecting Ordered Small Molecule Drug Aggregates in Live Macrophages: A Multi-Parameter Microscope Image Data Acquisition and Analysis Strategy	131
Chapter 7 The Adaptive Cargo Carrying Capacity of Macrophages Expands the Drug Volume of Distribution	158

Chapter 8	Liver Granulomas Function as Drug Sequestering Hepatoprotective Organoids.....	186
Chapter 9	Conclusions.....	221
Appendices.....		233

List of Figures

Figure 2-1 Human tissue plasminogen activator versus time in bronchoalveolar lavage fluid	41
Figure 2-2 LRP1-mediated uptake of mtPA in murine whole lung and liver cell suspensions	42
Figure 2-3 Concentration of intracellular mtPA in murine liver and lung cell suspensions.....	43
Figure 2-4 LRP1 protein quantification in murine liver and lung cells	44
Figure 2-5 LRP1 tissue staining in liver and lung sections	45
Figure 2-6 Macromolecular transport mechanisms within the lung	46
Figure 3-1 Synthesis scheme for phenazine derivatives	73
Figure 3-2 Phenazine derivatives and cellular staining patterns.....	74
Figure 3-3 Absorbance spectra of phenazine compounds in methanol and sulfuric acid.....	75
Figure 3-4 Quantitative polarization microscopy of cells incubated with phenazine derivatives .	76
Figure 3-5 Quantitative comparison of diattenuation of intracellular inclusions	77
Figure 3-6 Confocal fluorescence microscopy of cells incubated with fluorescent phenazine derivatives	78
Figure 3-7 Cellular accumulation of phenazine compounds	79
Figure 3-8 PCA plot of optical properties of phenazine inclusions within cells	80
Figure 3-9 Solubility of phenazine compounds in cell culture media related to intracellular accumulation.....	81
Figure 4-1 CFZ bioaccumulation and crystallization within the liver	101
Figure 4-2 CFZ bioaccumulation and pro- and anti-inflammatory signaling.....	102

Figure 4-3 CFZ bioaccumulation and crystallization dampens inflammatory response in mouse footpad	103
Figure 4-4 IL-1RA mediated anti-inflammatory activity	104
Figure 4-5 CFZ bioaccumulation enhances resistance to LPS-induced lung injury and improves survival.....	105
Figure 5-1 Curvature of CLDIs within macrophages and isolated CLDIs	121
Figure 5-2 Images and powder X-ray diffraction of CLDIs and CFZ-HCl.....	122
Figure 5-3 CFZ-HCl structure and crystal packing	123
Figure 5-4 Bending of synthetic CFZ-HCl crystal	124
Figure 5-5 Azimuth of CFZ-HCl before and after bending	125
Figure 6-1 Schematic of multi-parameter imaging system.....	145
Figure 6-2 Slide used to calibrate diattenuation polarization instrument	146
Figure 6-3 Generation of mask for automated data collection	147
Figure 6-4 Multi-parameter imaging of isolated spleen CLDIs.....	148
Figure 6-5 Multi-parameter images of CFZ and untreated alveolar macrophages.....	149
Figure 6-6 Scatter plot of relating optical properties of untreated and 8 week CFZ treated alveolar macrophages.....	151
Figure 7-1 Microscopic imaging cytometry reveals variations in cargo loading of macrophage and monocyte populations	173
Figure 7-2 Cargo accumulation induces reorganization in the internal membrane architecture of macrophages	174

Figure 7-3 Macrophages increase in number and actively sequester cargo primarily by stabilizing it in an insoluble form	179
Figure 8-1 CFZ treatment remodels the liver through granuloma formation	206
Figure 8-2 Increased drug loading results in macrophages becoming concentrated within granulomas, and increased drug accumulation mainly within the granuloma.....	207
Figure 8-3 Granuloma-associated macrophages are phenotypically different from both untreated and drug-treated macrophages	208
Figure 8-4 The accumulation of insoluble aggregates and granuloma formation is dependent on the isopropyl group in the CFZ molecule	209
Figure 8-5 TEM of 8-week CFZ treated liver showing granuloma surrounded by hepatocytes .	210
Figure 8-6 Chemical depletion of macrophages leads to signs of hepatic toxicity in animals fed CFZ	211
Figure 8-7 Formation of granulomas is necessary for the increased IL-1RA production within the liver of CFZ-treated mice.....	213
Figure SI. 1- Degradation of human tPA	233
Figure SI. 2- Brightfield images of LRP1 stained lung sections through different filters.....	234
Figure SI. 3- Thresholding of tissue sections.....	235
Figure SI. 4- Mouse liver and lung sections stained for LRP1	236
Figure SI. 5- Ratio of LRP1 staining in liver and lung.....	237
Figure SI. 6- Synthesis scheme for phenazine compounds.....	242
Figure SI. 7- CFZ accumulation in lung macrophages	265
Figure SI. 8- IL-1 β cleavage in spleen, lung, and kidney	266
Figure SI. 9- CFZ accumulation within IL-1RA knockout mice.....	267

Figure SI. 10- Vital signs of mice following injection LPS or PBS injection	268
Figure SI. 11- Curvature of drug biocrystals	274
Figure SI. 12- Face indexed image of CFZ-HCl crystals that was used for single crystal X-ray diffractions	275
Figure SI. 13- Asymmetric unit of CFZ-HCl.....	276
Figure SI. 14- C11 interaction with C5-H5 viewed along the b-axis to form a chain of CFZ-HCl molecules and along the c-axis to show the position of the C11 interaction within the zig-zag.	277
Figure SI. 15- Crystallographic projection of the major faces of the CFZ-HCl crystal	278
Figure SI. 16- Raman spectra of CFZ-HCl crystal pre- and post-bending	279
Figure SI. 17- Melting point of CFZ-HCl determined via DSC	280
Figure SI. 18- Comparison of cellular proliferation within untreated, CFZ-treated, and granulomatous regions of CFZ-treated livers	283
Figure SI. 19- TUNEL assay in untreated, 2 week, 4 week, and 8 week CFZ-treated livers	284
Figure SI. 20- Hepatic TLR2 expression measurement.....	285
Figure SI. 21- TEM image of granuloma within liver of 8-week CFZ treated mouse	286
Figure SI. 22- Hepatic apoptosis in clodronate- and PBS-treated mice	287
Figure SI. 23- Cellular proliferation in clodronate- and PBS-treated mice	288
Figure SI. 24- Hepatic macrophage quantification in clodronate- and PBS-treated mice.....	289
Figure SI. 25- Quantification of protonated CFZ within livers of clodronate- and PBS-treated mice.....	290

List of Tables

Table 6-1 Multi-parameter optical properties of untreated and 8 week CFZ treated alveolar macrophages	149
Table 7-1 Cellular vesicular volume and occupancy within alveolar macrophages.....	174
Table 7-2 Insoluble cargo loading within various macrophage populations	175
Table 7-3 Estimated volume of distribution within various macrophage populations following increased drug therapy	176
Table 7-4 Estimated volume of distribution within various organs following increased drug therapy.....	177
Table 8-1 Mean body mass and temperature of mouse groups during final week of liposome treatment	211
Table S1- Calculated physicochemical properties, predicted cell uptake and subcellular localization properties of clofazimine and related phenazine analogs with chlorophenyl substitutions	250
Table S2- Observed cellular staining pattern following 72 hour incubation with clofazimine and related phenazine analogs possessing R-imino group substitutions	251
Table S3- Calculated physicochemical properties, predicted cell uptake and subcellular localization properties of clofazimine and related phenazine analogs with different R-imino substitutions	254
Table S4- Observed cellular staining pattern following 72 hour incubation with clofazimine and related phenazine analogs possessing R-imino group substitutions	255

Table S5- Calculated physicochemical properties, predicted cell uptake and subcellular localization properties of clofazimine and related phenazine analogs with additional R-imino substitutions	258
Table S6- Observed cellular staining pattern following 72 hour incubation with clofazimine and related phenazine analogs possessing R-imino group substitutions	259
Table S7- Vital signs of control and clofazimine-treated mice	269
Table S8- Crystallographic data for CFZ-HCl.....	281
Table S9- Molecular interactions within the CFZ-HCl crystal structure.....	282

List of Appendices

Appendix A. Supporting Information in Chapter 2	233
Appendix B. Supporting Information in Chapter 3	240
Appendix C. Supporting Information in Chapter 4	263
Appendix D. Supporting Information in Chapter 5	270
Appendix E. Supporting Information in Chapter 8.....	283

Abstract

Drugs with poor aqueous solubility generally possess unfavorable pharmacokinetic properties. Upon oral administration, such drugs can form supersaturated solutions within the gastrointestinal tract, causing the formation of insoluble aggregates which may be prone to precipitate out in the body. Clofazimine, an oral leprostatic drug in clinical use since the 1960s, is known to massively bioaccumulate in the form of insoluble, crystal-like drug inclusions (CLDIs). These CLDIs are primarily found within tissue macrophages of the liver, spleen, and lungs. Here, we hypothesized that CLDIs are stabilized by an active, macrophage-dependent concentrative proton and chloride transport process. To test this, we developed a multi-parameter imaging and analysis system which combines polarization and fluorescence microscopy to track the accumulation and stabilization of CLDIs in different macrophage populations throughout treatment, revealing tissue-specific differences in the ability to stabilize intracellular drug aggregates, and an active remodeling of the internal arrangement of the macrophage's membranes to maximize drug loading. Additionally, following chemical depletion of macrophages in the liver and spleen, CLDI accumulation was significantly inhibited, resulting in a reduction in the total drug accumulation within the organs. Most importantly, depletion of hepatic macrophages alongside drug treatment caused liver damage and systemic toxicity, leading us to postulate that drug sequestration and subsequent granuloma formation by macrophages functions as a protective mechanism. When macrophage-depleted mice were injected with isolated CLDIs, there was a significant increase in the rate of decay of the crystals, indicating that phagocytosis by the macrophage stabilizes the crystal and prevents dissolution. Finally, we determined that CLDI-containing macrophages showed significantly higher levels TFEB activation, lysosomal content and autophagic flux, pointing to an active adaptation of the macrophages' endolysosomal system to accommodate and stabilize CLDIs. To conclude, macrophages are actively involved in sequestering drug and help to limit drug toxicity.

Chapter 1

Introduction

1.1 Background

1.1.1 Clofazimine

Leprosy is a devastating illness caused by the bacterium *Mycobacterium leprae*, and is a major problem throughout much of the developing world, with more than 180,000 new cases being diagnosed in 2013 [1]. The development of new therapies and the widespread availabilities of treatment options have led to a significant reduction in the number of new cases of leprosy, dropping from more than 550,000 in 1996 [2]. Nevertheless, this disease remains a significant public health dilemma throughout the world. One of the most effective treatment options for leprosy is the FDA approved drug clofazimine (CFZ), a red-pigmented phenazine compound developed in the 1950s. This drug shows powerful antimicrobial and anti-inflammatory activity, especially in the treatment of multiple drug resistant leprosy [3].

The physical and chemical properties of CFZ are very unique, and greatly influence the pharmacokinetics of the drug. Clofazimine is a highly lipophilic, weakly basic compound that contains two ionizable amine functionalities. Due to the high lipophilicity (cLogP=7) of CFZ, the drug accumulates within lipid-rich tissues during the initial stages of treatment [4]. The high degree of accumulation within lipid-rich tissues results in an extremely long half-life (about 70 days) and large apparent volume of distribution.

Following three weeks of continuous treatment, CFZ begins to accumulate within macrophages of the liver, spleen, and lung, among other locations. The accumulation of CFZ within these cells eventually leads to the formation of intracellular, highly ordered, crystal-like drug inclusions [5]. These crystals have not been found outside of the cell or in the vascular

system, indicating that their formation may be dependent on a cellular process or the result of an ion-trapping mechanism [6]; due to the presence of an ionizable amine group, the majority of the drug in solution will exist in the protonated form in the highly acidic environment of the lysosome [7], preventing it from freely diffusing across the membrane back into the cytosol. As the drug concentrates, it precipitates out of solution, forming the highly ordered crystal-like structures that are found throughout the body of CFZ-treated patients.

CLDIs are a different polymorphic form of CFZ than the form used in treatment. The formulations of CFZ that are used therapeutically are either the monoclinic or triclinic (TC) polymorphic form of the drug [8]. CLDIs can be isolated from the tissues of treated animals, and further experiments can be performed using these crystals. CLDIs can be separated from the surrounding tissue and cellular debris through the use of a sucrose density gradient. By using this gradient, one can separate CLDIs from the TC form of the drug due to the differences in their densities: TC CFZ has a density of 1.3 g/mL, while CLDIs have a slightly higher density of 1.36 g/mL [9].

Powder X-ray diffraction patterns obtained from the TC form of CFZ and isolated spleen CLDIs also indicate a polymorphic change occurs during CLDI formation: the TC form of CFZ contains a peak at $2\theta=9.3^\circ$ that is not seen in the isolated CLDIs, and isolated CLDIs contain a peak at $2\theta=7.2^\circ$ not present in the TC form [9]. Proton NMR spectroscopy was also performed on isolated CLDIs to shed further light on the biotransformation of CFZ within the body. This revealed that the CFZ present in CLDIs exists in a monoprotonated form [9]. Bulk elemental analysis was performed to determine the elemental composition of the CLDI, and this led to the discovery that CLDIs exist as a hydrochloride salt of CFZ. The X-ray powder diffraction pattern of synthetic CFZ hydrochloride crystals and CLDIs contained the same major peaks, and single crystal analysis was used to determine that the underlying crystal structure was orthorhombic [9]. Raman microscopy performed on CFZ powder and CLDIs isolated from the spleen of CFZ treated animals has also been used to demonstrate the polymorphic change that occurs during CLDI formation. The vibrational spectra of the crystalline CLDIs differs significantly from that of the dry CFZ powder, or other amorphously recrystallized forms: CLDIs possess two vibrational peaks at 1396 cm^{-1} and 1301 cm^{-1} that are very strong, but these peaks are absent in

the TC or other amorphously recrystallized forms of the drug [9, 10]. Thus, the formation of CLDIs can be tracked through a multitude of chemical and physical analysis methods.

Aside from their physical and chemical differences, the presence of one polymorph versus another can be detected by their differing optical properties. The TC form of CFZ shows a strong fluorescence in the FITC (495 nm excitation/ 519 nm emission) channel, which can be used to track cells that have taken up the drug [10]. Transformation from the TC form of CFZ to the orthorhombic form results in a loss of the FITC signal and development of signal in the Cy5 (650 nm excitation/ 670 nm emission) channel [11]. Isolated CLDIs polarize light as a single domain, and are homogeneously birefringent. Pure TC CFZ crystals, on the other hand, give a mixed yellow-orange birefringent signal [5]. Thus, due to these optical property differences, the accumulation of CFZ and formation of CLDIs can be studied at a cellular and subcellular level through polarization and fluorescence microscopy.

Clofazimine also displays potent anti-inflammatory properties. Treatment with CFZ leads to an increase in the levels of the anti-inflammatory protein IL1-RA, with significant down regulation of the pro-inflammatory signaling molecules Macrophage Inflammatory Protein 1- β (MIP-1 β) and TNF- α [6]. The formation of CLDIs may also be a protective mechanism put in place by the body to prevent toxic effects of CFZ accumulation. CLDIs are much more tolerated by isolated macrophages, displaying 80% viability when cultured with 10 μ M CLDIs versus 20% when cultured with 10 μ M soluble CFZ [12]. The presence of CLDIs within macrophages may be the reason behind the increase in anti-inflammatory signaling in treated animals: cultured macrophages which phagocytose CLDIs display increased IL1-RA production, along with decreased activity of Toll-like receptors 2 and 4, resulting in lowered NF- κ B translocation and TNF- α production [12]. Treatment with CFZ also alters the expression levels of various lysosomal enzymes, which may also play a role in the anti-inflammatory activity seen in treatment. Following treatment with CFZ for 21 days in mice, a significant increase in the levels of N-acetyl- β -D-glucosaminidase was seen in isolated macrophages [13]. There is also some evidence that CFZ treatment may lead to an increase in the synthesis of lysosomal enzymes [14] in macrophage cultures *in vitro*.

1.1.2 Drug Accumulation

The ability of a medication to effectively treat a disease is dependent on the drug reaching the therapeutic concentration at the appropriate site of action. For an oral drug to reach therapeutic levels, it must have favorable pharmacokinetic parameters. The bioavailability of a drug is one of the most important factors in determining the effectiveness of a therapeutic regimen. Bioavailability is defined as the fraction of a dose that enters the systemic circulation. For an intravenous treatment, bioavailability is 100%. Bioavailability will decrease with other dosage forms due to incomplete absorption of the drug in the small intestine, or metabolism of the drug by the liver and elimination in urine or feces. Hurdles such as this limit the ability of the drug to accumulate and reach therapeutic concentrations. The most frequent cause of poor oral bioavailability is poor solubility of the parent compound [15]. As drugs with poor solubility are often candidates for development, there are a variety of strategies used to improve solubility.

One common approach to improving poor solubility is the introduction of an ionizable functionality, such as a weakly acidic or basic functional group. The majority of drugs on the market today contain a weak acid or base moiety [16], demonstrating the power of ionization when it comes to improving solubility. The addition of a weakly basic functionality to a molecule, such as an amine group, greatly improves the solubility and dissolution profile of a compound [17]. However, this improvement in solubility can often result in unwanted drug accumulation. The pKa value of amine groups are usually between 8 and 10, which would result in the drug being mostly unionized after freely diffusing into the cytosol. Once in the cytosol, the unionized drug freely diffuses throughout the cell into various compartments. After entering the highly acidic (pH=4.5-6.0) endo-lysosomal system, the drug becomes ionized, and is unable to freely diffuse across the membrane back into the cytosol, causing the drug become trapped within the lysosome[18]. Chemicals with a propensity to accumulate in the endo-lysosomal system are commonly referred to as lysosomotropic agents.

The trapping and accumulation of a drug within the lysosome has a variety of implications. Studies by Krise *et. al* have demonstrated that drug accumulation by lysosomotropic agents results in an expanded volume of the lysosome [19], and they have also illustrated that the expansion of the volume of the lysosome is a potential drug interaction pathway that can form within the cell [20]. They hypothesize that these drug interactions result from changes in lysosomal sequestration, which alter the ability of the drug to interact with non-

lysosomal targets. Further work by this group has demonstrated that lysosomal drug accumulation results in nuclear localization of the transcription factor EB, which regulates lysosomal biosynthesis, and leads to an increase in the number of small, lipid-filled lysosomes [21]. The trapping and accumulation of a drug within the lysosome has significant biological outcomes, and can greatly impact the pharmacokinetics and pharmacodynamics of amine-containing drugs.

Aside from impacting the pharmacokinetics of the drug, accumulation can lead to toxicity. Transporters in the bile ducts of the liver are used to remove exogenous substrates from the body, and their inhibition can result in damage to hepatocytes. Drugs such as cyclosporine A have been shown to inhibit the canalicular transport protein Multidrug resistance-associated protein 2 (MRP2) when accumulating in the liver. The inhibition resulting from the accumulation leads to significant cytotoxicity towards the hepatocytes [22], which can severely damage the liver.

Accumulation of the soluble form of a drug can cause complications due to saturation of transport proteins, inhibition of enzymes, or due to changes of key pharmacokinetic parameters. The formation and accumulation of insoluble drug aggregates, however, poses entirely new problems. Drug precipitation *in vivo* often results from a change in the pH of the environment the drug is dissolved in, which is often seen when exiting the highly acidic environment of the stomach and entering the much more alkaline small intestine [23]. Crystallization is also commonly seen in the distal tubular lumen of the kidney due to poor solubility in urine, and can lead to crystal nephropathy [24]. The formation of drug crystals in the kidney can block urine flow, eventually causing renal failure. Antibiotics such as amoxicillin [25] and protease inhibitors such as indinavir [26] have the potential to form insoluble aggregates within the kidney and in urine, demonstrating that drug precipitation *in vivo* is a common hurdle which must be overcome when developing a new drug product.

1.1.3 Macrophages

One of the key functions of the immune system is the isolation and removal of “non-self” antigens from the body, and the mononuclear phagocytic system (MPS) is a major component in this. The MPS is comprised of “professional phagocytes”, which includes monocytes,

macrophages, and dendritic cells. Monocytes are one of the parent-cells of the MPS, and differentiate from hematopoietic stem cells in the bone marrow [27], which can then differentiate into various macrophage populations. The main function of the monocyte is to replenish resident tissue macrophage populations, respond to inflammatory signals, and to illicit immune responses. There are two main subsets of monocytes in the mouse, and they are classified based on their expression of the surface marker lymphocyte antigen 6C (LY6C) [28]. One subset expresses high levels of LY6C, while the second subset expresses lower levels of this marker. After maturation, LY6C^{high} monocytes exit the bone marrow and enter the systemic circulation via C-C chemokine receptor type 2 binding by C-C chemokine ligand [29]. LY6C^{high} macrophages can then differentiate into LY6C^{low} monocytes in circulation. LY6C^{high} monocytes are preferentially recruited to sites of inflammation due to CCL2 binding to the CCR2. Monocytes low in LY6C function to patrol the endothelium, and are more likely to differentiate into the anti-inflammatory macrophage subtype [28, 30].

There are distinct subsets of macrophage populations that play different roles in the immune system. When stimulated, macrophages will polarize to a phenotype dependent on the environment the macrophage is in, as well as the stimuli, which will promote or inhibit inflammation. During an inflammatory event, the first macrophages to enter the site of inflammation will be the pro-inflammatory macrophage population subset. These macrophages, called M1 macrophages, are activated by cytokines such as TNF- γ , and elicit a pro-inflammatory response in the tissue. M1 macrophages exhibit potent antimicrobial activity, and play a major role in fighting bacterial, viral, and fungal infections [27]. The other macrophage population, called M2 macrophages, exhibit more of an anti-inflammatory phenotype, participate in tissue repair, and secrete cytokines such as IL-10 [28]. Tissue macrophages are generally polarized more towards the M2, anti-inflammatory phenotype.

When monocytes extravasate across the endothelium, they differentiate into tissue macrophages. These tissue macrophages, which are found in the liver, lung, spleen, peritoneum, and brain, among other organs, are constantly surveying for inflammatory damage or foreign invaders [30]. Tissue macrophages mainly fulfill the role of fighting inflammation, immune surveillance and maintaining homeostasis in organs through the removal of apoptotic cells and communication with cells specialized for tissue repair, such as fibroblasts [31]. Macrophages are

constantly surveying their environment for signs of distress, foreign invaders, or xenobiotics through the use of phagocytosis, and this process will be explained further in later sections.

1.1.4 Macrophage Depletion

It has been reported by our laboratory that CFZ accumulates within tissue macrophages of the spleen, liver, and lung [5, 6, 12]. Because of the propensity of CFZ to accumulate within macrophages, depleting the population of macrophages within different tissues during the course of treatment is a potentially interesting avenue to explore. One well-studied model of macrophage depletion is the use of liposomal formulations of bisphosphonates, such as clodronate or alendronate [32, 33]. Clodronate is a bisphosphonate used to treat bone diseases due to its activity towards specialized bone degrading cells known as osteoclasts. The drug accumulates within the hydroxyapatite of the bone, and is absorbed by the osteoclast as it resorbs bone. Encapsulating these small, strongly hydrophilic molecules inside liposomes allows for them to be preferentially phagocytosed by macrophages. Once inside the cell, lysosomal enzymes break down the liposome, releasing the chemical intracellularly [32-35]. The clodronate is metabolized to a toxic analog of ATP that inhibits ATP/ADP translocase, interfering with mitochondrial membrane potential and cellular metabolism, eventually leading to apoptosis. Macrophage depletion by this method is specific towards macrophages and will not impact other cells, such as normal dendritic cells [33]. Non-phagocytic cells do not take in unformulated clodronate, nor is it toxic. Free, unformulated clodronate has a half-life of about fifteen minutes, and is rapidly eliminated via the renal system [34].

Depletion of specific tissue macrophage populations using liposomal formulations of bisphosphonates is possible, and can be controlled by the route of administration [32-36]. To this end, the depletion of various populations of macrophages and the effect that this has on CFZ accumulation can be studied. Injection of liposomal clodronate intravenously causes the depletion bone marrow macrophages and Kupffer cells in the liver within one day [33], and causes all macrophages within the red pulp and marginal zone of the spleen to die within two days [32]. Two injections two days apart were required to get complete depletion within the bone marrow. Subcutaneous injection in the foot pad eliminated macrophages within the draining lymph nodes [33], while intratracheal administration depletes alveolar macrophages [36]. Intraperitoneal injection has been shown to be the most effective at impacting the largest

population of macrophages, depleting macrophages of the parathymic lymph nodes, spleen, liver, and peritoneal cavity. This is due to the larger volume which can be administered via the IP route [33]. Performing these macrophage depletion experiments in both animals during a long-term CFZ treatment regimen and animals that have already formed CLDIs can test the idea that macrophages specifically stabilize CLDIs, if CLDIs can potentially form in other cell types, and the fate of CLDIs released from dead cells.

1.1.5 Endolysosomal Pathway

Macrophages, or “big-eaters”, utilize the cellular process of phagocytosis to take in foreign particles and pathogens to prevent them from damaging the body. As high concentrations of CFZ have been shown to be detrimental to the health of cells [37], it is believed that the massive accumulation of the drug in macrophages is a protective mechanism put in place to curtail the cytotoxic effects of the drug [5]. Clofazimine may accumulate in the highly acidic lysosomal compartment of the cell, potentially as a result of ion trapping. Ion trapping, as previously discussed, is a phenomenon which occurs due to the ionization of a molecule after crossing a biological membrane, which severely limits the ability of the molecule to freely diffuse.

Endocytosis is one of the major cellular pathways for the uptake of nutrients, destruction of pathogens, and degradation and recycling of cellular components [38]. Clofazimine accumulation most likely occurs within the endolysosomal system, and CLDIs are most likely formed in the highly acidic lysosomal environment of the macrophage [6]. Internalization occurs through a variety of mechanisms, such as formation of clathrin-coated pits or through other types of receptor-mediated endocytosis [39]. However, one thing that is common to the internalization of extracellular components is the fusion of the plasma membrane with the early endosome, where the intracellular location of the cargo is determined [40]. Proteins on the surface of the early endosome are often used to track the trafficking of internalized materials. The early endosome can be detected by the presence of a group of endocytic regulators referred to as Ras-associated binding proteins (Rab proteins) [40], with RAB5A and RAB4 unique to the EE compartment [38]. The early endosome is for all intents and purposes, a sorting compartment that is used to determine the fate of internalized goods.

If the contents of the early endosome are targeted for degradation by the cell, the early endosome transforms into a late endosome. During this process, the membrane of the early endosome begins to invaginate, and multivesicular bodies form within the compartment [40]. The late endosome is characterized by the presence of the surface protein markers RAB7 and RAB9, as well as two mannose receptors [41], which help differentiate it from both the early endosome and the lysosome.

Lysosomes contain the enzymes necessary to degrade the various proteins, lipids, and other waste products that pass through the endolysosomal system [38], and many of these enzymes require a highly acidic environment to function properly. The acidification of the lysosome most likely plays a very significant role in the formation of intracellular CLDIs, as previous work has shown that CFZ hydrochloride requires an acidic, chloride-rich environment to form [9]. Thus, it is believed that biomolecular proton and chloride transporters play a significant role in maintaining the CLDI within the cell.

1.1.6 Biomolecular Proton and Chloride Transport Mechanisms

During the various stages of the endolysosomal pathway, the pH of each compartment (early endosome, late endosome, endolysosome) becomes more acidic as the degradation process occurs. When first formed, the early endosome has a luminal pH between 6.1 and 6.8, which becomes more acidic as it transitions into a late endosome (pH=5.5) [41]. Fusion with the lysosome results in further acidification, with the luminal pH of lysosomes reaching as low as 4.5 [38]. The low pH and oxidizing environment present in the endolysosome is necessary for the function of many of the enzymes present, and this environment may also be the reason behind the stability of CLDIs in cells. Mammalian lysosomes range in size from 0.1 to 1.0 μm [42], and have an average volume of around a femtoliter, assuming a spherical shape. Given the typical pH of a lysosome of 4.5, this corresponds to 19,000 protons in the typical acidified lysosome. The average chloride concentration in the lysosome has been measured to be on the order of 30 mM [43], which means that the typical lysosome contains more than 18,000,000 chloride ions. Maintaining homeostasis of these ions is a complex process, and interference with these ions can significantly hamper the ability of the lysosome to properly function.

The acidification of the lysosome is the result of an interplay of many ion channels, transporters, and pores, each playing different roles. The primary membrane channel involved in the acidification of the endolysosomal system is vacuolar-type H⁺-ATPase (V-ATPase); this protein hydrolyzes ATP, providing the free energy needed for protons to be pumped against their concentration gradient into the lumen of the lysosome [42]. V-ATPase is present in nearly every eukaryotic cell type [44], and is found along many intracellular membranes, such as those in synaptic vesicles, Golgi vesicles, and endosomes [45]. Trafficking within the endolysosomal system is on many levels dependent on acidification of the various compartments by V-ATPase [38, 40, 41] due to the role pH changes play in binding and release of various surface markers. Inhibition of V-ATPase in the endolysosomal system has led to markedly slower cycling of receptors, showing that acidification is necessary for endolysosomal pathways [44, 46]. With respect to drug therapy, impairment in acidification of the lysosome is implicated in increased toxicity with certain chemotherapeutics. When lysosomal acidification is hindered through the use of the weak base chloroquine, co-administration of lysosomotropic anti-cancer agents resulted in hepatotoxicity, which was not observed following treatment with non-lysosomotropic agents [47].

V-ATPase is a unidirectional proton transporter, allowing two protons to cross into the lumen of the acidifying compartment for every molecule of ATP that is hydrolyzed [42]. As there is no concurrent ion transport coinciding with the addition of the two protons, the actions of V-ATPase are electrogenic, and will result in an increase in the membrane potential of the lysosomal compartment [48]. The resting membrane potential of the lysosome is between -20 mV and -40 mV [49], and addition of protons results in a shift towards a more neutral membrane potential. To effectively acidify the lysosome or other cellular compartment, this positive membrane potential needs to be dissipated. The membrane potential can be dissipated through the actions of counter-ion exchange channels. These channels could shuttle a cation from the lumen of the lysosome into the cytoplasm, or a channel could add an anion to the lysosome to counteract the electrogenicity of the V-ATPase [42].

Because CFZ accumulates as a hydrochloride salt [9], CLDI formation is most likely dependent on the activity of intracellular and extracellular chloride transporters. The chloride exchanger CIC-7 plays a key role in the acidification of endosomes and lysosomes, and may be

vital in the stabilization of CLDIs. CLC-7 is expressed ubiquitously throughout the body, and is found in the endosome and lysosome. In fact, CLC-7 colocalizes quite well with lysosomal-associated membrane protein-1 (LAMP-1) [50]. This exchanger works to dissipate the positive membrane potential by adding two chloride ions to the lumen of the endosome or lysosome, and concurrently removing one proton from the compartment [51]. This exchange system accounts for much of the chloride permeability into the lysosome [52, 53].

CLC-7 has a variety of roles throughout the body, and most functions are related to the acidification of lysosomes and endosomes. Genetic mutations associated with loss-of-function of CLC-7 lead to the development of neurodegenerative illnesses due to the accumulation of lipids within the lysosome, and animals with defective CLC-7 exchangers also display a phenotype of osteopetrosis due to the inability of osteoclasts to properly recycle bone as a result of incomplete lysosomal acidification [50]. Because a hydrochloride salt accumulates during CFZ treatment, it may play a major role in this accumulation.

There are many different transporters that are involved in maintaining chloride homeostasis. Another chloride transporter of interest that is found on both the plasma membrane and various intracellular membranes is the cystic fibrosis transmembrane conductance regulator (CFTR). CFTR is an anion-exchange channel that is permeable to chloride, and dysfunction of this channel leads to a clinical manifestation of cystic fibrosis [54, 55]. This transporter is expressed in a variety of epithelial cells, from the intestines to the lung [55]. CFTR is not only expressed in cells of the epithelium; in alveolar macrophages, CFTR plays a significant role in lysosomal acidification, and this may help kill pathogens which enter the body through the lung [56]. CFTR colocalizes with LAMP-1, and when phagocytosis was induced in macrophages, CFTR staining was observed surrounding the ingested latex beads [56]. When macrophages were treated with the CFTR inhibitor CFTR_{inh}-172, the cells failed to fully acidify the lysosome, being approximately one pH unit more alkaline than control cells. This indicates that CFTR, in conjunction with V-ATPase, may play a significant role in acidification of the lysosome in macrophages.

A cation-exchange channel may also be partially responsible for the stability of intracellular CLDIs. A family of channels known as the transient receptor potential (TRP) channels has been associated with the endolysosomal system, and one channel is of particular

interest. TRP Mucolipin 1 (TRPML1) is an ion channel permeable to calcium, sodium, manganese, and iron, and is comprised of six transmembrane-spanning domains [57]. TRPML-1 is expressed in almost every tissue in the body, with the highest amounts found in the brain, kidney, heart, liver, and spleen [58]. TRPML-1 is localized mostly to the late endosome and lysosome in humans, and plays a significant role in intracellular calcium release [59]. In humans, genetic mutations can lead to a loss-of-function of the TRPML-1 channel, resulting in a pathological state known as Mucopolidosis Type IV. This disease is characterized by psychomotor retardation, corneal clouding, and accumulation of lipids in endolysosomal-like compartments [60]. Cells isolated from TRPML *-/-* patients displayed enlarged vacuolar compartments where undigested lipids and biomaterials accumulate, indicating that TRPML-1 plays a role in the trafficking of endocytosed materials and the formation of lysosomes [60, 61].

Calcium is necessary for the formation and stabilization of the membranes of the late endosome/lysosome hybrid organelle [61]. The formation of lysosomes in TRPML *-/-* macrophages was studied, revealing that TRPML-1-mediated calcium release is required for the budding of lysosomes from the LEL; macrophages treated with calcium chelators displayed a similar phenotype as the TRPML-1 knockout macrophages, further illustrating the role calcium plays in lysosomal formation [58]. The TRPML-1 channel may play a role to maintain the pH environment of the endolysosome as well, but there are conflicting reports about the effects that loss of this channel plays in the acidification of the lysosome [58-60].

At a larger scale, the regulation of the lysosome and subsequent acidification mechanisms is controlled through a nuclear transcription factor known as transcription factor EB (TFEB) [62]. In normal cellular conditions (i.e., appropriate nutrient conditions or low lysosomal stress), TFEB is found in its phosphorylated form within the cytosol, where it is inactive. However, when cells are stimulated via nutrient or some other stressor, TFEB becomes dephosphorylated and translocates to the nucleus, becoming an active cellular transcription factor [49, 62]. The genes that TFEB controls regulate lysosome biogenesis, membrane formation, and autophagic functions within the cell [63, 64]. Additionally, it has been shown that TFEB and the expression of biomolecular ion transporters, in particular, V-ATPase, are closely linked [65, 66], and are regulated by the kinase mammalian target of rapamycin complex 1 (mTORC1). TFEB activation can also occur due to stresses to the lysosome brought about by ion-trapping. Lysosomotropic

compounds incubated with cultured cells have been shown to activate TFEB, resulting in increased lysosomal volume and intracellular vesicles [18-20, 67, 68]. TFEB activation and subsequent lysosomal biogenesis is also implicated as a potential mechanism behind chemoresistance to weakly basic anti-cancer agents [69] due to increased lysosomal exocytosis, indicating that this may be a cytoprotective mechanism.

1.1.7 Proton and Chloride Transporter Inhibition

In order to assess the role that these biomolecular proton and chloride transporters play in maintaining CLDI stability, pharmacological inhibitors of specific channels can be utilized. By interfering with the actions of these channels, the CLDI may become destabilized, leading to release of drug from the cell and into the surrounding environment.

The role of chloride transporters in maintaining the CLDI can be tested using the inhibitors 5-nitro-2-(3-phenylpropyl-amino) benzoic acid (NPPB), 4,4'-Diisothiocyano-2,2'-stilbenedisulfonic acid (DIDS), and 2-[3-(trifluoromethyl)anilino]nicotinic acid (Niflumic acid/NFA). DIDS is the most effective in inhibiting ClC-7, with a reported IC₅₀ of 40 μM [70], with other sources reporting an irreversible inhibition at concentrations above 30 μM [71]. This inhibits over 90% of the activity of the channel within isolated cells [70]. NPPB is also a very effective inhibitor of ClC-7, with a reported IC₅₀ of 150 μM [70], with other sources reporting values between 100 and 200 μM, depending on the tissue [71, 72]. NPPB has been shown to inhibit around 90% of the activity of ClC-7 when incubated with cells [70]. Niflumic acid is less specific in its activity toward ClC-7. NFA shows some inhibitory effects on ClC-7, inhibiting roughly 30% of the activity of ClC-7 channels when tested between 1 and 1000 μM [70]. NFA is a general inhibitor of chloride channel activity, and it is a very potent inhibitor of calcium-activated chloride channels [73].

Inhibitors for CFTR are more specific in their activity. The anti-diabetic drug glibenclamide is a powerful, widely used inhibitor of CFTR activity [74, 75]. Glibenclamide has a reported IC₅₀ of 20 μM, which will irreversibly inhibit more than 90% of CFTR activity [76]. Other sulfonylureas, such as tolbutamide inhibit CFTR; however, glibenclamide is the most potent in its activity [76]. A second CFTR inhibitor, 3-[(3-trifluoromethyl)phenyl]-5-[(4-carboxyphenyl)methylene]-2-thioxo-4-thiazolidinone (CFTR_{inh}-172), can also be tested.

CFTR_{inh}-172 inhibits greater than 90% of CFTR activity at concentrations above 10 μ M [77] and does not display cytotoxicity at concentrations below 50 μ M [78].

The calcium channel TRPML is permeable to divalent cations, such as Ca^{2+} and Fe^{2+} , and is inhibited by trivalent cations, such as Gd^{3+} , Fe^{3+} and La^{3+} [59-61]. Incubation of cells with 1 mM solutions of Gd^{3+} or La^{3+} resulted in a loss of more than 70% of the current from the TRPML channel [79]. Solutions of GdCl_3 , LaCl_3 , and FeCl_3 will be tested for their ability to inhibit TRPML-1. These trivalent ions work to inhibit channel function by blocking the pore, preventing the normal, divalent ions from passing. Treatment with Gd^{3+} has been shown to inhibit Kupfer cell function [80].

In order to probe the role of V-ATPase in maintaining the CLDI, two V-ATPase inhibitors can be tested. Bafilomycin A₁, a macrolide antibiotic produced by *Streptomyces* [81, 82], is an extremely potent inhibitor of V-ATPase, with an IC₅₀ on the order of 5 nM [83, 84]. Concanamycin A, a macrolide antibiotic in the same family as bafilomycin A₁, is another very potent inhibitor of V-ATPase. Con A inhibits V-ATPase with an IC₅₀ of 10 nM in yeast [85, 86], which is similar to what is seen with bafilomycin. These two inhibitors are very specific for V-ATPase at these concentrations, and should not impact other cellular transporters. However, there is some evidence that treatment with these antibiotics can lead to increased cell death via apoptosis [87].

1.1.8 Polarized Light and the Detection of Ordered Aggregates

Polarized light microscopy is a highly sensitive analytical tool which can be used to study changes in the optical properties of a material as a result of minute changes to its underlying molecular order or chemical composition [88]. This allows for polarized light to be used to study changes to the molecular structure of a biological material without the need for chemical labeling [89]. A material can interact with light in one of two ways: in an isotropic manner or in an anisotropic manner. An optically isotropic material is one whose optical properties do not change regardless of its orientation with respect to the incident light. An optically anisotropic material, on the other hand, interacts with light in a non-uniform manner, depending on the orientation of the material or incident light [90]. An example of an anisotropic optical property is the attenuation of light passing through a cell membrane; the membrane, composed of a complex

arrangement of phospholipids, carbohydrates, and proteins, differentially allows for light to pass through depending on its orientation with respect to the plane of the membrane. Optical anisotropy reflects the orientation of membrane-associated molecules in relation to the plane of the membrane, leading to variations in the absorption and scattering of polarized light transmitted through the samples in different directions with respect to the plane of the membrane [89-91].

By taking advantage of this, one can use linear diattenuation to study the molecular order of anisotropic materials. Linear diattenuation is a property of a material where the intensity of linearly polarized light transmitted through a sample is dependent on the polarization state of the light used to probe the sample [89, 92, 93]. When linearly polarized light passes through a material, any molecular alignment within the material creates two principal axes: a high transmittance and low transmittance axis, corresponding to the axis of molecular alignment [89]. Light that is not polarized parallel to the high or low axis of transmittance is split into two components when it enters a diattenuating material [89, 93]. One beam of light is polarized to the high transmittance axis, and the other beam is polarized orthogonally to the axis. When the two beams leave the material, they recombine and the intensity of the recombined light can be represented as a function of the angle of the incident polarized light. The intensity of this transmitted light displays a sinusoidal relationship with the angle of polarization of the incident light [89].

Using linear diattenuation, assessment of the optical anisotropy of histological and live cell samples can be used to identify and study the formation of insoluble ordered molecular aggregates within cells and tissues. To accomplish this, a specialized microscopic imaging platform has been developed for our laboratory: the LC-PolScope [94] is a microscope imaging system that utilizes a computer controlled liquid crystal (LC) compensator capable of generating linearly polarized light of any orientation [95]. This microscope set-up allows linear diattenuation, fluorescence, and brightfield images to be captured from the same field of view, allowing these optical properties to be correlated with one another during various stages of treatment and washout of the drug.

1.2 Rationale

Prolonged treatment with clofazimine (CFZ) leads to the formation of ordered, insoluble aggregates. This formation results from the accumulation of solubilized drug, which then undergoes a chemical transformation to form highly ordered, crystal-like drug inclusions (CLDIs). The inclusions that form are solid, bright red, birefringent objects with strong fluorescence in the Cy5 channel (650 nm excitation/ 670 nm emission). CLDIs are chemically different from the triclinic (TC), free base form of CFZ, which is the form present in commercial formulations of CFZ. The TC form is orange-red in color, slightly birefringent, and shows a strong fluorescence in the FITC channel (495 nm excitation/ 519 nm emission). The TC form of the drug does not show any signal in the Cy5 fluorescence channel. This, along with changes in the X-ray powder diffraction pattern of isolated CLDIs, indicates that a polymorphic change occurs during accumulation of the drug by the body. Crystal formation within cells is not harmful, and CLDI formation promotes an anti-inflammatory phenotype in macrophages by stimulating the production of various anti-inflammatory signaling molecules. These studies can also demonstrate other benefits of treatment with CFZ, such as the immunomodulatory effects of treatment. Once inside the cell, these crystals display great stability, and remain in the body long after treatment has ended. By characterizing the cell types which form CLDIs, as well as the time scale in which the crystals form and leave the body, we can provide valuable insight to not only the accumulation of CFZ, but also other drugs with the propensity to accumulate within cells and tissues, or drugs which form ordered, insoluble aggregates as a result of treatment.

1.3 Central Hypothesis

Clofazimine has been demonstrated to accumulate within F4/80 positive cells in the liver, spleen, lung, and almost every other organ in the body. These cells accumulate and sequester the drug in a manner to most likely protect the body from toxicity related to high levels of CFZ. There is no evidence of extracellular CLDI formation, and CLDIs have not been observed in non-macrophage like cells in histological sections. For example, in the liver, CLDIs are exclusively seen in Kupffer cells, with no insoluble aggregates seen in hepatocytes. Clofazimine also displays immunomodulatory properties, and this may result from accumulation within immune cells. CLDIs are incredibly stable once inside the macrophage, and do not readily degrade once CFZ treatment ends. The stability within the macrophage may be due to the action

of biomolecular proton and chloride transporters. CLDIs are formed and stabilized by an active, macrophage-dependent mechanism.

1.4 Specific Aims

1.4.1 Specific Aim 1

Clofazimine that is administered to patients is in the TC form, and possesses a strong signal in the FITC range and weak diattenuation anisotropy signal. Following prolonged treatment, insoluble aggregates of the drug form, and have optical properties that allow for it to be distinguished from the TC form. These properties include a loss of signal in the FITC range, appearance of signal in the Cy5 range, and the development of a strong diattenuation signal. The first aim of this project is to develop a microscopic imaging and analysis method to study the formation of CLDIs at a cellular and subcellular level.

1.4.2 Specific Aim 2

The accumulation of clofazimine and transformation into an insoluble salt form is hypothesized to be an active process dependent on the action of macrophages. In order to test this, the cell types that accumulate clofazimine will be determined to see if non-macrophages form CLDIs. The chemical depletion of macrophages with liposomal formulations of clodronate will be used to probe both the impact of macrophage depletion on CFZ accumulation and CLDI formation, as well as macrophage depletion on CLDI stability. This will allow us to confirm the role of macrophages in the formation and stabilization of CLDIs by specifically killing the cell type that preferentially accumulates the drug.

1.4.3 Specific Aim 3

Clofazimine, due to the fact that it contains a weakly basic, ionizable amine, most likely accumulates within the endolysosomal system. The insoluble form of CFZ precipitates as a hydrochloride salt, which indicates that the formation and stability of the crystals may rely on the action of a chloride transport system. One of the major lysosomal acidification channels is V-ATPase, but other channels and exchangers are necessary to dissipate the positive membrane potential gained. CLDIs are extremely stable in tissues and cells, and even following cessation of treatment, will remain in tissues for extended periods of time. The role

that these transporters play will allow us to identify specific mechanisms that mediate the stability of the CLDI within macrophages.

1.5 References

1. Organization, W.H. *Leprosy*. 2015 [cited 2015 June 1]; Available from: <http://www.who.int/mediacentre/factsheets/fs101/en/>.
2. Organization, W.H., *WHO Expert Committee on Leprosy*. WHO Technical Report Series. 1998, Geneva, Switzerland.
3. Arbiser, J. and S. Moschella, *Clofazimine: A review of its medical uses and mechanisms of action*. Journal of the American Academy of Dermatology, 1995. **32**(2): p. 241-247.
4. Cholo, M., et al., *Clofazimine: current status and future prospects*. Journal of Antimicrobial Chemotherapy, 2011.
5. Baik, J. and G.R. Rosania, *Macrophages Sequester Clofazimine in an Intracellular Liquid Crystal-like Supramolecular Organization*. PLOS ONE, 2012. **7**(10): p. e47494.
6. Baik, J., et al., *Multiscale Distribution and Bioaccumulation Analysis of Clofazimine Reveals a Massive Immune System-Mediated Xenobiotic Sequestration Response*. Antimicrob. Agents. Chemother., 2013. **57**(3): p. 1218-1230.
7. Information, N.C.f.B. *PubChem Compound Database; CID=2794*. [cited 2015 June 1]; Available from: <http://pubchem.ncbi.nlm.nih.gov/compound/2794>.
8. Rychlewska, U., et al., *Antileprosy Dihydrophenazines. Structural Characterization of Two Crystal Forms of Clofazimine and of Isoclofazimine, B.3857*. Journal of the American Chemical Society, 1984. **107**: p. 4768-4772.
9. Keswani, R., et al., *Chemical Analysis of Drug Biocrystals: A Role for Counterion Transport Pathways in Intracellular Drug Disposition*. Molecular Pharmaceutics, 2015.
10. Baik, J. and G.R. Rosania, *Molecular Imaging of Intracellular Drug-Membrane Aggregate Formation*. Molecular Pharmaceutics, 2011. **8**(5): p. 1742-1749.
11. Keswani, R., et al., *A Far-Red Fluorescent Probe For Flow Cytometric Xenobiotic-Sequestering Cell Functional Studies*. Cytometry Part A, 2015(Accepted Manuscript).

12. Yoon, G., et al., *Phagocytosed Clofazimine Biocrystals can Modulate Innate Immune Signaling by Inhibiting TNF Alpha and Boosting IL-1RA Secretion*. Mol. Pharmaceutics, 2015.
13. Sarracent, J. and C.M. Finlay, *In vivo effect of clofazimine in the lysosomal enzyme level and immune complex phagocytosis of mouse peritoneal macrophages*. Int J Lepr Other Mycobact Dis, 1984. **52**(2): p. 154-8.
14. Sarracent, J. and C.M. Finlay, *The action of Clofazimine on the level of lysosomal enzymes of cultured macrophages*. Clinical and Experimental Immunology, 1982. **48**(1): p. 261-267.
15. Savjani, K., A. Gajjar, and J. Savjani, *Drug Solubility: Importance and Enhancement Techniques*. ISRN Pharmaceutics, 2012. **2012**: p. 10.
16. Manallack, D., *The pKa Distribution of Drugs: Application to Drug Discovery*. Perspectives in Medicinal Chemistry, 2007. **2007**(1): p. 25-38.
17. Williams, H., et al., *Strategies to Address Low Drug Solubility in Discovery and Development*. Pharmacological Reviews, 2013. **65**(1): p. 315-499.
18. Kaufmann, A. and J. Krise, *Lysosomal Sequestration of Amine-Containing Drugs: Analysis and Therapeutic Implications*. Journal of Pharmaceutical Sciences, 2006. **96**(4): p. 729-746.
19. Logan, R., et al., *Amine-Containing Molecules and the Induction of an Expanded Lysosomal Volume Phenotype: A Structure-Activity Relationship Study*. Journal of Pharmaceutical Sciences, 2014. **103**: p. 1572-1580.
20. Funk, R. and J. Krise, *Cationic amphiphilic drugs cause a marked expansion of apparent lysosomal volume: implications for an intracellular distribution-based drug interaction*. Mol. Pharmaceutics, 2012. **9**(5): p. 1384-1395.
21. Logan, R., A. Kong, and J. Krise, *Time-Dependent Effects of Hydrophobic Amine-Containing Drugs on Lysosome Structure and Biogenesis in Culture Human Fibroblasts*. J. Pharm. Sci., 2014. **103**(10): p. 3287-3296.
22. Padda, M.S., et al., *Drug Induced Cholestasis*. Hepatology, 2011. **53**(4): p. 1377-1387.

23. Kostewicz, E., et al., *Predicting the precipitation of poorly soluble weak bases upon entry in the small intestine*. Journal of Pharmacy and Pharmacology, 2004. **56**: p. 43-51.
24. Naughton, C.A., *Drug-Induced Nephrotoxicity*. Am Fam Physician, 2008. **78**(6): p. 743-750.
25. Fogazzi, G., et al., *Amoxicillin, a rare but possible cause of crystalluria*. Images in Nephrology, 2003. **18**: p. 212-214.
26. Koop, J., et al., *Crystalluria and Urinary Tract Abnormalities Associated with Indinavir*. Annals of Internal Medicine, 1997. **127**(2): p. 119-125.
27. Murray, P.J. and T.A. Wynn, *Protective and pathogenic functions of macrophage subsets*. Nature Reviews Immunology, 2011. **11**(11): p. 723-737.
28. Yang, J., et al., *Monocyte and macrophage differentiation: circulation inflammatory monocyte as biomarker for inflammatory diseases*. Biomarker Research, 2014. **2**: p. 1-1.
29. Sunderkötter, C., et al., *Subpopulations of Mouse Blood Monocytes Differ in Maturation Stage and Inflammatory Response*. The Journal of Immunology, 2004. **172**(7): p. 4410-4417.
30. Epelman, S., K.J. Lavine, and G.J. Randolph, *Origin and Functions of Tissue Macrophages*. Immunity, 2014. **41**(1): p. 21-33.
31. Davies, L.C., et al., *Tissue-resident macrophages*. Nat Immunol, 2013. **14**(10): p. 986-995.
32. van Rooijen, N. and R. van Nieuwmegen, *Elimination of phagocytic cells in the spleen after intravenous injection of liposome-encapsulated dichloromethylene diphosphonate*. Cell and Tissue Research, 1984. **238**(2): p. 355-358.
33. van Rooijen, N. and E. Hendriks, *Liposomes for Specific Depletion of Macrophages from Organs and Tissues*, in *Liposomes*, V. Weissig, Editor. 2010, Humana Press. p. 189-203.
34. van Rooijen, N., J. Bakker, and N. Sanders, *Transient suppression of macrophage functions by liposome-encapsulated drugs*. Trends in Biotechnology, 1997. **15**(5): p. 178-185.

35. van Rooijen, N., N. Kors, and G. Kraal, *Macrophage subset repopulation in the spleen: differential kinetics after liposome-mediated elimination*. *J Leukoc Biol*, 1989. **45**(2): p. 97-104.
36. *Alveolar macrophage elimination in vivo is associated with an increase in pulmonary immune response in mice*. *The Journal of Experimental Medicine*, 1989. **170**(2): p. 499-509.
37. Fukutomi, Y., Y. Maeda, and M. Makino, *Apoptosis-Inducing Activity of Clofazimine in Macrophages*. *Antimicrobial Agents and Chemotherapy*, 2011. **55**(9): p. 4000-4005.
38. Repnik, U., M.H. Česen, and B. Turk, *The Endolysosomal System in Cell Death and Survival*. *Cold Spring Harbor Perspectives in Biology*, 2013. **5**(1).
39. Schmid, S.L., *CLATHRIN-COATED VESICLE FORMATION AND PROTEIN SORTING: An Integrated Process*. *Annual Review of Biochemistry*, 1997. **66**(1): p. 511-548.
40. Jovic, M., et al., *The early endosome: a busy sorting station for proteins at the crossroads*. *Histology and histopathology*, 2010. **25**(1): p. 99-112.
41. Piper, R.C. and J.P. Luzio, *Late Endosomes: Sorting and Partitioning in Multivesicular Bodies*. *Traffic*, 2001. **2**(9): p. 612-621.
42. Mindell, J.A., *Lysosomal Acidification Mechanisms*. *Annual Review of Physiology*, 2012. **74**(1): p. 69-86.
43. Hosogi, S., et al., *Cytosolic chloride ion is a key factor in lysosomal acidification and function of autophagy in human gastric cancer cell*. *Journal of Cellular and Molecular Medicine*, 2014. **18**(6): p. 1124-1133.
44. Finbow, M.E. and M.A. Harrison, *The vacuolar H⁺-ATPase: a universal proton pump of eukaryotes*. *Biochemical Journal*, 1997. **324**(Pt 3): p. 697-712.
45. Beyenbach, K.W. and H. Wieczorek, *The V-type H⁺ ATPase: molecular structure and function, physiological roles and regulation*. *Journal of Experimental Biology*, 2006. **209**(4): p. 577-589.
46. Lafourcade, C., et al., *Regulation of the V-ATPase along the Endocytic Pathway Occurs through Reversible Subunit Association and Membrane Localization*. *PLoS ONE*, 2008. **3**(7): p. e2758.

47. Ndolo, R.A., M.L. Forrest, and J.P. Krise, *The role of lysosomes in limiting drug toxicity in mice*. J Pharmacol Exp Ther, 2010. **333**(1): p. 120-8.
48. Dietz, K.J., et al., *Significance of the V-type ATPase for the adaptation to stressful growth conditions and its regulation on the molecular and biochemical level*. Journal of Experimental Botany, 2001. **52**(363): p. 1969-1980.
49. Xu, H. and D. Ren, *Lysosomal physiology*. Annu Rev Physiol, 2015. **77**: p. 57-80.
50. Kasper, D., et al., *Loss of the chloride channel ClC-7 leads to lysosomal storage disease and neurodegeneration*. European Molecular Biology Organization, 2005. **24**(5).
51. Leisle, L., et al., *ClC-7 is a slowly voltage-gated 2Cl(-)/1H(+)-exchanger and requires Ostm1 for transport activity*. The EMBO Journal, 2011. **30**(11): p. 2140-2152.
52. Ohgi, K., et al., *Antibodies against ClC7 inhibit extracellular acidification-induced Cl⁻ currents and bone resorption activity in mouse osteoclasts*. Naunyn-Schmiedeberg's Archives of Pharmacology, 2011. **383**(1): p. 79-90.
53. Edwards, J. and C. Kahl, *Chloride Channels of Intracellular Membranes*. FEBS Letters, 2010. **584**(10): p. 2102-2111.
54. Mehta, A., *CFTR: More than just a chloride channel*. Pediatric Pulmonology, 2005. **39**(4): p. 292-298.
55. Gadsby, D.C., G. Nagel, and T. Hwang, *The CFTR Chloride Channel of Mammalian Heart*. Annual Review of Physiology, 1995. **57**(1): p. 387-416.
56. Di, A., et al., *CFTR regulates phagosome acidification in macrophages and alters bactericidal activity*. Nat Cell Biol, 2006. **8**(9): p. 933-944.
57. Abe, K. and R. Puertollano, *Role of TRP Channels in the Regulation of the Endosomal Pathway*. Physiology (Bethesda, Md.), 2011. **26**(1): p. 14-22.
58. Zeevi, D.A., A. Frumkin, and G. Bach, *TRPML and lysosomal function*. Biochimica et Biophysica Acta (BBA) - Molecular Basis of Disease, 2007. **1772**(8): p. 851-858.

59. Grimm, C., et al., *Role of TRPML and Two-Pore Channels in Endolysosomal Cation Homeostasis*. Journal of Pharmacology and Experimental Therapeutics, 2012. **342**(2): p. 236-244.
60. Miller, A., et al., *Mucopolipidosis Type IV Protein TRPML1-Dependent Lysosome Formation*. Traffic, 2015. **16**(3): p. 284-297.
61. Cheng, X., et al., *Mucopolipins: Intracellular TRPML1-3 Channels*. FEBS letters, 2010. **584**(10): p. 2013-2021.
62. Napolitano, G. and A. Ballabio, *TFEB at a glance*. Journal of Cell Science, 2016.
63. Martina, J.A., et al., *TFEB and TFE3 are novel components of the integrated stress response*. Embo j, 2016. **35**(5): p. 479-95.
64. Raben, N. and R. Puertollano, *TFEB and TFE3: Linking Lysosomes to Cellular Adaptation to Stress*. Annu Rev Cell Dev Biol, 2016. **32**: p. 255-278.
65. Roczniak-Ferguson, A., et al., *The Transcription Factor TFEB Links mTORC1 Signaling to Transcriptional Control of Lysosome Homeostasis*. Science Signaling, 2012. **5**(228): p. ra42-ra42.
66. Peña-Llopis, S., et al., *Regulation of TFEB and V-ATPases by mTORC1*. Embo j, 2011. **30**(16): p. 3242-58.
67. Zhitomirsky, B. and Y.G. Assaraf, *Lysosomal sequestration of hydrophobic weak base chemotherapeutics triggers lysosomal biogenesis and lysosome-dependent cancer multidrug resistance*. Oncotarget, 2015. **6**(2): p. 1143-56.
68. Logan, R., A.C. Kong, and J.P. Krise, *Time-Dependent Effects of Hydrophobic Amine-Containing Drugs on Lysosome Structure and Biogenesis in Cultured Human Fibroblasts*. Journal of Pharmaceutical Sciences, 2014. **103**(10): p. 3287-3296.
69. Zhitomirsky, B. and Y.G. Assaraf, *Lysosomal accumulation of anticancer drugs triggers lysosomal exocytosis*. Oncotarget, 2017. **8**(28): p. 45117-32.

70. Schulz, P., et al., *The G215R Mutation in the Cl(-)/H(+)-Antiporter ClC-7 Found in ADO II Osteopetrosis Does Not Abolish Function but Causes a Severe Trafficking Defect*. PLoS ONE, 2010. **5**(9): p. e12585.
71. Malekova, L., et al., *Inhibitory effect of DIDS, NPPB, and phloretin on intracellular chloride channels*. Pflügers Archiv - European Journal of Physiology, 2007. **455**(2): p. 349-357.
72. Lukacs, G.L., et al., *The chloride channel blocker 5-nitro-2-(3-phenylpropyl-amino) benzoic acid (NPPB) uncouples mitochondria and increases the proton permeability of the plasma membrane in phagocytic cells*. FEBS Letters, 1991. **288**(1-2): p. 17-20.
73. Huang, F., et al., *Calcium-activated chloride channel TMEM16A modulates mucin secretion and airway smooth muscle contraction*. Proceedings of the National Academy of Sciences of the United States of America, 2012. **109**(40): p. 16354-16359.
74. Kim, J.-A., et al., *Glibenclamide Induces Apoptosis through Inhibition of Cystic Fibrosis Transmembrane Conductance Regulator (CFTR) Cl⁻ Channels and Intracellular Ca²⁺ Release in HepG2 Human Hepatoblastoma Cells*. Biochemical and Biophysical Research Communications, 1999. **261**(3): p. 682-688.
75. Sheppard, D.N. and K.A. Robinson, *Mechanism of glibenclamide inhibition of cystic fibrosis transmembrane conductance regulator Cl⁻ channels expressed in a murine cell line*. The Journal of Physiology, 1997. **503**(Pt 2): p. 333-346.
76. *Effect of ATP-sensitive K⁺ channel regulators on cystic fibrosis transmembrane conductance regulator chloride currents*. The Journal of General Physiology, 1992. **100**(4): p. 573-591.
77. Kopeikin, Z., et al., *On the mechanism of CFTR inhibition by a thiazolidinone derivative*. The Journal of General Physiology, 2010. **136**(6): p. 659-671.
78. Melis, N., et al., *Revisiting CFTR inhibition: a comparative study of CFTR(inh)-172 and GlyH-101 inhibitors*. British Journal of Pharmacology, 2014. **171**(15): p. 3716-3727.
79. Feng, X., et al., *Drosophila TRPML Forms PI(3,5)P(2)-activated Cation Channels in Both Endolysosomes and Plasma Membrane*. The Journal of Biological Chemistry, 2014. **289**(7): p. 4262-4272.

80. Andrés, D., et al., *Depletion of Kupffer cell function by gadolinium chloride attenuates thioacetamide-induced hepatotoxicity: Expression of metallothionein and HSP70*. *Biochemical Pharmacology*, 2003. **66**(6): p. 917-926.
81. Huss, M. and H. Wieczorek, *Inhibitors of V-ATPases: old and new players*. *Journal of Experimental Biology*, 2009. **212**(3): p. 341-346.
82. Mattsson, J.P., et al., *Omeprazole and bafilomycin, two proton pump inhibitors: Differentiation of their effects on gastric, kidney and bone H⁺-translocating ATPases*. *Biochimica et Biophysica Acta (BBA) - Biomembranes*, 1991. **1065**(2): p. 261-268.
83. Bowman, E.J., A. Siebers, and K. Altendorf, *Bafilomycins: a class of inhibitors of membrane ATPases from microorganisms, animal cells, and plant cells*. *Proceedings of the National Academy of Sciences of the United States of America*, 1988. **85**(21): p. 7972-7976.
84. Dröse, S. and K. Altendorf, *Bafilomycins and concanamycins as inhibitors of V-ATPases and P-ATPases*. *The Journal of Experimental Biology*, 1997. **200**(1): p. 1-8.
85. Muroi, M., et al., *Folimycin (Concanamycin A), a Specific Inhibitor of V-ATPase, Blocks Intracellular Translocation of the Glycoprotein of Vesicular Stomatitis Virus before Arrival to the Golgi Apparatus*. *Cell Structure and Function*, 1993. **18**(3): p. 139-149.
86. Muroi, M., et al., *Folimycin (concanamycin A) and Bafilomycin A1, Inhibitors Specific for V-ATPase, Exert Similar but Distinct Effects on Intracellular Translocation and Processing of Glycoproteins*. *Bioscience, Biotechnology, and Biochemistry*, 1994. **58**(2): p. 425-427.
87. Hong, J., et al., *Nitric Oxide Production by the Vacuolar-Type (H⁺)-ATPase Inhibitors Bafilomycin A1 and Concanamycin A and Its Possible Role in Apoptosis in RAW 264.7 Cells*. *Journal of Pharmacology and Experimental Therapeutics*, 2006. **319**(2): p. 672-681.
88. Sparenega, S.B., *The Importance of Polarized Light Microscopy in the Analytical Setting*. *Microsc and Microanal*, 2008. **14**(Suppl 2): p. 1032-1033.
89. Mehta, S.B., M. Shribak, and R. Oldenbourg, *Polarized light imaging of birefringence and diattenuation at high resolution and high sensitivity*. *Journal of Optics*, 2013. **15**(9): p. 094007.
90. Inoué, S., *Polarization Microscopy*, in *Current Protocols in Cell Biology*. 2002, John Wiley & Sons, Inc. p. 27.

91. Massoumian, F., et al., *Quantitative polarized light microscopy*. Journal of Microscopy, 2003. **209**(1): p. 13-22.
92. Chen, P.-C., et al., *Measurement of linear birefringence and diattenuation properties of optical samples using polarimeter and Stokes parameters*. Optics Express, 2009. **17**(18): p. 15860-15884.
93. Oldenbourg, R. *Diattenuation*. [Internet] 2013 May 8 2015]; Available from: openpolscope.org/pages/Diattenuation.htm.
94. Harris, G., A. Verma, and R. Oldenbourg, *LC-PolScope*. 2014.
95. Oldenbourg, R. *Polarization state generated by universal polarizer*. Tutorials 2013 [cited 2015 8 May]; Available from: openpolscope.org/pages/PolarizationEllipseUniversalPolarizer.htm.

Chapter 2

A Role for Low Density Lipoprotein Receptor-Related Protein 1 in the Cellular Uptake of Tissue Plasminogen Activator in the Lungs

2.1 Relevance to Thesis

Microscopy and the development of reproducible, broadly applicable quantitative image analysis algorithms form the basis of one of the three aims of the research of this dissertation. Prior to designing and implementing image analysis algorithms to study the accumulation of clofazimine and stabilization of biocrystals in tissue and live cell samples, work was performed to compare and quantify the expression of the plasma membrane receptor low-density lipoprotein receptor-related protein 1 (LRP1) within lung and liver tissues following immunohistochemical staining with 3-3'-diaminobenzidine (DAB). Because of the organization of the two organs, with the liver being a much more dense, cellular organ and the lung having large, empty pockets of air, an analysis strategy was required that would account for this difference in tissue organization, while at the same time allowing for an accurate comparison of the levels of protein expression.

Because of the pigmentation of the DAB within the tissue sections, as well as the unique absorbance spectrum of the molecule itself, my own contribution to the work presented in this chapter involved isolating the specific signal contribution of the DAB within each tissue section and relating that to the expression of LRP1 within the organ. Through the use of various optical filters ranging from the far red range to the blue range, tissue background signal was eliminated, allowing us to accurately isolate the DAB staining from the unstained tissue components, which in turn, let us quantify the total percentage of tissue area that was stained for the protein of interest through thresholding and use of other quantitative image analysis methodologies. The strategies implemented in this image analysis methodology helped guide the image analysis of cells isolated from clofazimine treated animals discussed in chapters 6, 7, and 8, in particular, by showing that the pigmentation and absorbance of the chemical can be an appropriate parameter

to use in quantitative image analysis methodology. Additionally, the image analysis methodologies used to quantify tissue staining of a cellular target of interest developed here were further applied to design and implement quantification of cellular and tissue markers of both chemically tagged markers through DAB and fluorescently tagged cellular markers in both live cells and tissue cryosections.

2.2 Abstract

Using an *in vivo* mouse model and *ex vivo* murine whole organ cell suspensions, we examined the capability of the lungs to utilize LRP1 receptor-mediated endocytosis (RME) for the uptake of exogenous tPA with and without an LRP1 inhibitor, receptor associated protein (RAP), and quantitatively compared it to the liver. We also used a novel imaging technique to assess the amount LRP1 in sections of mouse liver and lung. Following intratracheal administration, tPA concentrations in the BALF declined over time following two-compartment pharmacokinetics suggestive of RME clearance mechanism. *Ex vivo* studies showed that lung and liver cells are similarly capable of tPA uptake via LRP1 RME which was reduced by ~50% by RAP. The comparable lung and liver uptake of tPA is likely due to equivalent amounts of LRP1 of which there was an abundance of LRP1 in alveolar epithelium. Our findings indicate that LRP1 RME is a candidate clearance mechanism for inhaled tPA which has implications for the development of safe and effective dosing regimens of inhaled tPA for the treatment of plastic bronchitis and other fibrin-inflammatory airway diseases in which inhaled tPA may have utility.

2.3 Introduction

Plastic bronchitis is a rare, primarily pediatric disease that is characterized by the formation of obstructive, exudative, inflammatory fibrin casts in the tracheobronchial tree [1–4]. Inhaled nebulized tPA (alteplase, Genentech, South San Francisco, CA, USA) is often clinically used off-label to treat acute exacerbations of PB [5–9]. tPA is a serine protease that degrades fibrin via the activation of plasminogen which yields plasmin and is used therapeutically to dissolve thrombus associated with MI, pulmonary embolism, and AIS [10–12]. For PB treatment, inhalation of tPA permits targeted delivery to the site of drug action which requires repeated administration into the airways [5].

The dosing regimen of inhaled tPA for PB treatment was derived from the weight-based adult intravenous regimen used in the treatment of MI or AIS. Systemic administration and clearance of tPA in adults has been well characterized [10–12]. The drug has a reported initial (α) half-life of 5 minutes that is followed by a more prolonged terminal (β) phase which is characteristic of a two-compartment model [13, 14] and follows non-linear pharmacokinetics [15, 16]. Its clearance from the systemic circulation occurs by hepatic RME via LRP1 and mannose receptors [12, 16–19] and RME likely contributes to the nonlinearity of tPA clearance [15, 16]. LRP1 is ubiquitous and is expressed on hepatocytes and many other cell types [20], including lung fibroblasts and macrophages [21, 22] and it has been detected in pneumocytes and bronchial epithelium [23]. To date, most of the pulmonary LRP1 related research has focused on the receptor's role in inflammatory lung disease [24], pulmonary function [25] and lung cancer [26].

To study the fate of tPA in the lungs, animal studies have been performed following IT administration of tPA. Following IT dosing, tPA is detectable in BALF of healthy mice up to several hours after dosing and fatal pulmonary hemorrhage occurred in a group of mice that received high, repeated doses of tPA ($> 1\text{mg/kg/d}$), suggesting that tPA may accumulate in the airways [27, 28]. Since LRP1 plays an essential role in the elimination of tPA from the systemic circulation, we hypothesized that pulmonary LRP1 will bind and transport inhaled tPA from the airway lumen into the epithelial cell lining, and potentially into the circulation. We previously reported that lower levels of LRP1 in the airways compared with the liver, may explain slower elimination of inhaled tPA in the lungs [29]. Here, we have expanded on the details of these findings and now show that lung LRP1 is abundant in type II alveolar epithelium through a combined approach of ex vivo studies and state-of-the-science imaging techniques. In addition, whole organ cell studies show that the lung has a similar capability as the liver for LRP1-mediated uptake of tPA. This knowledge has significant implications for improving understanding of the fate of therapeutic macromolecules in the airways as well as for the development of safe and effective dosing regimens of inhaled tPA for the treatment of PB and other fibrin-inflammatory airway diseases [30–32] in which inhaled tPA may have utility.

2.4 Materials and Methods

Animals. Male mice (C57BL/6; 8 weeks old) were purchased from the Jackson Laboratory (Bar Harbor, ME, USA) and housed for at least one week prior to experimentation. The animal protocols were reviewed and approved by the Institutional Animal Care and Use Committee of the University of Michigan in accordance with the principles of the National Institutes of Health Guide for the Care and Use of Laboratory Animals.

Isolation of Mouse Alveolar Epithelial Cells. Murine type II alveolar epithelial cells were isolated using the method developed by Corti et al. [33] and as previously described [34]. Briefly, following CO₂ euthanasia, the pulmonary vasculature was perfused, and the lungs were first filled with dispase (1mL; Worthington, Lakewood, NJ) and then low melting point agarose (1mL) and placed in ice-cold PBS to harden. The lungs were then submerged in dispase for 45 min before being minced and incubated in DMEM with 0.01% DNase for 10 min. A single-cell suspension was obtained by passing the lung mince over a series of nylon filters. Myeloid cells were removed by first incubating cells with biotinylated antibodies against CD32 and CD45 (BD Pharmingen, San Diego, CA) and then streptavidin-coated microbeads (Promega, Madison, WI), followed by negative selection using a magnetic tube separator. Mesenchymal cells were removed by overnight adherence in a Petri dish. Non-adherent AEC were plated on fibronectin-coated plates and cultured for 72 h in complete DMEM. At the time of harvest, media was removed, lysis buffer was added to the plate and samples were frozen (−80°C). The method is known to result in a sample that consists of approximately 93% and 95% type II cells by Papanicolaou staining, which detects the lamellar bodies of type II cells [35], and ultrastructural analysis, respectively.

Administration of Tissue Plasminogen Activator (tPA). Human recombinant tissue plasminogen activator (htPA; alteplase, Activase®, Genentech, South San Francisco, CA, USA) was formulated and nebulized for pulmonary delivery as previously described [36]. The collected aerosol was assayed by UV spectroscopy to determine protein concentration and the extent of protein aggregation [28, 36]. Using the protein concentration derived from this method, mice received a single IT dose (via the oral route) of 0.3mg/kg. For this, mice were anesthetized under isoflurane (Fluriso; Vet One, Boise, ID), placed on a rodent intubation table (Hallowell EMC, Pittsfield, MA, USA), and the vocal cords were visualized using an otoscope (Welch-Allyn Medical Products, Skaneateles Falls, NY, USA) [27, 28]. The tip of a gavage needle (22G,

Hallowell EMC) attached to a syringe containing a dose of either pf-mtPA or an equivalent volume of sterile saline was gently moved past the vocal cords and into the trachea; the dose was delivered by depression of the syringe's plunger. Following drug or saline administration, the mouse was held upright for approximately 5 s, after which it was returned to a cage and allowed to recover from anesthesia.

Collection of BALF and Blood Samples and Measurement of htPA. At each respective time point, mice were anesthetized with ketamine (50mg/kg) and xylazine (5 mg/kg) administered by intraperitoneal injection. A blood sample was collected via cardiac puncture into a heparinized tube which was centrifuged ($1000 \times g$, 4°C for 5 min) to generate plasma. These samples were stored (-80°C) until the time of assay. After the collection of the blood sample, a tracheotomy was performed. The BALF was collected by flushing $2 \times 400\mu\text{L}$ of PBS into the lung via the tracheal cannula. The BALF was centrifuged ($1000 \times g$, 4°C for 5 min) and the supernatant was collected and frozen (-80°C) until the time of assay. At the time of assay, samples were thawed on ice and the concentration of htPA was measured using an enzyme-linked immunosorbent assay (ELISA). For this, the wells of a 96-well microtiter plate were coated with $100 \mu\text{L}/\text{well}$ of capture antibody ($1 \mu\text{g}/\text{mL}$; rabbit anti-human tPA, Molecular Innovations, Novi, MI) and incubated for 1 h (37°C). The plate was washed with wash buffer (0.05% Tween-20 in 1X PBS, pH 7.2) using a 96-well plate washer (BioTek ELx405, Winooski, VT) three times after which blocking reagent (5% milk in 1X PBS 0.05% Tween-20 buffer) was added to each well. The plate was covered and incubated (1 h) at room temperature (RT) and the wash step was repeated. Upon completion of the second wash, standards (htPA, 0–1000 ng/mL) and diluted samples ($100 \mu\text{L}/\text{well}$) in duplicate were added to respective wells and the plate was covered and incubated (1 h, RT). The plate was washed again and $100 \mu\text{L}$ of detection antibody ($1\mu\text{g}/\text{mL}$; mouse anti-human tPA, Calbiochem, Gibbstown, NJ) was added to each well and the plate was covered and incubated (1 h, RT). Following this incubation, the plate was washed and $100 \mu\text{L}$ of a horseradish peroxidase (HRP) conjugated antibody ($1\mu\text{g}/\text{mL}$; goat anti-mouse IgG HRP, Millipore, Billerica, MA) was added to each well followed by incubation (20 min, RT) and the addition of TMB substrate solution ($100 \mu\text{L}/\text{well}$). The reaction was stopped by the addition of sulfuric acid ($100\mu\text{L}$ of 2N). The assay was previously validated to show no cross reactivity with rat or mouse tPA and the lower limit of detection was determined to be $10 \text{ ng}/\text{mL}$. The absorbance data were acquired using a ThermoMax microplate reader (Molecular Devices,

Sunnyvale, CA). The total tPA concentration of each sample was derived from the linear phase of the standard curve as analyzed by reader's software (Softmax PRO 4.1, Molecular Devices). The resulting mean BALF htPA concentration data were plotted as ln concentration versus time which revealed a pharmacokinetic profile with a biphasic elimination pattern indicative of a two-compartment model [14]. Best line fitting of the first five, initial (α) phase, ln concentration measurements and the last three, terminal (β) phase, ln concentration measurements were used to calculate the elimination rate constants (Kd) of each phase. The elimination half-life ($t_{1/2}$) of each phase was calculated by dividing 0.693 by the respective Kd.

Generation of Primary Cell Suspensions. Whole lung and liver organs were harvested from mice for generation of primary lung and liver cell suspensions. Mice were euthanized under CO₂ in a contained chamber and following thoracotomy and appendectomy, the organs were perfused blood free with PBS (Life Technologies, Carlsbad, CA, USA). Blood-cleared lungs and livers were excised en bloc, placed into DMEM high glucose media (Life Technologies) and were manually dispersed and passed through cell strainers to remove connective tissues. The resulting whole organ cell suspensions were then centrifuged ($800 \times g$, 4°C, for 5 min) to acquire primary cells. The pelleted cells were resuspended in PBS and residual red blood cells (RBC) were lysed with the addition of RBC lysis buffer (Sigma-Aldrich, St. Louis, MO, USA). The cell suspension was washed with PBS and centrifuged an additional three times after which the final cell suspensions were maintained in DMEM on ice. Primary lung and liver cells were stained with trypan blue and counted using an automated cell counter (Countess, C10227, Life Technologies). For the experiments, 20,000 cells were plated per well into 24-well plates in DMEM media and maintained at 37°C (5% CO₂).

Mouse Tissue Plasminogen Activator (mtPA) Treatment. In advance of tPA treatment, 400 nM of receptor associated protein (RAP, P30533, Molecular Innovations), an inhibitor of LRP1, or an equivalent volume of PBS was added to some cells and they were incubated (30 min, 5% CO₂, 37°C). Recombinant mtPA protein (P11214, Molecular Innovations, Novi, MI, USA) in doses of 25, 50, or 100 ng or an equivalent volume of PBS was added to whole lung and liver primary cells and the plates were incubated (5% CO₂, 37°C) for 30 min. Following incubation, the contents of each well were transferred to a microcentrifuge tube and centrifuged ($800 \times g$, 4°C, for 5 min). The supernatant was removed and stored (-80°C). Cell pellets were washed

with PBS and centrifuged again, after which wash buffer supernatant was removed and stored (-80°C). The final cell pellet was resuspended in radioimmunoprecipitation assay (RIPA) buffer (Sigma-Aldrich) and frozen (-80°C). Time course studies (0–30 min) of mtPA uptake by whole lung and liver cell suspensions in the presence and absence of RAP (400 nM) were done as described above following the addition of mtPA (50 ng).

Western Blotting. Frozen samples containing 10,000 whole cell lysates were eluted with Laemmle 2X sample buffer (Sigma-Aldrich) with 5% β -mercaptoethanol and separated by 10% SDS-PAGE (BioRad, Hercules, CA). Proteins were transferred to polyvinylidene fluoride (PVDF) membranes and blocked (5% milk in PBS with Tween-20 (Sigma-Aldrich)). Membranes were immunoblotted overnight (4°C) with a nti-mouse tPA (ASMTPA-GF, Molecular Innovations) and LRP1 (ab92544, Abcam, Cambridge, MA, USA) in 1:5000 and 1:15,000 dilutions (5% milk in PBS with Tween 20), respectively. Post immunoblotting, membranes were washed with PBST (PBS with Tween 20, three times for 5 min each). Then membranes were incubated with a horseradish peroxidaseconjugated secondary antibody (goat antirabbit, AQ132P, Millipore, Billerica, MA, USA) in 1:10,000 dilution (2 hours at RT). Signal detection was achieved using enhanced chemiluminescence (Pierce ECL Western Blotting Substrate, Thermo Scientific, 32106, Rockford, IL) and exposure to radiographic film (BioMax Light Film, Z370371, Kodak, Rochester, NY). The image was acquired using a Medical Film Processor Model SRX-101A (Konica Minolta) and Image J (ImageJ 1.44b, NIH, Bethesda, MD, USA) was used to quantify protein band density.

Measurement of mtPA Uptake by Lung and Liver Cell Suspensions. The concentration of mtPA in lung and liver cell lysates (intracellular fraction) and supernatants (extracellular fraction) was detected using mtPA total antigen assay ELISA kit (MTPAKT-TOT, Molecular Innovations). The mtPA concentrations of the samples were derived from the standard curve.

Immunohistochemistry. Existing C57BL/6 mouse and 13N159 macaque monkey lung and liver formalin fixed, paraffin embedded (FFPE) samples were sectioned at the University of Michigan Unit for Laboratory Animal Medicine and analyzed by immunohistochemical staining for LRP1. Heat-induced antigen retrieval of the sample sections was performed using Rodent Decloaker (RD913, Biocare Medical LLC, Concord, CA) and EDTA Decloaker (CB917, Biocare Medical). Tissue sections were then blocked with Peroxidized 1 (PX968M, Biocare Medical) and Rodent

Block M (RBM961, Biocare Medical). Immunohistochemical staining was assessed using a titer titration of the primary antibody (1:500, 1:1000, and 1:5000) and the pathologist determined that the 1:1000 dilution was optimal. Samples were incubated in monoclonal LRP1 antibody diluted 1:1000 (rabbit α -mouse ab92544, Abcam). Secondary and tertiary incubations were carried out with Rabbit-on-Rodent HRP-polymer (RMR622, Biocare Medical) and IntelliPATH Universal HRP Tertiary Reagent (IPT5002, Biocare Medical), respectively. LRP1 was detected and visualized using 3'3'-diaminobenzidine (DAB) (IntelliPATH FLX™ DAB Chromogen Kit, IPK5010, Biocare Medical) followed by DAB post-enhancing solution (DAB sparkle, DS830G, Biocare Medical). All sections were counterstained with hematoxylin (CAT Hematoxylin, CATHE-M, Biocare Medical). Negative control slides were also generated by omitting the DAB staining step.

Image Acquisition and Analysis. Digital images of stained and unstained lung and liver sections at 40 \times magnification were acquired on a Ti Eclipse inverted microscope (Nikon Instruments, Inc., Melville, NY, USA) using bright field optics under Kohler illumination. To acquire and quantify DAB stained images, a red filter (655 ± 30 nm), which corresponds to the absorbance peak of the background staining, and a blue filter (480 ± 30 nm), which corresponds to the absorbance peak of DAB, were used. The density of DAB staining is indicative of LRP1 receptor density. To analyze quantify DAB staining density all images were analyzed with ImageJ.

Statistical Analysis. Statistical analyses were performed using PRISM 6 software (GraphPad, La Jolla, CA, USA) and differences between groups and treatments were estimated by unpaired Student's t-test or ANOVA with post-hoc analyses, as appropriate. Dose-response was assessed by linear regression. A p-value of ≤ 0.05 was considered statistically significant.

2.5 Results

2.5.1 BALF Levels of Lung Delivered htPA Declined Over Time. Instillation of htPA into the mouse lung resulted in detectable levels of htPA that declined over time (Figure 1). At no time point was htPA detected in the blood. Pharmacokinetic fitting of the htPA log concentration-time data revealed that the change in htPA concentration was most consistent with a two-compartment model.

2.5.2 Antagonism of the LRP1 Receptor Reduced mtPA Uptake in Whole Lung Cell Suspensions. To determine the role of LRP1 on lung clearance of tPA, we proceeded to establish that the uptake of mtPA into primary murine lung and liver whole cell suspensions was affected by the presence of a known LRP1 inhibitor, receptor associated protein (RAP). Quantitation and representative Western blots of both lung and liver cell uptake of mtPA in the presence and absence of RAP are shown in Figure 2. The amount of mtPA uptake into lung, but not liver cells, was dose dependent ($r^2=0.823$, $p=0.155$, respectively). In both lung and liver, mtPA uptake was reduced by 20–67% in the presence of RAP.

2.5.3 Timecourse of mtPA Uptake in the Presence and Absence of RAP is Similar in the Lung and Liver. To further substantiate the role of LRP1 in the uptake of mtPA, we assessed the time course of mtPA uptake in lung and liver whole cell suspensions. Pre-treatment with RAP reduced LRP1-mediated uptake of mtPA in both lung and liver cells as measured by Western blot (Figure 3A and Figure 3B). This finding was corroborated by a corresponding increase in intracellular fraction mtPA levels as measured by ELISA (Figure 3C and 3D). Although initial (time 0) intracellular fraction concentrations were lower in liver than in lung cells (Student's t-test $p=0.036$), RAP inhibited mtPA uptake in both liver and lung cells (Figure 2-3E and 2-3F). Using the extracellular fraction mtPA concentrations that are less prone to degradation than intracellular fraction mtPA, the average percent RAP-mediated reduction in LRP1 uptake of mtPA over the entire 30 min time course was similar for the lung and liver cell suspensions, 58% and 52%, respectively.

2.5.4 Lung and Liver Cell Suspensions Have Similar Amounts of LRP1 Protein. The relative amounts of LRP1 in murine lungs and murine liver samples were quantified and displayed similar amounts of the receptor. Based on a linear relationship between the measured LRP1 protein density (Figure 4A and 4B) and cell number, densitometry data show that the LRP1 protein density per cell is similar (mean \pm S.D.: 1.2 ± 1.1 vs. 1.0 ± 0.78 , $p = 0.81$) in liver and lung cells, respectively. LRP1 was also detected in isolated type II alveolar epithelial cells (Figure 4C).

2.5.5 The Lung and Liver Have Similar Ratios of LRP1 Staining. As an independent measurement of the relative amounts of LRP1 protein in liver and lung cells, FFPE liver and lung tissue sections were immunohistochemically stained for LRP1. Brightfield images were

acquired using a transmitted light microscopy set up (Appendix A, Image Acquisition and Analysis Workflow) with two different wavelengths of light (655nm and 480nm) corresponding to the peak absorbance signal of the LRP1-specific probe (brown DAB staining), and the peak absorbance of the nonspecific, background tissue signal (Figure SI. 1). In the liver (Figure 5A), brown DAB staining corresponding to the distribution of LRP1 was ubiquitous across the section (also see Figure SI. 3A and SI. 3B). In the lung (Figure 5B), brown DAB staining corresponding to the distribution of LRP1 was localized along the epithelial lining of the alveoli and in macrophages (Figure SI. 3C and SI. 3D). Based on quantitative image analysis, the density of LRP1 staining over the cellular regions of liver and lung sections was not different between the two organs (Figure 5C). Image analysis of LRP1 stained 13N159 macaque lung and liver sections produced similar staining results (Figure SI. 4).

2.6 Discussion

Inhalation of nebulized tPA has therapeutic potential as a treatment for the rare, pediatric illness, PB [5–9]. However, very little is known about the transport of tPA following delivery into the airways. Here, we show that the concentration of IT administered tPA declined over time in the BALF and that the time-dependent tPA concentration change followed two-compartment pharmacokinetics with an estimated α -phase elimination half-life of 0.7h and an estimated β -phase elimination half-life of 5.8h. We cannot confirm nonlinear kinetics because we only tested one dose of tPA. However, similar to what has previously been reported [15], the BALF tPA concentration versus time curve showed an upward trend suggesting a zero-order component. This is consistent with RME [16, 17] and suggests that tPA is either degraded or removed from the airway space. Potentially contributing to the clearance of tPA in the airways, is the significant expression of pulmonary LRP1, which was primarily detected in the alveolar epithelium, at levels comparable to the liver. In addition, our data show that, in both lung and liver cell suspensions, the peak measured intracellular fraction tPA concentration occurred within 1 min of the application of tPA to the cells and this concentration was reduced by half within 10 min. This observation implies that LRP1-mediated uptake into cells occurs very quickly [16, 17] and likely contributes to the $\alpha t_{1/2}$ of tPA in the airways. The longer $\beta t_{1/2}$ may be attributable to the diffuse distribution of tPA in the lungs that is known to occur after IT administration [36, 37] and involves other clearance mechanisms such as mucociliary action which is categorized as

slow (Figure 6) because it can take several hours for macromolecules to be cleared from the airway by this process. Transcellular absorptive transcytosis is also reported to occur over hours [38] but, to date, there is no evidence that tPA is removed from the airway via this mechanism. Thus, we infer that LRP1-mediated binding and uptake contributes, at least in part, to the early clearance of tPA from the airways. This conclusion is supported by the rapid time course of the α phase of BALF clearance and by two other pieces of evidence: First, using a whole lung cell suspension model, that lung cells are capable of taking up tPA from the surrounding media via LRP1 to the same extent as liver cells; and second, state-of-the-science image analysis techniques, which permitted measurements of a cell-associated LRP1 signal following immunohistochemical staining. This revealed that the expression of LRP1 protein by cells from the lung was comparable to that of cells from the liver in both mice and macaque monkeys. Western blotting also showed an abundance of LRP1 in type II alveolar epithelial cells.

Our findings are important and relevant because they point to a potential mechanism for removal of inhaled tPA from the airways. The clearance mechanisms affecting the half-life of pulmonary delivered therapeutic macromolecules from the airways, via absorption, metabolism or other routes have not been fully elucidated [38–40]. However, there is evidence that these mechanisms are distinct from those that regulate small molecule and ion transport in the lungs [41, 42]. Therapeutic proteins have been successfully delivered to the lungs via inhalation but issues related to utility and safety have been raised [38, 43]. Nevertheless, technological advances in pulmonary drug formulation and devices for the delivery of macromolecules, including siRNA and DNA, are being made [44, 45]. This active area of drug development highlights the need for more mechanistic knowledge about the fate of therapeutic proteins in the lungs.

Endocytosis of tPA by LRP1 in the liver has been well studied and is known to result in the degradation of this protein [12, 16–18]. This process is essential for the regulation of tPA plasma concentrations, contributes to the short elimination for the systemically administered drug, and is a saturable process [15, 16]. In our study, the rate of intracellular processing of tPA in liver cells appeared to occur at a faster rate than that in lung cells. This was evidenced by longer α and β elimination half-lives compared with those of systemically administered tPA [13, 14] and the lower intracellular fraction concentrations of mtPA present in liver cells compared to

lung cells, with similar extracellular fraction concentrations across both cell types (see Figure 3). Given the functional differences of these organs, it is reasonable to expect that the pharmacokinetics of tPA endocytosis in the lungs will be somewhat different from that of the liver. However, since LRP1 appears to function in lung epithelial cells in the same manner as it does in hepatocytes, it is reasonable to hypothesize that RME followed by degradation of tPA [12, 16–18] is also active in the lung. Collectively, details of this process remain to be elucidated as RME of tPA in alveolar epithelium is not yet fully understood (Figure 6).

The importance of improving understanding of the mechanisms of the fate of lung delivered proteins is further illustrated by the broad functions of the receptors that bind tPA protein and/or that participate in RME (Figure 6). While delivery of therapeutic proteins to the lungs can result in cellular uptake via endocytic receptors and ultimately lead to degradation in lysosomes, this process can also initiate subsequent cell signaling pathways. In the context of LRP1, which is a transmembrane receptor responsible for the endocytosis and degradation of a number of ligands including metalloproteinases (MMP) and apolipoproteins [22, 24], it can function as a signaling receptor (Figure 6). The expression of LRP1 in the airway epithelium suggests an important but not yet fully understood physiological role in the lungs. Its ability to mediate MMP endocytosis and other extracellular matrix proteins may be particularly important in inflammatory conditions, like acute respiratory distress syndrome, in which the extracellular domain is shed and results in dysregulation of MMP homeostasis [24]. It is also worth noting that tPA-mediated activation of LRP1 can lead to activation of the ERK1/2 pathway [46, 47] with consequent effects on cell physiology [48]. In fact, depending on the cell type, the tPA-LRP1 interaction can trigger a range of different responses [12]. Activation of downstream signaling can also occur via other tPA receptor proteins such as annexin A2 and mannose receptors both of which have been detected on alveolar macrophages [23]. Accordingly, as the use of inhaled tPA for PB or other fibrin-inflammatory lung diseases advances, it will be important to assess whether LRP1 binding leads to downstream effects on cell function.

We acknowledge that there are limitations of our study. Experimentally, it is possible that the intracellular fraction may contain contamination by extracellular tPA that occurred during the separation process. However, the purpose of our studies was to evaluate the role of LRP1-mediated uptake in the lung rather than the specific mass action of tPA. Since any contamination

would likely occur to similar extent across all samples it has little impact on the interpretation of our results. Next, as previously mentioned, additional mechanisms likely contribute to the clearance of tPA in the lungs. This includes the mannose receptor which may contribute to α -phase elimination and is prevalent on alveolar macrophages [18, 49]. The LRP1 receptor is also expressed by macrophages [50] and we did not separately account for macrophage-mediated uptake of tPA in our model. We also elected to conduct the bulk of our study in an ex vivo murine model using a small dose of tPA that was directly applied to the cells. This did not permit assessment of mucociliary clearance which likely contributes to the β -phase of airway elimination. While we generated evidence of LRP1 in the airway epithelium of Macaque monkeys, we recognize that LRP1-RME of tPA in the airways will need to be confirmed using in vivo models including the human model so that we can confirm this mechanism.

In conclusion, the abundance of LRP1 in the alveolar epithelium suggests that there is a site accessible mechanism of elimination for inhaled tPA. Furthermore, our study found that exposure of whole lung cell suspensions to exogenous tPA resulted in LRP1-mediated uptake of tPA that followed a similar extent and time course to that which occurred in whole liver cell suspensions. Therefore, LRP1-mediated cellular uptake is a candidate mechanism responsible for the fate of tPA in the airways.

2.7 Acknowledgements

This study was supported, in part, by a grant (HD065594 to KAS) from the Eunice Kennedy Shriver National Institute of Child Health and Human Development (NICHD), a grant (HL071439 to KAS) from the National Heart, Lung and Blood Institute (NHLBI), and a grant (GM078200 to GRR) from the National Institute of General Medical Sciences (NIGMS). The content is solely the responsibility of the authors and does not necessarily represent the official views of the NICHD, NHLBI, NIGMS or the National Institutes of Health. We would like to acknowledge and thank Dr. Katherine Eichinger (Benz) and Nicholas Lackowski for their help with the in vivo mouse work and Dr. Ingrid Bergin of the University of Michigan Laboratory Animal Medicine Pathology core for her invaluable help and guidance with the LRP1 staining.

2.8 Figures

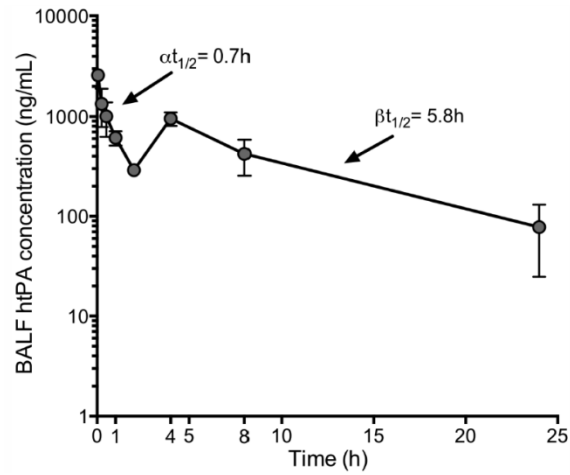


Figure 2-1 Human tissue plasminogen activator versus time in bronchoalveolar lavage fluid

Log_{10} concentration of human tissue plasminogen activator (htPA) versus time in bronchoalveolar lavage fluid (BALF) from mice that received a single intratracheal dose of nebulized htPA (0.3mg/kg). BALF was acquired from individual animals at each time point and at the same time an associated blood sample was obtained. Mice that received an equivalent volume of phosphate buffered saline (PBS) did not have detectable levels of htPA in the BALF and there was no detectable htPA in any of the blood samples from either htPA- or PBS-treated mice. The initial (α) elimination half-life ($t_{1/2}$) was followed by a more prolonged, terminal (β) $t_{1/2}$, which is indicative of a two-compartment model. Data are the mean (\pm S.E.M.) of 3-4 mice at each time point. htPA concentrations were determined by ELISA.

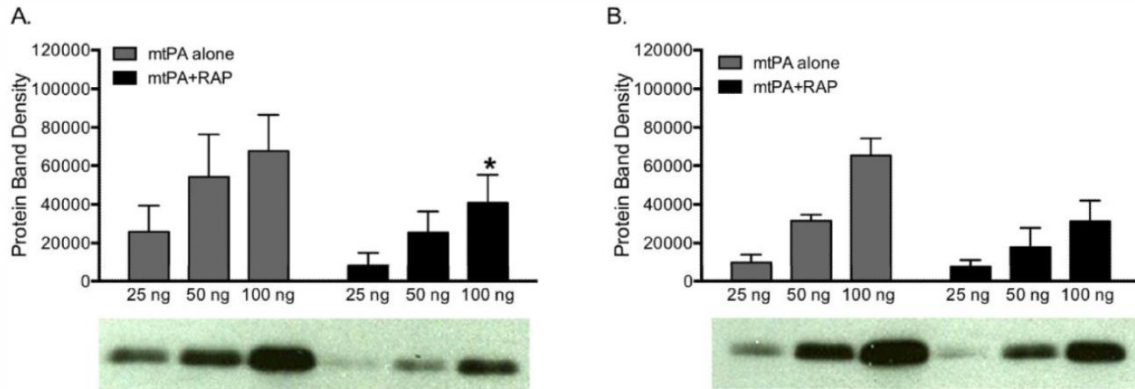


Figure 2-2 LRP1-mediated uptake of mtPA in murine whole lung and liver cell suspensions

Receptor associated protein (RAP) reduced LRP1-mediated uptake of mtPA in primary murine whole lung and liver cell suspensions. A total of 20,000 lung or liver cells in the presence or absence of LRP1 inhibitor, RAP (400 nM), were treated with mtPA (25-100 ng). A representative Western blot of intracellular fraction of mtPA and quantitated data from (A) primary liver cell suspension lysates and (B) primary lung cell suspension lysates show that RAP reduced the amount of intracellular fraction mtPA by an average of 67, 67, and 39% for 25, 50, and 100 ng of added mtPA, respectively, in liver cells and by an average of 20, 43, and 52% for 25, 50 and 100 ng of added mtPA, respectively, in lung cells. In the presence of RAP, the mean amount of mtPA (100 ng) was significantly lower in liver cells compared to the absence of RAP (* $p=0.014$ by ANOVA post-hoc Holm-Sidak test). In the lung, but not the liver, the mtPA dose response was significant by linear regression ($r^2=0.82$; $p<0.0001$ and $r^2=0.19$; $p=0.19$, respectively). Data are the mean (\pm S.E.M.) of 3-4 samples/group.

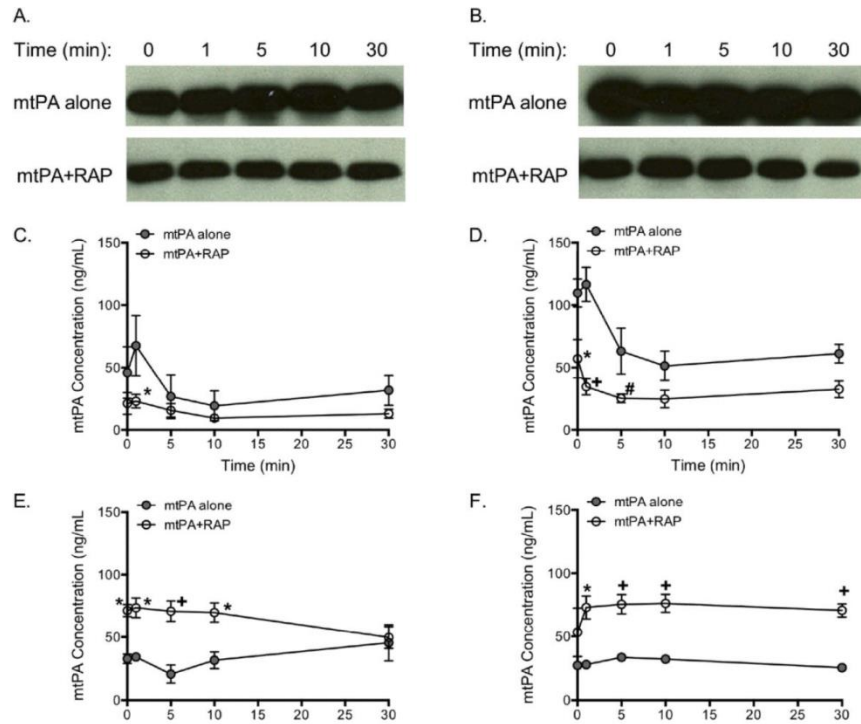


Figure 2-3 Concentration of intracellular mtPA in murine liver and lung cell suspensions

The concentration of intracellular fraction mtPA was lower over time in the presence of LRP1 inhibitor, receptor associated protein (RAP) in primary liver and lung cell suspensions (20,000 cells each). Cells were exposed to mtPA (50ng) at time 0 in the presence or absence of RAP (400nM). Representative Western blots of intracellular fraction mtPA over time in (A) primary whole liver cell lysates and (B) primary whole lung cell lysates. These findings were corroborated by the measurement of intracellular fraction mtPA concentrations measured by ELISA in (C) liver cell (*p=0.0132 at 1 min) and (D) lung cell (*p=0.009; +p<0.001; #p=0.066) lysates as well as in extracellular fraction (supernatant) media of (E) liver (*p=0.005; +p=0.0005) and (F) lung (*p=0.024; +p=0.001) cell suspensions. Data are the mean (\pm S.E.M.) of 3-4 samples/group and p values were generated from post ANOVA Holm-Sidak tests.

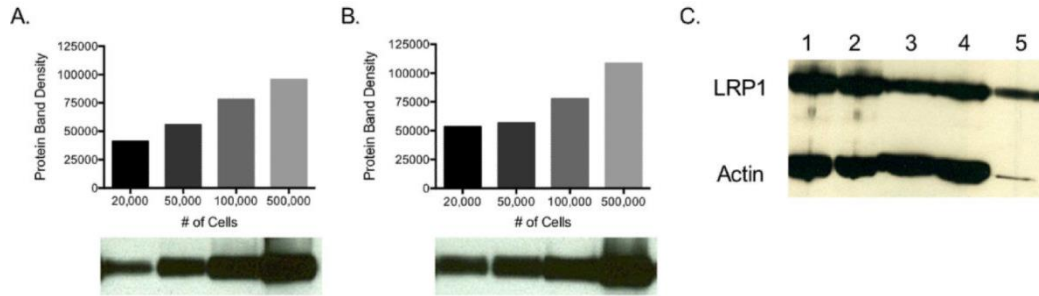


Figure 2-4 LRP1 protein quantification in murine liver and lung cells

Protein band density of LRP1 increases with increasing cell number in both murine whole liver and lung cells. Representative Western blot and quantitation of LRP1 in primary whole (A) liver cell and (B) lung cell lysates at cell densities from 20,000 to 500,000 cells. The correlation coefficient (r^2) for liver and lung LRP1 and cell number was 0.74 and 0.92, with p values of 0.13 and 0.04, respectively. (C) Representative Western blot of LRP1 in mouse type II alveolar epithelial cell (AEC) lysates with actin as a loading control. Lanes 1, 2: Mouse AEC (30 µg protein); Lanes 3, 4: Mouse AEC (20 µg protein); Lane 5: Mouse primary whole lung cell lysate (20,000 cells).

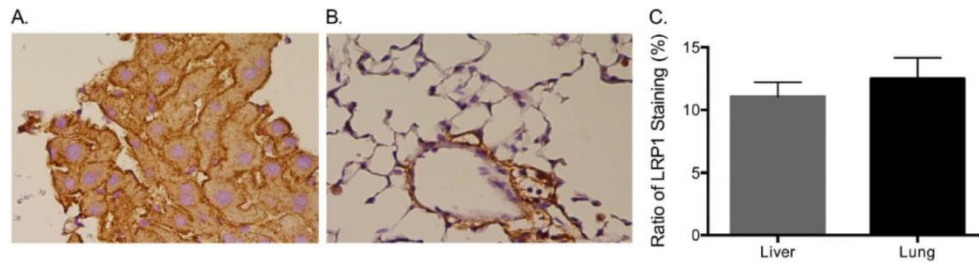


Figure 2-5 LRP1 tissue staining in liver and lung sections

The percent (%) tissue area with LRP1 staining in mouse liver and lung sections was similar. Representative color light micrographs of (A) liver and (B) lung sections (40X) stained for LRP1 using 3'3'-diaminozenzidene (DAB) as a chromogen lead to brown staining; see text for details. (C) Quantitative image analysis revealed that the % tissue area with LRP1 stain in liver and lung sections was not different ($p=0.483$ by unpaired Student's t-test). Data are mean (\pm S.E.M.) of 7 sections/group.

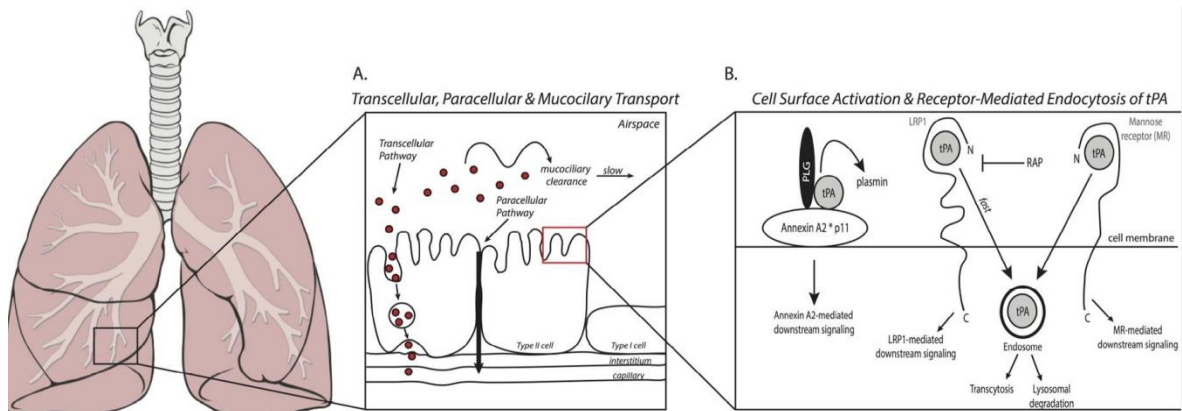


Figure 2-6 Macromolecular transport mechanisms within the lung

A number of transport mechanisms for macromolecules exist in the airways. **Panel A:** Transcellular transport can occur as either absorptive transcytosis or via transporter proteins (e.g., OAT P2B1) [42] and often involve movement of molecules through the cell, which can be a slow (hours) process [38]. Paracellular transport, in which macromolecules move through the airway epithelial barrier between cells, is thought to be a primary transport mechanism for small (≤ 40 kDa) proteins and can occur within minutes [39]. Mucociliary action is pivotal for maintaining the integrity of the airway environment and also serves as a mechanism for slow airway clearance of macromolecules [42]. **Panel B:** At the receptor level, membrane-associated tissue plasminogen activator (tPA) binding proteins include annexin A2 and p11 binding complex, LRP1 and the mannose receptor. The LRP1 and mannose receptors are transmembrane proteins which are the only known endocytic receptors for tPA [18, 49], the former of which can be blocked by receptor associated protein (RAP). Annexin A2 serves as the site where tPA assembles with plasminogen (PLG) for localized generation of plasmin [51]. Most abundant on endothelial cells, annexin A2 has been detected on macrophages and pneumocytes [23] and tPA binding to annexin A2 has been reported to lead to activation of downstream signaling pathways [47, 52]. The binding of tPA to LRP1, which is ubiquitous, and mannose receptors, which are prevalent on macrophages, is independent of tPA protease activity and can occur in the presence or absence of its primary physiological inhibitor, plasminogen activator inhibitor. Following tPA binding, the protein is endocytosed and packaged into endosomes. In the liver, this process leads to lysosomal degradation of tPA. Given this function and the abundance of LRP1 in the alveolar epithelium, it is reasonable to expect that the same occurs in the lung. In addition to the processing of macromolecules, activation of LRP1 and mannose receptors can trigger a cadre of downstream signaling events including the activation of ERK and MAP kinases [46, 53]. “Lungs diagram simple” by Patrick J. Lynch, medical illustrator - Patrick J. Lynch, medical illustrator. Licensed under CC BY 2.5 via Wikimedia Commons - http://commons.wikimedia.org/wiki/File:Lungs_diagram_simple.svg#mediaviewer/File:Lungs_diagram_simple.svg

2.9 Supporting Information Available

This material is published in *Pharmaceutical Research* and supplemental methods and figures are available in the Appendix A.

2.10 References

1. Heath L, Ling S, Racz J, Mane G, Schmidt L, Myers JL, Tsai WC, Caruthers RL, Hirsch JC, Stringer KA. Prospective, longitudinal study of plastic bronchitis cast pathology and responsiveness to tissue plasminogen activator. *Pediatric cardiology*. 2011; 32(8):1182–1189. [PubMed: 21786171]
2. Racz J, Mane G, Ford M, Schmidt L, Myers J, Standiford TJ, Schumacher KR, Fifer C, Russell MW, Stringer KA. Immunophenotyping and protein profiling of Fontan-associated plastic bronchitis airway casts. *Annals of the American Thoracic Society*. 2013; 10(2):98–107. [PubMed: 23607837]
3. Schumacher KR, Stringer KA, Donohue JE, Yu S, Shaver A, Caruthers RL, Zikmund-Fisher BJ, Fifer C, Goldberg C, Russell MW. Fontan-Associated Protein-Losing Enteropathy and Plastic Bronchitis. *The Journal of pediatrics*. 2015
4. Kunder R, Kunder C, Sun HY, Berry G, Messner A, Frankovich J, Roth S, Mark J. Pediatric plastic bronchitis: case report and retrospective comparative analysis of epidemiology and pathology. *Case reports in pulmonology*. 2013; 2013:649365. [PubMed: 23662235]
5. Brooks K, Caruthers RL, Schumacher KR, Stringer KA. Pharmacotherapy challenges of fontanassociated plastic bronchitis: a rare pediatric disease. *Pharmacotherapy*. 2013; 33(9):922–934. [PubMed: 23686915]
6. Costello JM, Steinhorn D, McColley S, Gerber ME, Kumar SP. Treatment of plastic bronchitis in a Fontan patient with tissue plasminogen activator: a case report and review of the literature. *Pediatrics*. 2002; 109(4):e67. [PubMed: 11927740]
7. Do TB, Chu JM, Berdjis F, Anas NG. Fontan patient with plastic bronchitis treated successfully using aerosolized tissue plasminogen activator: a case report and review of the literature. *Pediatric cardiology*. 2009; 30(3):352–355. [PubMed: 19005718]
8. Gibb E, Blount R, Lewis N, Nielson D, Church G, Jones K, Ly N. Management of plastic bronchitis with topical tissue-type plasminogen activator. *Pediatrics*. 2012; 130(2):e446–450. [PubMed: 22802609]
9. Lubcke NL, Nussbaum VM, Schroth M. Use of aerosolized tissue plasminogen activator in the treatment of plastic bronchitis. *The Annals of pharmacotherapy*. 2013; 47(3):e13. [PubMed: 23424228]

10. Collen D, Lijnen HR, Todd PA, Goa KL. Tissue-type plasminogen activator. A review of its pharmacology and therapeutic use as a thrombolytic agent. *Drugs*. 1989; 38(3):346–388. [PubMed: 2509190]
11. Loscalzo J, Braunwald E. Tissue plasminogen activator. *The New England journal of medicine*. 1988; 319(14):925–931. [PubMed: 3138537]
12. Kruithof EK, Dunoyer-Geindre S. Human tissue-type plasminogen activator. *Thrombosis and haemostasis*. 2014; 112(2):243–254. [PubMed: 24718307]
13. Seifried E, Tanswell P, Ellbruck D, Haerer W, Schmidt A. Pharmacokinetics and haemostatic status during consecutive infusions of recombinant tissue-type plasminogen activator in patients with acute myocardial infarction. *Thrombosis and haemostasis*. 1989; 61(3):497–501. [PubMed: 2508258]
14. Seifried E, Tanswell P, Rijken DC, Barrett-Bergshoeff MM, Su CA, Kluft C. Pharmacokinetics of antigen and activity of recombinant tissue-type plasminogen activator after infusion in healthy volunteers. *Arzneimittel-Forschung*. 1988; 38(3):418–422. [PubMed: 3132929]
15. Tanswell P, Heinzl G, Greischel A, Krause J. Nonlinear pharmacokinetics of tissue-type plasminogen activator in three animal species and isolated perfused rat liver. *The Journal of pharmacology and experimental therapeutics*. 1990; 255(1):318–324. [PubMed: 2120422]
16. Krippendorff BF, Kuester K, Kloft C, Huisinga W. Nonlinear pharmacokinetics of therapeutic proteins resulting from receptor mediated endocytosis. *Journal of pharmacokinetics and pharmacodynamics*. 2009; 36(3):239–260. [PubMed: 19554432]
17. Warshawsky I, Bu G, Schwartz AL. LRP and the receptor-mediated endocytosis of plasminogen activators. *Annals of the New York Academy of Sciences*. 1994; 737:70–87. [PubMed: 7944155]
18. Camani C, Kruithof EK. Clearance receptors for tissue-type plasminogen activator. *International journal of hematology*. 1994; 60(2):97–109. [PubMed: 7948967]
19. Bu G, Williams S, Strickland DK, Schwartz AL. Low density lipoprotein receptor-related protein/ alpha 2-macroglobulin receptor is an hepatic receptor for tissue-type plasminogen activator. *Proc Natl Acad Sci U S A*. 1992; 89(16):7427–7431. [PubMed: 1502154]

20. Lillis AP, Van Duyn LB, Murphy-Ullrich JE, Strickland DK. LDL receptor-related protein 1: unique tissue-specific functions revealed by selective gene knockout studies. *Physiol Rev.* 2008; 88(3):887–918. [PubMed: 18626063]
21. Moestrup SK, Gliemann J, Pallesen G. Distribution of the alpha 2-macroglobulin receptor/low density lipoprotein receptor-related protein in human tissues. *Cell and tissue research.* 1992; 269(3):375–382. [PubMed: 1423505]
22. Strickland DK, Gonias SL, Argraves WS. Diverse roles for the LDL receptor family. *Trends in endocrinology and metabolism: TEM.* 2002; 13(2):66–74. [PubMed: 11854021]
23. Uhlen M, Fagerberg L, Hallstrom BM, Lindskog C, Oksvold P, Mardinoglu A, Sivertsson A, Kampf C, Sjostedt E, Asplund A, Olsson I, Edlund K, Lundberg E, Navani S, Szigartyo CA, Odeberg J, Djureinovic D, Takanen JO, Hober S, Alm T, Edqvist PH, Berling H, Tegel H, Mulder J, Rockberg J, Nilsson P, Schwenk JM, Hamsten M, von Feilitzen K, Forsberg M, Persson L, Johansson F, Zwahlen M, von Heijne G, Nielsen J, Ponten F. Proteomics. Tissue-based map of the human proteome. *Science (New York, NY).* 2015; 347(6220):1260419.
24. Wygrecka M, Wilhelm J, Jablonska E, Zakrzewicz D, Preissner KT, Seeger W, Guenther A, Markart P. Shedding of low-density lipoprotein receptor-related protein-1 in acute respiratory distress syndrome. *American journal of respiratory and critical care medicine.* 2011; 184(4):438–448. [PubMed: 21471105]
25. Soler Artigas M, Loth DW, Wain LV, Gharib SA, Obeidat M, Tang W, Zhai G, Zhao JH, Smith AV, Huffman JE, Albrecht E, Jackson CM, Evans DM, Cadby G, Fornage M, Manichaikul A, Lopez LM, Johnson T, Aldrich MC, Aspelund T, Barroso I, Campbell H, Cassano PA, Couper DJ, Eiriksdottir G, Franceschini N, Garcia M, Gieger C, Gislason GK, Grkovic I, Hammond CJ, Hancock DB, Harris TB, Ramasamy A, Heckbert SR, Heliovaara M, Homuth G, Hysi PG, James AL, Jankovic S, Joubert BR, Karrasch S, Klopp N, Koch B, Kritchevsky SB, Launer LJ, Liu Y, Loehr LR, Lohman K, Loos RJ, Lumley T, Al Balushi KA, Ang WQ, Barr RG, Beilby J, Blakey JD, Boban M, Boraska V, Brisman J, Britton JR, Brusselle GG, Cooper C, Curjuric I, Dahgam S, Deary IJ, Ebrahim S, Eijgelsheim M, Francks C, Gaysina D, Granell R, Gu X, Hankinson JL, Hardy R, Harris SE, Henderson J, Henry A, Hingorani AD, Hofman A, Holt PG, Hui J, Hunter ML, Imboden M, Jameson KA, Kerr SM, Kolcic I, Kronenberg F, Liu JZ, Marchini J, McKeever T, Morris AD, Olin AC, Porteous DJ, Postma DS, Rich SS, Ring SM, Rivadeneira F, Rochat T, Sayer AA, Sayers I, Sly PD, Smith GD, Sood A, Starr JM, Uitterlinden AG, Vonk JM, Wannamethee SG, Whincup PH, Wijmenga C, Williams OD, Wong A, Mangino M, Marciante KD, McArdle WL, Meibohm B, Morrison AC, North KE, Omenaas E, Palmer LJ, Pietilainen KH, Pin I, Pola Sbreve Ek O, Pouta A, Psaty BM, Hartikainen AL, Rantanen T, Ripatti S, Rotter JJ, Rudan I, Rudnicka AR, Schulz H, Shin SY, Spector TD, Surakka I, Vitart V, Volzke H, Wareham NJ, Warrington NM, Wichmann HE, Wild SH, Wilk JB, Wjst M, Wright AF, Zgaga L, Zemunik T, Pennell CE, Nyberg F, Kuh D, Holloway JW, Boezen HM, Lawlor DA, Morris RW, Probst Hensch N, Kaprio J, Wilson JF,

- Hayward C, Kahonen M, Heinrich J, Musk AW, Jarvis DL, Glaser S, Jarvelin MR, Ch Stricker BH, Elliott P, O'Connor GT, Strachan DP, London SJ, Hall IP, Gudnason V, Tobin MD. Genome-wide association and large-scale follow up identifies 16 new loci influencing lung function. *Nature genetics*. 2011; 43(11):1082–1090. [PubMed: 21946350]
26. Meng H, Chen G, Zhang X, Wang Z, Thomas DG, Giordano TJ, Beer DG, Wang MM. Stromal LRP1 in lung adenocarcinoma predicts clinical outcome. *Clinical cancer research : an official journal of the American Association for Cancer Research*. 2011; 17(8):2426–2433. [PubMed: 21325077]
27. Lackowski NP, Pitzer JE, Tobias M, Van Rheen Z, Nayar R, Mosharaff M, Stringer KA. Safety of prolonged, repeated administration of a pulmonary formulation of tissue plasminogen activator in mice. *Pulmonary pharmacology & therapeutics*. 2010; 23(2):107–114. [PubMed: 19879371]
28. Stringer KA, Tobias M, Dunn JS, Campos J, Van Rheen Z, Mosharaff M, Nayar R. Accelerated dosing frequency of a pulmonary formulation of tissue plasminogen activator is well-tolerated in mice. *Clinical and experimental pharmacology & physiology*. 2008; 35(12):1454–1460. [PubMed: 18671720]
29. Stringer KA, Racz J, Heath L, Southard S, Lackowski NP, Tsai WC, Caruthers RL. Low Expression Of Low Density Lipoprotein Receptor-Related Protein (LRP)-1 In The Airway Contributes To The Slow Elimination Of Lung Delivered Tissue Plasminogen Activator (tPA). *American journal of respiratory and critical care medicine*. 2011; 183 30. Bauman KA, Wettlaufer SH, Okunishi K, Vannella KM, Stoolman JS, Huang SK, Courey AJ, White ES, Hogaboam CM, Simon RH, Toews GB, Sisson TH, Moore BB, Peters-Golden M. The antifibrotic effects of plasminogen activation occur via prostaglandin E2 synthesis in humans and mice. *The Journal of clinical investigation*. 2010; 120(6):1950–1960. [PubMed: 20501949]
31. Okunishi K, Sisson TH, Huang SK, Hogaboam CM, Simon RH, Peters-Golden M. Plasmin overcomes resistance to prostaglandin E2 in fibrotic lung fibroblasts by reorganizing protein kinase A signaling. *The Journal of biological chemistry*. 2011; 286(37):32231–32243. [PubMed: 21795691]
32. Millien VO, Lu W, Mak G, Yuan X, Knight JM, Porter P, Kheradmand F, Corry DB. Airway fibrinogenolysis and the initiation of allergic inflammation. *Annals of the American Thoracic Society*. 2014; 11(Suppl 5):S277–283. [PubMed: 25525732]
33. Corti M, Brody AR, Harrison JH. Isolation and primary culture of murine alveolar type II cells. *American journal of respiratory cell and molecular biology*. 1996; 14(4):309–315. [PubMed: 8600933]

34. Ballinger MN, Newstead MW, Zeng X, Bhan U, Horowitz JC, Moore BB, Pinsky DJ, Flavell RA, Standiford TJ. TLR signaling prevents hyperoxia-induced lung injury by protecting the alveolar epithelium from oxidant-mediated death. *Journal of immunology (Baltimore, Md : 1950)*. 2012; 189(1):356–364.
35. Chen J, Chen Z, Narasaraju T, Jin N, Liu L. Isolation of highly pure alveolar epithelial type I and type II cells from rat lungs. *Lab Invest*. 2004; 84(6):727–735. [PubMed: 15077123]
36. Dunn JS, Nayar R, Campos J, Hybertson BM, Zhou Y, Manning MC, Repine JE, Stringer KA. Feasibility of tissue plasminogen activator formulated for pulmonary delivery. *Pharmaceutical research*. 2005; 22(10):1700–1707. [PubMed: 16180128]
37. Foster WM, Walters DM, Longphre M, Macri K, Miller LM. Methodology for the measurement of mucociliary function in the mouse by scintigraphy. *Journal of applied physiology*. 2001; 90(3): 1111–1117. [PubMed: 11181627]
38. Patton JS, Brain JD, Davies LA, Fiegel J, Gumbleton M, Kim KJ, Sakagami M, Vanbever R, Ehrhardt C. The Particle has Landed-Characterizing the Fate of Inhaled Pharmaceuticals. *J Aerosol Med Pulm D*. 2010; 23:S71–S87.
39. Takano M, Kawami M, Aoki A, Yumoto R. Receptor-mediated endocytosis of macromolecules and strategy to enhance their transport in alveolar epithelial cells. *Expert opinion on drug delivery*. 2014:1–13.
40. Hastings RH, Folkesson HG, Matthay MA. Mechanisms of alveolar protein clearance in the intact lung. *American journal of physiology Lung cellular and molecular physiology*. 2004; 286(4):L679–689. [PubMed: 15003932]
41. Dobbs LG, Johnson MD. Alveolar epithelial transport in the adult lung. *Respiratory physiology & neurobiology*. 2007; 159(3):283–300. [PubMed: 17689299]
42. Sakamoto A, Matsumaru T, Yamamura N, Suzuki S, Uchida Y, Tachikawa M, Terasaki T. Drug Transporter Protein Quantification of Immortalized Human Lung Cell Lines Derived from Tracheobronchial Epithelial Cells (Calu-3 and BEAS2-B), Bronchiolar-Alveolar Cells (NCI-H292 and NCI-H441), and Alveolar Type II-like Cells (A549) by Liquid Chromatography-Tandem Mass Spectrometry. *Journal of pharmaceutical sciences*. 2015
43. Santos Cavaiola T, Edelman S. Inhaled insulin: a breath of fresh air? A review of inhaled insulin. *Clinical therapeutics*. 2014; 36(8):1275–1289. [PubMed: 25044021]

44. Weers JG, Bell J, Chan HK, Cipolla D, Dunbar C, Hickey AJ, Smith IJ. Pulmonary Formulations: What Remains to be Done? *J Aerosol Med Pulm D.* 2010; 23:S5–S23.
45. Hickey AJ. Back to the future: Inhaled drug products. *Journal of pharmaceutical sciences.* 2013; 102(4):1165–1172. [PubMed: 23381932]
46. Mantuano E, Lam MS, Gonias SL. LRP1 assembles unique co-receptor systems to initiate cell signaling in response to tissue-type plasminogen activator and myelin-associated glycoprotein. *The Journal of biological chemistry.* 2013; 288(47):34009–34018. [PubMed: 24129569]
47. Hu K, Yang J, Tanaka S, Gonias SL, Mars WM, Liu Y. Tissue-type plasminogen activator acts as a cytokine that triggers intracellular signal transduction and induces matrix metalloproteinase-9 gene expression. *The Journal of biological chemistry.* 2006; 281(4):2120–2127. [PubMed: 16303771]
48. Zhang C, An J, Strickland DK, Yepes M. The low-density lipoprotein receptor-related protein 1 mediates tissue-type plasminogen activator-induced microglial activation in the ischemic brain. *The American journal of pathology.* 2009; 174(2):586–594. [PubMed: 19147818]
49. Biessen EA, van Teijlingen M, Vietsch H, Barrett-Bergshoeff MM, Bijsterbosch MK, Rijken DC, van Berkel TJ, Kuiper J. Antagonists of the mannose receptor and the LDL receptor-related protein dramatically delay the clearance of tissue plasminogen activator. *Circulation.* 1997; 95(1): 46–52. [PubMed: 8994415]
50. Nilsson A, Vesterlund L, Oldenborg PA. Macrophage expression of LRP1, a receptor for apoptotic cells and unopsonized erythrocytes, can be regulated by glucocorticoids. *Biochemical and biophysical research communications.* 2012; 417(4):1304–1309. [PubMed: 22234309]
51. Luo M, Hajjar KA. Annexin A2 system in human biology: cell surface and beyond. *Seminars in thrombosis and hemostasis.* 2013; 39(4):338–346. [PubMed: 23483454]
52. Lin L, Wu C, Hu K. Tissue plasminogen activator activates NF-kappaB through a pathway involving annexin A2/CD11b and integrin-linked kinase. *Journal of the American Society of Nephrology: JASN.* 2012; 23(8):1329–1338. [PubMed: 22677557]
53. Liu Z, Ma Y, Moyer MP, Zhang P, Shi C, Qin H. Involvement of the mannose receptor and p38 mitogen-activated protein kinase signaling pathway of the microdomain of the integral

membrane protein after enteropathogenic *Escherichia coli* infection. *Infection and immunity*. 2012; 80(4): 1343–1350. [PubMed: 22290149]

Chapter 3

Massive Bioaccumulation and Self-Assembly of Phenazine Compounds in Live Cells

3.1 Relevance to Thesis

Studying the accumulation, biotransformation, and stabilization of intracellular biocrystals of clofazimine within live cells encompasses the overall scope of the three aims of the dissertation work presented here, as well as the central hypothesis guiding the work. Thus, studying how chemically similar, but distinct derivatives of clofazimine both accumulate within cultured macrophages, and become solubilized in different media conditions is an important first step in designing experiments to analyze the *in vivo* and *in vitro* stability of clofazimine biocrystals. In this study, chemical derivatives of clofazimine were synthesized and incubated with both macrophages and epithelial cells, revealing distinct differences in accumulation between the two groups of cells. Additionally, the accumulation of these chemicals, and subsequent intracellular aggregate formation was studied using polarized light microscopy. Using polarized light, the cellular accumulation pattern for each derivative was determined (i.e. if the cell formed insoluble ordered aggregates of the chemical). The accumulation of clofazimine, stabilization of intracellular aggregates, and their analysis with quantitative polarized light microscopy is further elaborated on and applied in chapters 5, 6, and 7, with different applications being utilized in each case. The chemical changes to the core clofazimine structure, unsurprisingly, altered its accumulation pattern within these cultured cells. As related to this thesis, my own contribution to the work presented in this chapter was to relate the visual changes in accumulation pattern within these cells detected via quantitative polarized light microscopy (i.e. the formation of an intracellular amorphous or insoluble aggregate) to a physical phenomenon (i.e. changes in the aqueous solubility of the phenazine derivative or solubility in the cellular media). To accomplish this, the solubility of each phenazine derivative was determined in cell culture media both in the

presence and absence of serum proteins to see if the observed differences in accumulation could be related to precipitation in the surrounding cellular media. It was determined that there was no specific correlation between the solubility of the derivative within the media and the cellular accumulation, hinting at a potential cellular mechanism behind the accumulation and sequestration of these phenazine compounds. The analysis methods and knowledge obtained from these experiments helped guide the work discussed further in chapters 6, 7, and 8, in particular the *in vivo* experiments related to clofazimine biocrystal stability.

3.2 Abstract

Clofazimine is an orally administered drug that massively bioaccumulates in macrophages, forming membrane-bound intracellular structures possessing nanoscale supramolecular features. Here, a library of phenazine compounds derived from clofazimine is synthesized and tested for ability to accumulate and form ordered molecular aggregates inside cells. Regardless of chemical structure or physicochemical properties, bioaccumulation is consistently greater in macrophages than in epithelial cells. Microscopically, some self-assembled structures exhibit a pronounced, diattenuation anisotropy signal, evident by the differential absorption of linearly polarized light, at the peak absorbance wavelength of the phenazine core. The measured anisotropy is well above the background anisotropy of endogenous cellular components, reflecting the self-assembly of condensed, insoluble complexes of ordered phenazine molecules. Chemical variations introduced at the R-imino position of the phenazine core lead to idiosyncratic effects on the compounds' bioaccumulation behavior as well as on the morphology and organization of the resulting intracellular structures. Beyond clofazimine, these results demonstrate how the self-assembly of membrane permeant, orally bioavailable small molecule building blocks can endow cells with unnatural structural elements possessing chemical, physical, and functional characteristics unlike those of other natural cellular components.

3.3 Introduction

In mammals, macrophages orchestrate many key physiological functions, including wound healing and regeneration, clearance of apoptotic and necrotic cells, recognition of foreign antigens, defense against invading pathogens, and mounting of protective immune responses [1-4]. In addition, macrophages play a physiological role in the disposition of lipophilic, poorly

soluble small molecule chemical agents. In the liver, for example, Kupffer cells sequester lipids, cholesterol, fat soluble vitamins, xenobiotics, and drugs [5-8]. Perhaps it is not too surprising that clofazimine, an old but highly effective antibiotic that is included in the World Health Organization's list of essential medications and part of the standard treatment of leprosy[9, 10], has been found to massively bioaccumulate in macrophages.⁴ In these cells, clofazimine forms crystal-like drug inclusions (CLDIs): highly organized, insoluble molecular complexes that are predominantly found in membrane-bound compartments within the cytoplasm[11, 12]. Although drug crystal formation has generally been regarded as an unwanted side effect, clofazimine is a well-tolerated, clinically useful drug. Thus, in the case of clofazimine, CLDIs may function as a biocompatible, intracellular drug depot mechanism. More generally, CLDI formation could be exploited as a means to target drugs to macrophages in living organisms and to endow these cells with unnatural structural and functional elements for diagnostic or therapeutic purposes.

Related to clofazimine, Neutral Red is a phenazine compound that undergoes accumulation in lysosomes [13], while Janus Green B is another phenazine compound that undergoes electrical potential dependent accumulation in mitochondria[14] . However, neither of these compounds exhibits the massive intracellular bioaccumulation or intracellular self-assembly properties that are characteristic of clofazimine[15]. Furthermore, because of differences in membrane partitioning, the transport mechanisms mediating the cellular uptake and intracellular distribution of clofazimine may be different from that of less lipophilic, more soluble phenazine derivatives [16, 17]. Therefore, to explore whether other phenazine compounds could provide a good a starting point for developing new kinds of self-assembling intracellular elements for drug delivery and bioimaging applications, we decided to examine the impact of variations in lipophilicity and chemical structure on the intracellular uptake and trafficking of phenazine compounds. For this purpose, we synthesized a small, focused library of phenazine derivatives of clofazimine, and assayed their bioaccumulation and self-assembly properties in RAW264.7 macrophages and Madin-Darby Canine Kidney (MDCK) epithelial cells.

Because phenazines are chromophores with a broad absorbance peak in the range of visible wavelengths, the interaction of the phenazine ring with monochromic, polarized light could be useful to specifically probe the intracellular accumulation, distribution, and molecular

organization of the phenazine compounds. Accordingly, a quantitative polarization microscope (LC-PolScope) [18-20] was adapted to assay the formation of condensed, ordered molecular aggregates of the compounds in live cells. With this instrument, we measured the manner in which the intracellular inclusions differentially influenced the transmittance of polarized light—an optical property known as diattenuation anisotropy [21]. By relating the extent of bioaccumulation to the measured optical properties of the intracellular inclusions formed by different phenazine derivatives, we determined that certain chemical modifications at the R-imino group promoted the self-assembly of phenazines, specifically in macrophages. The influence of these variations on bioaccumulation and structure formation seemed highly idiosyncratic. However, all compounds tended to preferentially accumulate in macrophages relative to epithelial cells, regardless of their chemical structure or physicochemical properties.

3.4 Materials and Methods

Materials for Chemical Synthesis. The starting materials, reagents, and solvents for the synthesis were purchased from Sigma Aldrich, Fisher Scientific Acros, Oakwood Products or Chem-Impex and used as such without purification. Biotage Initiator Classic, single-mode Microwave Synthesizer was used for Microwave Syntheses. Compounds were purified by either Column Chromatography using Silicycle's SiliaFlash P60 (220–240 mesh) under positive house nitrogen pressure or Silicycle or Biotage prepacked flash columns using Biotage SP1 Flash System using two solvent gradient system. Solvent/Reagent Abbreviations or Formulae used: DCM, dichloromethane; EtOH, ethanol; EtOAc, ethyl acetate; DMSO, dimethylsulfoxide; MeCN, acetonitrile; AcOH, acetic acid; K₂CO₃, potassium carbonate; KF, potassium fluoride; Na₂SO₄, sodium sulfate; KOH, potassium hydroxide; FeCl₃, ferric chloride; HCl, hydrochloric acid; Pd/C, palladium on carbon. NMR spectra were recorded on either Varian MR 400 MHz, or Varian Inova 500 MHz spectrometer. Chemical shifts were reported in δ (parts per million) in reference to the hydrogen peaks of tetramethylsilane, $\delta = 0.00$. Mass spectra were recorded on a Micromass LCT Time-of-Flight instrument utilizing electrospray ionization in the positive ion mode (ESI⁺).

Synthesis of Phenazine Derivatives: Figure 1 represents the overall synthesis procedures of the phenazine compounds. With the previously reported methods (using reagents, (a) KF/K₂CO₃ or

(b) KOH/DMSO) [22, 23], niline derivatives **1** and 2-fluoronitrobenzene **2** were treated to produce the secondary amine derivatives **3** (*N*-(4-aryl)-2-nitroaniline). Using 10% Pd/C catalyst under hydrogen atmosphere, the nitro group in **3** was reduced to yield the diamine **4** (*N*-arylbenzene-1,2-diamine). Then, derivative **4** was oxidized [24, 25] in aqueous ferric chloride solution to produce the corresponding phenazine salts **5** (3-imino-*N*,5-bis(aryl)-3,5-dihydrophenazin-2-amine hydrochloride). Following treatments with various primary amines, the phenazine salts **5** yielded the corresponding phenazine derivatives **6** ((*E*)-3-(isopropylimino)-*N*,5-bis(aryl)-3,5-dihydrophenazin-2-amine) with 10%–85% yield.

Absorbance Measurements. Phenazine derivatives were solubilized at 0.1 mg mL⁻¹ in methanol and in 9 M H₂SO₄. The UV–vis spectra of the different phenazine derivatives in methanol and in acidic solutions of H₂SO₄ were obtained in 96 well plates, using a Biotek microplate spectrophotometer.

Physicochemical Property Predictions. Estimation of various physicochemical properties of clofazimine and its chemical derivatives which could be important for predicting their behaviors when those chemicals are confronted by cellular/suborganellar membranes were made as follows: Clog *P* (the calculated logarithm of lipid/water partitioning coefficient of nonionic (neutral) forms of the compound) were calculated by Chemaxon software from Marvin Beans (<http://www.chemaxon.com/marvin>). Clog *P* values of ionized species were calculated using the procedures described by Hansch and Leo [26]. Multiple p*K*_a (the dissociation constant of the protonated functional group) values (p*K*_{a1}, p*K*_{a2}, or p*K*_{a3}) were calculated for the ionizable functional groups (amines) in these weakly basic molecules. Other structure parameters were estimated as described in the next section [27, 28]

Predicting Cellular Uptake and Intracellular Localization of Phenazine Compounds.

Intracellular localization was predicted for each plausible ionic species of each phenazine compound as follow. For each species, structure parameter values, as estimated above, were inserted into published quantitative structure activity relationship (QSAR) models predicting cell uptake and intracellular localizations [27, 28]. The poor-moderate-good predictions in Tables S1, S3, and S5 relate to the Clog *P* of the major species present, usually the free base, as follows:

Poor: $\text{Clog } P > 8$ or $\text{Clog } P < 0$ [and/or number of rotatable bonds > 40]; moderate: $8 > \text{Clog } P > 5$; Good: $5 > \text{Clog } P > 0$.

Species close to prediction boundaries in parameter space are indicated by use of terms such as moderate-good [i.e., the species falls into the moderate zone but close to the boundary with the good zone]. Predictions assume that $\text{p}K_{\text{a}}$ values of basic groups are such that for most analogues a large proportion of each compound will be present in solution as a free base, with rather less as monocations, and even less as polycations, under physiological conditions. Polycations would only be present within acidic organelles. In Tables S1, S3, and S5: E = endoplasmic reticulum, C = cytosol, G = generic biomembranes, L = lysosome, M = mitochondrion, P = plasma membrane.

Cell Culture. RAW264.7 macrophages or MDCK (Madin Darby Canine Kidney) epithelial cells (strain II) were obtained from American Type Culture Collection (ATCC) (Manassas, VA) and cultured in 75 cm² flasks at 37 °C, 5% CO₂ containing humidified incubator. RAW264.7 macrophages (passage numbers 5–15) were grown in the medium containing Dulbecco's Modified Eagle Medium (DMEM (Gibco 11145); Invitrogen, Carlsbad, CA) with 2×10^{-3} M L-glutamine, 4500 mg L⁻¹ of D-glucose, 110 mg L⁻¹ of sodium pyruvate, 1% penicillin–streptomycin (Gibco 10378), and 10% fetal bovine serum (FBS; Gibco 10082). Confluent macrophage cells were detached by scraping and subcultured at 1:8 split ratios to culture flasks. MDCK cells (passage numbers 60–80) were cultured with growth medium consisting of DMEM supplemented with 1X nonessential amino acids (Gibco 11140), 1% penicillin–streptomycin, and 10% FBS. After reaching 70–80% confluence, MDCK cells were detached from the culture flasks using trypsin-ethylenediaminetetraacetic acid (trypsin-EDTA) solution and subcultured at a split ratio of 1:5. Media in the flask was replaced every 3 days.

Solubility Measurements. Solutions containing the phenazine derivatives were made in cell culture media (DMEM) with or without FBS (10%). After a 24 h incubation, the solutions were centrifuged (10 000 × g, 10 min), the supernatant was removed and the precipitate was dissolved in 9 M H₂SO₄. The supernatant was diluted with 10 M NaOH to precipitate the remaining solubilized compound. The diluted supernatant was centrifuged (10 000 × g, 10 min) followed by dissolution of the precipitate in 9 M H₂SO₄. Both fractions were spectrophotometrically

measured with a Biotek microplate spectrophotometer ($\lambda = 540$ nm) and phenazine content was determined using calibrated clofazimine standards.

Cytotoxicity Measurements. A 3'-bis(4-methoxy-6-nitro)benzene-sulfonic acid hydrate (XTT) colorimetric assay was performed to assess the cytotoxicity of the clofazimine derivatives in RAW264.7 macrophages or MDCK epithelial cells using a Cell Proliferation Kit II (Roche Chemicals, Indianapolis, IN). Briefly, the cells were seeded in 96 well plates at a cell density of 8×10^3 cells cm^{-2} (RAW264.7 macrophages) or 1.5×10^4 cells cm^{-2} (MDCK epithelial cells) and after a 24 h incubation (37 °C, 5% CO_2), cells were exposed to media containing various concentrations of clofazimine or its chemical derivatives (100 μL of 0.5×10^{-6} , 1×10^{-6} , 2×10^{-6} , 4×10^{-6} , 6×10^{-6} , 8×10^{-6} , 10×10^{-6} , 15×10^{-6} , 20×10^{-6} , 25×10^{-6} , 50×10^{-6} , or 100×10^{-6} m) in DMEM (no phenol red; Gibco 21063) with 5% FBS and 1×10^{-3} m sodium pyruvate. After 72 h incubation with clofazimine or its derivatives, compound-containing media was removed and cells were washed twice with media. The XTT labeling reagent (3'-bis(4-methoxy-6-nitro)benzene-sulfonic acid hydrate) was freshly mixed with the electron coupling reagent (PMS: *N*-methyl dibenzopyrazine methyl sulfate) before use according to the manufacturer's instructions. Cells were incubated in 100 μL of media (DMEM with 5% FBS) with XTT labeling mixture for 3 h (37 °C, 5% CO_2). The absorbance value in each well was measured at 495 nm against a reference wavelength at 650 nm using a microplate reader (Synergy 2, BioTek Instruments, Winooski, VT). The experiments were repeated in three different sets for the various concentrations of compounds. The IC₅₀ value for each compound was calculated from the concentration-response curve generated by a nonlinear regression (curve fit) method in GraphPad Prism version 5.0 (GraphPad Software, Inc., San Diego, CA). The concentration of clofazimine or its chemical derivatives used for further in vitro cell studies was determined based on cell viability (%) assay results (see the next section).

Cell Accumulation Experiments and Transmitted Light Microscopic Examination. For cell cultures, RAW264.7 macrophages or MDCK epithelial cells were seeded in the 8-well Nunc Lab-Tek II chambered (#1.5) coverglasses (Thermo Scientific, Pittsburgh, PA) at a cell density of 8×10^3 cells cm^{-2} or 1.5×10^4 cells cm^{-2} , respectively. After a 24 h incubation (37 °C, 5% CO_2), cells were incubated with solution of clofazimine or its chemical derivatives (300 μL of 5×10^{-6} m concentration; measured cell viability ranging from 85% to 97% for all compounds

tested at this concentration; Figure 1) in DMEM (no phenol red; plus 1×10^{-3} m sodium pyruvate and 5% FBS). For Compound “I,” 2.5×10^{-6} m of compound solution in media was used for the RAW 264.7 macrophages incubation because of lower cell viability at higher concentrations ($IC_{50} = (3.95 \pm 0.11) \times 10^{-6}$ m). A solution of clofazimine or other chemical derivatives was made by a diluting stock solutions (2.5×10^{-3} m in DMSO; 10×10^{-3} m stock in DMSO were stored at -80 °C for further use) into DMEM with 5% FBS. Previously, we reported that clofazimine did not form visible precipitates in this media (DMEM with 5% FBS) [15]. For other phenazine derivatives, precipitates were avoided by including FBS in the media. The extracellular concentration of each compound in each well was maintained by daily replacement of the compound-containing media. After 72 h of incubation with clofazimine or its derivatives, compound-containing media were removed and cells were washed twice with media. Live cells in the chambered glasses were examined under inverted transmitted light microscopy (Nikon Eclipse Ti microscope) with a 40× objective and color camera. As a control experiment, fixed cells were also microscopically examined after incubation with the compounds. Cells were seeded on the chambered cover glasses at the density of 1.5×10^4 cells cm^{-2} (RAW264.7 macrophages) or 2.5×10^4 cells cm^{-2} (MDCK epithelial cells). After an overnight incubation (37 °C, 5% CO_2), media was removed from the wells and cold methanol (-20 °C) was added to each well. After 30 s, remaining methanol was removed by washing with media with 5% FBS. Fixed cells were incubated (37 °C, 5% CO_2) with clofazimine or derivatives (300 μ L of 5×10^{-6} m; 2.5×10^{-6} m for I) in media with 5% FBS. After 72 h, fixed RAW264.7 or MDCK cells were washed with media and examined using the same transmitted microscopy conditions as the live cells.

Cell Associated Mass Measurements. RAW264.7 macrophages or MDCK epithelial cells were seeded in 96 well plates at the density of 8×10^3 cells cm^{-2} or 1.5×10^4 cells cm^{-2} , respectively. After an overnight incubation (37 °C, 5% CO_2), cells were incubated with 100 μ L of the media (DMEM with 5% FBS) containing 5×10^{-6} m clofazimine or its chemical derivatives (2.5×10^{-6} m of Compound “I”). Media containing each compound was replaced every day during the 72 h incubation. After the incubation, media was removed and cells were washed with Hank's balanced salt solution (HBSS) buffer (No. 14025; Invitrogen) twice. RAW264.7 macrophage cells in buffer were scraped and MDCK epithelial cells were exposed to Trypsin-EDTA solution for detachment from the plates for cell number counting and quantification of cell-associated

masses. After centrifugation ($650 \times g$), supernatant was removed and cell pellets were resuspended in 0.1 M citric acid/0.1 M trisodium citrate buffer (pH 5) for cell counting as previously reported (7). Equal numbers of cells in 100 μ L in buffer were transferred to 96 well plates and 100 μ L of detergent (ATCC, 30-1010K) was added into wells for cell lysis. Chemical absorbance from each well was measured by the UV-vis microplate reader (Synergy 2, BioTek Instruments, Winooski, VT) at 490 nm wavelength and cell-associated mass of each compound was calculated by a standard curve generated separately using the same media and presented as pmole/cell by normalizing the amount of chemical in each cell population sample by the number of cells in each sample.

Linear Diattenuation Microscopy Instrument Set Up. The LC-PolScope was first developed as a birefringence imaging system at the Marine Biological Laboratory (Woods Hole, MA) by Oldenbourg and colleagues, which greatly increased the sensitivity and analytic power of the polarized light microscope [18-20]. Recently, the technique was extended to include quantitative imaging of diattenuation and polarized fluorescence in biological and man-made specimens [21, 29]. For our studies of absorption properties of intracellular aggregates of phenazine derivatives, we used the diattenuation LC-PolScope as reported earlier [21] and described on the website OpenPolScope.org. The optical design was built on a Nikon Eclipse Ti microscope equipped with the liquid crystal universal compensator consisting of a linear polarizer and a pair of liquid crystal devices. The LC compensator was part of the transillumination path and was used to illuminate the specimen with monochromatic, linearly polarized light of varying polarization orientation. There was no polarization analyzer present in the imaging path. Quantitative intensity images were recorded by a charge-coupled device camera and a desktop computer calculated the average transmittance, the differential transmittance and the polarization orientation leading to maximum transmittance for each optically resolved picture element (pixel). Acquisition and processing steps were controlled using OpenPolScope plugins for the open source imaging programs ImageJ and Micro-Manager (MMStudio version 1.4.15). With the combination of hardware and software, polarized light images were acquired at high sensitivity and high spatial resolution for measuring linear diattenuation.

Linear Diattenuation Microscopy Data Acquisition and Analysis. After RAW264.7 macrophages or MDCK epithelial cells were incubated with the compound in the chambered

cover glasses for 72 h, at the same time of performing transmitted microscopic examination, cell specimens were examined under linear diattenuation microscopy using the Nikon Eclipse Ti microscope with 40×/0.75 NA objective and monochromatic light of two different center wavelengths, 546 and 623 nm (passband 30 nm). In the OpenPolScope software, Pol-Acquisition and Pol-Analyzer plugins (version 2.0) were used to capture, process, and analyze the attenuation images. Before imaging the samples, the setup was calibrated using a specially prepared slide featuring four small pieces of linear polarization filters. The transmission axes of the filters were oriented in steps of 45° providing a means to calibrate the LC universal compensator settings. After the calibration, a sample slide was inserted and first a sequence of polarized light images of a clear, fully transmitting sample area was recorded, followed by an image sequence featuring the cells under investigation. The images of the clear area were used to determine instrument factors which were needed for computing the average and the polarization dependent loss in transmittance in cellular components visible in the second image [21].

Linear diattenuation is a material property that can occur in materials such as crystals, in which the light absorbing molecules are arranged with a preferred orientation. The molecular alignment creates principal axes in the material denoting polarization directions for which light is maximally and minimally transmitted. Diattenuation is the difference between maximal (T_{\max}) and minimal (T_{\min}) transmittance, divided by their sum (Equation (1)).

To simultaneously measure the attenuation of many crystals with arbitrary orientations, we developed algorithms based on four specimen images, each recorded using light of a different polarization orientation: 0°, 45°, 90°, and 135° [21]. The four raw images were used to calculate the average and differential transmittance and the orientation of maximum transmittance in every resolved image pixel. To isolate and analyze quantitative data of the objects (crystals), the anisotropy or maximum transmittance axis orientation image file opened in ImageJ was inverted (Ctrl + Shift + I) and thresholded using ImageJ's default automatic method ("Binary" → "Convert to Mask"). By using the ImageJ's algorithm, "Analyze Particles," data of anisotropy or maximum transmittance axis orientation of objects in images could be obtained automatically. Diattenuation ratios were calculated by dividing anisotropy at 623 nm by that at 546 nm. For images obtained from cells incubated with Compounds, P, U, V, or W, maximum transmittance

axis orientation lines in crystals were displayed by using OpenPolScope's plugin (Orientation-LinesV3) installed in ImageJ.

Confocal Fluorescent Microscopy. A Nikon A1 confocal microscope was used for further investigation of live cells incubated with chiral pairs of compounds (T and U) and the parent compound, P. Since crystals or vesicular forms containing chemicals inside the cells incubated with Compound P, T, or U were fluorescent when viewed with the TRITC filter sets, intracellular distribution of these compounds in RAW264.7 or MDCK cells were visualized using a Nikon A1 confocal microscopy (Nikon Instruments Inc., Melville, NY) equipped with diode-based lasers and a Nikon Apo 60×/1.4 NA oil immersion lens. Briefly, RAW264.7 macrophages or MDCK epithelial cells were seeded in the 8-well Nunc Lab-Tek II chambered (#1.5) cover glasses (Thermo Scientific, Pittsburgh, PA) at a density of 8×10^3 cells cm^{-2} (RAW264.7 cells) or 1.5×10^4 cells cm^{-2} (MDCK cells) and allowed to adhere overnight (37 °C, 5% CO_2). Then, 5×10^{-6} M of Compound “P” or the related isomers, “T” or “U” in DMEM with 5% FBS (300 μL) was added to the cells and the cells were incubated for 72 h (37 °C, 5% CO_2). For live cell imaging, after the removal of media, cells were washed with HBSS buffer twice. Hoechst 33342 (Invitrogen, Carlsbad, CA) was used for staining cell nuclei and FM 1-43 (Molecular Probes T35356, Invitrogen) for the plasma membrane. Cells were incubated with 300 μL of 1:1 (v/v) dye mixtures of 5 $\mu\text{g mL}^{-1}$ Hoechst 33342 and 7×10^{-6} M FM 1-43 in HBSS for 15 min at room temperature. Without fixative, the confocal imaging of the live cells was performed using lasers for DAPI (excitation/emission wavelength: 405 nm/450 \pm 25 nm), FITC (488 nm/525 \pm 25 nm), and TRITC (561 nm/596 \pm 25 nm) channels. Z-stack images of the cells were captured along the Z-axis (interval, 1 μm) in three fluorescence channels and analyzed by using the Nikon NIS-Elements 3.2 confocal software (Nikon Instruments Inc., Melville, NY). In 3D reconstructions of the confocal sections assembled with the Nikon software, the cell nuclei fluoresced in the Hoechst/DAPI channel; the cell membranes fluoresced in the FITC channel; and, the intracellular inclusions fluoresced in the TRITC channel.

Transmittance and Optical Density (OD) Calculations. For calculating the differential transmittance of the inclusions, images at four different angles of polarization (0°, 45°, 90°, and 135°) were acquired by linear attenuation microscopy as described above. To measure transmittance, a threshold was applied to the mean transmitted image generated by the linear

attenuation microscopy data acquisition. This threshold was determined using the ImageJ Auto-thresholding protocol—Moments. Based on this threshold, a region of interest (ROI) image mask was generated, and then used to measure the mean transmittance (T_{mean}) of the ROIs, expressed as mean pixel value. To generate transmittance image maps and for quantitative measurement of transmittance, pixel values were converted to absolute values by dividing the mean pixel value by 255 (8-bit images). For the corresponding OD image maps and measurements, we used the following formula: $\text{OD} = -\log_{10}(T_{\text{mean}})$. For each compound a total of five images were measured from experiments performed on three separate days (>200 cells analyzed per compound).

Principal Component Analysis. An “optical properties score” was calculated for each replicate measurement ($n = 5$) for each compound in each cell type (RAW264.7 macrophages and MDCK epithelial cells), by combining the anisotropy and optical density values at 546 and 623 nm wavelengths. PCA plots [30] were generated using soft independent modelling in class analysis (SIMCA, <http://www.umetrics.com/products/simca>; Umeå, Sweden).

3.5 Results and Discussion

First, we synthesized a focused library of clofazimine derivatives (Figure 1), by replacing the chlorophenyl moieties of clofazimine with different aromatic substituents (Figure 1a and Table S1, Compounds A–G). When these compounds were incubated with cells, they exhibited similar or decreased intracellular staining relative to clofazimine, irrespective of their higher or lower lipophilicity relative to clofazimine (Figure 1a' and Table S2). Small changes in the chemical structure of clofazimine were associated with visibly different cellular staining pattern in macrophages. In this first series of phenazine compounds (Compounds A–G), the chlorophenyl moiety of clofazimine was replaced with various other closely related substituents, yet most of these substituents (Compounds A–F) led to decreased cellular staining in relation to clofazimine. Only the replacement of chlorines with hydroxyls led to a staining pattern similar to that of clofazimine (Compound G).

For comparison, we synthesized a second, focused series of derivatives, in which the isopropyl group at the R-imino position of clofazimine was replaced with different achiral substituents (Figure 2b and Table S3, Compounds H–Q). Compared to clofazimine, replacing

the isopropyl group with other functional groups at the R-imino position generally led to similar or greater staining of macrophages (Figure 2b' and Table S4, Compounds H–Q). Three derivatives yielded cellular staining patterns comparable in morphology and intensity to those of clofazimine (Compounds H, I, and M) while two derivatives yielded more prominent staining patterns (Compounds P and Q). The most intense staining was associated with the formation of condensed cytoplasmic inclusions, either amorphous or crystal-like in morphology (Figure 2b' and Table S4; Compounds P and Q).

To assess the extent to which specific interactions with chiral components present in cells (or the cell culture medium) affected the bioaccumulation and self-organization behavior of the compounds, we proceeded to synthesize and screen a third, focused series of phenazine derivatives, which incorporated a stereochemical center at the R-imino position (Figure 2c and Table S5, Compounds R–W). As observed in the second series of achiral R-imino phenazines, small variations in the chemical structure and physicochemical properties of these chiral R-imino phenazine compounds led to pronounced differences in cellular staining (Figure 2c' and Table S6). Three of the six chiral R-imino derivatives exhibited prominent cellular staining, associated with the formation of yellow, orange, red, or brown cytoplasmic inclusions (Figure 2c' and Table S6) Compounds U, V, and W). In control experiments, untreated cells showed no visible yellow or brown staining when viewed using the same optical set up under transmitted, brightfield illumination (Figure 2d, Control). Furthermore, staining was also not observed when cells were fixed prior to incubation with the compounds (Table S6), indicating that the observed staining patterns reflected underlying differences in physiological, small molecule transport mechanisms present in live cells. Because all phenazine compounds exhibited similar absorbance spectra under different conditions (Figure 3a, Figure 3b), the variations in cellular staining patterns most likely reflected differences in the accumulation and distribution of the compounds in the cells, independently from the compounds' optical properties.

Next, we proceeded to characterize the optical properties of the inclusions using a quantitative, polarization microscope [18-20] to perform diattenuation anisotropy measurements on cells incubated with the different compounds [21]. By transmitting linearly polarized, monochromatic light of wavelengths near the absorbance maxima of the phenazine molecules, the diattenuation anisotropy signal can be used to detect and quantify the presence of ordered

aggregates of phenazine molecules in live cells. For isotropic, disordered intracellular inclusions, polarized light is expected to be transmitted in the same manner irrespective of the orientation of the polarization vector, resulting in diattenuation anisotropy close to 0. For ordered intracellular inclusions of phenazine molecules (as occurs when molecules are aligned with each other), the diattenuation anisotropy should increase, as the ordered molecular aggregates will preferentially transmit light that is polarized in a particular direction. Accordingly, by comparing the diattenuation anisotropy image maps for treated and untreated control cells, we observed clear diattenuation anisotropy signals in association with dense inclusions formed specifically by phenazine compounds (see Compounds P, U, V, and W in Figure 4). Interestingly, Compounds U, V, and W exhibited optically anisotropic inclusions only in macrophages, whereas Compound P formed optically anisotropic inclusions in both macrophages (Figure 4a) and epithelial cells (Figure 4b). By visual inspection, we observed significant variations in the molecular organization of the inclusions formed by different compounds: Some compounds formed monolithic aggregates comprised of a single domain with uniform orientation (Compound P; Figure 4a, Figure 4b), while other compounds formed complex aggregates comprised of segregated domains with subdomains organized in different directions (Compounds U, V, and W; Figure 4a).

We quantitatively confirmed that Compounds P and Q showed higher diattenuation anisotropy in both macrophages and epithelial cells than seen with clofazimine (Figure 5a). Notably, chiral Compounds U, V, and W exhibited even higher anisotropy as compared to clofazimine but only in macrophages (Figure 5a). The measured diattenuation anisotropy signals for all chiral compounds were well above the background, diattenuation anisotropy signal of untreated cells (Figure 5a). On average, the anisotropy diattenuation ratio measured at a wavelength of 546 nm relative to 623 nm did not reveal significant wavelength-dependent differences in diattenuation anisotropy (Figure 5b), although some compounds exhibited higher variability in the measured diattenuation anisotropy ratios in macrophages than in epithelial cells (Figure 5; Compounds V and W).

In relation to the compounds' chemical structures, the self-assembly and resulting optical properties of intracellular structures formed by phenazine compounds appeared to be highly idiosyncratic: only one pair of enantiomers (Figure 4 and Figure 5a, Compounds T and U)

exhibited enantioselective differences in their optical anisotropy signal and this was observed only in macrophages. Compounds V and W did not show enantioselective differences in diattenuation anisotropy (Figure 6a, Figure 6b). The other pair of enantiomers (Compounds R and S) did not yield a measurable, diattenuation anisotropy signal in either macrophages or epithelial cells. Furthermore, Compound P, an achiral phenazine compound, formed inclusions with strong diattenuation anisotropy signals in both macrophages and epithelial cells (Figure 4 and 5), indicating that the formation of ordered, R-imino phenazine aggregates can occur regardless of stereochemistry.

To confirm the intracellular localization of the inclusions, we took advantage of the fluorescence properties of the phenazine Compounds P, T, and U. Following intracellular accumulation, these compounds exhibited strong fluorescence excitation and emission signals that were visible through the standard (tetramethylrhodamine isothiocyanate) TRITC channel of a fluorescence, confocal microscope. Accordingly, we acquired confocal optical sections through cells incubated with these compounds to confirm that the inclusions were intracellularly localized (Figure 6). For counterstaining, cells were also incubated with an orthogonally fluorescent nuclear marker (Hoechst 33342), as well as an orthogonally fluorescent, plasma membrane-specific marker (FM-143). FM-143 yielded a green, plasma membrane signal in the fluorescein isothiocyanate (FITC) channel of the microscope, while Hoechst 33342 yielded a blue, nuclear signal in the 4',6-diamidino-2-phenylindole (DAPI) channel. In both macrophages and epithelial cells, optical sections through the cells clearly revealed that Compounds P, T, and U (red signals) were localized at the periphery of the cell nuclei (blue signal) and within the confines of the cells' plasma membrane (green signal) (Figure 6).

To establish the extent to which the differences in staining and self-assembly of phenazine compounds may be due to cell type-dependent differences in bioaccumulation, the total amount of compounds present in macrophages (Figure 7a) and epithelial cells (Figure 7b) following an incubation period was measured and normalized by the number of cells. Overall, phenazine compounds tended to accumulate more in macrophages than in epithelial cells, regardless of ordered aggregate formation (Figure 7c). Nevertheless, compounds that exhibited the greatest accumulation in macrophages (Figure 7c, Figure 7d) also yielded the most ordered inclusions (Compounds P, Q, U, V, and W). To confirm the cell type-dependence of the

bioaccumulation and intracellular self-assembly properties of the phenazine compounds, principal component analysis (PCA) was performed on the cumulative bioaccumulation and diattenuation anisotropy data (Figure 8). Because the first two components of the resulting PCA plots captured >97% of the variation in the measured properties of the compounds in macrophages and epithelial cells (Figure 8) the PCA plot indicates that most of the observed variation was associated with cell type specific differences in bioaccumulation and diattenuation anisotropy, without a clear association with chirality, chemical structure or the lipophilicity of the compounds.

Finally, we tested whether the bioaccumulation of the compounds was related to the precipitation of the compounds in cell culture media or to their solubility. In serum containing media, solutions of clofazimine and the other phenazine compounds were stably solubilized at the concentrations that were added to the cells, so the formation of extracellular precipitates is an unlikely explanation for the measured differences in bioaccumulation in either macrophages (Figure 9a) or epithelial cells (Figure 9b). Only one of the phenazine analogs (Compound J) was not completely solubilized under these conditions. In the absence of serum (Figure 9c, Figure 9d), the phenazine compounds exhibited significant variation in their solubility with some of the compounds precipitating in the media. However, the solubility of the compounds did not show a correlation with the measured bioaccumulation in macrophages (Figure 9c) or epithelial cells (Figure 9d).

Considering the biological mechanisms that may account for the observed variations in bioaccumulation properties of phenazine compounds, clofazimine and other small molecule drugs can be subject to chemical transformation by metabolic enzymes. Furthermore, small organic molecules can also be substrates of active transport mechanisms. These metabolic and active transport mechanisms are differentially expressed in macrophages and epithelial cells and they are highly specific and sensitive to the presence of different functional groups on the compounds.

3.6 Conclusions

To conclude, our results demonstrate that, in addition to clofazimine, other membrane-permeant small molecule phenazine compounds can bioaccumulate and self-assemble in

macrophages, to a greater extent than in epithelial cells. Our results also demonstrate the use of monochromatic polarized light to measure diattenuation for monitoring the formation of ordered, insoluble complexes, which can be useful for assaying intracellular self-assembly of phenazine compounds. This is an advantage of this approach compared to other types of optical techniques that have been developed to detect the presence of insoluble drug complexes inside cells [31]. Indeed, with the quantitative polarization microscope, the presence of ordered molecular aggregates accompanying bioaccumulation of phenazine compounds was readily measurable and analyzable. Independently, we confirmed the bioaccumulation of the molecules by chemical analysis and the intracellular localization of the inclusions was confirmed with confocal microscopy by taking advantage of the compounds' fluorescence signals.

Similar to other structure–property relationship studies, our results demonstrate how the molecular organization of self-assembling intracellular elements can be analyzed in relation to specific chemical features of the individual, small molecule building blocks. Based on staining patterns, the uptake of clofazimine was inhibited by replacing its chlorophenyl group with different aromatic functionalities. Notably, modification of the R-imino group did not suppress intracellular inclusion formation. Instead, several R-imino phenazine derivatives exhibited greater bioaccumulation than clofazimine, forming highly condensed cytoplasmic inclusions, which exhibited strong diattenuation anisotropy signals. In addition, biological factors affecting the preferential bioaccumulation of phenazine molecules in macrophages exerted the most dominant effect on self-organization and intracellular inclusion formation, independently of the lipophilicity, solubility, and chirality of the molecules.

The condensation and phase separation of phenazine compounds into insoluble aggregates especially influences the bioaccumulation and retention of these compounds inside macrophages. In this regard, it is important to note that the measured concentration of phenazine compounds inside cells is far greater than one would expect from a nonspecific partitioning or a specific binding mechanism. For all the compounds that bioaccumulated inside cells, the measured numbers of phenazine molecules per cell ($>0.03 \pm 0.01$ picomoles) exceeded the amounts of the most concentrated, endogenous biomolecules and metabolites (e.g., adenosine triphosphate [32] or glutathione [33]). Only potassium and water are expected to be present in greater amounts [34, 35]. Considering the possibility that bioaccumulation may reflect the

partitioning of the molecules in membranes, there are in the order of 15 picograms of total lipids per leukocyte [36, 37]. This corresponds to 0.03 picomoles of total lipids per cell (calculated based on 500 g mol^{-1} of phospholipid). Interestingly, such intracellular precipitation behavior has been reported for other kinds of drugs [38]. In fact, the size, faceted shapes, and overall morphology of these inclusions are inconsistent with the typical size, shapes and morphology of natural organelles[31] and do not resemble the typical staining patterns of mitochondria[39, 40] or other cellular components stained with fluorescent probes[41]. Therefore, one can infer that in addition to cell type-specific differences in bioaccumulation, the propensity of poorly soluble phenazine molecules to aggregate into insoluble molecular complexes and phase separate from other cellular components also exerts an important influence on their intracellular disposition properties.

3.7 Acknowledgements

The authors acknowledge financial support from NIH (Grant R01GM078200 to G.R.R. and R01EB002583 to R.O.), a Rackham Predoctoral Fellowship Award to K.A.M., and University of Michigan M-Cubed funds awarded to K.A.S. and G.R.R.; R.W.H. thanks Dr. R. Aitken, School of Life Sciences, University of Glasgow for provision of facilities.

3.8 Figures

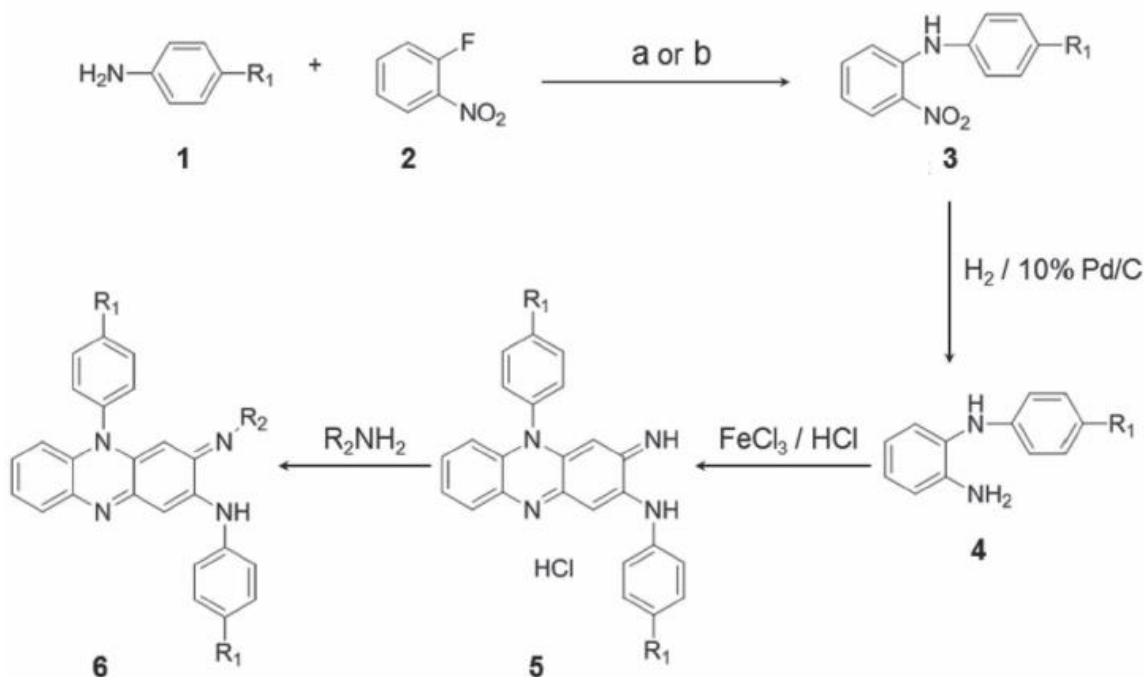


Figure 3-1 Synthesis scheme for phenazine derivatives

Synthesis of phenazine derivatives. Treatment of aniline derivatives **1** with 2-fluoronitrobenzene **2** (using reagents: a) KF/K₂CO₃ or b) KOH/DMSO) gave the secondary amine derivatives **3** in 22–63% yield. Reduction of the nitro group was carried out using 10% Pd/C catalyst under hydrogen atmosphere to yield the diamine **4** in 55–99% yield. Then the diamine **4** was oxidized in aqueous ferric chloride solution to give the corresponding phenazine salts **5** in 70–96% yield. The phenazine salts **5** on treatment with variety of primary amines gave the corresponding phenazine derivatives **6** in 10–85% yield. These methods are elaborated in detail in the Supporting Information.

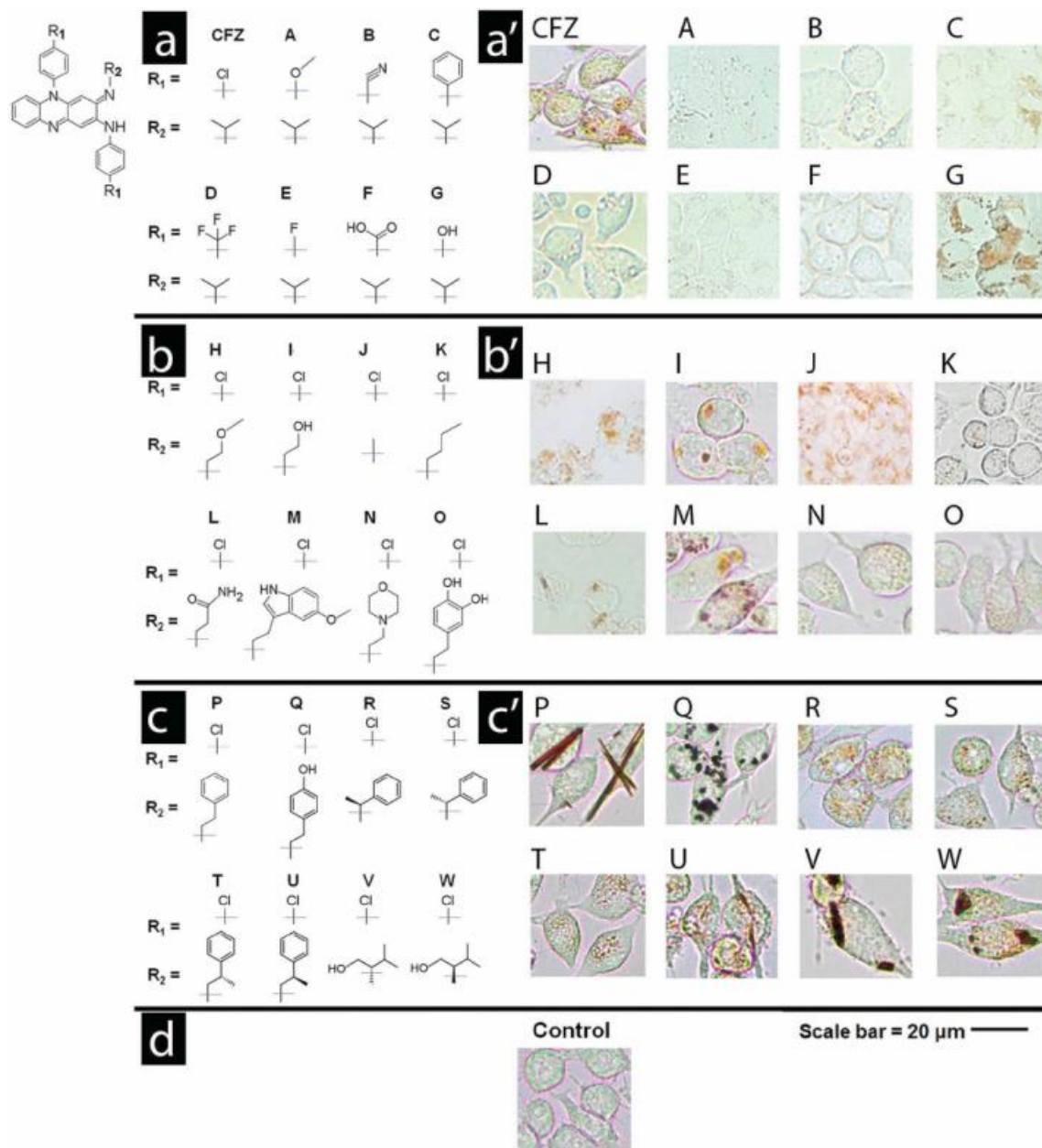


Figure 3-2 Phenazine derivatives and cellular staining patterns

Three series of phenazine derivatives of clofazimine were synthesized to probe the relationship between clofazimine's chemical structure a–c) and its cellular staining patterns a'–c'). The common phenazine core shared by all phenazine compounds is shown in the top left corner of the figure. In the first series of derivatives a,a'), the chlorophenyl groups of clofazimine were substituted with different functionalities. In the second series b,b'), the isopropyl R-imino group of clofazimine was substituted with achiral functional groups. In the third series c,c'), the isopropyl R-imino group of clofazimine was substituted with additional functional groups that probed the effects of an added stereochemical center. Scale bar = 20 μ m.

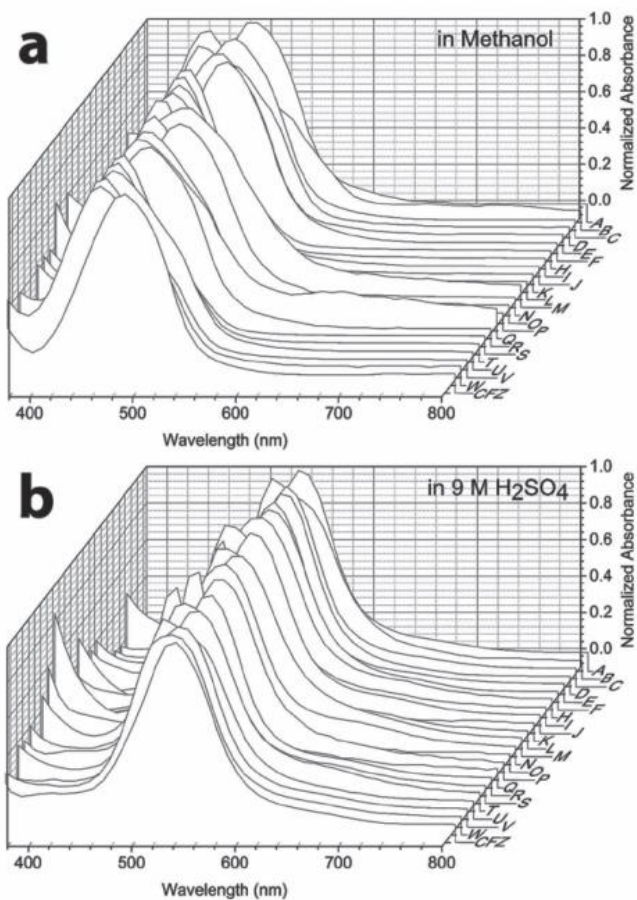


Figure 3-3 Absorbance spectra of phenazine compounds in methanol and sulfuric acid

Absorbance spectra of phenazine compounds were very similar to that of clofazimine. Absorption peaks were between 450 and 490 nm when measured in methanol and between 510 and 540 nm when measured in H₂SO₄.

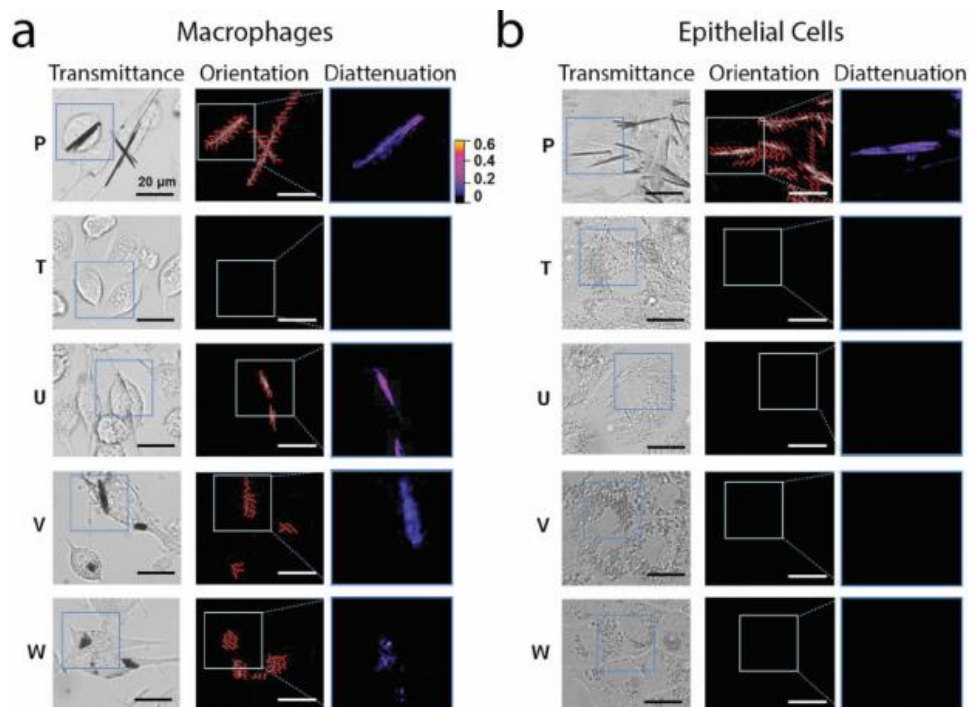


Figure 3-4 Quantitative polarization microscopy of cells incubated with phenazine derivatives

Quantitative polarization microscopy of macrophages and epithelial cells incubated with the different phenazine compounds revealed cell type-specific differences in transmittance, diattenuation anisotropy, and the orientation of the polarization axis maximal transmittance of the intracellular inclusions. For the experiments, live RAW264.7 macrophages a) or MDCK epithelial cells b) were incubated for 72 h with clofazimine or other phenazine analogs and analyzed with the diattenuation anisotropy microscope imaging set up, using monochromatic light of 546 nm wavelength. Transmittance corresponds to the image map of the transmitted light intensity at 546 nm wavelength (white corresponds to 100% transmittance and black corresponds to 0% transmittance) and orientation corresponds to the measured direction of maximal light transmittance of linearly polarized light across the sample, indicated with a grid of red lines superimposed on the image. Diattenuation corresponds to the quantitative diattenuation anisotropy image map measured using linearly polarized light of 546 nm wavelength. The color-gradient calibration bar corresponds to diattenuation anisotropy values ranging from 0 to 0.6. Scale bar = 20 μm .

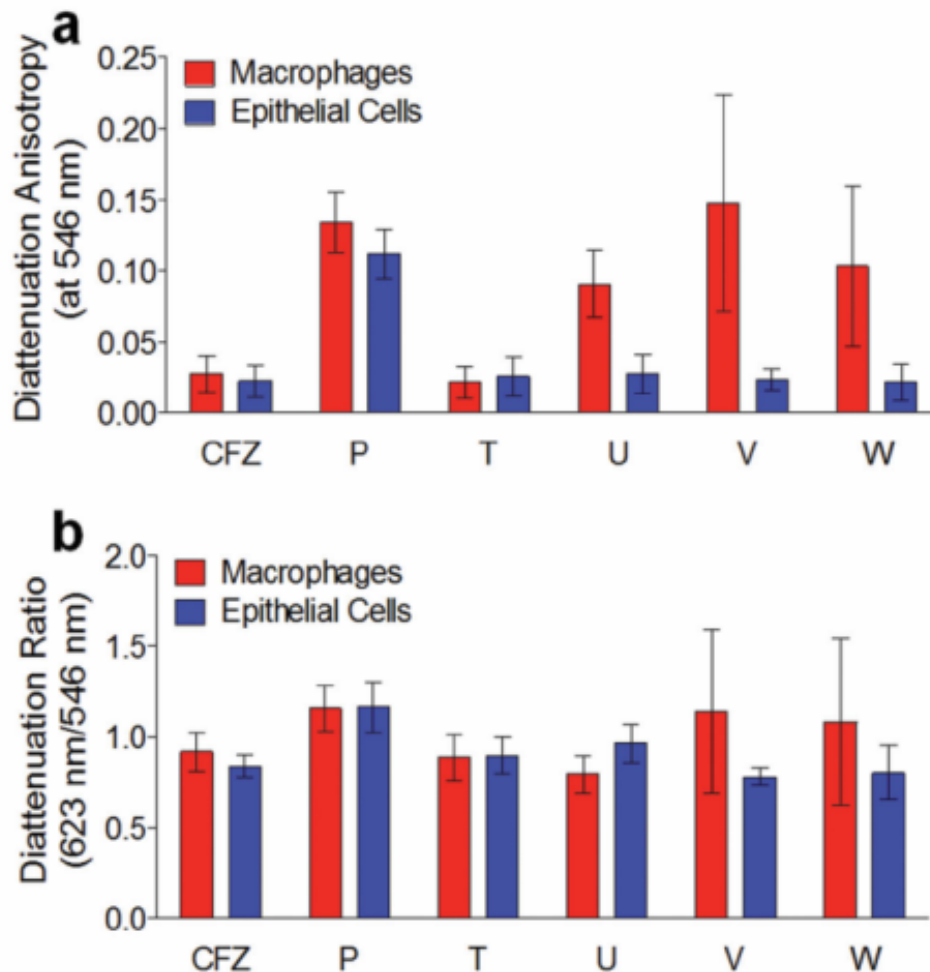


Figure 3-5 Quantitative comparison of diattenuation of intracellular inclusions

Quantitative comparison of the diattenuation anisotropy measurements of intracellular inclusions formed by clofazimine and other phenazine derivatives showing the most prominent diattenuation anisotropy signals (Compounds P, U, V, and W). Compound T was included as well, since it corresponds to the mirror image (chiral pair) of Compound U. a) Compared to clofazimine, Compounds U, V, and W show stronger diattenuation anisotropy signals in macrophages, while Compound P shows stronger diattenuation anisotropy signals in both macrophages and epithelial cells. b) The ratio of 623 nm/546 nm diattenuation anisotropy signals of the phenazine compounds was similar to that of clofazimine. Suggesting greater variability in the organization of the intracellular inclusions, Compounds V and W exhibited greater standard deviations, corresponding to greater differences in the measured diattenuation anisotropy ratios amongst individual inclusions.

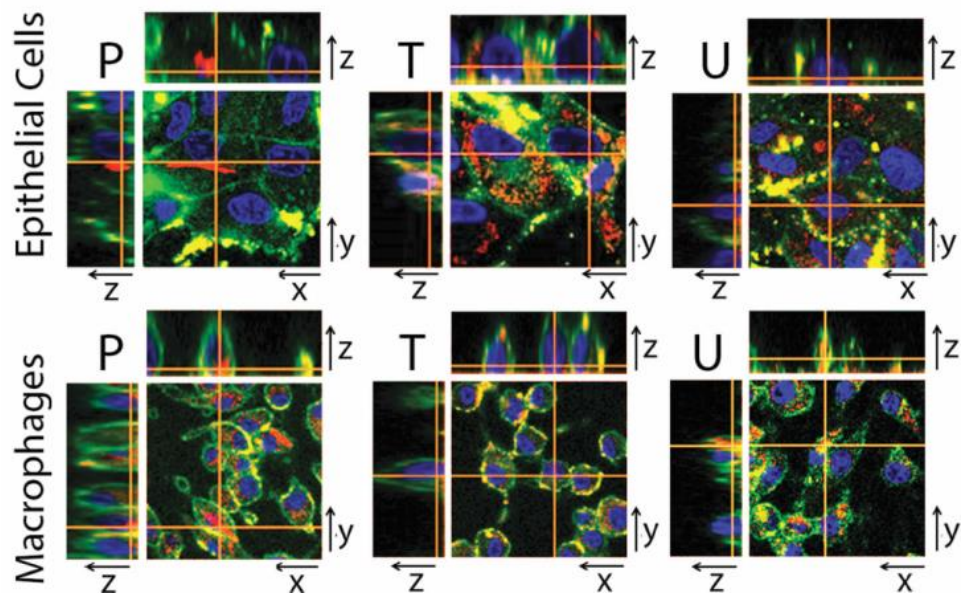


Figure 3-6 Confocal fluorescence microscopy of cells incubated with fluorescent phenazine derivatives

Confocal fluorescence microscopy of RAW264.7 macrophages or MDCK epithelial cells after incubation with fluorescent phenazine Compounds, P, T, or U. 2D images in xy planes show the location of cell nuclei (blue) and plasma membranes (green), together with the corresponding, intracellular location of phenazine compounds (red). 3D reconstructions of optical sections through orthogonal planes (xz and yz planes) confirm intracellular, cytoplasmic signals of compounds (red), in relation to the position of the nuclei and plasma membrane signals. Scale bar = 20 μm .

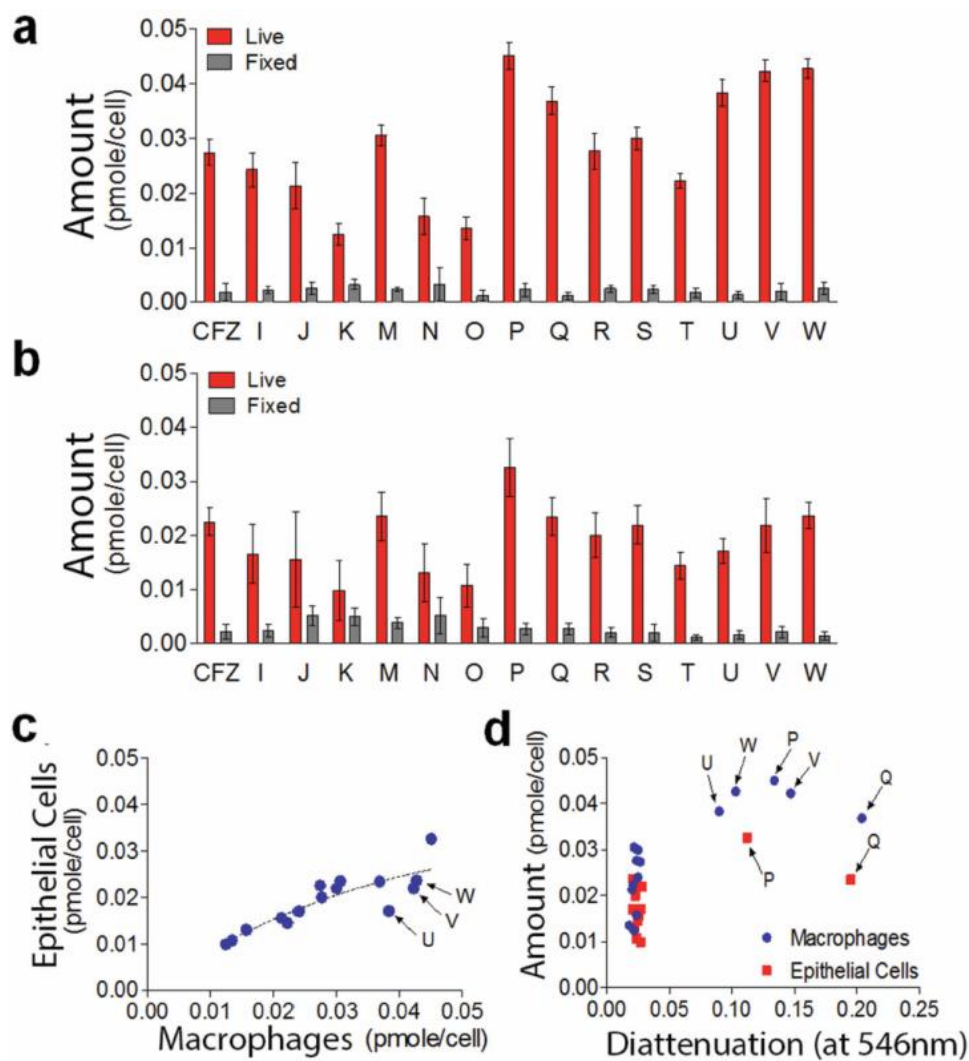


Figure 3-7 Cellular accumulation of phenazine compounds

Measured differences in the accumulation of clofazimine or its phenazine derivatives (in pmols per cell) in RAW264.7 macrophages or MDCK epithelial cells following a 72 h incubation period. a) Measurements indicate significant differences in the accumulation of the compounds in live versus fixed macrophages. b) Measurements also indicate significant differences in the accumulation of the compounds in live versus fixed epithelial cells. c) Plot of mass accumulation of compounds in macrophages versus epithelial cells reveals overall trend towards higher accumulation of the compounds in macrophages. d) Plot of the cellular accumulation of phenazine compounds in macrophages and epithelial cells in relation to the diattenuation anisotropy of the resulting intracellular inclusions, measured using linearly polarized light at 546 nm wavelength.

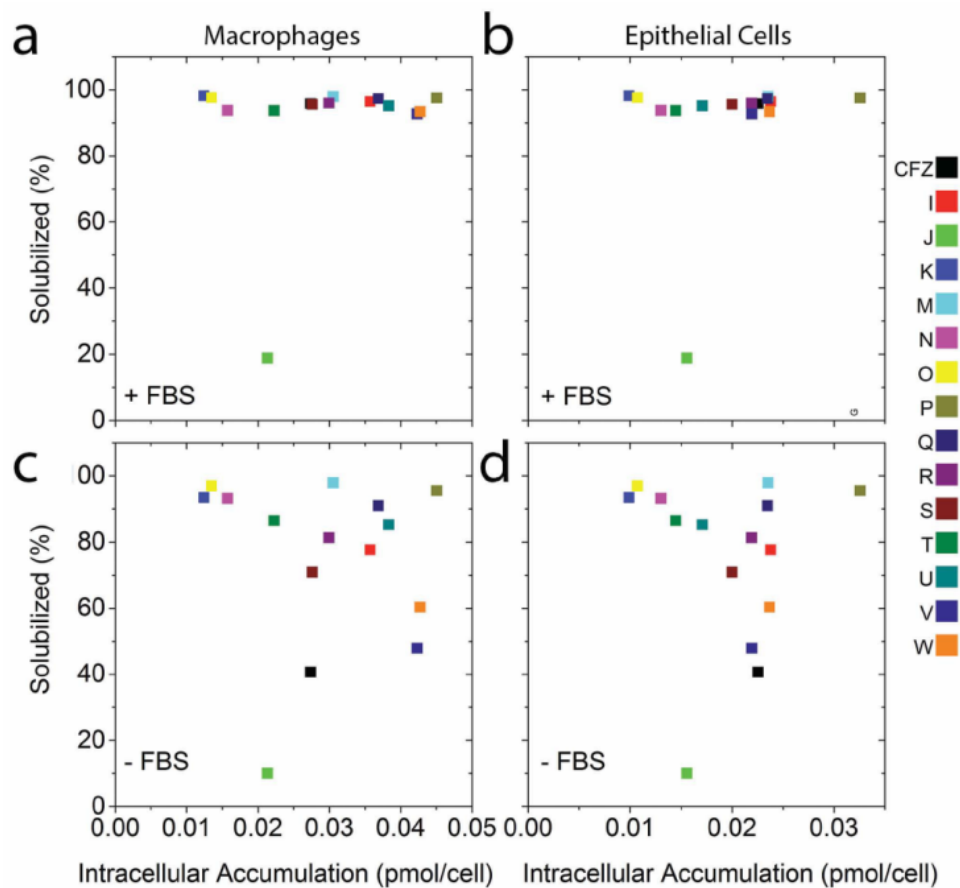


Figure 3-9 Solubility of phenazine compounds in cell culture media related to intracellular accumulation

The solubility of phenazine compounds in cell culture media a,b) with FBS (+FBS) and c,d) without FBS (-FBS) plotted in relation to their cellular accumulation in a,c) RAW264.7 macrophages and b,d) MDCK epithelial cells.

3.9 Supporting Information Available

This material is published in *Advanced Science* and supplemental figures and tables are available in Appendix B.

3.10 References

1. Murray, P.J. and T.A. Wynn, *Protective and pathogenic functions of macrophage subsets*. Nature Reviews Immunology, 2011. **11**(11): p. 723-737.
2. Ricardo, S.D., H. van Goor, and A.A. Eddy, *Macrophage diversity in renal injury and repair*. J Clin Invest, 2008. **118**(11): p. 3522-30.
3. Mantovani, B., M. Rabinovitch, and V. Nussenzweig, *Phagocytosis of immune complexes by macrophages. Different roles of the macrophage receptor sites for complement (C3) and for immunoglobulin (IgG)*. J Exp Med, 1972. **135**(4): p. 780-92.
4. Serbina, N.V., et al., *Monocyte-mediated defense against microbial pathogens*. Annu Rev Immunol, 2008. **26**: p. 421-52.
5. Conalty, M.L., V.C. Barry, and A. Jina, *The antileprosy agent B.663 (Clofazimine) and the reticuloendothelial system*. Int J Lepr Other Mycobact Dis, 1971. **39**(2): p. 479-92.
6. Reasor, M.J., *Influence of a pre-existing phospholipidosis on the accumulation of amiodarone and desethylamiodarone in rat alveolar macrophages*. Res Commun Chem Pathol Pharmacol, 1991. **72**(2): p. 169-81.
7. Brown, M.S. and J.L. Goldstein, *Lipoprotein metabolism in the macrophage: implications for cholesterol deposition in atherosclerosis*. Annu Rev Biochem, 1983. **52**: p. 223-61.
8. Anderson, N. and J. Borlak, *Drug-induced phospholipidosis*. FEBS Lett, 2006. **580**(23): p. 5533-40.
9. Atkinson, A.J., Jr., et al., *Evaluation of B.663 in human leprosy*. Int J Lepr Other Mycobact Dis, 1967. **35**(2): p. 119-27.
10. Organization, W.H. *WHO Model Lists of Essential Medicines*. [cited 2015; Available from: <http://www.who.int/medicines/publications/essentialmedicines/en/>].
11. Baik, J. and G.R. Rosania, *Macrophages Sequester Clofazimine in an Intracellular Liquid Crystal-Like Supramolecular Organization*. PLoS ONE, 2012. **7**(10): p. e47494.

12. Baik, J., et al., *Multiscale Distribution and Bioaccumulation Analysis of Clofazimine Reveals a Massive Immune System-Mediated Xenobiotic Sequestration Response*. *Antimicrob. Agents. Chemother.*, 2013. **57**(3): p. 1218-1230.
13. Kaufmann, A. and J. Krise, *Lysosomal Sequestration of Amine-Containing Drugs: Analysis and Therapeutic Implications*. *Journal of Pharmaceutical Sciences*, 2006. **96**(4): p. 729-746.
14. Horobin, R.W., S. Trapp, and V. Weissig, *Mitochondriotropics: a review of their mode of action, and their applications for drug and DNA delivery to mammalian mitochondria*. *J Control Release*, 2007. **121**(3): p. 125-36.
15. Baik, J. and G.R. Rosania, *Molecular Imaging of Intracellular Drug-Membrane Aggregate Formation*. *Molecular Pharmaceutics*, 2011. **8**(5): p. 1742-1749.
16. Fahr, A., et al., *Lipophilic drug transfer between liposomal and biological membranes: what does it mean for parenteral and oral drug delivery?* *J Liposome Res*, 2006. **16**(3): p. 281-301.
17. Fahr, A., et al., *Transfer of lipophilic drugs between liposomal membranes and biological interfaces: consequences for drug delivery*. *Eur J Pharm Sci*, 2005. **26**(3-4): p. 251-65.
18. Oldenbourg, R., *A new view on polarization microscopy*. *Nature*, 1996. **381**(6585): p. 811-2.
19. Oldenbourg, R. and G. Mei, *New polarized light microscope with precision universal compensator*. *J Microsc*, 1995. **180**(Pt 2): p. 140-7.
20. Shribak, M. and R. Oldenbourg, *Techniques for fast and sensitive measurements of two-dimensional birefringence distributions*. *Appl Opt*, 2003. **42**(16): p. 3009-17.
21. Mehta, S.B., M. Shribak, and R. Oldenbourg, *Polarized light imaging of birefringence and diattenuation at high resolution and high sensitivity*. *Journal of Optics*, 2013. **15**(9): p. 094007.
22. Huang, L.Z., et al., *A Facile and Efficient Synthesis of Diaryl Amines or Ethers under Microwave Irradiation at Presence of $KF/Al(2)O(3)$ without Solvent and Their Anti-Fungal Biological Activities against Six Phytopathogens*. *Int J Mol Sci*, 2013. **14**(9): p. 18850-60.

23. Kirsch, P., A. Schönleben-Janás, and R.H. Schirmer, *Synthesis and characterization of water-soluble and photolabile 10-arylisalloxazines: Tools for studying the mechanism of action of flavin-type antimalarials*. Liebigs Annalen, 1995. **1995**(7): p. 1275-1281.
24. O'Sullivan, J.F., M.L. Conalty, and N.E. Morrison, *Clofazimine analogues active against a clofazimine-resistant organism*. J Med Chem, 1988. **31**(3): p. 567-72.
25. O'Sullivan, J.F., J. Chem Re. Miniprint, 1984. **29**(52).
26. Hansch, C. and L. A., in *Substituent Constants for Correlation Analysis in Chemistry and Biology*. 1979, Wiley: New York. p. 18.
27. Horobin, R.W., et al., *Predicting small molecule fluorescent probe localization in living cells using QSAR modeling. 1. Overview and models for probes of structure, properties and function in single cells*. Biotech Histochem, 2013. **88**(8): p. 440-60.
28. Horobin, R.W. and F. Rashid-Doubell, *Predicting small molecule fluorescent probe localization in living cells using QSAR modeling. 2. Specifying probe, protocol and cell factors; selecting QSAR models; predicting entry and localization*. Biotech Histochem, 2013. **88**(8): p. 461-76.
29. DeMay, B.S., et al., *Rapid and quantitative imaging of excitation polarized fluorescence reveals ordered septin dynamics in live yeast*. Biophys J, 2011. **101**(4): p. 985-94.
30. Abdi, H. and L.J. Williams, *Principal component analysis*. Wiley Interdisciplinary Reviews: Computational Statistics, 2010. **2**(4): p. 433-459.
31. Boland, M.V. and R.F. Murphy, *A neural network classifier capable of recognizing the patterns of all major subcellular structures in fluorescence microscope images of HeLa cells*. Bioinformatics, 2001. **17**(12): p. 1213-23.
32. Beis, I. and E.A. Newsholme, *The contents of adenine nucleotides, phosphagens and some glycolytic intermediates in resting muscles from vertebrates and invertebrates*. Biochem J, 1975. **152**(1): p. 23-32.
33. Hwang, C., A.J. Sinskey, and H.F. Lodish, *Oxidized redox state of glutathione in the endoplasmic reticulum*. Science, 1992. **257**(5076): p. 1496-502.

34. Lodish, H.F., *Molecular Cell Biology*. 2008, New York: W.H. Freeman and Company.
35. GM, C., *The Cell A Molecular Approach*. 2 ed. 2000, Sunderland, MA: Sinauer Associates.
36. Gottfried, E.L., *Lipids of human leukocytes: relation to celltype*. J Lipid Res, 1967. **8**(4): p. 321-7.
37. Machaiah, J.P. and U.K. Vakil, *Protein deficiency and age related alterations in rat peritoneal macrophage lipids*. Journal of Biosciences, 1989. **14**(4): p. 367-377.
38. Fu, D., et al., *Imaging the intracellular distribution of tyrosine kinase inhibitors in living cells with quantitative hyperspectral stimulated Raman scattering*. Nat Chem, 2014. **6**(7): p. 614-22.
39. Rin Jean, S., et al., *Molecular vehicles for mitochondrial chemical biology and drug delivery*. ACS Chem Biol, 2014. **9**(2): p. 323-33.
40. Mourtada, R., et al., *Re-directing an alkylating agent to mitochondria alters drug target and cell death mechanism*. PLoS One, 2013. **8**(4): p. e60253.
41. Vendrell, M., J.S. Lee, and Y.T. Chang, *Diversity-oriented fluorescence library approaches for probe discovery and development*. Curr Opin Chem Biol, 2010. **14**(3): p. 383-9

Chapter 4

Clofazimine Biocrystal Accumulation in Macrophages Upregulates Interleukin 1 Receptor Antagonist Production to Induce a Systemic Anti-Inflammatory State

4.1 Relevance to Thesis

The accumulation of clofazimine and CLDIs within a mouse model, and experiments related to that are the primary experimental methodology that is utilized in the thesis work of this dissertation. Relating the physiological changes brought about to the body (i.e., weight gain or loss, changes in body temperature, and heart rate) to treatment with the drug can prove to be a useful marker for numerous clinical endpoints, among the most important for the work discussed in chapter 8 is systemic toxicity or damage to the overall health of the animal. In the studies presented here, the accumulation and presence of clofazimine biocrystals within mice was tested for its ability to protect against inflammatory agents, in particular, LPS-induced lung injury and a carrageenan-induced paw injury. As related to this thesis, my own contribution to the work presented in this chapter was monitoring the body weight, temperature, heart rate, breathing rate, oxygen saturation, and pulse distention of mice daily to determine the effect that the lung-injury and drug therapy had on the general health of the animal, and in turn, if the animal was moribund. The knowledge and skills obtained from assisting with this work helped provide the necessary hands-on animal training and experience needed to design and perform the *in vivo* experiments that were performed in chapters 6, 7, and 8. Additionally, these experiments guide the experimental design and techniques utilized in the macrophage-depletion and toxicity experiments that are performed in chapters 7 and 8, and how this relates to a systemic toxic event. The key finding discussed in this manuscript is related to the upregulation of anti-inflammatory activity related to the accumulation of insoluble drug, rather than treatment with

the soluble form of clofazimine. To that end, my contributions also included quantifying these anti-inflammatory cytokines using enzyme-linked immunosorbent assay (ELISA), which were thoroughly utilized in chapter 8. Through these analyses, the relationship between anti-inflammatory activity and insoluble drug aggregate accumulation was determined, and helped guide the work that is discussed in chapter 8, in particular the link between macrophage-dependent drug bioaccumulation, granuloma formation, production of anti-inflammatory cytokines, and a potential protective mechanism behind CLDI accumulation.

4.2 Abstract

Clofazimine (CFZ) is a poorly soluble antibiotic and anti-inflammatory drug indicated for the treatment of leprosy. In spite of its therapeutic value, CFZ therapy is accompanied by the formation of drug biocrystals that accumulate within resident tissue macrophages, without obvious toxicological manifestations. Therefore, to specifically elucidate the off-target consequences of drug bioaccumulation in macrophages, we compared the level of inflammasome activation in CFZ-accumulating organs (spleen, liver and lung) in mice after 2 and 8 weeks of CFZ treatment when the drug exists in soluble and insoluble (biocrystalline) forms, respectively. Surprisingly, the results showed a drastic reduction in caspase 1 and interleukin-1 β (IL-1 β) cleavage in the livers of mice treated with CFZ for 8 weeks (8-week-CFZ-treated mice) compared to 2-week-CFZ-treated and control mice, which was accompanied by a 3-fold increase in hepatic IL-1 receptor antagonist (IL-1RA) production and a 21-fold increase in serum IL-1RA levels. In the lung and spleen, IL-1 β cleavage and tumor necrosis factor alpha expression were unaffected by soluble or biocrystal CFZ forms. Functionally, there was a drastic reduction of carrageenan- and lipopolysaccharide-induced inflammation in the footpads and lungs, respectively, of 8-week-CFZ-treated mice. This immunomodulatory activity of CFZ biocrystal accumulation was attributable to the upregulation of IL-1RA, since CFZ accumulation had minimal effect in IL-1RA knockout mice or 2-week-CFZ-treated mice. In conclusion, CFZ accumulation and biocrystal formation in resident tissue macrophages profoundly altered the host's immune system and prompted an IL-1RA-dependent, systemic anti-inflammatory response.

4.3 Introduction

Clofazimine (CFZ) is an antimycobacterial agent listed in the World Health Organization's List of Essential Medicines that has been in use as part of the standard treatment of leprosy since the 1960s [1, 2]. The number of leprosy cases has drastically dropped from 12 million/year in 1981 to 216,000/year in 2013 [3], a testament to the effectiveness of CFZ, which has gained considerable attention recently as part of a treatment regimen for drug-resistant tuberculosis [4–6]. The efficacy of oral CFZ against leprosy is due, in part, to its well-documented anti-inflammatory activity [2]. However, CFZ's mechanism of anti-inflammatory action and atypical pharmacokinetic properties are not well understood, and its high oral bioavailability and poor solubility leads to significant bioaccumulation in tissues [7].

In previous studies, it has been shown that following prolonged oral administration of CFZ, the drug massively bioaccumulates as intracellular biocrystals in resident tissue macrophages [8–12]. Therefore, it is natural to assume that this bioaccumulation phenomenon contributes to the drug's toxicity, whereas the soluble form of CFZ, which circulates and partitions to and from the different organs, is responsible for CFZ's mechanism of action. Indeed, insoluble particles and crystals that accumulate in macrophages under various pathological conditions are known to activate immune signaling pathways that lead to caspase 1 (Casp 1) activation and increased interleukin-1 β (IL-1 β) secretion [13–16]. This so-called “inflammasome” activation pathway is often associated with many downstream pathological changes, as has been shown by the accumulation of cholesterol monohydrate crystals in atherosclerosis [13], monosodium urate crystals in gout [14], and inhaled foreign particles in the case of asthma and other chronic inflammatory lung diseases [15, 16].

In spite of its bioaccumulation, several clinical trials have established CFZ as a potentially useful therapeutic agent for treating a variety of chronic inflammatory diseases [17–22]. Furthermore, *in vitro* studies have shown that intracellular CFZ biocrystals dampen pro-inflammatory pathways while enhancing anti-inflammatory signals [23].

In order to distinguish between the potential adverse effects of insoluble drug biocrystals from those of the soluble molecules, we designed an experimental strategy to compare how the accumulation of insoluble drug biocrystals might influence the immune signaling response of macrophages in live mice. We reasoned that macrophages exposed to the soluble form of CFZ (after 2 weeks of treatment) may behave differently from those that are exposed to its

biocrystalline form (after 8 weeks of treatment). Accordingly, we tested the specific hypothesis that CFZ biocrystals that accumulate in resident tissue macrophages can modulate (or activate) these cells' inflammatory signaling pathways *in vivo* that lead to systemic changes in the inflammatory response. By assessing tumor necrosis factor alpha (TNF- α) and IL-1 receptor antagonist (IL-1RA) expression, as well as Casp 1 and IL-1 β maturation, in the vital organs and blood of CFZ-treated mice, our results demonstrate that CFZ biocrystals in macrophages, but not the soluble form, is specifically associated with an IL-1RA-mediated anti-inflammatory response.

4.4 Materials and Methods

Reagents. Anti-caspase 1 and anti-IL-1 β antibodies were purchased from Thermo Pierce (Rockford, IL) and Novus Biologicals (Littleton, CO), respectively. Anti-F4/80 and anti-CD68 antibodies were purchased from Abcam (Cambridge, MA). Anti-actin antibody and lipopolysaccharide (LPS; from *E. coli* O55:B5) were purchased from Sigma (St. Louis, MO).

Mice clofazimine treatment. Clofazimine (CFZ; Sigma-Aldrich, catalog no. C8895) was prepared in sesame oil (Shirakiku, Japan, or Roland, China) and Powdered Lab Diet 5001 (PMI International, Inc., St. Louis, MO) and orally administered to wild-type (WT) C57BL/6 mice or IL-1RA knockout mice (4 to 5 weeks old; Jackson Laboratory, Bar Harbor, ME) for up to 8 weeks *ad libitum* as previously described [8, 24]. Control mice were fed with the same diet without CFZ. The animal protocol was approved by the University of Michigan's Animal Care and Use Committee in accordance with the National Institutes of Health guidelines (UCUCA, no. PRO00005542).

Carrageenan footpad edema test. Footpad edema in response to carrageenan (CAR; Sigma) injection was measured in CFZ-treated and control mice as previously described [25]. In IL-1RA knockout (KO) mice, these experiments were performed at 6 weeks and not at 8 weeks because the IL-1RA KO mice weighed less than the WT mice and their livers were smaller (see Fig. S4). In brief, the volume of each hind paw was measured before and after the intraplantar injection of 30 μ l of 2% CAR (60 μ g per paw) in phosphate-buffered saline (PBS) or an equal volume of PBS in the contralateral paw. Paw swelling was measured at 4 and 48 h after injection, after which the animals were euthanized by exsanguination while deeply anesthetized with an

intraperitoneal injection of ketamine (100 mg/kg) and xylazine (10 mg/kg), and the skin tissues of the plantar region were harvested for cytokine assay (see the Materials and Methods in Appendix C).

Acute lung injury and infrared pulse oximetry. Since C57BL/6 mice are relatively resistant toward a single dose of intratracheal (i.t.) LPS instillation [26], two i.t. injections of LPS (16 mg/kg; 50 μ l) were administered, one on day 0 and the second on day 3. Briefly, mice treated with CFZ for 8 weeks (8-week-CFZ-treated mice) and control mice were anesthetized using intraperitoneal injections of xylazine (50 mg/kg) and ketamine (5 mg/kg). Under direct visualization of the vocal cords using an otoscope, either LPS or an equivalent volume of PBS in a 1-ml syringe attached to an oral gavage needle (22G) was instilled into the lungs via the oral route. The mouse was then placed in a temperature-controlled cage (37°C) for recovery from anesthesia. The general health status of each PBS/LPS-instilled mice was monitored by measuring body weight and rectal temperature (microprobe thermometer; Physitemp Instruments, Clifton, NJ), and cardiopulmonary function (arterial oxygen saturation, respiratory rate, heart rate, and pulse distention) was monitored using MouseOx with a collar clip sensor (Starr Life Sciences Corp., Oakmont, PA) as previously described [27, 28]. In brief, 1 day before i.t. instillations (day -1), the hair around the neck of each mouse was removed using Nair (Church & Dwight, Princeton, NJ) to enable data acquisition using the collar clip sensor. The next day (day 0), immediately prior to the first LPS/PBS dose, and every 24 h afterward until day 6, the body weight, temperature, and MouseOx readings were recorded. MouseOx data were acquired by very brief anesthesia of the mouse using 5% isoflurane to facilitate the placement of the collar clip sensor. The mouse was then placed in an enclosed chamber with ambient light and allowed to acclimatize for 5 min, at which point the animals had recovered normal activities and physiological readings. Arterial oxygen saturation, respiratory rate, heart rate, and pulse distention measurements were then simultaneously recorded for 6 min (15 readings/s), and any errors caused by motion during recording were excluded, after which the mean value of each parameter was used for further data analysis.

Terminal endpoint assessment. To objectively assess LPS-induced mortality, we used a multiparametric scoring system that relied on the daily changes in vital signs associated with inflammatory injury progression and mortality, which included arterial oxygen saturation [27],

body weight, and temperature [29, 30]. First, the percent change from baseline (day 0) in arterial oxygen saturation, body weight, and temperature in each mouse caused by i.t. instillation of PBS/LPS were measured and calculated daily until day 6 after instillation. These data were then used in a vector equation to calculate the distance between each LPS-treated mouse and the mean of the PBS-treated mice to assess the terminal endpoint for each LPS-instilled mouse (see Materials and Methods in Appendix C). CFZ-treated and control mice were calculated separately, and LPS-instilled mice that scored a total of 18 or higher were determined as terminal, since these mice also displayed severe signs of sickness evidenced by impaired mobility, lack of grooming, hunched posture, and muscle weakness that could be felt while handling the mice. These mice were immediately euthanized with ketamine-xylazine (100 mg/kg, 10 mg/kg) and the bronchoalveolar lavage (BAL) fluid and lungs were harvested for cellular and biochemical analysis (see below). Remaining mice that did not reach terminal endpoint were all euthanized on day 6 after PBS/LPS instillation.

Cytokine measurements. The harvested organs (liver, spleen, lungs, and kidneys) and footpads designated for cytokine assays were cut and homogenized by sonication (2-s pulses repeated five times on ice, level 5; Fisher model 100) in radioimmunoprecipitation assay buffer (Sigma) with added protease inhibitors (Halt protease and phosphatase inhibitor cocktail and 0.5 M EDTA; Thermo Pierce, Rockford, IL). After centrifugation ($18,000 \times g$, 15 min, 4°C), the supernatants were assayed for IL-1 β , IL-1RA, and TNF- α by enzyme-linked immunosorbent assay (ELISA; Duoset; R&D Systems, Minneapolis, MN) in duplicate wells according to the manufacturer's instructions. Cytokines in the BAL were measured after the removal of the cells. Albumin was assayed by ELISA (Innovative Research, Novi, MI). The cytokine concentrations were expressed (i) as pico-, nano-, or micrograms per milligram of protein for the organs, (ii) as pico-, nano-, or micrograms of paw weight, or (iii) as pico- or micrograms per milliliter of BAL fluid.

Mouse BAL fluid harvesting, immunohistochemistry and imaging, and SDS-PAGE and Western blotting. The mouse BAL fluid harvesting, immunohistochemistry and imaging, and SDS-PAGE and Western blotting procedures are described in Appendix C.

Data processing and statistics. All data are expressed as means \pm the standard deviations (SD). For multiple comparisons, statistical analysis was performed with one-way analysis of variance (ANOVA) and Tukey's post *hoc* comparisons. For two-group comparisons, an unpaired

Student *t* test was used. All statistical analyses employed the Sigmaplot version 13 (Systat Software, San Jose, CA) software and $P \leq 0.05$ was considered statistically significant.

4.5 Results

4.5.1 CFZ crystallization and bioaccumulation in the liver occurs after 2 weeks

During the first 2 weeks of CFZ treatment, CFZ-associated diffuse red staining was present throughout the liver (Fig. 1A, brightfield). However, by 4 weeks, CFZ accumulated in the biocrystalline form. At 8 weeks, red CFZ biocrystals were evident throughout the liver (Fig. 1A, top panel). Taking advantage of solvatochromic changes in the fluorescent excitation and emission spectra of CFZ [31, 32], fluorescence microscopy enabled *in vivo* detection of the soluble and biocrystalline forms of CFZ. After 2 weeks of CFZ treatment, the drug was mostly present in the soluble form with its fluorescence mostly detectable in the FITC channel (Fig. 1A, fluorescein isothiocyanate [FITC] and Cy5 panels; Fig. 1B). At later time points, the fluorescence signal in the FITC channel declined, while the fluorescence signal in the Cy5 channel increased, indicating the relative accumulation of the biocrystalline form (Fig. 1A and B). By 8 weeks, most of the fluorescence signal was detectable in the Cy5 channel (Fig. 1A and B), indicating that CFZ was present almost entirely in biocrystalline form. Immunohistochemistry of 8-week-CFZ-treated liver sections showed that CFZ biocrystals are sequestered inside F4/80-positive macrophages (Fig. 1C). Such targeted accumulation of CFZ biocrystals was also detected in other organs such as CD68⁺ alveolar macrophages (see Fig. SI. 7), and F4/80⁺ splenic macrophages [8, 31].

4.5.2 CFZ biocrystal formation in the liver downregulates Casp 1/IL-1 β processing while enhancing IL-1RA expression

Intracellular crystals, such as those formed by cholesterol or uric acid, have been implicated in the activation of the NLRP3-Casp 1 inflammasome, which plays a major role in the pathogenesis of chronic inflammatory disorders [14, 33, 34]. The uptake of other nano- and microparticles has also been reported to cause inflammasome activation in macrophages [35–37]. Therefore, to assess whether the bioaccumulation of CFZ crystals leads to activation of the inflammasome, we measured and compared cleaved Casp 1 and IL-1 β in organs that bioaccumulate CFZ—i.e., the liver, spleen, and lungs—and kidneys, that do not accumulate

CFZ, after 2 and 8 weeks of either CFZ or control treatment. Two weeks of CFZ exposure resulted in only moderate cleavage of hepatic Casp 1 and IL-1 β (Fig. 2A, left panel, and Fig. 2B). However, by 8 weeks, Casp 1 and IL-1 β cleavage was significantly reduced by CFZ treatment (Fig. 2A, right panel, and Fig. 2B); IL-1 β levels in the spleen, lung, and kidneys did not change (see Fig. SI. 8). The expression of the proinflammatory cytokine, TNF- α , was unchanged by CFZ at both 2 and 8 weeks (Fig. 2C), except in the liver, where it was decreased at 2 weeks compared to control livers.

Similar to previous observations [8], we found that after 8 weeks of oral administration CFZ caused a major upregulation of IL-1RA expression in CFZ biocrystal-accumulating organs, such as the spleen, the lungs, and especially the liver, which increased by 3-fold (Fig. 2D). IL-1RA levels in the kidney were unaffected (Fig. 2D). In contrast, after 2 weeks of oral CFZ administration there were more modest increases in only the spleen and lungs, while the liver was unaffected (Fig. 2D). Since the liver is known to be the major source of circulating IL-1RA [38, 39], we observed a corresponding increase in serum IL-1RA levels in CFZ-treated mice at 8 weeks but not at 2 weeks (Fig. 2E). Under all conditions, neither TNF- α nor IL-1 β was detected in the serum. In aggregate, these findings suggest that crystallized CFZ, which is evident after 8 weeks of CFZ administration, decreased the activation of the inflammasome *in vivo*. In parallel with this decline, crystallized CFZ induced an upregulation of endogenous IL-1RA.

4.5.3 Systemic CFZ bioaccumulation and crystallization dampens CAR-mediated acute footpad inflammation

To test the physiological impact of the CFZ-induced serum IL-1RA levels, we tested the acute inflammatory response of CFZ-treated mice by using a well-established footpad injury model [25]. The paws of 8-week-CFZ-treated mice displayed strikingly reduced swelling at 48 h after the injection of CAR compared to the paws of untreated CAR-injected mice (Fig. 3A). Paw volume measurements showed that there was a significant reduction (57%) in footpad swelling as early as 4 h after the injection of CAR in 8-week-CFZ-treated mice compared to control mice, and the animals continued to exhibit reduced swelling over the 48-h study period (Fig. 3B). CAR-induced increases in footpad IL-1 β and TNF- α levels were dramatically reduced by 8-week-CFZ treatment (Fig. 3C and 3D). In contrast to the 8-week-treated mice, 2-week-CFZ-treated mice produced only a modest reduction in paw swelling compared to control mice (Fig.

3E and 3 F). The IL-1 β and TNF- α levels in footpad homogenates from these animals were similar in both CFZ-treated and control mice at 48 h (Fig. 3G and 3H). Accordingly, these results suggest that the accumulation of CFZ biocrystals modulated the immune response to profoundly dampen CAR-induced footpad inflammation, and this action is not evident for the soluble form of the drug after 2 weeks of treatment.

4.5.4 CFZ biocrystals dampen the acute inflammatory response in the footpad by increasing blood IL-1RA

IL-1RA is known to be an early-acting acute-phase anti-inflammatory cytokine [38], and circulating IL-1RA has been reported to dampen a broad spectrum of inflammatory conditions by inhibiting the activity of IL-1 β at the site of injury [40, 41]. Therefore, we hypothesized that the anti-inflammatory response observed after 8 weeks of CFZ treatment may be mediated by increased serum IL-1RA concentrations, which are not evident after 2 weeks of CFZ treatment (Fig. 2E). Detection of serum IL-1RA in 2-week-CFZ-treated and control mice showed comparable IL-1RA levels before (0 h) and after (48 h) CAR injection (Fig. 4A). However, serum IL-1RA levels in 8-week-CFZ-treated mice rapidly declined 4 h after CAR injection (Fig. 4B). After 48 h, IL-1RA returned to similar levels in the plasma of control and 8-week-CFZ-treated mice (Fig. 4B). For all mice, the plasma levels of TNF- α and IL-1 β were below the detection limit of ELISAs (15 pg/ml). These results suggest that increased circulating IL-1RA levels associated with CFZ bioaccumulation and crystallization could be responsible for the anti-inflammatory activity observed in 8-week-CFZ-treated mice.

In order to test the possibility that elevated IL-1RA expression mediates the anti-inflammatory activity of CFZ after crystal formation, we administered oral CFZ to age-matched IL-1RA KO and WT mice and then subjected the animals to the CAR footpad injury model. IL-1RA KO mouse livers also increased in weight to an extent similar to that of WT mice after 6 weeks of CFZ treatment (see Fig. SI. 9B). Also, IL-1RA KO mice formed and accumulated CFZ biocrystals in the liver at a level similar to WT animals without noticeable differences in crystal shape or Cy5 fluorescence intensity (see Fig. SI. 9C and SI. 9D). Remarkably, the anti-inflammatory action of CFZ bioaccumulation was greatly diminished in IL-1RA KO mice, since CFZ-treated and CAR-injected IL-1RA KO mice displayed similar swelling compared to untreated and CAR-injected IL-1RA KO mice (Fig. 4C and 4D, right panels). In the CFZ-treated

WT mice, we observed significantly reduced CAR-induced swelling compared to control mice at 4 and 48 h postinjury (Fig. 4C and 4D, WT panels). As expected, the footpad IL-1 β and TNF- α levels were significantly reduced in WT CFZ-treated and CAR-injected mice compared to WT untreated and CAR-injected mice (Fig. 4E). However, the IL-1 β and TNF- α levels were comparable in the CAR-injected IL-1RA KO mice with or without CFZ treatment (Fig. 4F). IL-1RA KO mice with or without CFZ treatment showed higher cytokine levels than the control WT mice after CAR injection (Fig. 4E versus Fig. 4F), but the footpad swelling was similar (Fig. 4D). These results are consistent with CFZ bioaccumulation exerting a systemic anti-inflammatory action via the elevation of blood IL-1RA levels.

4.5.5 CFZ bioaccumulation enhances resistance to acute lung injury and improves mouse survival

Given the massive bioaccumulation of CFZ observed in the lungs, we proceeded to determine whether the presence of CFZ biocrystals in these organs may sensitize mice to a sublethal pro-inflammatory injury. Although CFZ treatment and bioaccumulation did cause some physiological changes, these changes were within ranges of normal physiological readings and overall mouse health was normal (see Table S7).

To determine whether CFZ bioaccumulation induced a latent proinflammatory state in mouse lungs, a sublethal dose of LPS (16 mg/kg) was delivered i.t. to control and CFZ-treated mice. Strikingly, CFZ-treated mice were highly resistant to LPS-induced acute lung injury, with a 92% survival rate compared to the 42% survival rate of control mice (Fig. 5A). The difference in the arterial oxygen saturation levels between control and CFZ-treated mice was more prominent after the second LPS injection. CFZ-treated mice displayed significantly higher arterial oxygen levels at days 5 and 6 than control mice because most control mice experienced levels of hypoxia that required euthanasia, indicating that control mice showed progressive deterioration in lung function compared to CFZ-treated mice (see Fig. SI. 10A). Paralleling the impaired lung function, LPS-injected control mice lost weight more rapidly than CFZ-treated mice, such that six control mice lost >15% of their body weight compared to a similar weight loss in one CFZ-treated mouse (see Fig. SI. 10B). Both control and CFZ-treated LPS-injected mice displayed large drops in body temperature one day after LPS injection (days 1 and 4). However, CFZ-treated mice were more resistant to a decline in body temperature after the

second injection compared to control mice (day 4) (see Fig. SI. 10C). CFZ-treated mice also displayed less reduction in heart rate, respiratory rate, and pulse distention after the second LPS injection (see Fig. SI. 10D to 10F) compared to control mice. Gross lung examination lungs after LPS-induced injury showed a notable reduction of hemorrhaging in CFZ-treated mice compared to control mice (Fig. 5B). Cellular and biochemical analyses of BAL fluid to assess lung injury revealed that CFZ treatment reduced the LPS-induced BAL fluid cell count (Fig. 5C) and reduced the BAL fluid albumin concentrations (Fig. 5D). This CFZ-mediated reduction in lung injury was corroborated by CFZ-induced reductions in LPS-induced levels of BAL fluid TNF- α and IL-1 β (Fig. 5E and 5F). These results demonstrate that CFZ biocrystal accumulation in the lungs did not impair lung function but instead increased resistance to LPS-induced inflammatory lung injury.

4.6 Discussion

Previously, CFZ bioaccumulation has been associated with atypical pharmacokinetics, as well as more serious side effects, ranging from gastrointestinal problems to splenic infarcts [42]. Although expecting that CFZ bioaccumulation would lead to an upregulation of proinflammatory signaling pathways in macrophages, we were surprised to find the opposite. Instead, our experimental results indicate that long-term oral administration of CFZ and its sequestration as biocrystals within the macrophages of the lung, the spleen, and especially the liver can dramatically suppress inflammation in peripheral tissues and increase mouse survival in response to acute lung injury. This systemic anti-inflammatory response parallels the accumulation of CFZ biocrystals throughout the animal and is accompanied by elevated IL-1RA levels in these organs and a corresponding boost in IL-1RA levels in serum. Of noteworthy significance, the formation and accumulation of cholesterol monohydrate and monosodium urate crystals have been implicated in the pathogenesis of chronic inflammatory diseases, such as atherosclerosis, nonalcoholic steatohepatitis (NASH) [34], and gout [43]. Moreover, other artificial nano- and microparticles, such as silica crystals [37], aluminum salt crystals [44], silver nanoparticles [35], poly(lactide-co-glycolide) (PLG), and polystyrene microparticles [36], have also been reported to cause inflammasome activation in macrophages. At the cellular level, the aforementioned particles or crystals are known to augment Toll-like receptor signaling and activate the NLRP3 inflammasome via lysosomal destabilization, which leads to Casp 1 activation and the

production of cleaved IL-1 β [13, 14]. Therefore, the finding that inflammasome activity was inhibited in the CFZ biocrystal-containing liver, evidenced by the suppression of Casp 1 activation and mature IL-1 β processing, was unexpected. Moreover, the presence of CFZ biocrystals in the lung, spleen, or liver did not alter the TNF- α levels, a finding consistent with a lack of proinflammatory signaling.

These results prompt us to question whether CFZ bioaccumulation is an inherently toxic phenomenon. It is well known that soluble CFZ is toxic *in vitro*, with a 50% inhibitory concentration of approximately 5 μ M, whereas the insoluble crystalline form of CFZ that bioaccumulates in macrophages leads to very few signs of toxicity even at 100 μ M [23]. Indeed, in spite of its massive accumulation in the liver, the hepatotoxicity of CFZ in mice and human patients has not been a significant concern [45–47]. Like humans, mice treated with therapeutic CFZ doses (10 mg/kg/day) did not show signs of deteriorated health. In fact, the CFZ-induced reduction of heart rate could be linked with increased longevity in mice [48]. Also, hypothermia, which is most often used as an indicator of drug toxicity in mice [49], was not seen in 8-week-CFZ-treated mice.

Regarding the therapeutic implications of these results, CFZ has proven to be highly effective for treating leprosy and active against a broad range of Gram-positive bacteria strains (*Staphylococcus*, *Streptococcus*, *Bacillus*, and *Listeria* spp.) [50] and even against drug-resistant *Staphylococcus aureus* clinical isolates that are methicillin resistant (MRSA) and vancomycin intermediate resistant (VISA) [51]. Indeed, CFZ has been clinically used since the 1960s and has helped cure over 16 million leprosy patients. Many of these microorganisms tend to infect and reside within macrophages. Interestingly, chemical analysis of CFZ biocrystals has revealed that they are composed of protonated hydrochloride salt of CFZ (CFZ-HCl) within membrane-bound intracellular compartments [9]. Therefore, the bioaccumulation of CFZ biocrystals in macrophages could serve to maximize the therapeutic efficacy of CFZ without significant side effects. Accordingly, it may be possible to reformulate CFZ as injectable micro- or nanocrystals to specifically target macrophages at sites of infection. Targeted local delivery could maximize CFZ benefit as a therapeutic agent while minimizing the systemic side effects that have curtailed the more widespread use of CFZ.

Considering possible signal transduction mechanisms underlying the anti-inflammatory activity of CFZ biocrystals, the cellular integrated stress response pathway is a candidate [52, 53]. Although soluble CFZ can cause membrane destabilization and cell death at high concentrations [54], lower concentrations of CFZ lead to accumulation within intracellular compartments. Previously, we observed that CFZ biocrystals can also be phagocytosed by macrophages, where they are stable inside low-pH [4, 5] and counterion (Cl^-)-containing [9] membrane-bound compartments. As a weakly basic lysosomotropic drug, CFZ is prone to pH-dependent ion trapping in lysosomes and could therefore activate transcription factor EB (TFEB [55], a master transcription factor of lysosomal biogenesis and homeostasis [56,–58]. In turn, this could attenuate inflammasome activation pathways and IL-1 β processing [59]. Alternatively, like intracellular protein aggregates and other crystalline inclusions that form in the endoplasmic reticulum (60), CFZ biocrystals may activate the unfolded protein response pathway, which could lead to downstream effects on inflammatory signaling [61, 62].

Our experiments indicate that CFZ biocrystals induce a considerable upregulation of IL-1RA production without triggering pro-inflammatory signaling. Since the evidence points to IL-1RA mediating the anti-inflammatory effects downstream of CFZ bioaccumulation in macrophages, future experiments aimed at elucidating the signaling pathway leading from CFZ biocrystals to IL-1RA expression should reveal further mechanistic details about the mechanism of action of CFZ and perhaps serve as the starting point for the development of new kinds of anti-inflammatory drugs. Thus, the present study strongly warrants further investigation into the mechanisms and therapeutic potential of CFZ for treating inflammatory and infectious diseases in humans. To conclude, CFZ biocrystal accumulation in macrophages could be triggering a previously unknown anti-inflammatory/immunomodulatory signaling pathway(s) of potential therapeutic value.

4.7 Acknowledgements

We thank Jean Nemzek (Medical School, University of Michigan) and Pathology Cores for Animal Research at the University of Michigan for histological support and Avery Lui for help with image analysis. This study was supported by the National Institute of General Medical Sciences (NIGMS; R01GM078200 to G.R.R.), an MICHR B-to-B Pilot Seed grant (R.K.K., G.R.R.), and the University of Michigan MCubed Initiative (<http://mcubed.umich.edu/>). The

contents of this report are solely the responsibility of the authors and do not necessarily represent the official views of the NIGMS or the National Institutes of Health.

4.8 Figures

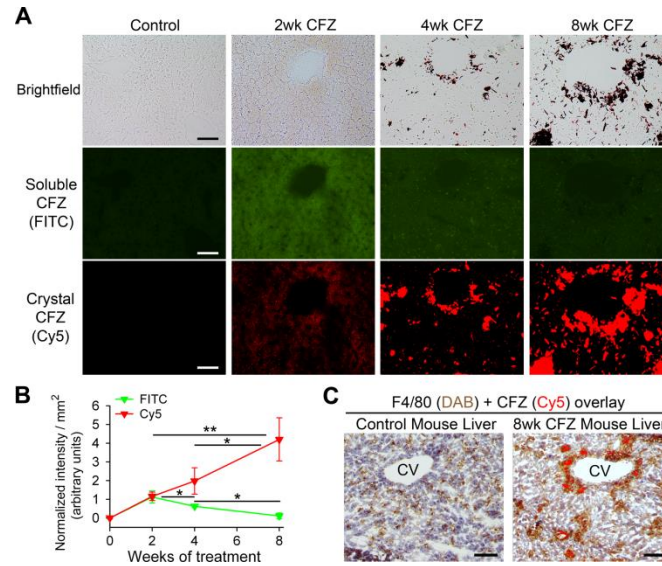


Figure 4-1 CFZ bioaccumulation and crystallization within the liver

CFZ bioaccumulation and crystal formation in the liver occurs after 2 weeks. (A) Representative bright-field and fluorescence (FITC for soluble CFZ and Cy5 for crystalline CFZ) images of liver sections from control mice and mice treated with CFZ for 2, 4, and 8 weeks. Scale bar, 50 μm . (B) Fluorescence intensity values (FITC and Cy5 channels) of liver sections from control and CFZ-treated mice. Baseline (0 week) intensity values of controls were subtracted from CFZ-treated sections. The data are the means \pm the SD of results from three to four images/time point. One-way ANOVA was used to compare fluorescence intensity between time points and $P \leq 0.05$ was considered statistically significant. *, $P \leq 0.05$; **, $P \leq 0.01$. (C) F4/80 (DAB) immunohistochemistry of a representative liver section from an 8-week-CFZ-treated mouse in which CFZ crystals (Cy5) are sequestered inside F4/80⁺ macrophages. CV, central vein. Scale bar, 100 μm .

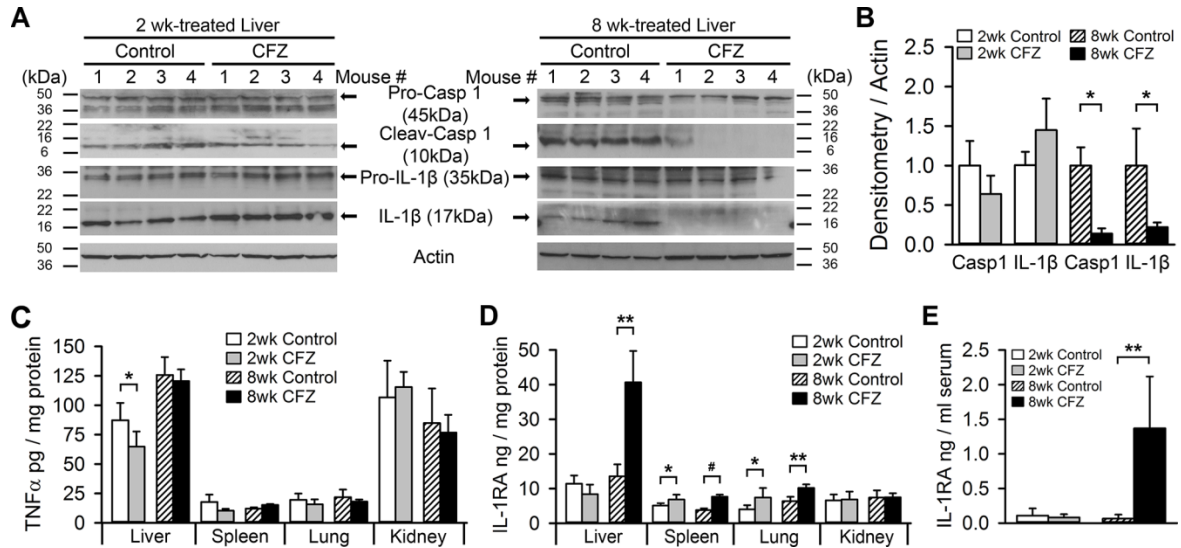


Figure 4-2 CFZ bioaccumulation and pro- and anti-inflammatory signaling

CFZ bioaccumulation reduces Casp 1 and IL-1 β cleavage levels in the liver but increases IL-1RA expression. (A) Representative Western blots of liver homogenates showing that Casp 1 and IL-1 β cleavage was not altered by 2 weeks of CFZ treatment but that 8 weeks of treatment reduced the detection of Casp 1 and IL-1 β cleavage. (B) Densitometry of cleaved Casp 1 and IL-1 β protein in 2- and 8-week-treated liver blots, normalized to actin ($n = 4$). Hepatic Casp 1 and IL-1 β cleavage were reduced by 86 and 78%, respectively, in 8-week-CFZ-treated mice. (C) The levels of TNF- α in the spleen, lungs, and kidneys were unchanged by CFZ treatment, but there was a significant decrease in liver TNF- α from 2-week-CFZ-treated mice ($n = 4$ to 5). (D) The organs that bioaccumulate CFZ crystals—liver, spleen, and lung—displayed increased IL-1RA expression, whereas the kidney, which does not accumulate CFZ, did not show changes in IL-1RA expression ($n = 4$ to 5). (E) Serum IL-1RA levels were unchanged after 2 weeks but were increased 21-fold after 8 weeks of CFZ treatment. The serum TNF- α and IL-1 β levels were below the limit of detection of the assay ($n = 6$). *, $P \leq 0.05$; **, $P \leq 0.01$; #, $P \leq 0.001$. Data are means \pm the SD, and an unpaired Student t test was used to compare control mice versus CFZ-treated mice.

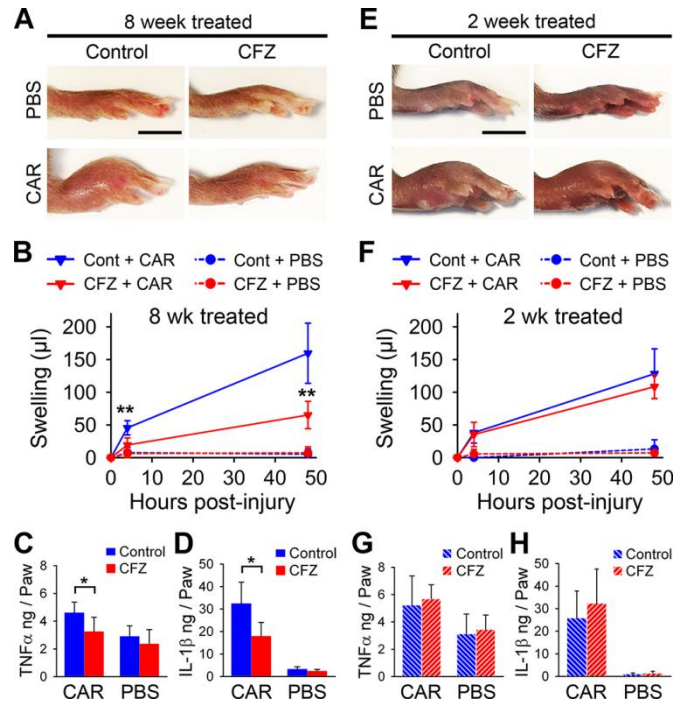


Figure 4-3 CFZ bioaccumulation and crystallization dampens inflammatory response in mouse footpad

Systemic CFZ bioaccumulation and crystal formation dampens CAR-induced inflammatory response in the mouse footpad. (A) Representative photographs of paws 48 h after CAR or PBS footpad injection show markedly reduced paw swelling in 8-week-CFZ-treated mice compared to control mice. Scale bar, 5 mm. (B) Paw swelling, as measured by foot volume, was reduced on average by 57% as early as 4 h after CAR injection in 8-week-CFZ-treated mice compared to control mice and was sustained through 48 h. The footpad homogenate cytokine levels of IL-1 β (C) and TNF- α (D) were reduced in 8-week-CFZ-treated mice at 48 h compared to untreated and injured paws. (E and F) Representative photographs of paws 48 h after CAR or PBS footpad injection in 2-week-CFZ-treated or control mice (E), which resulted in only a minor reduction in swelling at 4 and 48 h (F). Scale bar, 5 mm. (G and H) Associated footpad homogenate TNF- α (G) and IL-1 β (H) levels were unchanged. PBS-injected paws did not show any difference in cytokine expression between CFZ-treated or control paws. Data are means \pm the SD of $n = 5$ to 6/experiment. An unpaired Student t test was used to compare control versus CFZ-treated mice. *, $P \leq 0.05$; **, $P \leq 0.01$.

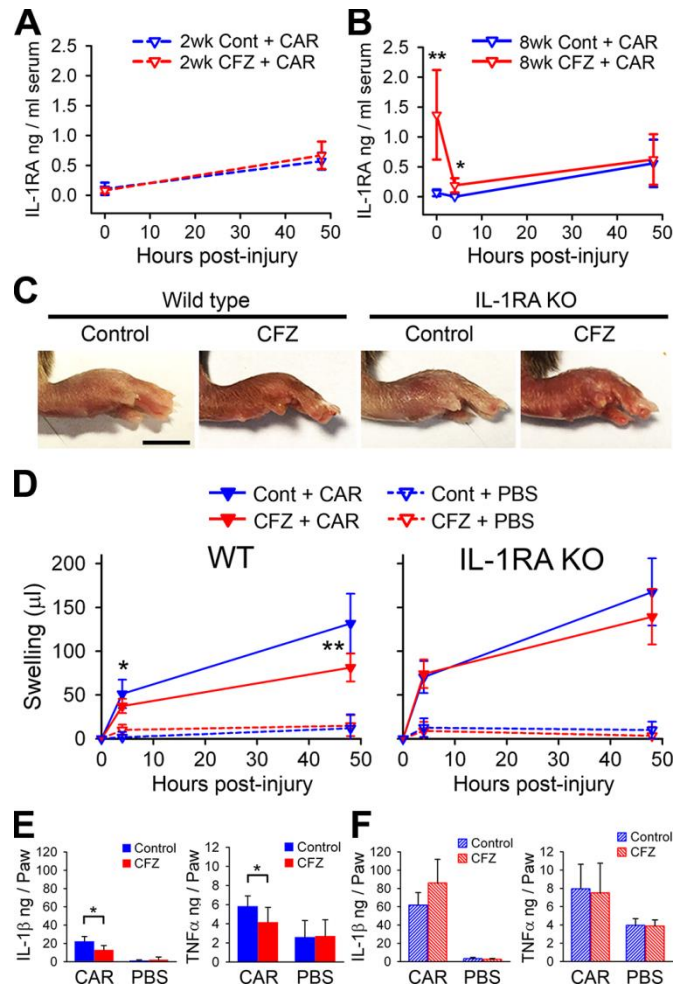


Figure 4-4 IL-1RA mediated anti-inflammatory activity

The CFZ-induced dampening of the acute inflammatory response in the CAR footpad model is mediated by circulating IL-1RA. (A) Two-week-CFZ-treated and control wild-type (WT) mice displayed similar serum IL-1RA levels before (0 h) and after (48 h) CAR injection. (B) Serum IL-1RA concentrations were significantly increased after 8 weeks of CFZ treatment compared to controls in WT mice (0 h). CAR injection in 8-week-CFZ-treated mice caused a sharp decline in serum IL-1RA concentrations by 4 h, whereas the levels in control CAR mice remained constant. At 48 h after CAR injection, the serum IL-1RA increased to similar levels in both control and CFZ-treated WT mice (data are means \pm the SD of $n = 5$ to 8 animals/group/time point). (C) Representative images of inflamed paws of 6-week-CFZ-treated WT mice and IL-1RA KO mice at 48 h after CAR injection. (D) Footpad swelling, as measured by foot volume, was reduced by 27 and 38% at 4 and 48 h after CAR injection, respectively, in 6-week-CFZ-treated WT mice compared to control WT mice. In IL-1RA KO mice with CFZ treatment, paw swelling was similar at 4 h compared to untreated littermates, and at 48 h, swelling was marginally reduced (17%) compared to untreated IL-1RA KO mice. (E) Footpad homogenate levels of IL-1 β and TNF- α were dampened in 6-week-CFZ-treated and CAR-injected WT mice at 48 h compared to control and CAR-injected paws. (F) Footpad homogenate levels of IL-1 β and TNF- α were unaffected in 6-week-CFZ-treated and CAR-injected IL-1RA KO mice at 48 h compared to control and CAR-injected paws. Data are the compilation of two separate experiments and are presented as means \pm the SD ($n = 7$ to 9). A Student t test was used to compare untreated versus CFZ-treated mice at each time point. *, $P \leq 0.05$; **, $P \leq 0.01$. Scale bar, 5 mm.

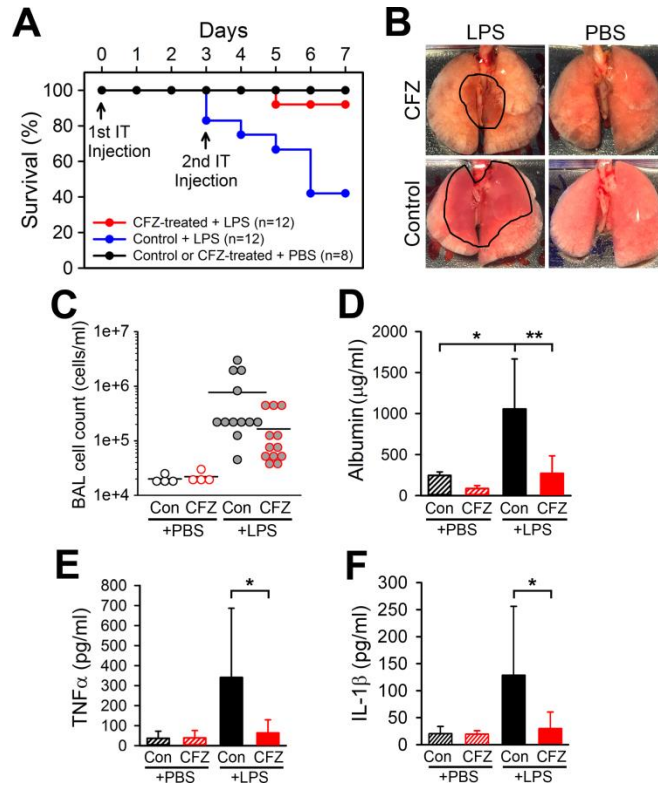


Figure 4-5 CFZ bioaccumulation enhances resistance to LPS-induced lung injury and improves survival

CFZ bioaccumulation enhances resistance to LPS-induced lung injury and improves mouse survival. (A) Kaplan-Meier survival curve showing the 92% survival rate of 8-week-CFZ-treated mice after LPS-induced acute lung injury compared to the 42% survival rate of control mice with LPS-induced injury. (B) A representative photograph shows the gross appearance of the lungs after PBS or LPS injection in control and CFZ-treated mice. Hemorrhaged areas caused by LPS injection are outlined in black lines. (C to F) CFZ treatment reduced LPS-induced increases in the BAL fluid cell count (C), albumin level (D), TNF- α level (E), and IL-1 β level (F). The data are the compilation of two separate experiments and are presented as means \pm the SD (PBS, $n = 4$; LPS, $n = 12$). One-way ANOVA was used to compare control versus CFZ-treated mice with PBS or LPS injections, and $P \leq 0.05$ was considered statistically significant. *, $P \leq 0.05$; **, $P \leq 0.01$.

4.9 Supporting Information Available

This material is published in *Antimicrobial Agents and Chemotherapy* and supplemental methods, figures and tables are available in Appendix C.

4.10 References

1. Barry VC, Belton JG, Conalty ML, Denney JM, Edward DW, O'Sullivan JF, Twomey D, Winder F. 1957. A new series of phenazines (rimino-compounds) with high antituberculosis activity. *Nature* 179:1013–1015. doi:10.1038/1791013a0.
2. Cholo MC, Steel HC, Fourie PB, Germishuizen WA, Anderson R. 2012. Clofazimine: current status and future prospects. *J Antimicrob Chemother* 67:290–298. doi:10.1093/jac/dkr444.
3. Reibel F, Cambau E, Aubry A. 2015. Update on the epidemiology, diagnosis, and treatment of leprosy. *Med Mal Infect* 45:383–393. doi:10.1016/j.medmal.2015.09.002.
4. Tyagi S, Ammerman NC, Li S-Y, Adamson J, Converse PJ, Swanson RV, Almeida DV, Grosset JH. 2015. Clofazimine shortens the duration of the first-line treatment regimen for experimental chemotherapy of tuberculosis. *Proc Natl Acad Sci U S A* 112:869–874. doi:10.1073/pnas.1416951112.
5. Lechartier B, Cole ST. 2015. Mode of action of clofazimine and combination therapy with benzothiazinones against *Mycobacterium tuberculosis*. *Antimicrob Agents Chemother* 59:4457–4463. doi:10.1128/AAC.00395-15.
6. Williams K, Minkowski A, Amoabeng O, Peloquin CA, Taylor D, Andries K, Wallis RS, Mdluli KE, Nuermberger EL. 2012. Sterilizing activities of novel combinations lacking first- and second-line drugs in a murine model of tuberculosis. *Antimicrob Agents Chemother* 56:3114–3120. doi:10.1128/AAC.00384-12.
7. Banerjee DK, Ellard GA, Gammon PT, Waters MF. 1974. Some observations on the pharmacology of clofazimine (B663). *Am J Trop Med Hyg* 23:1110–1115.
8. Baik J, Stringer KA, Mane G, Rosania GR. 2013. Multiscale distribution and bioaccumulation analysis of clofazimine reveals a massive immune system-mediated xenobiotic sequestration response. *Antimicrob Agents Chemother* 57:1218–1230. doi:10.1128/AAC.01731-12.
9. Keswani RK, Baik J, Yeomans L, Hitzman C, Johnson AM, Pawate AS, Kenis PJA, Rodriguez-Hornedo N, Stringer KA, Rosania GR. 2015. Chemical analysis of drug biocrystals: a role for counterion transport pathways in intracellular drug disposition. *Mol Pharm* 12:2528–2536. doi:10.1021/acs.molpharmaceut.5b00032.

10. Harbeck RJ, Worthen GS, Lebo TD, Peloquin CA. 1999. Clofazimine crystals in the cytoplasm of pulmonary macrophages. *Ann Pharmacother* 33:250. doi:10.1345/aph.18170.
11. Sukpanichnant S, Hargrove NS, Kachintorn U, Manatsathit S, Chanchairujira T, Siritanaratkul N, Akaraviputh T, Thakerngpol K. 2000. Clofazimine-induced crystal-storing histiocytosis producing chronic abdominal pain in a leprosy patient. *Am J Surg Pathol* 24:129–135. doi:10.1097/00000478-200001000-00016.
12. Jadhav MV, Sathe AG, Deore SS, Patil PG, Joshi NG, Joghi NG. 2004. Tissue concentration, systemic distribution, and toxicity of clofazimine: an autopsy study. *Indian J Pathol Microbiol* 47:281–283.
13. Tall AR, Yvan-Charvet L. 2015. Cholesterol, inflammation and innate immunity. *Nat Rev Immunol* 15:104–116. doi:10.1038/nri3793.
14. Martinon F, Pétrilli V, Mayor A, Tardivel A, Tschopp J. 2006. Gout-associated uric acid crystals activate the NALP3 inflammasome. *Nature* 440:237–241. doi:10.1038/nature04516.
15. Gehring U, Wijga AH, Brauer M, Fischer P, de Jongste JC, Kerkhof M, Oldenwening M, Smit HA, Brunekreef B. 2010. Traffic-related air pollution and the development of asthma and allergies during the first 8 years of life. *Am J Respir Crit Care Med* 181:596–603. doi:10.1164/rccm.200906-0858OC.
16. Sint T, Donohue JF, Ghio AJ. 2008. Ambient air pollution particles and the acute exacerbation of chronic obstructive pulmonary disease. *Inhal Toxicol* 20:25–29. doi:10.1080/08958370701758759.
17. Mackey JP, Barnes J. 1974. Clofazimine in the treatment of discoid lupus erythematosus. *Br J Dermatol* 91:93–96. doi:10.1111/j.1365-2133.1974.tb06723.x.
18. Lo JS, Berg RE, Tomecki KJ. 1989. Treatment of discoid lupus erythematosus. *Int J Dermatol* 28:497–507. doi:10.1111/j.1365-4362.1989.tb04599.x.
19. Chuaprapaisilp T, Piamphongsant T. 1978. Treatment of pustular psoriasis with clofazimine. *Br J Dermatol* 99:303–305. doi:10.1111/j.1365-2133.1978.tb02001.x.
20. Podmore P, Burrows D. 1986. Clofazimine: an effective treatment for Melkersson-Rosenthal syndrome or Miescher's cheilitis. *Clin Exp Dermatol* 11:173–178. doi:10.1111/j.1365-2230.1986.tb00443.x.

21. Medeiros Bezerra EL, Pereira Vilar MJ, Da Trindade Neto PB, Sato EI. 2005. Double-blind, randomized, controlled clinical trial of clofazimine compared with chloroquine in patients with systemic lupus erythematosus. *Arthritis Rheum* 52:3073–3078. doi:10.1002/art.21358.
22. Venkateswarlu B, Venkataramana D, Rao AV, Prabhakar MC, Reddy BM. 1992. Role of rifampin and clofazimine ointments in the treatment of leprosy. *Int J Lepr Other Mycobact Dis* 60:269–270.
23. Yoon GS, Sud S, Keswani RK, Baik J, Standiford TJ, Stringer KA, Rosania GR. 2015. Phagocytosed clofazimine biocrystals can modulate innate immune signaling by inhibiting TNF- α and boosting IL-1RA secretion. *Mol Pharm* 12:2517–2527. doi:10.1021/acs.molpharmaceut.5b00035.
24. Baik J, Rosania GR. 2011. Molecular imaging of intracellular drug-membrane aggregate formation. *Mol Pharm* 8:1742–1749. doi:10.1021/mp200101b.
25. Otterness IG, Moore PF. 1988. *Immunochemical techniques. L. Chemotaxis and inflammation. In Methods enzymology.* Elsevier, New York, NY.
26. Matute-Bello G, Frevert CW, Martin TR. 2008. Animal models of acute lung injury. *Am J Physiol Lung Cell Mol Physiol* 295:L379–L399. doi:10.1152/ajplung.00010.2008.
27. Lax S, Wilson MR, Takata M, Thickett DR. 2014. Using a noninvasive assessment of lung injury in a murine model of acute lung injury. *BMJ Open Respir Res* 1:e000014. doi:10.1136/bmjresp-2013-000014.
28. Nayak S, Doerfler PA, Porvasnik SL, Cloutier DD, Khanna R, Valenzano KJ, Herzog RW, Byrne BJ. 2014. Immune responses and hypercoagulation in ERT for Pompe disease are mutation and rhGAA dose dependent. *PLoS One* 9:e98336. doi:10.1371/journal.pone.0098336.
29. Toth LA. 2000. Defining the moribund condition as an experimental endpoint for animal research. *ILAR J* 41:72–79. doi:10.1093/ilar.41.2.72.
30. Nemzek JA, Xiao H-Y, Minard AE, Bolgos GL, Remick DG. 2004. Humane endpoints in shock research. *Shock* 21:17–25. doi:10.1097/00024382-200403001-00067.
31. Baik J, Rosania GR. 2012. Macrophages sequester clofazimine in an intracellular liquid crystal-like supramolecular organization. *PLoS One* 7:e47494. doi:10.1371/journal.pone.0047494.

32. Keswani RK, Yoon GS, Sud S, Stringer KA, Rosania GR. 2015. A far-red fluorescent probe for flow cytometry and image-based functional studies of xenobiotic sequestering macrophages. *Cytometry A* 87:855–867. doi:10.1002/cyto.a.22706.
33. Duewell P, Kono H, Rayner KJ, Sirois CM, Vladimer G, Bauernfeind FG, Abela GS, Franchi L, Nuñez G, Schnurr M, Espevik T, Lien E, Fitzgerald KA, Rock KL, Moore KJ, Wright SD, Hornung V, Latz E. 2010. NLRP3 inflammasomes are required for atherogenesis and activated by cholesterol crystals. *Nature* 464:1357–1361. doi:10.1038/nature08938.
34. Ioannou GN, Haigh WG, Thorning D, Savard C. 2013. Hepatic cholesterol crystals and crown-like structures distinguish NASH from simple steatosis. *J Lipid Res* 54:1326–1334. doi:10.1194/jlr.M034876.
35. Simard J-C, Vallières F, de Liz R, Lavastre V, Girard D. 2015. Silver nanoparticles induce degradation of the endoplasmic reticulum stress sensor activating transcription factor-6 leading to activation of the NLRP-3 inflammasome. *J Biol Chem* 290:5926–5939. doi:10.1074/jbc.M114.610899.
36. Demento SL, Eisenbarth SC, Foellmer HG, Platt C, Caplan MJ, Mark Saltzman W, Mellman I, Ledizet M, Fikrig E, Flavell RA, Fahmy TM. 2009. Inflammasome-activating nanoparticles as modular systems for optimizing vaccine efficacy. *Vaccine* 27:3013–3021. doi:10.1016/j.vaccine.2009.03.034.
37. Peeters PM, Eurlings IMJ, Perkins TN, Wouters EF, Schins RPF, Borm PJA, Drommer W, Reynaert NL, Albrecht C. 2014. Silica-induced NLRP3 inflammasome activation in vitro and in rat lungs. *Part Fibre Toxicol* 11:58. doi:10.1186/s12989-014-0058-0.
38. Gabay C, Smith MF, Eidlen D, Arend WP. 1997. Interleukin 1 receptor antagonist (IL-1Ra) is an acute-phase protein. *J Clin Invest* 99:2930–2940. doi:10.1172/JCI119488.
39. Gabay C, Gigley J, Sipe J, Arend WP, Fantuzzi G. 2001. Production of IL-1 receptor antagonist by hepatocytes is regulated as an acute-phase protein in vivo. *Eur J Immunol* 31:490–499. doi:10.1002/1521-4141(200102)31:2<490::AID-IMMU490>3.0.CO;2-H.
40. Dinarello CA, van der Meer JWM. 2013. Treating inflammation by blocking interleukin-1 in humans. *Semin Immunol* 25:469–484. doi:10.1016/j.smim.2013.10.008.
41. Arend WP. 2002. The balance between IL-1 and IL-1Ra in disease. *Cytokine Growth Factor Rev* 13:323–340. doi:10.1016/S1359-6101(02)00020-5.

42. McDougall AC, Horsfall WR, Hede JE, Chaplin AJ. 1980. Splenic infarction and tissue accumulation of crystals associated with the use of clofazimine (Lamprene; B663) in the treatment of pyoderma gangrenosum. *Br J Dermatol* 102:227–230. doi:10.1111/j.1365-2133.1980.tb05697.x.
43. Shi Y, Mucsi AD, Ng G. 2010. Monosodium urate crystals in inflammation and immunity. *Immunol Rev* 233:203–217. doi:10.1111/j.0105-2896.2009.00851.x.
44. Riteau N, Baron L, Villeret B, Guillou N, Savigny F, Ryffel B, Rassendren F, Le Bert M, Gombault A, Couillin I. 2012. ATP release and purinergic signaling: a common pathway for particle-mediated inflammasome activation. *Cell Death Dis* 3:e403. doi:10.1038/cddis.2012.144.
45. Bulakh PM, Kowale CN, Ranade SM, Burte NP, Chandorkar AG. 1983. The effect of clofazimine on liver function tests in lepra reaction (ENL). *Lepr India* 55:714–718.
46. Cariello PF, Kwak EJ, Abdel-Massih RC, Silveira FP. 2015. Safety and tolerability of clofazimine as salvage therapy for atypical mycobacterial infection in solid organ transplant recipients. *Transpl Infect Dis* 17:111–118. doi:10.1111/tid.12340.
47. Kaluarachchi SI, Fernandopulle BM, Gunawardane BP. 2001. Hepatic and haematological adverse reactions associated with the use of multidrug therapy in leprosy: a five year retrospective study. *Indian J Lepr* 73:121–129.
48. Gent S, Kleinbongard P, Dammann P, Neuhäuser M, Heusch G. 2015. Heart rate reduction and longevity in mice. *Basic Res Cardiol* 110:2. doi:10.1007/s00395-014-0460-7.
49. Stokes WS. 2002. Humane endpoints for laboratory animals used in regulatory testing. *ILAR J* 43(Suppl):S31–S38.
50. Van Rensburg CE, Jooné GK, O'Sullivan JF, Anderson R. 1992. Antimicrobial activities of clofazimine and B669 are mediated by lysophospholipids. *Antimicrob Agents Chemother* 36:2729–2735. doi:10.1128/AAC.36.12.2729.
51. Oliva B, O'Neill AJ, Miller K, Stubbings W, Chopra I. 2004. Anti-staphylococcal activity and mode of action of clofazimine. *J Antimicrob Chemother* 53:435–440. doi:10.1093/jac/dkh114.
52. Fulda S, Gorman AM, Hori O, Samali A. 2010. Cellular stress responses: cell survival and cell death. *Int J Cell Biol* 2010:214074.

53. Kroemer G, Mariño G, Levine B. 2010. Autophagy and the integrated stress response. *Mol Cell* 40:280–293. doi:10.1016/j.molcel.2010.09.023.
54. Fukutomi Y, Maeda Y, Makino M. 2011. Apoptosis-inducing activity of clofazimine in macrophages. *Antimicrob Agents Chemother* 55:4000–4005. doi:10.1128/AAC.00434-11.
55. Sardiello M, Palmieri M, di Ronza A, Medina DL, Valenza M, Gennarino VA, Di Malta C, Donaudy F, Embrione V, Polishchuk RS, Banfi S, Parenti G, Cattaneo E, Ballabio A. 2009. A gene network regulating lysosomal biogenesis and function. *Science* 325:473–477. doi:10.1126/science.1174447.
56. Logan R, Kong AC, Krise JP. 2014. Time-dependent effects of hydrophobic amine-containing drugs on lysosome structure and biogenesis in cultured human fibroblasts. *J Pharm Sci* 103:3287–3296. doi:10.1002/jps.24087.
57. Parks A, Charest-Morin X, Boivin-Welch M, Bouthillier J, Marceau F. 2015. Autophagic flux inhibition and lysosomogenesis ensuing cellular capture and retention of the cationic drug quinacrine in murine models. *PeerJ* 3:e1314. doi:10.7717/peerj.1314.
58. Zhitomirsky B, Assaraf YG. 2015. Lysosomal sequestration of hydrophobic weak base chemotherapeutics triggers lysosomal biogenesis and lysosome-dependent cancer multidrug resistance. *Oncotarget* 6:1143–1156. doi:10.18632/oncotarget.2732.
59. Emanuel R, Sergin I, Bhattacharya S, Turner JN, Epelman S, Settembre C, Diwan A, Ballabio A, Razani B. 2014. Induction of lysosomal biogenesis in atherosclerotic macrophages can rescue lipid-induced lysosomal dysfunction and downstream sequelae. *Arterioscler Thromb Vasc Biol* 34:1942–1952. doi:10.1161/ATVBAHA.114.303342.
60. Hasegawa H. 2013. Aggregates, crystals, gels, and amyloids: intracellular and extracellular phenotypes at the crossroads of immunoglobulin physicochemical property and cell physiology. *Int J Cell Biol* 2013:604867.
61. Hasegawa H, Wendling J, He F, Trilisky E, Stevenson R, Franey H, Kinderman F, Li G, Piedmonte DM, Osslund T, Shen M, Ketchum RR. 2011. In vivo crystallization of human IgG in the endoplasmic reticulum of engineered Chinese hamster ovary (CHO) cells. *J Biol Chem* 286:19917–19931. doi:10.1074/jbc.M110.204362.
62. Bettigole SE, Glimcher LH. 2015. Endoplasmic reticulum stress in immunity. *Annu Rev Immunol* 33:107–138. doi:10.1146/annurev-immunol-032414-112116.

Chapter 5

Elasticity in Macrophage-Synthesized Biocrystals

5.1 Relevance to Thesis

The accumulation and stability of clofazimine biocrystals within macrophages forms the basis for the central hypothesis of this work, and studying CLDIs with a quantitative, microscopic imaging methodology is one of the three aims guiding this research. To that end, this work is a study of the biomechanical properties of clofazimine-hydrochloride, and how this relates to the underlying crystal structure of the biocrystal. As related to this thesis, my own contribution to the work presented in this chapter involved the utilization of the quantitative polarized light microscope within our laboratory. Live CLDI containing macrophages and isolated CLDIs were imaged under polarized light to study the curvature of the crystals both inside of and outside of a cellular environment. Following this analysis, we determined that intracellular CLDIs show a significant curvature, which may be actively controlled by cellular processes, while CLDIs that have been removed from a cellular environment show significantly less curvature. Based off of this, we hypothesized that is due to intracellular forces acting on the CLDI that causes this bending, which may be a result of an active process being performed by the macrophage to stabilize the crystal. Additionally, using the polarized light microscope, we revealed that these crystals are highly flexible and that upon application of an external stress (i.e. manual bending of the crystal), the internal stress brought about by this external bending force alters the orientation of maximum transmission of polarized light through the crystal. This alteration in the orientation of maximum transmission of polarized light resulted from minute changes to the underlying molecular organization of the clofazimine hydrochloride due to the bending and subsequent return to an unbent state, which is a result of the flexible packaging of the clofazimine-hydrochloride within the unit cell of the crystal. Further chemical analysis showed that no chemical change occurred within the crystal following bending. The quantitative polarized light microscopy that was performed here was the first attempt at analysis of these crystals, revealing

their high degrees of diattenuation anisotropy and extensive underlying molecular organization, resulting from a cellular self-assembly. The techniques developed to both image and analyze these crystals were further refined and utilized throughout chapters 6, 7, and 8 to analyze CLDIs within live cells and in tissue cryosections.

5.2 Abstract

Supramolecular crystalline assembly constitutes a rational approach to bioengineer intracellular structures. Here, biocrystals of clofazimine (CFZ) that form *in vivo* within macrophages were measured to have marked curvature. Isolated crystals, however, showed reduced curvature suggesting that intracellular forces bend these drug crystals. Consistent with the ability of biocrystals to elastically deform, the inherent crystal structure of the principal molecular component of the biocrystals—the hydrochloride salt of CFZ (CFZ-HCl)—has a corrugated packing along the (001) face and weak dispersive bonding in multiple directions. These characteristics were previously found to be linked to the elasticity of other organic crystals. Internal stress in bent CFZ-HCl led to photoelastic effects on the azimuthal orientation of polarized light transmittance. We propose that elastic, intracellular crystals can serve as templates to construct functional microdevices with different applications.

5.3 Results and Discussion

Abnormal morphology of crystals has been a subject of significant study over the last century [1-6]. Particularly, crystalline growth and distribution within living organisms such as cells, tissues and clinically in humans has allowed an understanding of how solid-state crystal chemistry can modulate biological and biophysical environments [7-12]. Specifically, the interaction of crystalline matter with cells such as macrophages within clinical microenvironments has garnered much attention [13-15]. Macrophages (M ϕ s) are critical self–non-self-recognizing immune cells capable of maintaining mammalian homeostasis and resolving inflammatory conditions responsible for many diseases. Concurrently, M ϕ s are cellular “vacuum cleaners” eliminating foreign matter, typically referred to as xenobiotics. Such elimination may also be preceded by massive bioaccumulation, self-assembly and intracellular crystallization of sequestered foreign molecular agents such as clofazimine (CFZ), a red-pigmented, anti-inflammatory, antimycobacterial, FDA-approved drug molecule [16, 17].

Specifically, CFZ accumulates within M ϕ s upon prolonged oral dosage in humans [18-21] and rodent models [13, 22-24] (protocol in Appendix D) to form biocrystals containing clofazimine hydrochloride (CFZ-HCl) crystalline domains [25].

In order to characterize the crystal structure and physical morphology of biocrystals, peritoneal and alveolar M ϕ s from an 8-week CFZ-fed mouse were harvested. Through brightfield microscopy, several cell-associated dark red crystals were identified, some of which were surprisingly curved (Figure 1a). Moreover, after 10 minutes, the crystals turned over likely due to mechanical forces exerted by its parent M ϕ (Figure 1a). Upon closer inspection, we observed that another biocrystal in close proximity to the curved biocrystal also had a minor curvature that straightened out when the curved biocrystal flipped (Figure 1 a). In light of this empirical evidence, we further characterized the biocrystals for their curvature (κ) within or isolated from M ϕ s (Figure 1 b and SI. 11). The curvature per unit length (κ/L) of biocrystals was significantly higher when present in peritoneal M ϕ s (4.8-fold change in mean, $p < 0.005$) or alveolar M ϕ s (3.6-fold change in mean, $p < 0.005$) compared to when isolated from M ϕ s. A greater number of biocrystals were found to be inherently straight or having zero curvature when isolated (26) than when present in peritoneal M ϕ s (10) or alveolar M ϕ s (18) (Figure 1b, Figure SI. 11). Such a reduction in curvature of isolated biocrystals are indicative of forces acting on the crystals curving them when present inside M ϕ s and secondly of inherent elasticity of the biocrystals.

Mechanical properties of crystals (moduli, plasticity, and elasticity) are known to be dependent on the atoms, ions or molecules forming the crystals and the interactions between these particles (molecular packing and intramolecular bonding) [26-30]. Further, recent work has explored the relationship between elasticity in organic crystals and their molecular and structural properties. Ghosh and Reddy reported an elastic and bendable organic cocrystal solvate formed from caffeine, 4-chloro-3-nitrobenzoic acid and methanol with weak and dispersive C–H $\cdots\pi$ interactions in three nearly perpendicular directions, suggesting that elastic deformation is due to isotropic molecular packing [28, 29]. Subsequently, Ghosh et al. studied *n*-benzylideneanilines and elucidated design rules for elastic organic crystals [26-28]. Accordingly, elastic organic crystals should have 1) multi-directional weak dispersive bonds that can be easily broken to dissipate energy as the crystal is bending and that can be easily formed when no force is applied

and 2) corrugated packing along a crystallographic face to prevent long range dislocation within the crystal [26-28]. In these studies, when crystals did not align with these design rules, they did not demonstrate elastic behavior. As such, we explored if elasticity and curvature of biocrystals could be explained via these design parameters.

As the primary component of the biocrystals is CFZ-HCl, we hypothesized that the inherent crystal structure of CFZ-HCl plays a role in the flexibility (being able to adopt non-linear morphologies) and elasticity (being able to return to linear conformations upon removal of force) of the biocrystals. A synthetic crystallization route was developed to grow CFZ-HCl crystals with similar crystal structure to the biocrystals (protocol in Appendix D). The synthetic CFZ-HCl crystals form dark red rectangular plates (Figure 2a) that closely resemble the crystal habit and color of the biocrystals (Figure 2b) as observed with brightfield microscopy. The CFZ-HCl crystals can grow to be much larger than the biocrystals allowing for optimal structural characterization. The powder XRD (Figure 2c) suggests a strong agreement in the observed peaks of CFZ-HCl with those from the biocrystals as previously reported [25]. Both samples show strong preferential orientation of the crystals along the (001) face, consistent with face indexing of single crystals (Figure SI. 12). The most intense peak on the p-XRD spectra is the (002) peak due to a systematic absence at (00*l*) when $l=2n$ for *Pbca* space groups. Thus, the synthesized CFZ-HCl crystals are a suitable model for characterizing the mechanical behavior of the biocrystals.

Single-crystal XRD was also performed to determine the crystal structure of CFZ-HCl. The CFZ-HCl crystals grow in an orthorhombic *Pbca* space group with unit cell parameters; $a=10.266 \text{ \AA}$, $b=19.828 \text{ \AA}$, and $c=24.156 \text{ \AA}$, $\alpha=\beta=\gamma=90^\circ$ and $Z=8$ (CCDC number: 1497722). One CFZ and one HCl molecule make up the asymmetric unit (Figure 3 a). Cl3 (the Cl associated with the HCl) associates with the CFZ through two N-H...Cl hydrogen bond interactions between N3-H...Cl3 and N4-H...Cl3 (D, d, θ : 3.172 \AA , 2.376 \AA , 166.45° , and 3.104 \AA , 2.243 \AA , 174.51°). The data set was solved to 99.8% completeness. Water was incorporated into the crystal structure at an occupancy of 0.13, and there was some disorder in the isopropyl group. The presence of water likely caused a change in the orientation of the isopropyl group, thereby contributing to the observed disorder (Figure SI. 13). A summary of the unit cell parameters and diffraction data can be found in Table S8.

A key design feature of the CFZ-HCl crystal structure is the corrugated packing along the (001) face (Figure 3 b,c). One CFZ-HCl molecule makes up one step of the zig-zag and together the steps make up one corrugated sheet. The steps of the zig-zag are held together with weak C–H \cdots π and C–H \cdots Cl interactions, highlighted by light blue dotted lines and orange solid lines, respectively (Figure 3 b). Cl3 is situated in the crease of the zig-zags and serves as an anchor by coordinating with 3 additional molecules strengthening interactions within the crease and coordinating with adjacent sheets. Bond distances and angles are as follows: C14–H \cdots Cl3, 3.503 Å, 2.724 Å, 139.72°, C24–H \cdots Cl3, 3.457 Å, 2.757 Å, 131.19°, and C4–H \cdots Cl3, 3.625 Å, 2.900 Å, 133.9°. These interactions are in 3 nearly perpendicular directions. Weak dispersive bonding between the sheets of the zig-zags from $\pi\cdots\pi$ interactions between the aromatic rings is also present (grey dotted lines, Figure 3 b). Cl1 interacts with C5 (C5–H \cdots Cl1, 3.516 Å, 2.937 Å, 120.48°) to create a ribbon of CFZ molecules down the *b*-axis (Figure SI. 14). When viewed along the *c*-axis this interaction is located in the crease and it stabilizes interactions between the sheets of the zig zag. As such, the weak multi-directional interactions are located at critical parts of the zig-zag, particularly associated with Cl3 and support the previously proposed design rules for crystal elasticity [26]. The angle between the corrugated steps is 82°. All intermolecular interactions are listed in Table S9. Face indexing of the crystal during XRD showed that the (001) face is the largest surface which corresponds to the previous p-XRD data. The projection of the (001) face is shown in Figure 3 c to better show the corrugated packing. Projections of all the crystallographic faces can be found in Figure SI. 15.

Interestingly, while harvesting CFZ-HCl crystals for single crystals XRD, the crystals would noticeably bend when force was applied to pick up the crystals. As soon as the force was removed the crystals would promptly return to their original linear morphologies. Subsequently, video microscopy of bending crystals with tweezers was performed to further demonstrate their observed elastic response (Movie 1). Crystallization experiments yielded a very wide size distribution of crystals out of which crystals between 500 μm and 2 mm long and ca. 20 μm thick were chosen. The CFZ-HCl crystals typically lie with the (001) face normal to the substrate (Figure 4 a). When a slight force was applied, the crystal rotated 90° about the *a*-axis (Figure 4 b). When a force was applied to the (001) face, the crystal bent (Figure 4 c,d) and assumed its original shape upon removal of the force (Figure 4 e). The crystal arched again when a second force was applied, Figure 4 f. As such, the crystals can be bent many times without noticeable

deformation to the crystal. In one experiment, a crystal was bent 8 times without noticeable deformation (Movie 2). However, upon applying a larger force, the crystal snapped and the crystalline fragments adopted the original straight configuration (Movies 1 and 2).

To confirm the elastic deformation of CFZ-HCl, polarization microscopy was performed as a way of measuring the photoelastic phenomena that is commonly observed with application of stress and development of strain [31]. In this particular study, linear dichroism could be measured using hardware configured on an epifluorescence-brightfield microscope [32, 33] (see the Appendix D for protocol). Crystals were imaged under polarized light following which the anisotropy in transmittance and importantly, the azimuth (the polarization orientation that results in maximum transmittance) were computed (Figure 5) [34]. Crystals were first identified as regions with low transmittance (Figure 5 a,c). Given the structural packing of the CFZ-HCl lattice and absence of polycrystalline elements in the biocrystals, the azimuth distribution was expectedly isotropic across the crystal plane when unstressed and straight (Figure 5 b). In contrast, the azimuth was anisotropic in the elastically deformed region of the crystal wherein two approximately orthogonal azimuthal orientations were measured (Figure 5 d). In the concave region, the azimuth was perpendicular to the long axis of the crystal whereas in the convex region, the azimuth was retained along the long-axis of the crystal as observed in the straight crystals. Such anisotropy is clearly indicative of a stress network resulting in the development of an elastic strain through the crystal [35]. As such, given the extent of cross-interactions within the crystal lattice as described before (Figure 3, SI.11–SI.14), the development of an elastic stress–strain network through an expectedly isotropic crystal structure was accomplished and verified through photoelastic azimuth measurements.

Further, no differences in vibrational spectra (Raman) were evident before and after bending at the point of maximum curvature in these crystals (Figure SI. 16). Naturally curved crystals also showed no differences in molecular vibrations compared to the reference CFZ-HCl crystals. Finally, the melting point for CFZ-HCl was measured to be 275 °C (Figure SI. 17), which is 53 °C degrees higher than CFZ while other salts of CFZ also have melting points <246 °C [36]. As indicated by their melting points, the salts of CFZ are more stable than CFZ. The stabilization of CFZ as CFZ-HCl within mammalian cells therefore favors the formation of a highly stable crystalline polymorph and as reported here has appropriate structural packing

features, reinforced by the additional Cl from HCl (Cl₃ in Figure 3 a) that allow it to adapt to intracellular mechanical stressors.

In summary, we show that the inherent structural packing features of CFZ-HCl within biocrystals indeed contribute to their elasticity and naturally adjustable curvature. As such, formation of biocrystals mediated by M ϕ s leads to the development of elastic and curved crystalline elements with structural packing features that showcase the classical design rules designated for organic crystal flexibility [26-29]. The presence of CFZ biocrystals in the M ϕ endows them with potent anti-inflammatory characteristics [37, 38] and specific fluorescent [39] and photoacoustic [40, 41] signatures for cellular optical tracking. Such dual therapeutic and diagnostic (theranostic) applications make biocrystals a potent cellular device that could be harnessed for biomedical applications. M ϕ -mediated crystallization is an important example of how these cells self-assemble a crystal with features that allow for easier adaptability to the mechanical environment of the cell, thereby allowing a massive drug loading within the cell. Importantly, the additional Cl (in HCl) is most likely reinforced within CFZ biocrystals through the presence of multiple chloride channels in macrophages and their highly regulated role in cellular physiology [42-44]. Here, we show that the salt chloride also plays an integral role in the structural stability and intracellular mechanical adaptation of biocrystals via elasticity.

Furthermore, mechanical flexibility of exogenous elements within cells could be a critical design parameter toward engineering organic intracellular constructs to endow cells with unnatural yet stable and beneficial features for therapeutic applications. Finally, viscoelasticity, pressures and connected mechano-transductive elements are connected to inflammatory cell phenotypes [45-49]. As such, the mechanochemical characterization of intracellular properties could be important for cell-based mechano-biological applications leading to a new class of pharmaceuticals: mechano-pharmaceuticals.

5.4 Acknowledgements

We thank the National Science Foundation (NSF) for a Graduate Research Fellowship to E.M.H. (DGE-1144245), National Institute of General Medical Sciences (NIGMS) for funding support to G.R.R. (R01GM078200), University of Michigan of Office of Research MCubed Program funding to G.R.R., Michigan Institute for Clinical & Health Research Pilot Seed funding to

G.R.R. and R.K.K. (NIH: UL1TR000433) and the Interdisciplinary REU (Research Experiences for Undergraduates) Program housed in the College of Pharmacy, University of Michigan for funding B.A.F. through the NSF-Division of Biological Infrastructure (NSF-DBI) (DBI-1263079). We acknowledge the support of Dr. Gislaine Kuminek, Dr. Nair Rodriguez-Hornedo, Dr. Gi Sang Yoon and Sudha Sud (Department of Pharmaceutical Sciences, College of Pharmacy, University of Michigan) for help with DSC and animal experiments, Dr. Danielle Gray, George L. Clark (X-ray Facility and 3M Materials Laboratory, University of Illinois) for discussion about crystallographic data, and Lucas C. Gonzalez (Department of Chemical and Biomolecular Engineering, University of Illinois) for help with crystallization experiments.

5.5 Figures

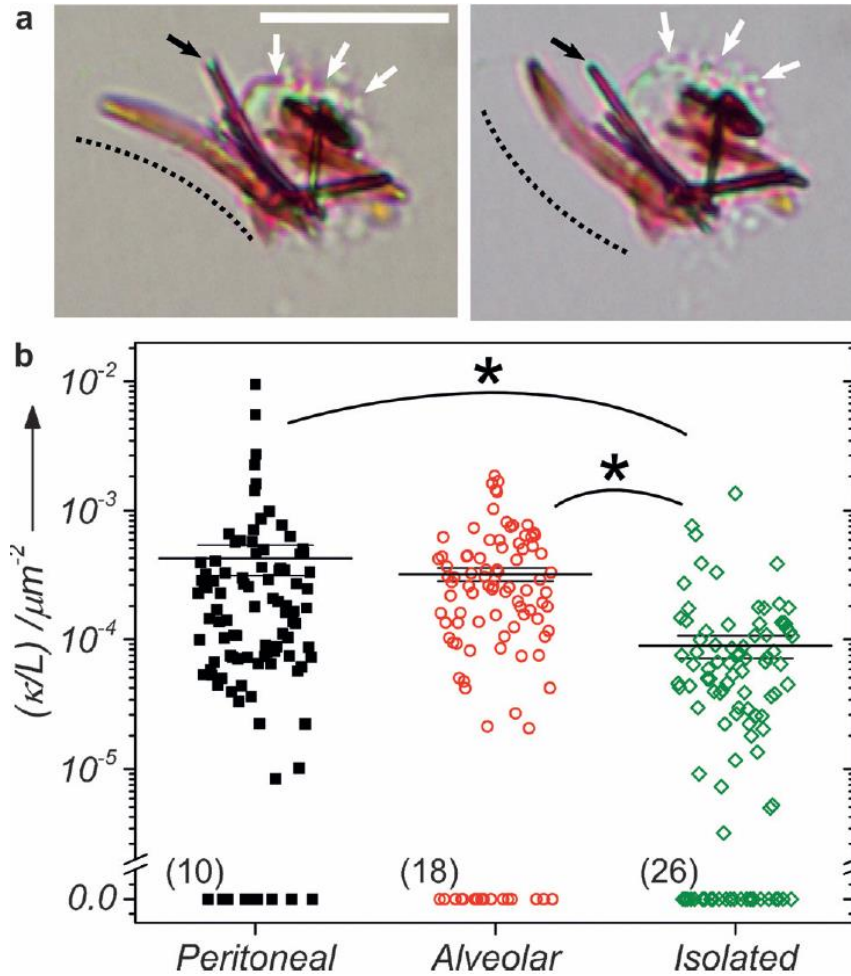


Figure 5-1 Curvature of CLDIs within macrophages and isolated CLDIs

a) Peritoneal macrophages from a CFZ-fed mouse with the curvature of the curved biocrystal marked with dotted lines (white arrows show cell membrane, black arrows mark the crystal in physical contact with the first curved crystal). Scale bar: 10 μm . b) Curvature per unit arc length (κ/L) of biocrystals in peritoneal M ϕ s or alveolar M ϕ s or when isolated from splenic M ϕ s. ($n=100$ biocrystals, *: $p < 0.005$). The wider and thick horizontal line indicates the mean of the distribution whereas the other smaller two lines indicate the mean \pm SE. Number in brackets indicates the number of biocrystals measured to have zero curvature.

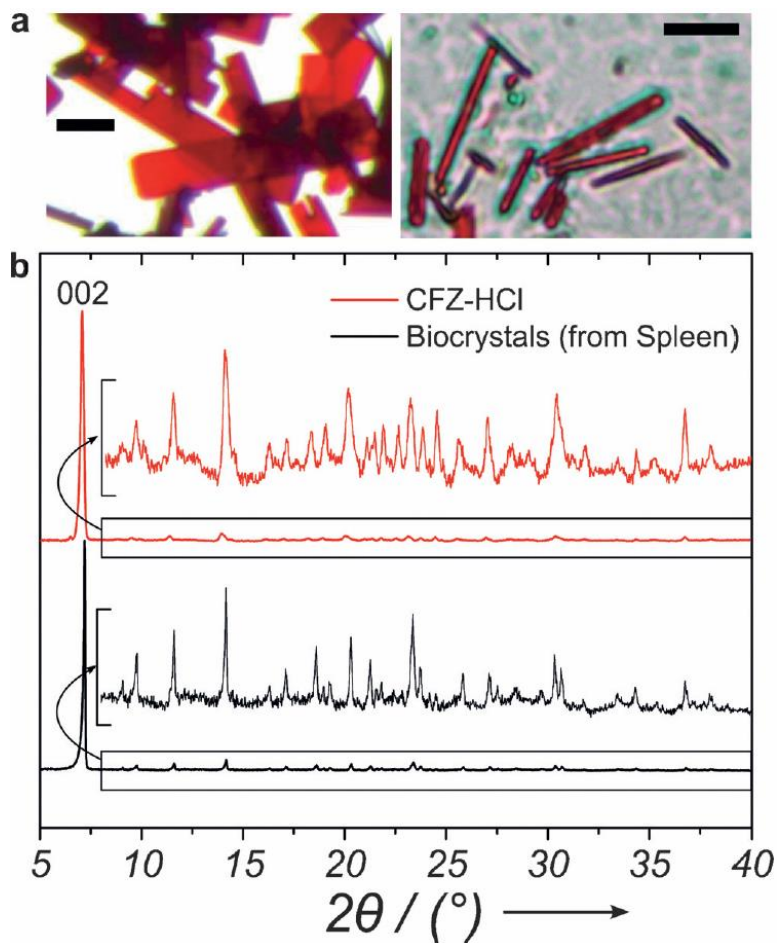


Figure 5-2 Images and powder X-ray diffraction of CLDIs and CFZ-HCl

Optical micrograph of a) synthesized CFZ-HCl crystals, scale bar: 50 μm and b) harvested biocrystals from a 8-week CFZ-fed mouse spleen, scale bar: 10 μm . c) Powder X-ray diffraction data from biocrystals and CFZ-HCl crystals. Both samples display preferential orientation favoring the (001) face. The diffraction data from $2\theta = 8\text{--}40^\circ$ is zoomed in for convenient comparisons.

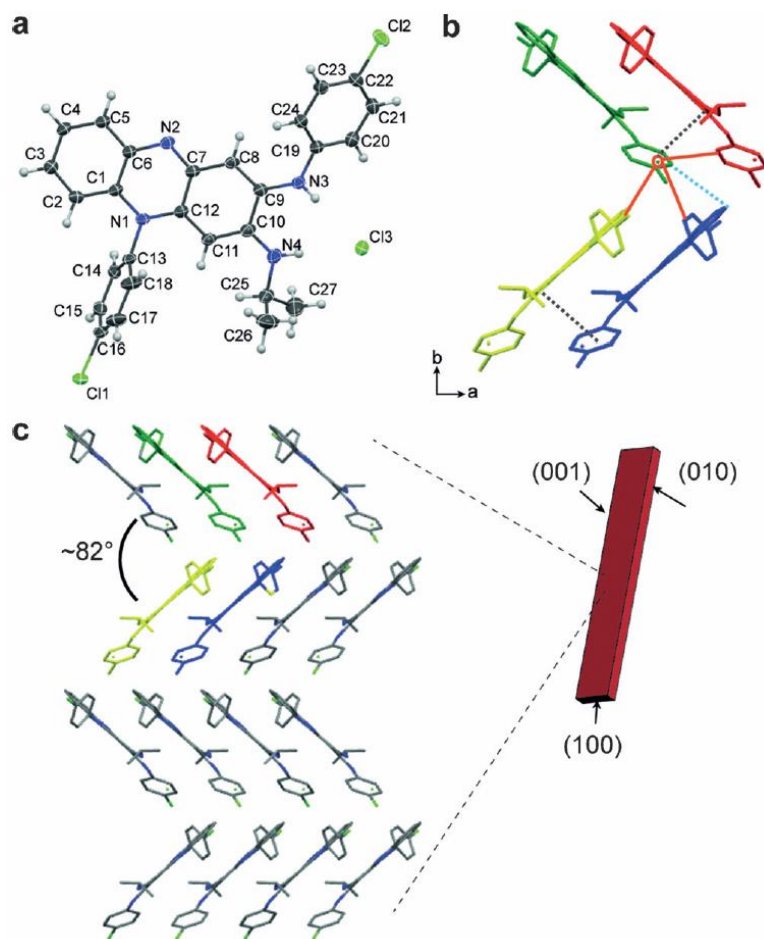


Figure 5-3 CFZ-HCl structure and crystal packing

a) Asymmetric unit of CFZ-HCl displayed as an ellipsoid plot with 50 % probability. The atomic positions for all non-hydrogen atoms are labeled. b) One section of the corrugated packing with solid orange lines indicating C–H⋯Cl interactions, C–H⋯ π indicated with a light blue dotted line and π ⋯ π interactions indicated by light grey dotted lines (unit cell looking along the c -axis). The molecules are displayed as capped sticks with the hydrogen atoms removed for better visualization of the crystals packing. c) Crystallographic projections of packing along the (001) face showing the corrugated packing. The projection is made up of $2 \times 2 \times 0.5$ ($a \times b \times c$) unit cells.

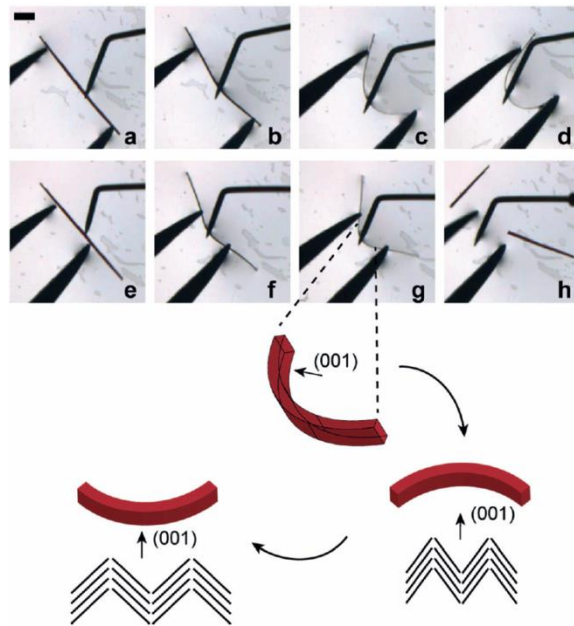


Figure 5-4 Bending of synthetic CFZ-HCl crystal

a–d) A CFZ-HCl crystal was bent by applying a force with a crystallization probe while the crystal was held stationary against a pair of tweezers. e) The force was removed and the crystal quickly regained the original position before f) another force was applied to the crystal. Scale bar is 100 μm . The bottom schematic shows how the angle of corrugation would look like on the convex and concave edges of the crystal during bending.

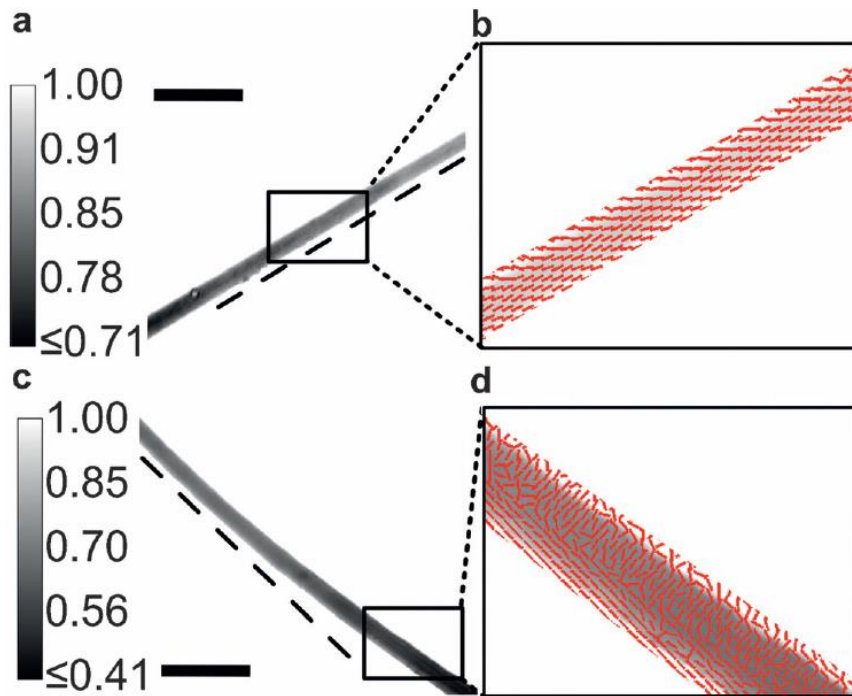


Figure 5-5 Azimuth of CFZ-HCl before and after bending

a) Computed transmittance image of a a,b) straight vs. c,d) bent crystal. Calibration bar in (a,c) shows the range of transmittance. Dark regions (with low transmittance) follow the crystal with the dotted tangential line from one edge of the crystal confirming the curvature in the crystal. Azimuth: polarization orientation of maximum transmittance overlaid on the transmittance image indicating unidirectional axes in the b) straight crystal while in the d) bent crystal, there is a bidirectional axes depending on the direction of compressional (inward bending edge leads to an orthogonal axes) or tensile stress (outward bending edge leading to a longitudinal axis). Scale bar in (a,b) is 100 μm .

5.6 Supporting Information Available

This material is published in *Angewandte Chemie* and supplemental figures and tables are available in Appendix D. Supplemental videos are also available online.

5.7 References

1. L. J. Spencer, *Mineral.Mag.*, **1921**, *19*, 263 –274.
2. M. K. Panda, S. Ghosh, N. Yasuda, T. Moriwaki, G. D. Mukher- jee, C.M. Reddy, P. Naumov, *Nat. Chem.*, **2015**, *7*,65–72.
3. C. M. Reddy, R.C. Gundakaram, S. Basavoju, M. T. Kirchner, K. A. Padmanabhan, G. R. Desiraju, *Chem. Commun.*, **2005**, 3945 –3947.
4. H. Koshima, R. Matsuo, M.Matsudomi, Y. Uemura, M. Shiro, *Cryst. Growth Des.*, **2013**, *13*, 4330 –4337.
5. K. Godwod, A. T. Nagy, Z. Rek, *Phys.Status Solidi A*, **1976**, *34*, 705.
6. F. Terao, M. Morimoto, M. Irie, *Angew.Chem. Int. Ed.*, **2012**, *51*, 901 –904; *Angew.Chem.*, **2012**, *124*,925 –928.
7. J. Baumgartner, G. Morin, N. Menguy, T. Perez Gonzalez, M. Widdrat, J. Cosmidis, D. Faivre, *Proc.Natl. Acad. Sci. USA*, **2013**, *110*, 14883 –14888.
8. M. I. Siponen, P. Legrand, M. Widdrat, S. R. Jones, W.-J. Zhang, M. C. Y. Chang, D. Faivre, P. Arnoux, D. Pignol, *Nature*, **2013**, *502*, 681 –684.
9. Y. Wang, A. Lomakin, T. Hideshima, J. P. Laubach, O. Ogun, P. G. Richardson, N. C. Munshi, K. C. Anderson, G. B. Benedek, *Proc.Natl. Acad. Sci. USA*, **2012**, *109*, 13359 –13361.
10. P. F. Weller, E.J. Goetzl, K. F. Austen, *Proc.Natl. Acad. Sci. USA*, **1980**, *77*, 7440 –7443.
11. S. R. Mulay, H.-J. Anders, *N. Engl. J. Med.*, **2016**, *374*, 2465 –2476.
12. D. J. Sullivan, Jr., I.Y. Gluzman, D. E. Goldbery, *Science*, **1996**, *271*, 219 –222.
13. R. T. Aplin, A. C. McDougall, *Experientia*, **1975**, *31*, 468 –469.
14. P. Vicari, V. M. Sthel, *N. Engl. J. Med.*, **2015**, *373*, e27.

15. F. Martinon, V. Petrilli, A. Mayor, A. Tardivel, J. Tschopp, *Nature*, **2006**, *440*, 237 – 241.
16. M. C. Cholo, H.C. Steel, P. B. Fourie, W.A. Germishuizen, R. Anderson, *J. Antimicrob. Chemother.*, **2012**, *67*, 290 –298.
17. V. C. Barry, J.G. Belton, M. L. Conalty, J.M. Denny, D.W. Edwards, J. F. O’Sullivan, D. Twomey, F. Winder, *Nature*, **1957**, *179*, 1013 –1015.
18. L. Levy, *Am. J. Trop.Med. Hyg.*, **1974**, *23*, 1097 –1109.
19. P. Belaube, J.Devaux, M. Pizzi, R. Boutboul, Y. Privat, *Int. J. Lepr.Other Mycobact. Dis.*, **1983**, *51*, 328 –330.
20. D. K. Banerjee, G. A. Ellard, P. T. Gammon, M. F. R. Waters, *Am. J. Trop.Med. Hyg.*, **1974**, *23*, 1110 –1115.
21. A. C. McDougall, W. R. Horsfall, J. E. Hede, A.J. Chaplin, *Br.J. Dermatol.*, **1980**, *102*,227 –230.
22. J. Baik, K. A. Stringer, G. Mane, G.R. Rosania, *Antimicrob. Agents Chemother.*, **2013**, *57*, 1218 –1230.
23. J. Baik, G. R. Rosania, *PLoS One*, **2012**, *7*, e47494.
24. M. L. Conalty, R.D. Jackson, *Br.J.Exp.Pathol.*, **1962**, *43*, 650 –654.
25. R. K. Keswani, J. Baik, L. Yeomans, C. Hitzman, A. Johnson, A. Pawate, P.J.A. Kenis, N. Rodriguez-Hornedo, K.A. Stringer, G. R. Rosania, *Mol. Pharm.*, **2015**, *12*, 2528 –2536.
26. S. Ghosh, M. K. Mishra, S. B. Kadambi, U. Ramamurty, G.R. Desiraju, *Angew.Chem. Int. Ed.*, **2015**, *54*, 2674 –2678; *Angew. Chem.*, **2015**, *127*, 2712 –2716.
27. S. Ghosh, M. K. Mishra, S. Ganguly, G.R. Desiraju, *J. Am. Chem. Soc.*, **2015**, *137*, 9912 –9921.

28. S. Ghosh, C. M. Reddy, *Angew.Chem. Int. Ed.*, **2012**, *51*, 10319 –10323; *Angew.Chem.*, **2012**, *124*, 10465 –10469.
29. C.-T. Chen, S. Ghosh, C. M. Reddy, M.J. Buehler, *Phys. Chem. Chem. Phys.*, **2014**, *16*,13165 –13171.
30. S. Hayashi, T. Koizumi, *Angew.Chem. Int. Ed.*, **2016**, *55*, 2701 –2704; *Angew.Chem.*, **2016**, *128*, 2751 –2754.
31. H. Mueller, *Phys.Rev.*, **1935**, *47*, 947 –957.
32. K. A. Min, W. G. Rajeswaran, R. Oldenbourg, G.Harris, R.K. Keswani, M. Chiang, P. Rzczycki, A. Talattof, M. Hafeezma, R. Horobin, et al., *Adv.Sci.*, **2015**, *2*, 1500025.
33. M. Koike-Tani, T. Tani, S. B. Mehta, A. Verma, R. Oldenbourg, *Mol. Reprod. Dev.*, **2015**, *82*, 548 –562.
34. S. B. Mehta, M. Shribak, R. Oldenbourg, *J. Opt.*, **2013**, *15*, 094007.
35. A. Curtis, L. Sokolikova-Csaderova, G. Aitchison, *Biophys.J.*, **2007**, *92*, 2255 –2261.
36. G. Bolla, A. Nangia, *Cryst. Growth Des.*, **2012**, *12*, 6250 –6259.
37. G. S. Yoon, S. Sud, R. K. Keswani, T. J. Standiford, K. A. Stringer, G. R. Rosania, *Mol. Pharm.*, **2015**, *12*, 2517 –2527.
38. G. S. Yoon, R. K. Keswani, S. Sud, P. Rzczycki, M. Murashov, T. Koehn, T. J. Standiford, K. A. Stringer, G.R. Rosania, *Antimicrob.Agents Chemother.*, **2016**, *60*, 3470 –3479.
39. R. K. Keswani, G. S. Yoon, S. Sud, K. A. Stringer, G.R. Rosania, *Cytom. Part A*, **2015**, *87*, 855 –867.
40. C. Tian, R. K. Keswani, G. Gandikota, G.R. Rosania, X. Wang, *Proc.SPIE*, **2016**, 9708,97084L-1.
41. R. K. Keswani, C. Tian, T. Peryea, G. Girish, X. Wang, G.R. Rosania, *Sci. Rep.*, **2016**, *6*,23528.

42. T. J. Jentsch, *J. Physiol.*, **2007**, 578,633 –640.
43. A. R. Graves, P.K. Curran, C. L. Smith, J. A. Mindell, *Nature*, **2008**, 453,788 –792.
44. L. Jiang, K. Salao, H. Li, J. M. Rybicka, R. M. Yates, X.W. Luo, X. X. Shi, T. Kuffner, V.W.-W. Tsai, Y. Husaini, et al., *J. Cell Sci.*, **2012**, 125, 5479 –5488.
45. N. R. Patel, M. Bole, C. Chen, C. C. Hardin, A. T. Kho, J. Mih, L. Deng, J. Butler, D. Tschumperlin, J. J. Fredberg, et al., *PLoS One*, **2012**, 7,e41024.
46. K. M. Adlerz, H. Aranda-Espinoza, H. N. Hayenga, *Eur.Bio-phys.J.*, **2016**, 45,301 –309.
47. J. Pugin, I. Dunn, P. Jolliet, D. Tassaux, J. L. Magnenat, L. P. Nicod, J. C. Chevrolet, *Am. J. Physiol.*, **1998**, 275, L1040 –L1050.
48. H. Shiratsuchi, M. D. Basson, *Am. J. Physiol. Cell Physiol.*, **2004**, 286, C1358 –C1366.
49. H. Y. Shin, D. M. Frechette, N. Rohner, X. Zhang, D.A. Puleo, L. M. Bjursten, *J. Tissue Eng.Regener.Med.*, **2013**, 2, 408 –417.

Chapter 6

Detecting Ordered Small Molecule Drug Aggregates in Live Macrophages: A Multi-Parameter Microscope Image Data Acquisition and Analysis Strategy

6.1 Abstract

Following prolonged administration, certain orally bioavailable but poorly soluble small molecule drugs are prone to precipitate out and form crystal-like drug inclusions (CLDIs) within the cells of living organisms. In this research, we present a quantitative multi-parameter imaging platform for measuring the fluorescence and polarization diattenuation signals of cells harboring intracellular CLDIs. To validate the imaging system, the FDA-approved drug clofazimine (CFZ) was used as a model compound. Our results demonstrated that a quantitative multi-parameter microscopy image analysis platform can be used to study drug sequestering macrophages, and to detect the formation of ordered molecular aggregates formed by poorly soluble small molecule drugs in animals.

6.2 Introduction

For studying complex cell populations, fluorescence-based multi-parameter cytometric analysis techniques are routinely used for monitoring the expression of multiple phenotypic markers at a single cell level. For this purpose, fluorescence-based flow and image cytometry instruments can be used to quantify the expression of different molecular markers down to the level of individual cells, using fluorescently tagged antibodies that recognize specific cell surface receptors, intracellular proteins or other cellular targets of interest. These antibodies are labeled with fluorophores that are excited and emit light specific wavelengths, allowing for simultaneous detection of multiple different fluorescence signals at different excitation and emission wavelengths [1].

While many multi-parameter, cytometric analysis instruments are available for analyzing samples based on a single optical modality (e.g. fluorescence), the development of multi-parameter imaging platforms for phenotypic analysis of cell populations based on various optical properties (e.g. fluorescence, transmittance, and birefringence) is an emerging area of research. For example, the combination of polarization, transmittance and fluorescence imaging modalities could be useful to study protein aggregation at a single cell level [2].

Indeed, the ability to combine fluorescence, transmittance, and polarization microscopy measurements could be useful in obtaining new insights into the organization of molecules in biological specimens [3]. Similar to conventional, transmitted light microscopy, polarization microscopy instruments can employ polarized, transmitted light to study the structure of supramolecular aggregates within individual cells [4-7]. Because of the manner in which polarized light interacts with ordered molecular structures, differences in the organization of molecular components can be detected and quantified based on the fraction of light that is transmitted through the material when it is illuminated with polarized light [8]. At the simplest level, the diattenuation anisotropy of a material can be measured as the maximal difference in light transmittance of a perpendicular pair of planes of polarized light passing through a material, as the material is rotated in the direction perpendicular to both polarized planes of light. These measurements allow distinguishing between homogenous and heterogeneous materials comprised of subdomains of molecules arranged in a particular direction. Polarization microscopy can also be used to obtain information about how the molecules within these subdomains are oriented, providing insight into the underlying molecular order of the material [9-11].

Previously, polarization microscopy has been used extensively to image ordered supramolecular structures in live cells [12-16], as well as to study the formation of intracellular aggregates [17]. This led us to consider combining quantitative polarization microscopy together with fluorescence and transmittance measurements to facilitate multi-parameter cytometric analysis of molecular aggregates formation at a single cell level.

Here, we present a multi-parameter imaging instrument and analysis platform for the analysis of live cell populations, at a single cell level. For demonstration purposes, we used this imaging platform to study the formation of intracellular crystal-like drug inclusions (CLDIs)

formed by clofazimine (CFZ) -an FDA-approved drug that accumulates as highly ordered supramolecular aggregates in macrophages of drug-treated mice [18, 19]. In flow cytometric experiments, CLDIs have been shown to exhibit a strong signal in the Cy5 fluorescence range (650 nm excitation/670 nm emission) [20]. Taking advantage of this intrinsic fluorescence of these biocrystals, we proceeded to analyze the optical anisotropy and fluorescent properties of live cells containing CLDIs, and probe for any relationship between these properties within cells. Our results demonstrate how this multi-parameter imaging platform can be used to study drug accumulation and detect ordered aggregates within live-cells.

6.3 Materials and Methods

Clofazimine administration to mice. Mice (4 week old, male C57Bl6) were purchased from the Jackson Laboratory (Bar Harbor, ME) and acclimatized for 1 week in a specific-pathogen-free animal facility. Clofazimine (CFZ) (C8895; Sigma, St. Louis, MO) was dissolved in sesame oil (Roland, China, or Shirakiku, Japan) to achieve a concentration of 3 mg/ml, which was mixed with Powdered Lab Diet 5001 (PMI International, Inc., St. Louis, MO) to produce a 0.03% drug to powdered feed mix, and orally administered *ad libitum* for 8 weeks. A corresponding amount of sesame oil was mixed with chow for vehicle treatment (control). Animal care was provided by the University of Michigan's Unit for Laboratory Animal Medicine (ULAM), and the experimental protocol was approved by the Committee on Use and Care of Animals (Protocol PRO00005542).

Isolation of spleen CLDIs. CLDIs were isolated from the spleen of 8 week CFZ fed mice using a previously described method [21]. In brief, the spleens were homogenized with a syringe plunger and then filtered through a 40 μ m cell strainer to remove connective tissue debris. The spleen filtrate was centrifuged (300 \times g for 10 min) to remove large cell debris and the pelleted CLDIs were resuspended in 10% sucrose in Dulbecco's PBS (DPBS; Life Technologies, Carlsbad, CA) without CaCl₂ and MgCl₂, pH 7.4. CLDIs were further purified using a 3-layer discontinuous gradient (50%, 30% and 10% sucrose in DPBS) centrifugation method (3200 \times g for 30 min).

Isolation of alveolar macrophages. CFZ or control chow-fed mice (n=3 per group) were euthanized by carbon dioxide asphyxiation followed by exsanguination. The trachea was

surgically exposed and cannulated with an 18G needle and the lungs were lavaged by instilling DPBS containing 0.5 mM EDTA (Sigma) in 1 ml aliquots for a total of 6 ml. Approximately 90% of the bronchoalveolar lavage (BAL) was retrieved. BAL was then centrifuged for 10 min at 400 x g, 4°C, resuspended in RPMI 1640 media (Life Technologies) and the cells were pooled together. The cells were then plated onto 4 or 8 chamber coverglass (#1.5, Lab-Tek II, Nunc, Rochester, NY) for imaging studies. The cells were allowed to attach for 45 min and then washed with media, enabling the isolation of alveolar macrophages by adherence.

Multi-parameter Imaging Instrument Set Up. The multi-parameter imaging instrument utilized by our laboratory combines three imaging separate imaging modalities onto a single instrument, allowing for the fluorescence, transmittance, and polarization properties of a sample to be rapidly acquired. Polarization measurements are acquired utilizing the diattenuation LC-Pol-Scope microscope, a custom built microscopic imaging system similar to the birefringence LC-PolScope designed by Oldenbourg et al [4], but without the polarization analyzer. Our LC-PolScope is built on the Nikon Eclipse Ti inverted microscope (Nikon Instruments, Melville, New York), with the computer-controlled universal compensator (Hinds Instrumentation, Hillsboro, Oregon) placed between the interference filter (623±23 nm, Semrock Optics, Rochester, New York) and condenser lens (Figure 1). Illuminating light is narrowed to 623 nm by the interference filter, and the light is linearly polarized by passing through a universal compensator, allowing for the diattenuation of the sample to be measured. The LC in the universal compensator is controlled by Image J “Micro-manager” software (Vale Laboratory, UCSF) [22] and is automatically rotated to produce polarized light at 0°, 45°, 90° and 135° angles, respective to the horizontal, during image acquisition. The image maps of diattenuation, mean transmittance, and angle of high transmittance are then generated by image analysis algorithms.

Brightfield and fluorescence images are captured using the Nikon DS-U3 camera (Nikon Instruments) and Photometrics CoolSnap MYO camera system (Photometrics, Tucson, Arizona), respectively, under the control of Nikon NIS-Elements AR software (Nikon Instruments). The software allows for multiple fluorescent filters to be readily switched back and forth, and controls the exposure time for each fluorescent filter. Illumination for the fluorescence imaging is generated using the X-Cite 120Q Widefield Fluorescence Microscope Excitation Light Source

(Excelitas Technology, Waltham, MA). Light generated from the mercury lamp enters the filter cube, and a dichroic mirror filters this light to the appropriate wavelength, which then passes through the sample. This current set-up allows for the acquisition of polarization, brightfield and fluorescence images of the same sample at the same field of illumination.

Calibration of LC-PolScope for Diattenuation Measurements. Prior to sample analysis, the LC-PolScope was calibrated using a reference standard consisting of a microscope slide comprised of four squares of perfectly polarized glass, oriented at 0, 45, 90, or 135 degrees. The PolScope software utilizes an individual region of interest (ROI) calibration method. In order to calibrate each polarization setting, the glass that is polarized orthogonally to that angle setting was chosen - for example, to calibrate 0° polarized light, an ROI square on the glass oriented 90° relative to the horizontal was selected. To verify the calibration, a blank region of the slide was visualized, brought out of focus, and a background image was taken. The calibration slide was then visualized and brought back into focus, and a sample image data set of the reference slide standards was generated (Figure 2B-E) and the PolScope measurements were analyzed in relation to the known optical properties of the reference standards. The mean transmittance image map of the slide (Figure 2B) is the average transmittance of each of the four polarization orientations (Figure 2E). As this material is highly anisotropic, each of the four sheets gives a strong diattenuation signal (Figure 2C). The high transmittance angle is measured with respect to the horizontal axis, or in this case, the surface of the slide, and is represented as a pixel intensity value [23]. The angle of high transmittance corresponds to the angle to which the sheet is polarized, i.e. the high transmittance angle of the 0 degree polarized sheet is 0 degrees (Figure 2D, top left, yellow square). As previously described, the mean transmittance (Figure 2B), diattenuation (Figure 2C), and high transmittance angle (Figure 2D) image maps are all calculated using the four polarization orientation images (Figure 2E).

Multi-parameter image acquisition of isolated CLDIs and alveolar macrophages. Isolated CLDIs and alveolar macrophage samples were imaged using a 40x objective lens. The LC-PolScope was used to capture the linear diattenuation of the sample using a 623±23 nm interference filter (Semrock Optics, Rochester, New York). Once the polarized light images were captured, the filter and universal compensator were removed, and the color camera was used to

take a brightfield image of the sample. The fluorescence camera was then used to assess the fluorescent properties of the sample, using a standard Cy5 filter set.

Multi-parameter Cytometric Image Analysis. All images generated using the LC-PolScope software were analyzed using ImageJ [24-26]. These images are 8-bit images, yielding intensity values from 0-255. The values for diattenuation, mean transmittance, and fluorescence are obtained by extracting the pixel values from the image maps at exact locations, denoted as (x,y) coordinates. Each pixel will have an intensity value z associated with it, located such that $1 \leq x \leq X$ and $1 \leq y \leq Y$, where X and Y define the total dimensions of the image such that the resolution of the image is defined as $R=X*Y$. The image maps generated represent the values of diattenuation, mean transmittance, and Cy5 fluorescence as such:

Diattenuation: $D_{\lambda}(x,y)$ is the diattenuation signal at wavelength λ for the pixel located at (x,y)

Mean Transmittance: $T_{M,\lambda}(x,y)$ is the mean transmittance at wavelength λ for the pixel located at (x,y)

Fluorescence: $F_{Cy5}(x,y)$ is the Cy5 fluorescence of the pixel located at (x,y)

To compare the diattenuation, optical density, and Cy5 fluorescence of cells at a whole cell level, an automated data acquisition strategy was put in place, and is summarized in figure 3. First, the zero-degree polarization state image was selected (Figure 3, Panel A), and the brightness and contrast are manually adjusted to allow for cells to stand out from the well-plate background (Figure 3, Panel B). Following this, the adjusted image was then subjected to a manual thresholding, which generates a binary mask to discriminate between objects and background (Figure 3, Panel C). The binary mask was then subjected to the “Fill Holes” function in ImageJ, which fills holes within each object, allowing for a more complete cellular mask to be generated (Figure 3, Panel D). Once the mask has been generated, the dichroism, mean transmittance, and fluorescence image maps for a single field of view were opened and the cells in the image were analyzed using the “Analyze Particles” function within ImageJ, and, using the previously generated binary image as a mask, a region of interest (ROI) was selected to analyze the pixels contained within the cell, and is denoted as $p(c)$. The objects across each image were analyzed, with objects greater than 250 pixels^2 in area being selected for, measuring the total,

integrated signal intensity of diattenuation, mean transmittance, and Cy5 fluorescence for the same cell 'c' in the following manner:

$$(1) D_{\lambda}(c) = \sum_{(x,y) \in p(c)} D_{\lambda}(x, y)$$

$$(2) T_{m,\lambda}(c) = \sum_{(x,y) \in p(c)} T_{m,\lambda}(x, y)$$

$$(3) F_{Cy5}(c) = \sum_{(x,y) \in p(c)} F_{Cy5}(x, y)$$

The integrated optical density (OD) of the drug crystals was determined using the integrated mean transmittance as follows:

$$(4) OD_{\lambda}(c) = \sum_{(x,y) \in p(c)} -\log_{10}(T_{m,\lambda}(x, y))$$

To correct for background signal, the integrated OD was corrected by subtracting the average integrated background optical density as follows:

$$(5) OD_{\lambda}(c) = \sum_{(x,y) \in p(c)} -\log_{10}(T_{m,\lambda}(x, y)) - \sum_{(x,y) \in p(c)} -\log_{10}(T_{m,\lambda}(BG))$$

To obtain the average diattenuation, optical density, or Cy5 fluorescence within an object of interest, the values obtained from equations (1), (3), and (5) are divided by the total area analyzed, as such:

$$(6) \bar{D}_\lambda(c) = \frac{\sum_{(x,y) \in p(c)} D_\lambda(x,y)}{A}$$

$$(7) \overline{OD}_\lambda(c) = \frac{\sum_{(x,y) \in p(c)} -\log_{10}(T_{m,\lambda}(x,y)) - \sum_{(x,y) \in p(c)} -\log_{10}(T_{m,\lambda}(BG))}{A}$$

$$(8) \bar{F}_{Cy5}(c) = \frac{\sum_{(x,y) \in p(c)} F_{Cy5}(x,y)}{A}$$

All average values are reported on a 0-1 scale by dividing by 255. All integrated signal values are reported as the total signal value, with each individual pixel ranging from 0-255.

Statistical analysis. Statistical tests were performed with IBM SPSS Statistics version 24.0 (IBM Software, Armonk, New York). Results are reported as average \pm standard deviation. P values less than 0.05 were considered statistically significant.

6.4 Results

6.4.1 Imaging and Quantification of Diattenuation, Optical Density, and Cy5 Fluorescence of CLDIs using Multi-parameter imaging system

To demonstrate the capabilities of this multi-parameter imaging system, the drug clofazimine was chosen as a model compound. Clofazimine (CFZ) is a bright red phenazine drug that accumulates extensively in tissues throughout the organism, leading to the formation of deep red, crystal-like drug inclusions *in vivo* [27]. Following eight weeks of CFZ treatment, CLDIs were isolated from the spleen of a mouse and imaged with the polarization and fluorescence imaging system. These CLDIs are deep red, and have a rod-like polygonal shape, with an average size of $17.6 \pm 10.9 \mu\text{m}^2$ (Figure 4A). These crystals strongly absorbed linearly polarized light of 623 nm wavelength, and had an average optical density (OD) of 0.31 ± 0.12 (Figure 4B). Interestingly, CLDIs are able to interact with different orientation states of polarized light,

resulting in a strong diattenuation signal. As a result of the crystallinity and molecular order present in the CLDI, different orientations of polarized light are absorbed to different extents by the crystal, yielding an average diattenuation signal of 0.26 ± 0.05 (Figure 4C). The CLDIs are also highly fluorescent in the Cy5 channel (excitation/emission), which occurs due to the formation of a mono-protonated, hydrochloride salt during the process of clofazimine accumulation and biocrystallization [20] (Figure 4D). The crystals had an average Cy5 fluorescence of 0.06 ± 0.02 . After analyzing isolated CLDIs from mice treated with CFZ, we decided to probe the utility of this instrument in studying live cells isolated from animals fed the drug for a period of eight weeks.

6.4.2 Multi-Parameter Live Cell Imaging and Quantification of Diattenuation, Optical Density, and Fluorescence of Drug-Treated Alveolar Macrophages

Based off of previous work, it has been shown that CLDIs tend to be found within tissue macrophages, such as Kupffer cells of the liver, red pulp macrophages of the spleen, and alveolar macrophages within the lung [18, 28, 29]. Due to the extensive accumulation within alveolar macrophages, these cells were chosen to test this multi-parameter imaging and analysis system in live cells. These cells serve as the first barrier to incoming airborne pathogens and other inhaled xenobiotics, and have been shown to be greatly impacted by the accumulation of these materials [30]. Alveolar macrophages were isolated from mice treated with CFZ for eight weeks or mice fed a control diet, and imaged using the combined polarization and fluorescence imaging system.

Upon visual inspection of the brightfield image, control diet-fed macrophages are small, rounded cells, ranging in size from 10 to 25 microns in diameter. Imaging of these cells using the multi-parameter imaging system revealed a low, but detectable, dichroism signal of 0.018 ± 0.005 (Table 1). This signal arises due to interactions of the polarized light with cellular components, such as membranes and organelles, which have some degree of molecular organization. The mean transmittance image shows cells with very low optical density, with an average intensity of 0.021 ± 0.029 . These cells are, by and large, transparent, with occasional dark spots, which may correspond to cellular components, such as lysosomes or other membrane-bound organelles. Control alveolar macrophages show little to no fluorescence in the Cy5 channel, as is expected (0.0002 ± 0.00005). Representative images of the untreated alveolar macrophages are seen in figure 5, top panel.

Following eight weeks of sustained therapy with CFZ, the alveolar macrophages are loaded with large amounts of intracellular crystals of the drug, consistent with previous reports from our laboratory [29]. As a result of the accumulation of intracellular drug complexes, intracellular dichroism increased significantly (0.042 ± 0.013 , $p < 0.01$, Two-Tailed Student's T-Test), revealing that CLDIs are highly organized, self-assembling supra-molecular entities, and that the dichroism of these crystals can be detected within a cell. CLDI accumulation and formation also resulted in a significant increase in the optical density of the macrophages (0.054 ± 0.071 , $p < 0.01$, Two-Tailed Student's T-Test), as a result of the deep red color associated with these biocrystals. Consistent with previous reports [20], CLDI accumulation also resulted in a concomitant increase in the Cy5 fluorescence associated with the macrophages as well (0.012 ± 0.019 , $p < 0.01$, Two-Tailed Student's T-Test).

The analyses performed also studied how each of these three properties related to one another in both control and CFZ-treated cells. By plotting the total integrated dichroism, optical density, and fluorescence of the cells, one can gain further understanding on how the molecular order (represented by dichroism), degree of accumulation (represented by optical density), and protonation state (represented by fluorescence) of the drug relate to one another following eight weeks of sustained therapy. Performing this analysis also allows for the study of the optical properties of an entire population of cells to be observed, which can be a useful analysis when determining how different cell populations accumulate drugs both *in vitro* and *in vivo*. Figure 6 compares the optical properties from both control alveolar macrophages (A, D) and those from a mouse fed 8 weeks (B, C). In Panel A, one can see that, on a whole population level, these cells display very low fluorescence and optical density, with a more varied dichroism signal. In all, the control cells display little variability with respect to their optical signals, and this is captured in the plots shown in Panels A and D. On the other hand, treatment with CFZ, and the subsequent accumulation and biocrystal formation which occurs as a result, causes there to be three populations of cells which can be segregated. In Panel B, there is a population of cells aggregated very near the origin, showing low fluorescence, optical density, and dichroism. These cells are most likely red blood cells which were not eliminated during the collection and plating of the macrophages. The second population of cells shows an elevated fluorescence, optical density, and dichroism compared to the previously described population; these cells are most likely macrophages which have accumulated soluble CFZ, but have not yet formed a CLDI

(Panel B). The final population of cells can be seen in Panel C. These cells display very high fluorescence, optical density, and dichroism, indicating that these cells are most likely alveolar macrophages which contain at least one intracellular crystal.

6.5 Discussion

The development and refinement of polarized light microscopy measurements to study changes in the organization of molecular components in individual cells has had many applications in cell biology and beyond [4, 31, 32]. To study the bioaccumulation of small molecule drugs inside cells, the experiments presented here indicate how a quantitative multi-parameter imaging system combining polarization, transmittance and fluorescence measurements can be useful for studying the cellular mechanisms of drug disposition from the cellular to the molecular level. Previously, our lab has used polarization microscopy to study the optical properties of drug inclusions formed *in vitro*. Cells were incubated with CFZ and other phenazine derivatives to study the self-assembly of drug aggregates in live cells, revealing that, even after 72 hours, the self-assembly of CFZ aggregates within cells yields a measurable diattenuation signal [33]. Cultured cells, however, are not the optimal model for studying intracellular drug crystallization for a variety of factors, namely the length of time necessary for the crystals to form. Thus, a long term *in vivo* study was performed to develop a method to accurately quantify changes in intracellular dichroism, absorbance, and fluorescence induced following eight weeks of CFZ therapy.

Through the development of this multi-parameter imaging and analysis system, drug accumulation, as well as the changes this accumulation has within the cell with respect to molecular order can be studied at the level of single cells in a rapid manner. Further applications of this instrument can potentially be used to study large populations of cells which can allow for researchers to discriminate which cells have a propensity to accumulate and sequester soluble drug, or potentially form an insoluble aggregate. Due to the automated nature of the analysis, all of the objects analyzed may not be macrophages, but rather red blood cells or other immune cells, such as B cells. However, by analyzing each of the three cellular properties measured using this method, one can place each cell in a category on the basis of the intensity of the signals measured. For example, cells which display a high level of fluorescence, dichroism, and optical density are most likely macrophages containing an intracellular crystal. Red blood cells, on the

other hand, would show low levels of fluorescence and optical density. Further refinement of the imaging and analysis technique can be used to rapidly image and analyze large populations of live cells from drug treated animals, allowing for investigators to determine how, if at all, various drugs accumulate within these cells without the need for time-consuming chemical analyses.

Previously, we have characterized the molecular organization and chemical composition of CLDIs following biochemical isolation, using nuclear magnetic resonance, powder X-ray diffraction, transmitted electron microscopy, freeze fracture electron microscopy, liquid chromatography and mass spectrometry [18, 19, 34]. Our results demonstrated that CLDIs are comprised of subdomains of pure CFZ-hydrochloride crystals [34], bounded by multilamellar membrane structure of biological origin [18, 19]. Consistent with these previous results, quantitative polarization microscopy revealed the manner in which microscopic domains of ordered CFZ molecules within CLDIs of live macrophages obtained from CFZ-treated mice differentially interact with polarized light. Nevertheless, unlike the aforementioned chemical analysis techniques, quantitative multi-parameter observations were performed on functional, viable cells.

In terms of its implications for drug targeting and delivery, the formation and fate of intracellular drug biocrystals has remained a poorly understood aspect of pharmacokinetics, precisely because of the lack of practical, quantitative techniques to study intracellular drug bioaccumulation. Nevertheless, understanding the mechanisms responsible for the accumulation of drugs within intracellular compartments is important as it may explain why some drugs fail to reach proper therapeutic concentrations at a site of action or to explain unfavorable drug-drug interactions that may occur through bioaccumulation dependent pathways [35]. Drug trapping and accumulation can lead to alterations in the structure and function of organelles, affecting cell physiology [36]. Accumulation of small molecule drugs in organs such as the liver and kidney are particularly concerning as a potential cause of toxicity [37, 38]. For example, the antiviral drug *cidofovir* (Gilead Sciences) tends to accumulate in the kidneys, leading to nephrotoxicity [39]. Yet, there are also specific cases in which drug bioaccumulation may be beneficial. Many of the anti-malarial drugs in the 4-aminoquinolone class have been shown to be more effective in treating the illness due to preferential accumulation within an acidic compartment of the parasite [40, 41].

The development and refinement of a multi-parameter imaging system which combines polarization and fluorescence microscopy may further the understanding of intracellular drug bioaccumulation via the mechanism of CLDI formation in macrophages and potentially other cell types. In addition to CLDIs formed by clofazimine, this quantitative multi-parameter imaging set up could be used to detect ordered molecular aggregates formed inside cells by other drugs. Imaging systems such as this can also be applied in drug discovery: by looking for drugs which induce similar changes in intracellular molecular organization, drugs that potentially crystallize intracellularly can be identified as potential target molecules for therapeutics. While CFZ and CLDIs are deeply red and fluorescent, other drugs which accumulate may not be as easy to detect with the naked eye. Through the use of polarization microscopy, minute changes in the underlying structure which may be induced by drug accumulation can potentially be detected; this may provide information about the subcellular localization of drug. Indeed, much remains to be discovered about the physiological function of xenobiotic sequestering macrophages, and the underlying biological mechanisms responsible for CLDI formation. Furthermore, beyond the study of drug transport phenomena, a quantitative multi-parameter imaging set up could also be used for studying many other kinds of phenomena associated with the formation of ordered molecular aggregates, such as the formation of hemoglobin crystals in sickled red blood cells [42]; the formation of atherosclerotic plaques [43]; the formation of misfolded protein fibrils as seen in Parkinson's and Alzheimer's disease and other forms of dementia [44, 45]; and the formation of lipid aggregates as is characteristic of certain lysosomal storage diseases [46].

6.6 Conclusions

To conclude, this research describes how a quantitative, fluorescence-transmittance-polarization multi-parameter imaging system can be used for detecting and studying CLDIs in isolation, as well as studying the accumulation of drug in live macrophages obtained from drug treated animals at differing stages in treatment. CLDI formation leads to the development of a highly organized molecular structure that homogeneously interacts with linearly polarized light. While all experiments reported herein were performed with alveolar macrophages, other macrophage populations, such as those in the spleen, liver, bone marrow and in the peritoneal cavity have been previously implicated in the disposition of clofazimine, and should also be

amenable for comparative analysis. In the future, establishing how the optical properties of CLDIs vary amongst different macrophage populations, as a function of clofazimine dose, and in mouse mutants harboring mutations that affect macrophage function, will be especially useful to elucidate the molecular mechanisms driving the pharmacokinetics of clofazimine accumulation.

6.7 Acknowledgements

The authors would like to thank Rudolf Oldenbourg and Grant Harris for help with the LC-Polyscope and associated image analysis algorithms. This work was funded by NIH grant R01GM078200 to GRR.

6.8 Figures

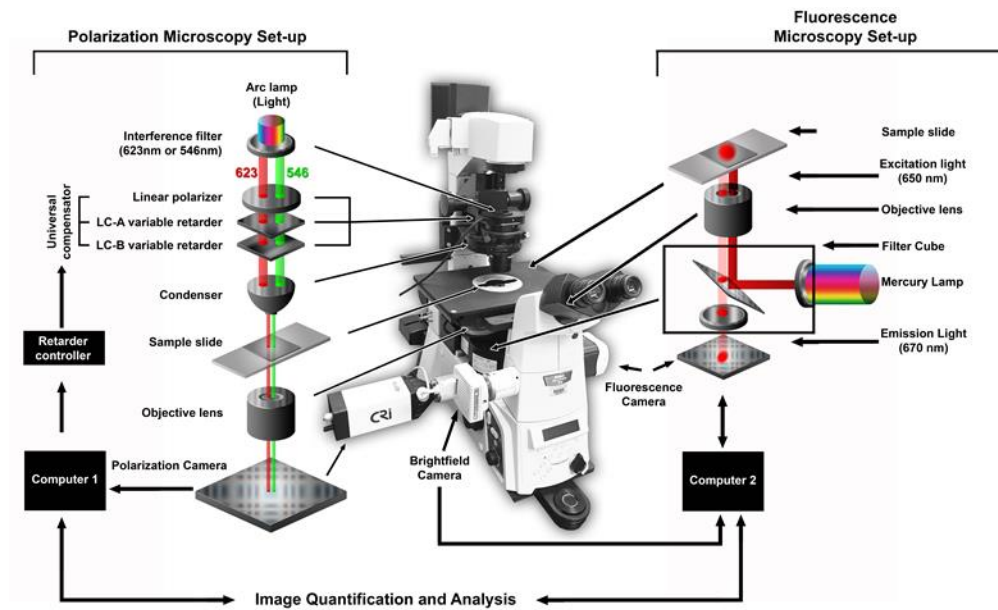


Figure 6-1 Schematic of multi-parameter imaging system

Schematic diagram of multi-parameter instrument used for live alveolar macrophage diattenuation imaging at 623nm or 546nm wavelengths and fluorescence microscopy. Adapted from Mehta et al. 2010 Journal of Optics.

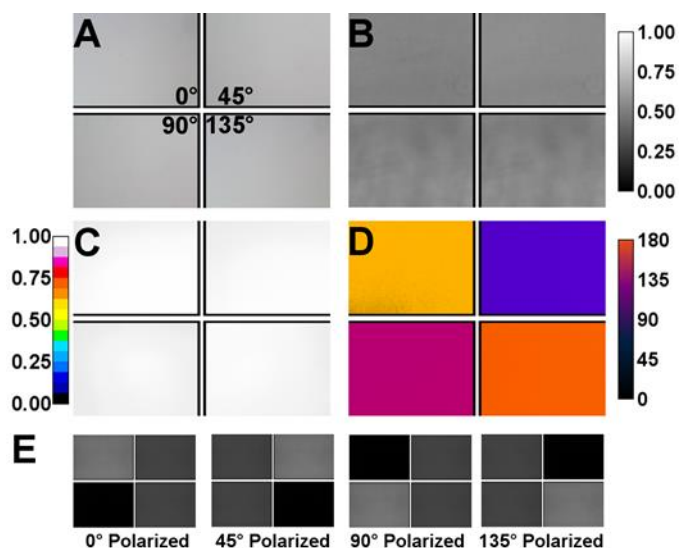


Figure 6-2 Slide used to calibrate diattenuation polarization instrument

Calibration of the LC-PolScope instrumentation and software. A slide comprised of four sheets of perfectly polarized glass, with each sheet polarized to light at either 0° , 45° , 90° , or 135° relative to the horizontal is used for calibration. (A) Brightfield image, (B) mean transmittance and (C) diattenuation image map of the calibration slide. (D) Colored schematic representing the angle of high transmittance, or the orientation of light which is most transmitted by the object. (E) Images generated from passing linearly polarized light at 0° , 45° , 90° , and 135° , from left to right, which are used to calculate the angle of high transmittance, diattenuation, and mean transmittance image maps.

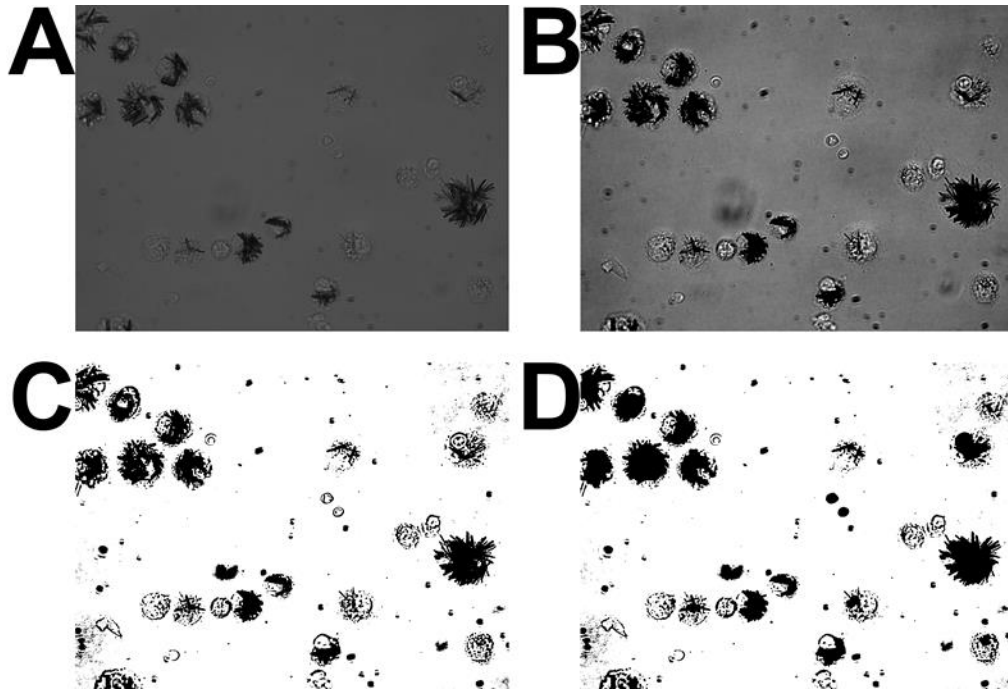


Figure 6-3 Generation of mask for automated data collection

Representative schematic of mask generation for data collection. The 0-degree polarization state image is selected (Panel A) and has the brightness and contrast adjusted (Panel B). Following this, the image undergoes a manual threshold in ImageJ, delineating between objects and background (Panel C). The image then undergoes the “Fill Holes” function, generating the mask for data analysis (Panel D)

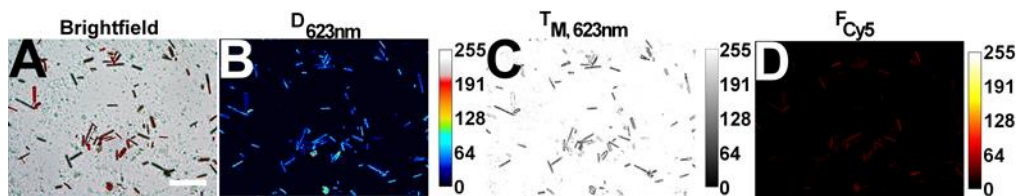


Figure 6-4 Multi-parameter imaging of isolated spleen CLDI

Pol-Scope images of CLDI isolated from the spleen of 8wk CFZ-treated mice. (A) Brightfield image displaying deep red color, rod-like shape of CLDI. (B) Diattenuation, (C) mean transmittance and (D) Cy5 fluorescence of CLDI with illuminating light at 623 nm. The high degree of diattenuation and Cy5 fluorescence of the CLDI is readily visible. Scale bar is 50 μ m.

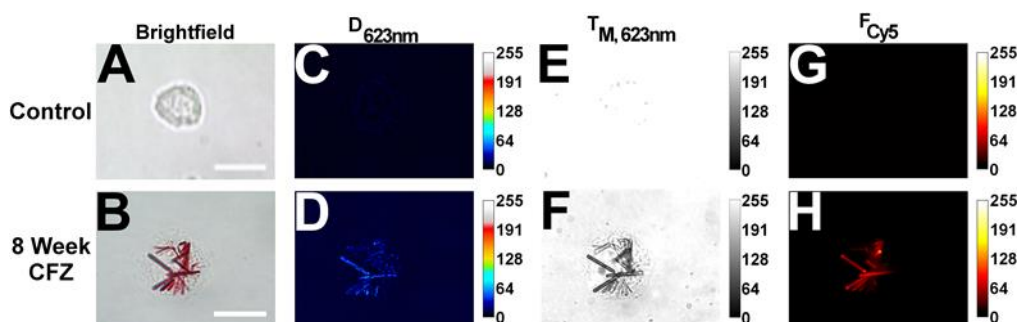


Figure 6-5 Multi-parameter images of CFZ and untreated alveolar macrophages

Comparison of CFZ treated and control alveolar macrophages. Macrophages from mice following 8 weeks of treatment, displayed the characteristic CLDI formation. Brightfield (A, B), diattenuation (C, D), mean transmittance (E, F), and Cy5 fluorescence (G,H) images of isolated alveolar macrophages from treated and non-treated (control) mice. Both diattenuation and mean transmittance images were generated using illuminating light at 623nm. Note that the diattenuation and mean transmittance signal is entirely contained within the CLDIs. Scale bar is 15 μ m.

	Control Alveolar Macrophage (n=215)	8 Week CFZ Fed Alveolar Macrophage (n=201)
$\overline{\mathbf{D}}_{623}$	0.017 ± 0.004	0.042 ± 0.013 *
$\overline{\mathbf{OD}}_{623}$	0.017 ± 0.019	0.054 ± 0.071 *
$\overline{\mathbf{F}}_{\text{Cy5}}$	0.0002 ± 0.00004	0.012 ± 0.019 *

Table 6-1 Multi-parameter optical properties of untreated and 8 week CFZ treated alveolar macrophages

Average Signal Intensity of Macrophages (*=p<0.001, Two-Tailed Student's T-Test)

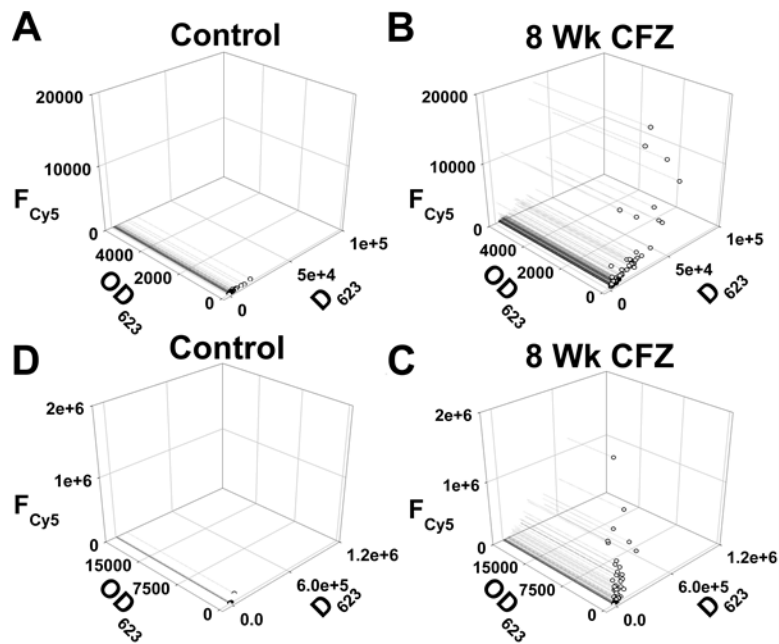


Figure 6-6 Scatter plot of relating optical properties of untreated and 8 week CFZ treated alveolar macrophages

Scatter plot displaying relationship between Cy5 fluorescence, optical density, and dichroism in control alveolar macrophage populations (A, D) and 8 week CFZ fed alveolar macrophage populations (B,C). Panels A and B show the same population of cells shown in panels D and C, but zoomed into the lower signal values. Treatment with CFZ results in a heterogeneous population of macrophages on basis of optical signals, while untreated cells remain homogenous.

6.9 Supporting Information Available

This material is published in *Biomedical Optics Express*.

6.10 References

1. C. J. Hewitt and G. Nebe-Von-Caron, "The application of multi-parameter flow cytometry to monitor individual microbial cell physiological state," *Advances in biochemical engineering/biotechnology* **89**, 197-223 (2004).
2. G. S. Kaminski Schierle, M. Sauer, and C. F. Kaminski, "Chapter 10 - Probing Amyloid Aggregation and Morphology In Situ by Multiparameter Imaging and Super-Resolution Fluorescence Microscopy," in *Bio-nanoimaging*, V. N. U. L. Lyubchenko, ed. (Academic Press, Boston, 2014), pp. 105-120.
3. S. B. Sparenga, "The Importance of Polarized Light Microscopy in the Analytical Setting," *Microsc and Microanal* **14**, 1032-1033 (2008).
4. S. B. Mehta, M. Shribak, and R. Oldenbourg, "Polarized light imaging of birefringence and diattenuation at high resolution and high sensitivity," *Journal of Optics* **15**, 094007 (2013).
5. R. Oldenbourg, "Polarization state generated by universal polarizer" (2013), retrieved 8 May, 2015, openpolscope.org/pages/PolarizationEllipseUniversalPolarizer.htm.
6. G. Harris, A. Verma, and R. Oldenbourg, LC-PolScope, 2014.
7. W. Kaminsky, K. Claborn, and B. Kahr, "Polarimetric imaging of crystals," *Chemical Society reviews* **33**, 514-525 (2004).
8. W. Kaminsky, E. Gunn, R. Sours, and B. Kahr, "Simultaneous false-colour imaging of birefringence, extinction and transmittance at camera speed," *J Microsc* **228**, 153-164 (2007).
9. C. A. Valades Cruz, H. A. Shaban, A. Kress, N. Bertaux, S. Monneret, M. Mavrikis, J. Savatier, and S. Brasselet, "Quantitative nanoscale imaging of orientational order in biological filaments by polarized superresolution microscopy," *Proc Natl Acad Sci U S A* **113**, E820-828 (2016).
10. R. Turcotte, J. M. Mattson, J. W. Wu, Y. Zhang, and C. P. Lin, "Molecular Order of Arterial Collagen Using Circular Polarization Second-Harmonic Generation Imaging," *Biophys J* **110**, 530-533 (2016).
11. B. d. C. Vidal, E. H. M. dos Anjos, and M. L. S. Mello, "Optical anisotropy reveals molecular order in a mouse entheses," *Cell Tissue Res.* **362**, 177-185 (2015).

12. J. A. Byrne, D. A. Pedersen, L. L. Clepper, M. Nelson, W. G. Sanger, S. Gokhale, D. P. Wolf, and S. M. Mitalipov, "Producing primate embryonic stem cells by somatic cell nuclear transfer," *Nature* **450**, 497-502 (2007).
13. L. Liu, R. Oldenbourg, J. R. Trimarchi, and D. L. Keefe, "A reliable, noninvasive technique for spindle imaging and enucleation of mammalian oocytes," *Nat Biotech* **18**, 223-225 (2000).
14. P. A. A. S. Navarro, L. Liu, J. R. Trimarchi, R. A. Ferriani, and D. L. Keefe, "Noninvasive imaging of spindle dynamics during mammalian oocyte activation," *Fertility and Sterility* **83**, 1197-1205 (2005).
15. B. S. DeMay, X. Bai, L. Howard, P. Occhipinti, R. A. Meseroll, E. T. Spiliotis, R. Oldenbourg, and A. S. Gladfelter, "Septin filaments exhibit a dynamic, paired organization that is conserved from yeast to mammals," *The Journal of Cell Biology* **193**, 1065-1081 (2011).
16. R. Oldenbourg, E. D. Salmon, and P. T. Tran, "Birefringence of Single and Bundled Microtubules," *Biophysical Journal* **74**, 645-654 (1998).
17. W. Kaminsky, L.-W. Jin, S. Powell, I. Maezawa, K. Claborn, C. Branham, and B. Kahr, "Polarimetric imaging of amyloid," *Micron* **37**, 324-338 (2006).
18. J. Baik and G. R. Rosania, "Macrophages Sequester Clofazimine in an Intracellular Liquid Crystal-Like Supramolecular Organization," *PLoS ONE* **7**, e47494 (2012).
19. J. Baik and G. R. Rosania, "Molecular Imaging of Intracellular Drug-Membrane Aggregate Formation," *Molecular Pharmaceutics* **8**, 1742-1749 (2011).
20. R. Keswani, G. Yoon, S. Sud, K. Stringer, and G. Rosania, "A Far-Red Fluorescent Probe For Flow Cytometric Xenobiotic-Sequestering Cell Functional Studies," *Cytometry Part A* (2015).
21. G. Yoon, S. Sud, R. Keswani, J. Baik, T. Standiford, K. Stringer, and G. Rosania, "Phagocytosed Clofazimine Biocrystals can Modulate Innate Immune Signaling by Inhibiting TNF Alpha and Boosting IL-1RA Secretion," *Mol. Pharmaceutics* (2015).
22. A. Edelstein, N. Amodaj, K. Hoover, R. Vale, and N. Stuurman, "Computer Control of Microscopes Using μ Manager," in *Current Protocols in Molecular Biology*, (John Wiley & Sons, Inc., 2010).

23. R. Oldenbourg, "Diattenuation" (2013), retrieved May 8 2015, openpolscope.org/pages/Diattenuation.htm.
24. M. D. Abramoff, P. J. Magalhaes, and S. J. Ram, "Image Processing With ImageJ," *Biophotonics International* **11**, 36-42 (2004).
25. T. Ferreira and W. Rasband, "ImageJ User Guide," (FIJI, rsbweb.nih.gov, 2012).
26. C. A. Schneider, W. S. Rasband, and K. W. Eliceiri, "NIH Image to ImageJ: 25 years of image analysis," *Nat Meth* **9**, 671-675 (2012).
27. J. Baik, K. A. Stringer, G. Mane, and G. R. Rosania, "Multiscale Distribution and Bioaccumulation Analysis of Clofazimine Reveals a Massive Immune System-Mediated Xenobiotic Sequestration Response," *Antimicrob. Agents. Chemother.* **57**, 1218-1230 (2013).
28. G. S. Yoon, S. Sud, R. K. Keswani, J. Baik, T. J. Standiford, K. A. Stringer, and G. R. Rosania, "Phagocytosed Clofazimine Biocrystals Can Modulate Innate Immune Signaling by Inhibiting TNF α and Boosting IL-1RA Secretion," *Molecular Pharmaceutics* **12**, 2517-2527 (2015).
29. G. S. Yoon, R. K. Keswani, S. Sud, P. M. Rzeczycki, M. D. Murashov, T. A. Koehn, T. J. Standiford, K. A. Stringer, and G. R. Rosania, "Clofazimine Biocrystal Accumulation in Macrophages Upregulates IL-1RA Production to Induce a Systemic Anti-Inflammatory State," *Antimicrobial Agents and Chemotherapy* (2016).
30. L. D. Loose, J. B. Silkworth, T. Charbonneau, and F. Blumenstock, "Environmental chemical-induced macrophage dysfunction," *Environmental health perspectives* **39**, 79-92 (1981).
31. S. Inoué, "Polarization Microscopy," in *Current Protocols in Cell Biology* (John Wiley & Sons, Inc., 2002), p. 27.
32. F. Massoumian, R. Juskaitis, M. A. A. Neil, and T. Wilson, "Quantitative polarized light microscopy," *Journal of Microscopy* **209**, 13-22 (2003).
33. K. A. Min, W. G. Rajeswaran, R. Oldenbourg, G. Harris, R. K. Keswani, M. Chiang, P. Rzeczycki, A. Talattof, M. Hafeez, R. W. Horobin, S. D. Larsen, K. A. Stringer, and G. R. Rosania, "Massive Bioaccumulation and Self-Assembly of Phenazine Compounds in Live Cells," *Advanced science* **2**, 1500025 (2015).

34. R. Keswani, J. Baik, L. Yeomans, C. Hitzman, A. Johnson, A. Pawate, P. Kenis, N. Rodriguez-Hornedo, K. Stringer, and G. Rosania, "Chemical Analysis of Drug Biocrystals: A Role for Counterion Transport Pathways in Intracellular Drug Disposition," *Molecular Pharmaceutics* (2015).
35. R. Funk and J. Krise, "Cationic amphiphilic drugs cause a marked expansion of apparent lysosomal volume: implications for an intracellular distribution-based drug interaction," *Mol. Pharmaceutics* **9**, 1384-1395 (2012).
36. R. Logan, A. Kong, and J. Krise, "Time-Dependent Effects of Hydrophobic Amine-Containing Drugs on Lysosome Structure and Biogenesis in Culture Human Fibroblasts," *J. Pharm. Sci.* **103**, 3287-3296 (2014).
37. H. J. Zimmerman, *Hepatotoxicity: The Adverse Effects of Drugs and Other Chemicals on the Liver* (Lippincott Williams & Wilkins, 1999).
38. C. A. Naughton, "Drug-Induced Nephrotoxicity," *Am Fam Physician* **78**, 743-750 (2008).
39. S. Ciesla, J. Trahan, W. Wan, J. Beadle, K. Aldern, G. Painter, and K. Hostetler, "Esterification of cidofovir with alkoxyalkanols increases oral bioavailability and diminishes drug accumulation in kidney," *Antiviral Res* **59**, 163-171 (2003).
40. S. Hawley, P. Bray, M. Mungthin, J. Atkinson, P. O'Neill, and S. Ward, "Relationship between Antimalarial Drug Activity, Accumulation, and Inhibition of Heme Polymerization in *Plasmodium falciparum* In Vitro," *Antimicrob. Agents. Chemother.* **42**, 682-686 (1998).
41. S. Hawley, P. Bray, P. O'Neill, B. Park, and S. Ward, "The Role of Drug Accumulation in 4-Aminoquinoline Antimalarial Potency," *Biochem. Pharmacol.* **52**, 723-733 (1996).
42. W. Mickols, M. Maestre, I. Tonoco, and S. Embury, "Visualization of oriented hemoglobin S in individual erythrocytes by differential extinction of polarized light," *Proc. Natl. Acad. Sci* **82**, 6527-6531 (1985).
43. P. Libby, "Molecular and cellular mechanisms of the thrombotic complications of atherosclerosis," *J Lipid Res.* **50**, S352-S357 (2009).
44. J. Rose and V. Molano, "Dementia with Lewy Bodies," *Semin Neurol.* **33**, 330-335 (2013).

45. H. Z. Amin, S. Mori, N. Sasaki, and K.-I. Hirata, "Diagnostic Approach to Cardiac Amyloidosis," *Kobe J Med Sci.* **60**, 5-11 (2014).

46. M. Biegstraaten, G. E. Linthorst, I. N. v. Schaik, and C. E. M. Hollak, "Fabry Disease: A Rare Cause of Neuropathic Pain," *Curr Pain Headache Report* **17**, 1-6 (2013).

Chapter 7

The Adaptive Cargo Carrying Capacity of Macrophages Expands the Drug Volume of Distribution

7.1 Abstract

Through phagocytosis or fluid phase pinocytosis, cultured macrophages are capable of internalizing massive amounts of solids and solutes from the extracellular medium ('massive' defined as surpassing every other cellular component, except water). Nevertheless, the cargo carrying capacity of macrophages has never been measured *in vivo*. Here, we used an orally bioavailable drug -clofazimine- as a molecular reporter of the extent of macrophage loading. Upon increasing the whole body drug cargo load, macrophages adjusted their size, number and membrane organization to accommodate an increasing cargo volume. Ultimately, the total volume of intracellular cargo exceeded 5% of the total cell volume across the entire macrophage population. Most interestingly, macrophages adaptively maximized their cargo capacity, not only by stabilizing and reshaping the intracellular cargo space, but also by remodeling their intracellular membrane architecture to minimize the surface area of the cargo space while maximizing the cargo volume. By stabilizing a solute-to-solid phase transition, the apparent volume of distribution of the reporter probe continuously increased through treatment, and exceeded the cell volume by more than ten thousand-fold. As expected from an active sequestration mechanism, experimentally depleting macrophages in liver and spleen reduced the total amount of drug cargo accumulated in those organs, without affecting the loading of the remaining cells. Altogether, the results indicate a coordinated, immunological response mechanism across the entire macrophage population, which expands their endolysosomal cargo carrying capacity to accommodate an increasingly massive load of drug cargo.

7.2 Introduction

Throughout the body, macrophages are especially equipped to internalize extracellular solutes and particles through pinocytosis and phagocytosis, respectively. This allows them to carry out a number of critical cellular immune functions ranging from destruction of pathogens to removal and recycling of dead cells and aged tissue components [1-3]. In addition to being highly phagocytic, the endolysosomal system of the macrophage is especially capable of accommodating and degrading foreign material due to higher expression levels of lysosomal acidification mechanisms [4], particularly the vacuolar-type proton ATP-ase (V-ATPase) [5]. Little is known about the *in vivo* phagocytic capacity of macrophages, with the majority of work having been performed *in vitro* using fluorescent tracer molecules [6] or inert beads of varying sizes [7]. For example, Cannon et al performed a study to determine the extent to which murine bone marrow macrophages were able to phagocytose polystyrene beads of various sizes, revealing that the phagocytic capacity of these cells is limited by the amount of membrane that is available to spread out and engulf the particle, rather than the volume of the cell [8].

Even though the macrophage is a major immune regulator, its role as a determinant of drug distribution is underappreciated. Due to their high rates of endocytosis, pinocytosis and phagocytosis, and because of their ubiquitous presence throughout the body, they are poised to impact the performance and efficacy of many therapeutic agents. For example, liposomal formulations must be optimized to avoid phagocytosis of particles and removal of drug from the systemic circulation, increasing therapeutic efficiency [9, 10]. The action of macrophages may also impact small molecule drugs, such as antibiotics [11-13]. Many antibiotics will display large volumes of distribution and long elimination half-lives [14], causing them to linger within the body for extended periods of time. The accumulation of weakly basic, hydrophobic drug molecules within acidic subcellular compartments is a well-documented phenomenon, referred to as ion-trapping [15]. Cationic, amphiphilic molecules, particularly weakly basic molecules, tend to become trapped within lysosomes following protonation within the acidic lysosomal microenvironment [15-17]. Because macrophages have very active endolysosomal systems and express high levels of biomolecular ion transporters, they could significantly impact the volumes of distribution of many weakly basic drugs.

Here, in order to study both how macrophages impact the volume of distribution of a therapeutic agent, and to determine the *in vivo* cargo carrying capacity of the macrophage, the

FDA-approved and biocompatible antibiotic clofazimine was chosen as a reporter probe. Clofazimine is an anti-mycobacterial agent clinically used to treat leprosy and multi-drug resistant tuberculosis [18-20]. It exhibits extensive accumulation throughout the body following oral administration, in both humans and in animal models [21-23]. Because clofazimine is both highly lipophilic ($\text{LogP} > 7$) and contains a weakly basic, ionizable amine group, it is expected to accumulate in adipose tissue, intracellular membranes and in acidic organelles such as lysosomes. In both human and animal models, it has been shown that following prolonged oral dosing, CFZ accumulates extensively within macrophages [24].

Previously, we have shown that the accumulation of clofazimine within macrophages leads to the formation of large, insoluble crystal-like drug inclusions (CLDIs) within these cells comprised of highly organized domains of clofazimine hydrochloride [25, 26]. In this manner, CLDIs can provide a solid, stable volume marker to assess the macrophage's cargo carrying capacity and its contribution to the drug's volume of distribution. Because of the crystallinity and low solubility, CLDIs are easily isolated and are readily detectable through a variety of analytical techniques [24, 26]. Thus, we proceeded to study the cargo loading capacity of different macrophage populations to probe the patterns of macrophage loading in different organs, and to determine how the macrophages impact the volume of distribution. Additionally, the effects of macrophage depletion on cargo loading was probed, and the theoretical macrophage loading capacity within different tissues was calculated and related to the measured, tissue-specific variations in macrophage loading and its contribution to the volume of distribution.

7.3 Materials and Methods

Clofazimine Administration to Mice. Animal care was provided by the University of Michigan's Unit for Laboratory Animal Medicine (ULAM), and the experimental protocol was approved by the Committee on Use and Care of Animals (Protocol PRO00005542). Mice (4 week old, male C57Bl6) were purchased from the Jackson Laboratory (Bar Harbor, ME) and acclimatized for 1 week in a specific-pathogen-free animal facility. Clofazimine (C8895; Sigma, St. Louis, MO) was dissolved in sesame oil (Shirakiku, Japan) to achieve a concentration of 3 mg/ml, which was mixed with Powdered Lab Diet 5001 (PMI International, Inc., St. Louis, MO) to produce a 0.03% drug to powdered feed mix, and orally administered ad libitum for up to

eight weeks. A corresponding amount of sesame oil was mixed with chow for vehicle treatment (control). For washout experiments, mice were fed the vehicle-containing diet for eight weeks, after an eight week loading period with the CFZ-containing diet. Mice were euthanized via carbon dioxide asphyxiation and exsanguination.

Alveolar Macrophage Isolation. Following euthanasia, the trachea was surgically exposed and cannulated with an 20G needle and the lungs were lavaged by instilling DPBS (Life Technologies) containing 0.5 mM EDTA (Sigma) in 1 ml aliquots for a total of 6 ml. Approximately 90% of the bronchoalveolar lavage (BAL) was retrieved. The BAL was then centrifuged for 10 min at 400 x g, 4°C, resuspended in RPMI 1640 media (Life Technologies) with 5% FBS (Life Technologies) and Penicillin/Streptomycin (ThermoFisher), macrophages were counted, and an aliquot of cells were then plated onto 4 or 8 chamber coverglass (#1.5, Lab-Tek II, Nunc, Rochester, NY) for imaging studies. The cells were allowed to attach overnight and then washed with media. The remaining cells were analyzed for drug content.

Peritoneal Macrophage Isolation. Following euthanasia, a small incision was made in the lower abdomen. The peritoneal cavity was then flushed 10 mL of ice cold DPBS containing 5% FBS (Sigma) and collected. The peritoneal lavage was centrifuged for 10 min at 400 x g, 4°C, and then resuspended in DMEM media (Life Technologies) with 5% FBS and Penicillin/Streptomycin, macrophages were counted, and an aliquot of cells were then plated onto 4 or 8 chamber coverglass (#1.5, Lab-Tek II, Nunc, Rochester, NY) for imaging. The cells were allowed to attach overnight and then washed with media. The remaining cells were analyzed for drug content.

Bone Marrow Monocyte Isolation. Following euthanasia, an incision was made above the hip bone and the skin was removed down the entire leg. The femur was then cut from the knee joint and the hip, the muscle was removed, and the bone was placed in ice cold DPBS. The tips of the femur were then cut, and the bone was flushed with 5 mL of ice cold PBS to collect the bone marrow monocytes. The suspension was centrifuged for 10 min at 400 x g, 4°C, and resuspended in RPMI 1640 media with 5% FBS and Penicillin/Streptomycin, counted with a hemocytometer, and an aliquot of cells were plated onto 4 or 8 chamber coverglass (#1.5, Lab-Tek II, Nunc, Rochester, NY) for imaging. The cells were allowed to attach overnight and then washed with media. The remaining cells were analyzed for drug content.

Kupffer Cell Isolation. Following euthanasia, the portal vein was injected with 10 mL of 1 mg/mL Collagenase D (Worthington Biochemical Corporation, Lakewood, NJ) in DMEM-low glucose (Life Technologies) with 15 mM HEPES (Life Technologies). The tissue was then removed, placed in a sterile petri dish, and minced into small (2-4 mm) pieces using a sterile scalpel blade. 15 mL of the Collagenase solution was added, and the tissue was incubated for 40 minutes at 37°C, with occasional pipetting to dissociate tissue. The suspension was then filtered through a 100 µm cell strainer (Fisher Scientific, Waltham, MA) and centrifuged at 200 x g for 5 minutes. The supernatant was discarded, and the cells were resuspended in 15 mL DMEM-low glucose with 15 mM HEPES, and centrifuged at 200 x g for 5 minutes. This was repeated for two additional washes. After the final wash, the cells were suspended in DMEM:F/12 (1:1) (Life Technologies) with 10% FBS and Penicillin/Streptomycin, macrophages were counted, and an aliquot was plated onto 4 or 8 chamber coverglass(#1.5, Lab-Tek II, Nunc, Rochester, NY) coated with Collagen 1 (Corning, Corning, New York) for imaging. The cells were allowed to attach overnight and then washed with media.

Multi-parameter Microscope Imaging and Analysis of Xenobiotic Sequestering Macrophage Populations. Multi-parameter polarization, brightfield, and fluorescence imaging and analysis were performed using the imaging method previously described by Rzeczycki et al [26]. Briefly, cells were plated on chamber slides and allowed to attach overnight. Following attachment, cells were imaged with brightfield, fluorescence, and polarization imaging modalities. Images were then analyzed using ImageJ software [27, 28]. Values for dichroism and optical density are reported as an average signal per cell, from 0-1. At least 150 cells of each type were analyzed at each time point. Following loading with 7 and 14 mg of cargo, macrophages were classified as xenobiotic sequestering based on whether or not they contained a detectable Cy5 signal from clofazimine hydrochloride [24] using a K-means clustering analysis, with the clusters set to 2 based off of the $\text{Log}_{10}(\text{Intracellular Cy5 fluorescence})$.

Biochemical Analysis of Clofazimine in Cells. The concentration of clofazimine in cells was determined after measuring clofazimine content in isolated macrophage populations and organ homogenates using established methods [22, 24, 25, 29]. For isolated macrophage populations, cells were counted within each cell sample using a hemocytometer to determine the total recovered macrophage population. The cells were then centrifuged and the media was removed.

The cell pellet was suspended in 1 mL of DI water, and the drug was extracted with three passes of 1 mL of xylenes. The drug was then extracted from the xylene with three 1 mL passes of 9M sulfuric acid. The concentration of clofazimine present in the cell sample was then determined using a plate reader (Biotek Synergy 2, Winooksi, VT) at wavelength 450 nm, and background corrected at wavelength 750 nm, with the concentration determined using a standard curve made of standards with known concentrations of clofazimine, and is reported as fmol clofazimine/xenobiotic sequestering cell.

Sample Preparation for Microscopy. Cryosectioning was carried out using a Leica 3050S Cryostat (Leica Biosystems Inc., Buffalo Grove, IL). Samples were sectioned to 5 μm . In preparation for cryosectioning, portions of the organ were removed, immediately submerged in OCT (Tissue-Tek catalog no. 4583; Sakura), and frozen (-80°C). For transmission electron microscopy, organs were submerged in fixative and cut into small (<1 mm) sized pieces. The organs were preserved in a glass vial with fixative and stored at 4°C . After three rinses with Sorensen's buffer (0.1 M), tissues were stained with 1% osmium tetroxide in Sorensen's buffer and washed three times in Sorensen's buffer. Dehydration was carried out with a graded ethanol-water series (50, 70, and 90% and two changes of 100%) for 15 min each. After washing with three changes of propylene oxide, the tissues were treated with Epon resin (Electron Microscopy Sciences) and polymerized at 60°C for 24 hours. The blocks were then sectioned to 70 nm using an ultramicrotome and mounted on a copper EM grid (Electron Microscopy Sciences), which was then stained with uranyl acetate and lead citrate before imaging. Immunohistochemistry of F4/80 (Abcam, 1:500 dilution) was performed using Alexa-Fluor 488 (Abcam, 1:500 dilution).

Clofazimine Volume Occupancy. The volume that clofazimine occupies within the macrophage was determined using the reported crystal-packing density of 1.36 g/mL [25] for clofazimine-HCl, which was then converted to a molar volume of $0.377 \mu\text{m}^3/\text{fmol}$. Cellular volume occupancy was then estimated using the measured drug loading per cell and this calculated molar volume.

Determination of Vesicle Size and Shape. Vesicle loading per cell was performed using the Cy5 fluorescence of the alveolar macrophage. Using ImageJ [27, 28], the radius of each vesicle was determined. Vesicles which showed Cy5 fluorescence were counted as clofazimine

sequestering. Volume of the vesicle for 3.5 and 7 mg treated cells was estimated assuming spherical shape, while CLDI volume was estimated assuming a cylindrical shape.

Macrophage Expansion Analysis. To determine the expansion in macrophage population in lung, liver and spleen from animals treated with clofazimine, cryosections were obtained of the same thickness. The relative number of macrophages in a volume of tissue was determined by dividing the total F4/80 signal staining intensity between 8 week clofazimine-treated sample by the total F4/80 signal staining intensity of a vehicle-treated sample (the area and thickness of the sections analyzed was kept the same). The expanded macrophage population was then determined by multiplying literature reported (baseline) macrophage population values for each organ [30] by the relative expansion factor. To determine the percentage of xenobiotic sequestering cells, the total number of cells which showed Cy5 fluorescence and F4/80 staining were determined using a mask of the F4/80 staining. 5 images per organ per animal were analyzed, for each measurement.

Measurement of CLDI Mass within Tissues. The CLDI mass present in lung, liver, and spleen tissues at eight weeks of treatment was determined using established protocols [29]. Tissues (n=3) were removed, weighed, and placed in a sterile petri dish, where it was manually minced and homogenized using a scalpel and syringe plunger. The tissue homogenate was filtered through a 40 μm cell strainer to remove larger cellular debris. The filtrate was then centrifuged for 10 min at 300 \times g to pellet the CLDIs. The supernatant was removed and the pellet was resuspended in 10% sucrose in DPBS (Life Technologies, Carlsbad, CA) without calcium chloride or magnesium chloride, pH=7.4. CLDIs were further purified using a 3-layer sucrose gradient (50%, 30%, and 10% sucrose in DPBS) centrifugation method (3200 \times g for 60 minutes). The pelleted CLDIs were then dissolved in 9M H_2SO_4 and the mass of drug was determined using a plate reader (Biotek Synergy 2, Winooksi, VT) at wavelength 450 nm, and background corrected at wavelength 750 nm, determined using a standard curve with solutions of known concentration.

CLDI Loading Within Individual Macrophages. Using the total recovered mass of CLDIs within the liver, lung, and spleen, the CLDI loading within individual xenobiotic-sequestering macrophages was estimated using the total expanded macrophage population, corrected for the percentage of cells which contained a CLDI. Using literature reported values for cellular volume

of the macrophage [31], the percentage of cellular volume that is occupied by the CLDI was estimated.

Macrophage Depletion. To deplete tissue macrophages, mice were treated with liposomes containing either 7 mg/mL of clodronate or phosphate-buffered saline (PBS) (FormuMax Scientific Inc., Sunnyvale, CA). Liposomes were injected intraperitoneally, as previously described [32]. Mice were initially treated with 200 μ L of liposomes followed by 100 μ L injections twice per week to ensure continual macrophage depletion. Mice were fed clofazimine or control diet continuously for a four week period. Following two weeks of feeding, liposome administration began for two weeks. After completing four weeks of feeding and two weeks of liposome treatment, mice were sacrificed and tissues were collected.

Biochemical Analysis of Clofazimine in Tissues. After loading with clofazimine, mice were euthanized via CO₂ asphyxiation, and organs removed and weighed. Tissue (20-30 mg) was homogenized in 500 μ L of radioimmunoprecipitation assay buffer (Sigma) with added protease inhibitors (Halt protease and phosphatase inhibitor cocktail and 0.5 M EDTA; Thermo Pierce, Rockford, IL), and 350 μ L of homogenate was removed drug was extracted with three passes of 1 mL of xylenes. The drug was then extracted from the xylene with three 1 mL passes of 9M sulfuric acid. The recovery yield was determined by spiking samples with a known concentration of clofazimine. The concentration of clofazimine present in the tissue was then determined using the plate reader assay (Biotek Synergy 2, Winooksi, VT) at wavelength 450 nm, and background corrected at wavelength 750 nm, with the aid of a standard curve made with solutions of known concentration.

Biochemical Analysis of Clofazimine in Plasma. Blood was collected and centrifuged (7,000 \times g for 5 minutes). The resulting supernatant serum was extracted with acetonitrile (90% extraction efficiency) for 10 min at 4°C with vortexing. After centrifugation (15,000 rpm, 4°C), the supernatant was injected into a Waters Acquity UPLC H-Class (Waters, Milford, MA) equipped with an Acquity UPLC BEH C18 column (1.7 μ m, 2.1 mm [inner diameter] by 100 mm; Waters, Milford, MA). Mobile phase A was 5 mM ammonium acetate, adjusted to pH 9.9 with ammonium hydroxide, and mobile phase B was acetonitrile. The flow rate was 0.35 ml/min, with a linear gradient from 50 to 100% phase B over 1.5 min, followed by holding at 100% for 1.5 min, a return to 50% phase B, and then re-equilibration for 2.5 min. Standards were prepared by

spiking untreated plasma samples with known amounts of clofazimine, ranging from 0 to 30 μM . Peak area was determined using Empower 3 Software (Waters, Milford, MA).

Determination of the Volume of Distribution of Clofazimine at Various Stages of Drug Loading. Following treatment with 5.25 or 14 mg of clofazimine, mice ($n=3$ per time point) were euthanized and the liver, spleen, small intestine, fat, kidney, and lung were removed, weighed, and the mass of clofazimine within each tissue and concentration within plasma was determined using the previously described protocols. The volume of distribution of the drug within macrophages, tissue and the whole body at the different loading amounts was determined using the ratio between the total drug within tissues or individual cells and the measured plasma concentration, and is reported as L/kg tissue or L/kg body weight, assuming a 25 gram mouse.

CLDI Injection and Stabilization Assay. To determine how macrophages stabilize CLDIs, mice were treated with either liposomal PBS or liposomal clodronate, as previously described [32]. 48 hours after liposome administration, mice were injected I.P. with 200 μg of CLDIs suspended in 1 mL of PBS ($n=3$ mice per group per time point). At time points ranging from 0 to 48 hours, the mice were euthanized, the peritoneal lavage was collected and pelleted, and the drug content within the pellet was analyzed using the previously described spectrophotometric analysis method. Using a simple exponential regression with recovered drug content, the half-life was estimated.

Statistical Analysis. All data are expressed as means \pm the standard deviations (SD). For multiple comparisons, statistical analysis was performed with one-way analysis of variance (ANOVA) and Tukey's post hoc comparisons. The half-life of injected CLDIs was determined using a simple, first order exponential regression of the recovered drug mass. All statistical analyses were performed using IBM SPSS Statistics version 24.0 (IBM Software, Armonk, New York). P values less than 0.05 were considered statistically significant.

7.4 Results

7.4.1 Macrophages adjusted internal membrane arrangement to maximize cargo loading

Experimentally, a moderate, whole body cargo load (3.5 mg, Figure 1) mostly led to accumulation in alveolar macrophages (Figure 1a). This cargo was associated with red, optically

dense cytoplasmic vesicles which exhibited little dichroism signal, corresponding to a disordered, amorphous supramolecular organization [33, 34] (Figure 1b). A larger cargo load resulted in a modest increase in accumulation in the alveolar macrophages (Figure 1c), plus a fraction of peritoneal and liver macrophages were also loaded; however, the structure of the intracellular cargo became more organized (Figure 1b) as reflected in the elevated optical density and dichroism of peritoneal and liver macrophages (Figure 1b-d). Doubling the whole body cargo load caused all macrophages to redistribute their internal cargo loads into large, highly ordered CLDIs exhibiting strong dichroism signals (Figure 1b). Under all loading conditions, the less mature bone marrow monocytes were free of cargo. At a population level, these trends were confirmed by multi-parameter image-based cytometric analyses (Figure 1c, d).

The results of chemical analyses confirmed the observed, uneven distribution of cargo amongst the different macrophage populations. At low (3.5 mg) cargo loading, alveolar macrophages sequestered 29.9 ± 12.4 fmol of cargo/cell, with the other populations showing minimal loading (Figure 1e). Within the alveolar macrophages, after a whole body load of 3.5 mg, less than 0.3% of the maximal phagocytic capacity of the cells was reached (Figure 1f). At a larger (7 mgs) whole body cargo load, alveolar macrophages accumulated 34.0 ± 20.3 fmol cargo/cell, which primarily remained in disordered form as reflected in the low dichroism signal (Figure 1b,d). Peritoneal and liver macrophage populations, due to their differential accumulation pattern (Figure 1b), increased their cargo loading per cell to 105.7 ± 10.0 and 63.5 ± 16.2 fmol/cell, respectively. At the highest loads of cargo (14 mgs), alveolar, peritoneal, and liver macrophage populations showed similar levels of cargo loading (Figure 1e). By accumulating cargo as CLDIs, the macrophages maximized intracellular cargo loading. The highest cargo volume corresponded to ~1% of the reported, maximal phagocytic capacity of macrophages (Figure 1f) [8]. Thus, with CLDI formation, only a small fraction of the potential, intracellular cargo space was occupied at the highest loading capacity measured *in vivo*.

In order to efficiently accommodate this massive cargo load, macrophages also adjusted their intracellular membrane organization. At low levels of loading (3.5 mgs), the alveolar macrophage population accumulated an average of 21.6 ± 5.0 vesicles per cell, with each vesicle occupying a mean volume of $0.43 \pm 0.29 \mu\text{m}^3$ (Table 1). Transmission electron micrographs of alveolar macrophages revealed numerous dark, lipid bound inclusions within the cytoplasm

(Figure 2a). An even larger (7 mgs) whole body cargo load resulted in the cytoplasmic vesicles increasing to 32.6 ± 6.8 per cell ($n=30$ cells, $p<0.05$, ANOVA, Tukey's HSD), with the vesicular volume increasing slightly to $0.97 \pm 0.96 \mu\text{m}^3$ (Table 1). Nevertheless, at 14 mg of cargo loading, the AM Φ 's membrane bound cargo compartment was visibly expanded (Figure 2b). At this point, the number of loaded vesicles per cell dropped to 18.4 ± 11.1 and their volume increased to $13.8 \pm 10.4 \mu\text{m}^3$. The larger, solid, membrane bound compartments were stable and remained within the macrophage even after an eight-week cargo washout period (Figure 2c).

7.4.2 Insoluble cargo accounts for majority of intracellular loading, and leads to increased volume of distribution

Of noteworthy significance, the amount of cargo in the isolated macrophage populations effectively accounted for most of the total cargo load measured in whole organ homogenates (Table 2). Based on the amount of cargo within each organ, the volume of blood that was cleared by the macrophages in the different organs was estimated (the organ-specific Volume of Distribution, V_{OD} ; Table 3). In pharmacokinetic terms, the whole body V_D of a molecule is the ratio between the amount of drug in the organism and the plasma concentration of the drug [35]. V_D represents the extent of tissue distribution [36] as reflected in the theoretical volume required to contain an administered amount of drug, at the same concentration as found in the plasma. With an increasing cargo load, each macrophage population significantly contributed to the increase in V_{OD} and hence, to V_D (Table 3). Given that the volume of a single macrophage is ~ 1 pL, the macrophages' contribution to V_D was mostly due to the solute-to-solid phase transition that accompanied CLDI formation. At the whole organ level, there was a nearly 100-fold increase in the V_{OD} within the liver and small intestine, a 60-fold increase within the spleen and 10-fold increase within the lung upon increasing the whole body cargo loading from 5.25 to 14 mg (Table 4). Within the fat and kidney, which do not contain the large populations of tissue macrophages typical of the previously mentioned organs, there were modest increases in the V_{OD} , but nowhere near the increases in V_{OD} observed in liver, spleen, lung and intestine (Table 4).

7.4.3 Macrophages are necessary to acquire and stabilize intracellular cargo

Interestingly, the number of macrophages in various organs increased following loading with the maximum cargo treatment (Figure 3a). Thus, to test whether macrophages played an active role in determining cargo accumulation and distribution, liposomal clodronate injections were used to deplete hepatic and splenic macrophages [32]. Following clodronate treatment, the cargo carrying capacity of liver and spleen was significantly reduced; however, within the kidney, which did not undergo depletion, there was no significant reduction in cargo load (Figure 3b). Quantitatively, due to the reduction in macrophage numbers (Figure 3c), there was a concomitant reduction in CLDI accumulation within the liver and spleen (Figure 3d). Most interestingly, cargo loading within liver and spleen macrophages was similar between the two treatment groups (Figure 3e). Furthermore, the serum concentration of clofazimine was similar between the groups (Figure 3f), indicating that the effects of clodronate on cargo accumulation were specifically due to macrophage depletion, and not to a decrease in circulating drug concentrations or an associated decrease in drug bioavailability, absorption or macrophage loading, which would have been apparent as a decrease in drug accumulation in the remaining macrophages. Finally, injecting CLDIs directly into the peritoneal cavity of macrophage-depleted mice led to a significant reduction in half-life compared to their control, PBS-treated counterparts (Figure 3g). The peritoneal macrophages imparted stability to the injected CLDI by internalizing them via phagocytosis, while extracellular CLDIs more rapidly degraded (Figure 3h). These results indicate that the macrophages are actively involved in the sequestration and stabilization of cargo as insoluble, highly organized and biocompatible supramolecular complexes.

7.5 Discussion

While the volume of distribution of most hydrophobic drugs is typically ascribed to drug partitioning into adipose tissue, the experimental results presented in this study indicate how macrophages can account for most of the accumulation and distribution of the reporter probe *in vivo*, with macrophage cargo carrying capacity increasing in parallel to the increase in whole body load. In the experiments reported in this study, the mass and volume of cargo per cell was nowhere near the maximal cargo capacity of macrophages, as determined *in vitro* following phagocytosis of spherical beads of increasing size [8]. When macrophages of the liver and spleen were depleted, there was a reduction in the whole-organ cargo carrying capacity in proportion to

the decrease in the macrophage population, but the cargo carrying capacity of the remaining macrophages was unaffected. There has been extensive research in the past on how therapeutic agents can impact the immune system [37]; however, few, if any small molecule drugs have been shown to have their ADME properties dependent on the action of macrophages or other specific populations of immune cells. Using clofazimine as a weakly basic reporter molecule [38], we found that the extent of tissue distribution was actively impacted by the action of tissue macrophages. Lung and liver macrophages are often where bacteria reside during persistent bacterial infections (particularly with infections of *Mycobacterium tuberculosis* [39] and *Mycobacterium leprae* [40]). By extension, the efficacy of many of the antibiotics used to treat these infections may be dependent on a synergistic interaction between the macrophages, which harbor these intracellular pathogens, and the antibiotic, which is accumulated by these cells and ultimately destroys these pathogens.

Most interestingly, our results indicate that macrophage-mediated small molecule drug sequestration can have a profound impact on pharmacokinetics. While it is often assumed that the volume of distribution of a therapeutic is a constant, and is only significantly impacted by disease states affecting organ function [41, 42], our measurements indicate that this is not necessarily the case. Rather, in the case of drugs that show significant levels of bioaccumulation, that undergo phase transitions (solute-solid or solute-amorphous), or that are able to become concentrated within particular cellular populations, it is possible that the volume that the drug distributes can change significantly as treatment progresses. With clofazimine, this remarkable phenomenon was first evident as a significant reduction in the plasma concentration of the drug from weeks 3 to 8 in treatment [22]. Concurrently, in this study we found a ~100-fold increase in the organ-specific volume of distribution (V_{OD}) within the liver and spleen, and a ~10-fold increase of V_{OD} within the lung. The blood volume cleared by different organs corresponded to the extent of loading of the macrophages in those organs, with the spleen showing the highest loading per unit tissue weight, followed by liver and lung [22]. The preferential accumulation of the cargo in spleen was primarily associated with the accumulation of drug molecules as an insoluble, ordered supramolecular aggregates[43]. By depleting the macrophages of the liver and spleen with clodronate, we deduce that this phenomenon is largely due to the action of macrophages. Beyond clofazimine, it is known that the intracellular sequestration of other hydrophobic, cationic drugs such as amiodarone [44] or quinacrine [45] is highly dependent on

the proton pump V-ATPase, which is expressed at higher levels within macrophages [5]. Thus, beyond clofazimine, this mechanism is likely to impact the pharmacokinetics of other therapeutic agents.

In terms of the biological mechanisms that underpin their ability to sequester an increasingly massive load of cargo, the macrophage endolysosomal system is particularly adept at accommodating an increasing cargo load due to the low-pH and high chloride environment of their lysosome [43]. The high levels of V-ATPase expressed in macrophage lysosomes are a likely explanation for the active solute to solid transition that seems to occur selectively within these cells. Due to the active concentrative proton and chloride pumping [46] within the endolysosomal system, massive amounts of solid cargo can be sequestered and accommodated within membrane bound intracellular compartments. In addition to the activity of lysosomal proton and chloride transporters present in macrophage lysosomes, these cells can also alter their internal membrane architecture to maximize the volume of cargo within a minimal amount of membrane surface area. As our results indicate, at low levels of cargo treatment, macrophages acquired soluble cargo in the form of small, spherical vesicles. Continued accumulation of cargo led to the formation of larger volume vesicles and to the disappearance of the smaller vesicles. We infer that, by expanding the volume of intracellular vesicles, macrophages maximized the available cargo space while minimizing the overall membrane surface area delimiting the cargo compartments [47, 48], allowing for increased cargo accumulation within the cell, and consequently, an increase in V_{OD} .

In addition to the adaptive changes that were observed to occur at the level of the individual macrophages, measurements of the entire cell population of liver, lung, and spleen indicated an increase in the number of macrophages occurring in parallel to the increase in cargo loading. Pathologically, an expansion in the macrophage population is typically associated with a pro-inflammatory response [49, 50]. However, the accumulation of insoluble intracellular drug cargo in macrophages of clofazimine-treated animals was accompanied by the activation of anti-inflammatory signaling pathways and was not associated with obvious toxicological manifestations [29, 51]. As a candidate, anti-inflammatory signaling mechanism, it is possible that the lysosomal accumulation of weakly basic molecules may induce activation of transcription factor EB (TFEB) [52, 53]. Increased cargo loading can therefore lead to TFEB

becoming chronically activated, resulting in increased lysosomal biogenesis, which would reduce lysosomal stress and actively allow for increased intracellular cargo sequestration. Nevertheless, because this macrophage-mediated drug sequestration phenomenon is also linked to concomitant changes in organ mass (e.g. splenomegaly [22]) and histological organization (e.g. granuloma formation [22, 54]), these results warrant additional studies into the functional sequelae of the pro- and anti-inflammatory signaling mechanisms that are activated in response to a massive intracellular cargo load.

7.6 Conclusion

To conclude, the results presented in this study point to a stimulus-dependent, macrophage-mediated biological response mechanism that is activated by the extent of cargo accumulation in these cells. In this process, macrophages actively stabilize intracellular drug as insoluble complexes that are trapped within membrane-bound compartments. To accommodate increasingly massive loads of cargo, macrophages increase in numbers and adapt their intracellular membrane organization so as to maximize the intracellular cargo space. While resident macrophages of different organs demonstrated significant variations in their response to increasing loads of cargo, all differentiated macrophage populations were capable of sequestering large loads of cargo. The adaptive cargo carrying capacity of macrophages ultimately accounted for the observed expansion in the drug volume of distribution, which was directly measured based on the amount of drug cargo sequestered within each organ. Of noteworthy significance, to our knowledge, this is the first time that the volume of distribution of a small molecule drug has been directly measured and associated with an adaptive, immune system-mediated biological response.

7.7 Acknowledgements

The authors acknowledge funding from the University of Michigan M-Cubed program and NIH grant RO1GM078200.

7.8 Figures

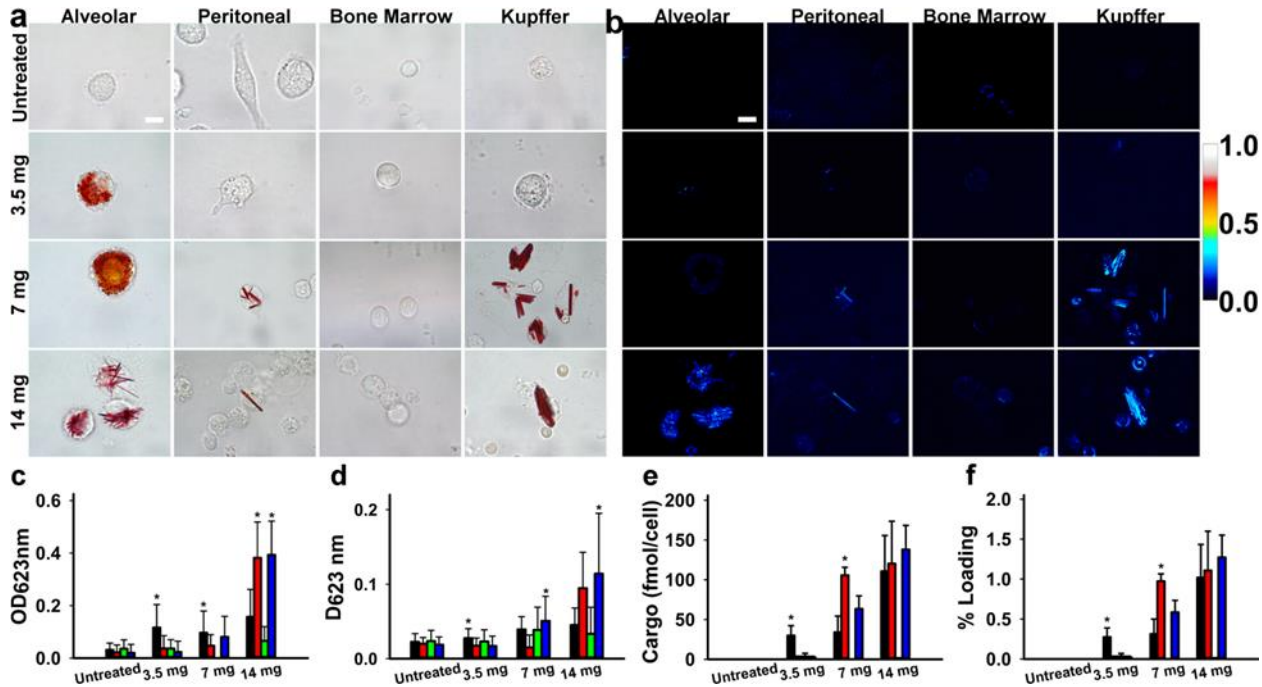


Figure 7-1 Microscopic imaging cytometry reveals variations in cargo loading of macrophage and monocyte populations

a, Brightfield images of isolated macrophage and monocytes following increasing whole-body cargo loading. **b**, Linear diattenuation images of isolated macrophage and monocytes following increasing whole-body cargo loading. **c**, Mean optical density of alveolar macrophage (black), peritoneal macrophage (red), bone marrow monocyte (green), and Kupffer cell (blue) at increasing cargo loading. **d**, Mean linear diattenuation of alveolar macrophage (black), peritoneal macrophage (red), bone marrow monocyte (green), and Kupffer cell at increasing cargo loading. **e**, Mean cargo loading per xenobiotic-sequestering cell at increasing cargo loading. **f**, Percentage of maximal cargo loading within each cell type at increasing cargo loading. Error bars represent standard deviation. (n=150 cells per time point for imaging studies, n=3 mice per cargo treatment for drug accumulation, *=p<0.05, ANOVA, Tukey's HSD) (Scale bar is 10 μ m).

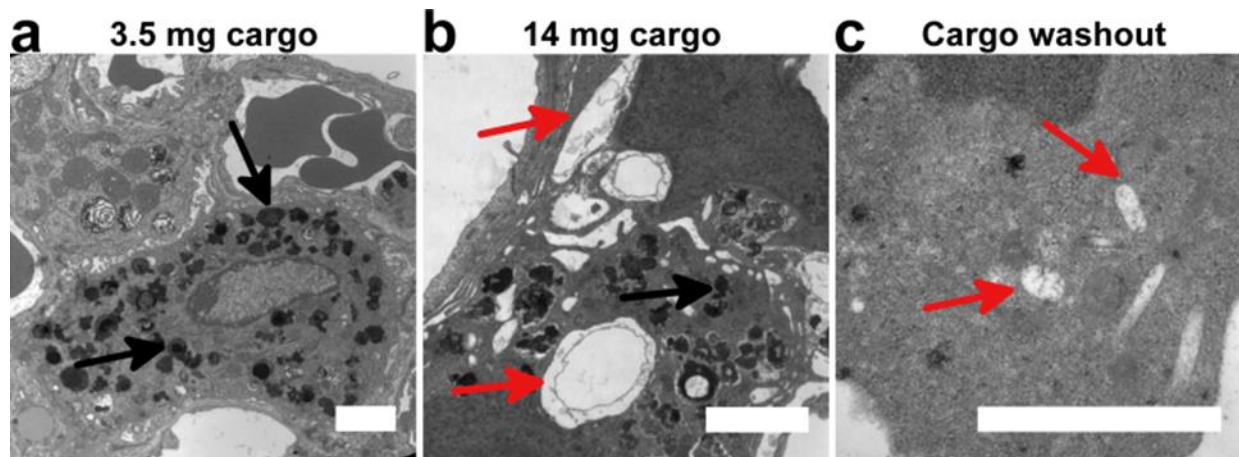


Figure 7-2 Cargo accumulation induces reorganization in the internal membrane architecture of macrophages

a, Following whole-body loading of 3.5 mg of the cargo volume marker, macrophages of the lung are loaded with small vesicles that fill the cytoplasm. **b**, Increasing doses of the marker results in accumulation of crystal-like drug inclusions (CLDIs) throughout the cytoplasm. **c**, These larger aggregates remain stable intracellularly even following an eight week washout period. Black arrows denote cargo-laden vesicles and red arrows denote cavities left from CLDIs removed during sample preparation. Scale bar is 2000 nm.

Cargo Loading	Mean number of vesicles per cell (n=30 cells)	Mean vesicle volume (n=50 vesicles)	Mean total volume occupied by vesicles (n=50 vesicles)
3.5 mg	21.6 ± 5.0	0.43 ± 0.29 μm ³	9.2 ± 6.7 μm ³
7 mg	32.6 ± 6.8*	0.97 ± 0.96 μm ³	31.7 ± 32.1 μm ³
14 mg	18.4 ± 11.1	13.8 ± 10.4 μm ³ *	253.8 ± 244.5 μm ³

Table 7-1 Cellular vesicular volume and occupancy within alveolar macrophages

Changes in vesicle number, size, and volume occupancy in cargo-treated alveolar macrophages. (*=p<0.05, ANOVA, Tukey's HSD).

Macrophage Population	Cargo mass (mg)	Percent Xenobiotic Sequestering	Total Xenobiotic Sequestering Population	Fmol Cargo/Xenobiotic Sequestering Cell	% Cell Volume Occupied by Cargo
Liver	4.57 ± 0.78	88.5 ± 3.3%	8.0 x 10 ⁷ ± 1.9 x 10 ⁷	120.9 ± 35.3	2.11 ± 0.62%
Spleen	3.23 ± 0.27	83.9 ± 12.5%	2.2 x 10 ⁷ ± 5.9 x 10 ⁶	310.5 ± 86.9	5.42 ± 1.52%
Lung	0.32 ± 0.06	81.1 ± 3.2%	3.7 x 10 ⁶ ± 1.7 x 10 ⁶	183.2 ± 91.5	3.20 ± 1.60%

Table 7-2 Insoluble cargo loading within various macrophage populations

Estimated cargo loading within liver, spleen, and lung macrophages following 14 mg of cargo loading.

Macrophage Population	5.25 mg cargo V_{OD} (nL/macrophage)	14 mg cargo V_{OD} (nL/macrophage)
Liver	0.66 ± 9.8x10 ⁻⁵	33.51 ± 0.01*
Lung	5.51 ± 9.5x10 ⁻⁵	42.73 ± 0.01*
Spleen	0.49 ± 2.5x10 ⁻⁴	64.25 ± 0.01*

Table 7-3 Estimated volume of distribution within various macrophage populations following increased drug therapy

Volume of distribution of cargo marker in liver, lung, and spleen macrophage, at 5.25 and 14 mg of whole-body loading (*=p<0.05, Two-Tailed Student's T-Test)

Tissue (n=3 per treatment)	5.25 mg cargo V_{OD} (L/kg tissue)	14 mg cargo V_{OD} (L/kg tissue)
Liver	33.9 ± 13.1	2232.5 ± 958.2*
Spleen	118.8 ± 85.4	6139.3 ± 2637.0*
Fat	91.8 ± 15.2	129.1 ± 61.1
Jejunum and Ileum	11.1 ± 6.3	1085.2 ± 606.2*
Lung	91.2 ± 12.0	902.3 ± 524.1
Kidney	31.1 ± 7.3	125.6 ± 55.5

Table 7-4 Estimated volume of distribution within various organs following increased drug therapy

Volume of distribution of cargo marker in various organs, at 5.25 and 14 mg of whole-body loading (*=p<0.05, Two-Tailed Student's T-Test)

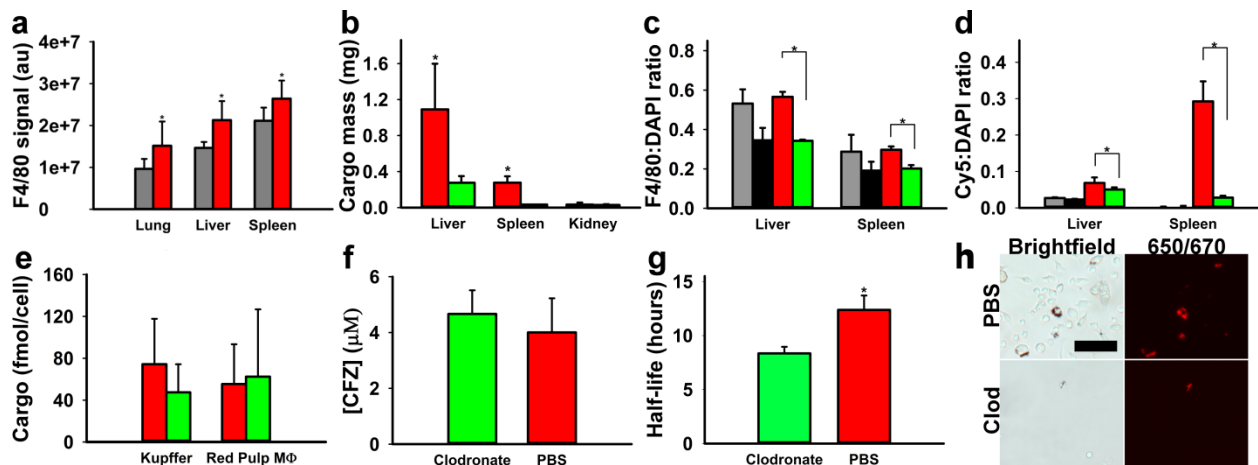


Figure 7-3 Macrophages increase in number and actively sequester cargo primarily by stabilizing it in an insoluble form

a, Comparison of total F4/80 macrophage signal in untreated (grey) and 14 mg cargo loading (red) tissue sections. **b**, Total cargo loading in PBS- (red) and clodronate-liposome (green) tissues. **c**, Quantification of tissue macrophage population in PBS-vehicle diet (grey), clodronate-vehicle diet (black), PBS-cargo diet (red), and clodronate-cargo diet (green) using F4/80 signal. **d**, Quantification of insoluble cargo accumulation in PBS-vehicle diet (grey), clodronate-vehicle diet (black), PBS-cargo diet (red), and clodronate-cargo diet (green) using Cy5 fluorescence. **e**, Individual macrophage cargo loading in PBS-cargo diet (red) and clodronate-cargo diet (green). **f**, Serum concentration of clofazimine in clodronate- and PBS-cargo diet treatment groups. **g**, Estimated half-life of injected CLDIs within peritoneal cavity of clodronate and PBS liposome treated mice. **h**, Peritoneal lavage of PBS and clodronate treated liposome groups 48 hours post injection, scale bar is 50 μm. Error bars represent standard deviation (*= $p < 0.05$, Student's Two-tailed T-test or ANOVA, Tukey's HSD).

7.9 Supporting Information

This manuscript is currently in preparation for publication.

7.10 References

1. Epelman, S., K.J. Lavine, and G.J. Randolph, *Origin and Functions of Tissue Macrophages*. Immunity, 2014. 41(1): p. 21-33.
2. Murray, P.J. and T.A. Wynn, *Protective and pathogenic functions of macrophage subsets*. Nature Reviews Immunology, 2011. 11(11): p. 723-737.
3. Davies, L.C., et al., *Tissue-resident macrophages*. Nat Immunol, 2013. 14(10): p. 986-995.
4. Mindell, J.A., *Lysosomal Acidification Mechanisms*. Annual Review of Physiology, 2012. 74(1): p. 69-86.
5. Wang, S.-P., et al., *Regulation of Enhanced Vacuolar H⁺-ATPase Expression in Macrophages*. Journal of Biological Chemistry, 2002. 277(11): p. 8827-8834.
6. Hamczyk, M.R., R. Villa-Bellosta, and V. Andrés, *In Vitro Macrophage Phagocytosis Assay*, in *Methods in Mouse Atherosclerosis*, V. Andrés and B. Dorado, Editors. 2015, Springer New York: New York, NY. p. 235-246.
7. Steinberg, B.E. and S. Grinstein, *Analysis of macrophage phagocytosis: quantitative assays of phagosome formation and maturation using high-throughput fluorescence microscopy*. Methods Mol Biol, 2009. 531: p. 45-56.
8. Cannon, G.J. and J.A. Swanson, *The macrophage capacity for phagocytosis*. Journal of Cell Science, 1992. 101(4): p. 907-913.
9. Broz, P., et al., *Inhibition of macrophage phagocytotic activity by a receptor-targeted polymer vesicle-based drug delivery formulation of pravastatin*. J Cardiovasc Pharmacol, 2008. 51(3): p. 246-52.
10. Hirota, K. and H. Terada, *Endocytosis of Particle Formulations by Macrophages and Its Application to Clinical Treatment*, in *Molecular Regulation of Endocytosis*, B. Ceresa, Editor. 2012, InTech: Rijeka. p. Ch. 16.
11. Lemaire, S., P.M. Tulkens, and F. Van Bambeke, *Cellular Pharmacokinetics of the Novel Biaryloxazolidinone Radezolid in Phagocytic Cells: Studies with Macrophages and Polymorphonuclear Neutrophils*. Antimicrobial Agents and Chemotherapy, 2010. 54(6): p. 2540-2548.

12. Carryn, S., et al., *Intracellular pharmacodynamics of antibiotics*. Infect Dis Clin North Am, 2003. 17(3): p. 615-34.
13. Stamler, D.A., M.A. Edelstein, and P.H. Edelstein, *Azithromycin pharmacokinetics and intracellular concentrations in Legionella pneumophila-infected and uninfected guinea pigs and their alveolar macrophages*. Antimicrob Agents Chemother, 1994. 38(2): p. 217-22.
14. Foulds, G., R.M. Shepard, and R.B. Johnson, *The pharmacokinetics of azithromycin in human serum and tissues*. Journal of Antimicrobial Chemotherapy, 1990. 25(suppl_A): p. 73-82.
15. Logan, R., et al., *Amine-Containing Molecules and the Induction of an Expanded Lysosomal Volume Phenotype: A Structure–Activity Relationship Study*. Journal of Pharmaceutical Sciences, 2014. 103(5): p. 1572-1580.
16. Funk, R. and J. Krise, *Cationic amphiphilic drugs cause a marked expansion of apparent lysosomal volume: implications for an intracellular distribution-based drug interaction*. Mol. Pharmaceutics, 2012. 9(5): p. 1384-1395.
17. Kaufmann, A. and J. Krise, *Lysosomal Sequestration of Amine-Containing Drugs: Analysis and Therapeutic Implications*. Journal of Pharmaceutical Sciences, 2006. 96(4): p. 729-746.
18. Arbiser, J. and S. Moschella, *Clofazimine: A review of its medical uses and mechanisms of action*. Journal of the American Academy of Dermatology, 1995. 32(2): p. 241-247.
19. Cholo, M., et al., *Clofazimine: current status and future prospects*. Journal of Antimicrobial Chemotherapy, 2011.
20. DrugBank, *Clofazimine*. 2013: drugbank.ca.
21. Baik, J. and G.R. Rosania, *Macrophages Sequester Clofazimine in an Intracellular Liquid Crystal-Like Supramolecular Organization*. PLoS ONE, 2012. 7(10): p. e47494.
22. Baik, J., et al., *Multiscale Distribution and Bioaccumulation Analysis of Clofazimine Reveals a Massive Immune System-Mediated Xenobiotic Sequestration Response*. Antimicrob. Agents. Chemother., 2013. 57(3): p. 1218-1230.

23. Sukpanichnant, S., et al., *Clofazimine-induced crystal-storing histiocytosis producing chronic abdominal pain in a leprosy patient*. *Am J Surg Pathol*, 2000. 24(1): p. 129-35.
24. Keswani, R., et al., *A Far-Red Fluorescent Probe For Flow Cytometric Xenobiotic-Sequestering Cell Functional Studies*. *Cytometry Part A*, 2015(Accepted Manuscript).
25. Keswani, R., et al., *Chemical Analysis of Drug Biocrystals: A Role for Counterion Transport Pathways in Intracellular Drug Disposition*. *Molecular Pharmaceutics*, 2015.
26. Rzeczycki, P., et al., *Detecting ordered small molecule drug aggregates in live macrophages: a multi-parameter microscope image data acquisition and analysis strategy*. *Biomedical Optics Express*, 2017. 8(2): p. 860-872.
27. Schneider, C.A., W.S. Rasband, and K.W. Eliceiri, *NIH Image to ImageJ: 25 years of image analysis*. *Nat Meth*, 2012. 9(7): p. 671-675.
28. Abramoff, M.D., P.J. Magalhaes, and S.J. Ram, *Image Processing With ImageJ*. *Biophotonics International*, 2004. 11(7): p. 36-42.
29. Yoon, G., et al., *Phagocytosed Clofazimine Biocrystals can Modulate Innate Immune Signaling by Inhibiting TNF Alpha and Boosting IL-1RA Secretion*. *Mol. Pharmaceutics*, 2015.
30. Lee, S., P. Starkey, and S. Gordon, *Quantitative analysis of total macrophage content in adult mouse tissues. Immunochemical studies with monoclonal antibody F4/80*. *J Exp Med*, 1985. 161(3): p. 475-89.
31. Champion, J.A. and S. Mitragotri, *Role of target geometry in phagocytosis*. *Proceedings of the National Academy of Sciences of the United States of America*, 2006. 103(13): p. 4930-4934.
32. van Rooijen, N. and E. Hendriks, *Liposomes for Specific Depletion of Macrophages from Organs and Tissues*, in *Liposomes*, V. Weissig, Editor. 2010, Humana Press. p. 189-203.
33. Mehta, S.B., M. Shribak, and R. Oldenbourg, *Polarized light imaging of birefringence and diattenuation at high resolution and high sensitivity*. *Journal of Optics*, 2013. 15(9): p. 094007.

34. Oldenbourg, R., *Polarized Light Microscopy: Principles and Practice*. Cold Spring Harbor Protocols, 2013. 2013(11): p. pdb.top078600.
35. Toutain, P.L. and A. Bousquet-MÉLou, *Volumes of distribution*. Journal of Veterinary Pharmacology and Therapeutics, 2004. 27(6): p. 441-453.
36. Smith, D.A., et al., *Volume of Distribution in Drug Design*. Journal of Medicinal Chemistry, 2015. 58(15): p. 5691-5698.
37. Kidd, B.A., et al., *Mapping the effects of drugs on the immune system*. Nat Biotech, 2016. 34(1): p. 47-54.
38. Logan, R., et al., *Drug-drug interactions involving lysosomes: mechanisms and potential clinical implications*. Expert Opin Drug Metab Toxicol, 2012. 8(8): p. 943-58.
39. Flynn, J.L. and J. Chan, *Immunology of tuberculosis*. Annu Rev Immunol, 2001. 19: p. 93-129.
40. Organization, W.H. *Leprosy*. 2015 [cited 2015 June 1]; Available from: <http://www.who.int/mediacentre/factsheets/fs101/en/>.
41. Blot, S.I., F. Pea, and J. Lipman, *The effect of pathophysiology on pharmacokinetics in the critically ill patient — Concepts appraised by the example of antimicrobial agents*. Advanced Drug Delivery Reviews, 2014. 77: p. 3-11.
42. Shamma, F.V. and K. Dickstein, *Clinical pharmacokinetics in heart failure. An updated review*. Clin Pharmacokinet, 1988. 15(2): p. 94-113.
43. Woldemichael, T., et al., *Reverse Engineering the Intracellular Self-Assembly of a Functional Mechanopharmaceutical Device*. Nature Biomedical Engineering, 2017.
44. Morissette, G., et al., *Intracellular sequestration of amiodarone: role of vacuolar ATPase and macroautophagic transition of the resulting vacuolar cytopathology*. Br J Pharmacol, 2009. 157(8): p. 1531-40.
45. Marceau, F., et al., *Vacuolar ATPase-mediated cellular concentration and retention of quinacrine: a model for the distribution of lipophilic cationic drugs to autophagic vacuoles*. Drug Metab Dispos, 2009. 37(12): p. 2271-4.

46. Leisle, L., et al., *ClC-7 is a slowly voltage-gated 2Cl(-)/1H(+)-exchanger and requires Ostm1 for transport activity*. The EMBO Journal, 2011. 30(11): p. 2140-2152.
47. Stachowiak, J.C., F.M. Brodsky, and E.A. Miller, *A cost-benefit analysis of the physical mechanisms of membrane curvature*. Nat Cell Biol, 2013. 15(9): p. 1019-1027.
48. Vigant, F., N.C. Santos, and B. Lee, *Broad-spectrum antivirals against viral fusion*. Nat Rev Micro, 2015. 13(7): p. 426-437.
49. Movita, D., et al., *Inflammatory Monocytes Recruited to the Liver within 24 Hours after Virus-Induced Inflammation Resemble Kupffer Cells but Are Functionally Distinct*. Journal of Virology, 2015. 89(9): p. 4809-4817.
50. Shi, C. and E.G. Pamer, *Monocyte recruitment during infection and inflammation*. Nature Reviews Immunology, 2011. 11(11): p. 762-774.
51. Yoon, G.S., et al., *Clofazimine Biocrystal Accumulation in Macrophages Upregulates Interleukin 1 Receptor Antagonist Production To Induce a Systemic Anti-Inflammatory State*. Antimicrob Agents Chemother, 2016. 60(6): p. 3470-9.
52. Napolitano, G. and A. Ballabio, *TFEB at a glance*. Journal of Cell Science, 2016.
53. Zhitomirsky, B. and Y.G. Assaraf, *Lysosomal sequestration of hydrophobic weak base chemotherapeutics triggers lysosomal biogenesis and lysosome-dependent cancer multidrug resistance*. Oncotarget, 2015. 6(2): p. 1143-56.
54. Trexel, J., et al., *Macrophage-Mediated Clofazimine Sequestration Is Accompanied by a Shift in Host Energy Metabolism*. J Pharm Sci, 2017. 106(4): p. 1162-1174.

Chapter 8

Liver Granulomas Function as Drug Sequestering Hepatoprotective Organoids

8.1 Abstract

The liver is the major organ affecting the metabolism and disposition of drugs in the body. Here, we aimed to determine how the liver adapts to long term bioaccumulation of a poorly soluble, weakly basic drug. We also sought to determine whether granuloma macrophages played a distinct role in drug disposition, compared to Kupffer cells. The ability of granuloma-associated macrophages and resting Kupffer cells to accumulate a weakly basic drug and a related analog with different solubility properties was studied. The expression of proteins related to intracellular accumulation of the weakly basic drug molecule within acidic organelles was characterized. Additionally, macrophage-depletion via liposomal clodronate was used to inhibit granuloma formation and assess its effect on the health status of the liver in response to drug bioaccumulation. Granuloma-associated macrophages were distinctively different from other macrophages of the same liver, which resembled resting Kupffer cells of untreated animals, exhibiting signs of high turnover. They were specifically drug-induced, and were not evident in animals treated with a related derivative that is less prone to intralysosomal precipitation. Granuloma-associated macrophages accumulated massive amounts of insoluble drug, specifically as the protonated, hydrochloride salt form. These cells exhibited increased TFEB activation, enlarged endolysosomal compartment and showed signs of mitochondrial degeneration. Liposomal clodronate inhibited granuloma formation, which was accompanied by increased hepatic necrosis and systemic toxicity. Granuloma-associated macrophages possessed distinctive, differentiated features that make them uniquely different from other drug-exposed macrophages and untreated Kupffer cells. Granuloma-associated macrophages are especially equipped to stabilize insoluble drug aggregates within an enlarged endolysosomal compartment.

As such, granulomas function as drug sequestering “organoids” –organs within an organ that protect neighboring hepatocytes by sequestering drug and confining the drug’s toxicity.

8.2 Introduction

Macrophages mediate inflammatory responses and have been implicated in a multitude of disease states, ranging from obesity [1, 2] to some types of cancers [3, 4]. One particular inflammatory response, granuloma formation, has been observed to occur almost everywhere in the body, from the skin to the lungs. A granuloma is a specialized collection of macrophages that functions to compartmentalize a foreign body, away from the surrounding tissues [5-7]. This reaction is commonly seen in bacterial and fungal infections. In leprosy, granulomas form within the skin and near nerves, causing severe neuropathy [8]. In tuberculosis, granulomas form “tuber”-like structures around the bacteria, to limit their spread [9]. Other inflammatory diseases of unknown origins can also be accompanied by the formation of granulomas. For example, Crohn’s disease is an inflammatory condition in which chronic inflammation induces granuloma formation throughout the gut [10]. Yet another kind of granuloma are the so called “foreign body granulomas”, which are formed by macrophages attempting to engulf exogenous materials, from splinters to surgical equipment, that are accidentally introduced in the body [11].

Hepatic granulomas are often observed in human liver biopsy samples, and can arise due to tuberculosis, brucellosis [12], or treatment with certain classes of drugs, such as sulfonamides [13] and quinidine [14]. Drug-induced liver granulomas are especially perplexing, in part, because the mechanisms by which drugs trigger granuloma formation are unknown. Kupffer cells, the macrophages of the liver, are among the first cells to interact with foreign substances ingested through the gut and have been implicated in protecting the host from harmful xenobiotics [15]. Kupffer cells have also been shown to play a major role in regulating the activity of drug-metabolizing enzymes such as the cytochrome P450 complex [16, 17], which can lead to drug-induced liver injury. Drugs like acetaminophen or bacterial products like lipopolysaccharide can activate Kupffer cells [18, 19]. The activation of Kupffer cells can lead to an inflammatory response, resulting in tissue damage and hepatotoxicity [20].

Here, we hypothesized that granuloma-associated macrophages play a specific role in ameliorating drug-induced liver damage and toxicity. To test this hypothesis, we turned to the FDA-approved antibiotic, clofazimine (CFZ), a highly lipophilic, poorly soluble, weakly basic

phenazine drug. CFZ, which has been used to successfully treat and cure leprosy since the 1950s [21] and is currently recommended as a treatment for multi-drug resistant tuberculosis [22] is known to induce liver granulomas. Due to its lipophilicity and unique pharmacokinetic properties [23], it bioaccumulates extensively during long term oral administration. Aside from causing skin pigmentation, prolonged oral administration of CFZ (>3 weeks) [24, 25] leads to its precipitation within liver, lung and spleen [26, 27]. These precipitates can be ingested by phagocytosis [28] and accumulate within macrophage lysosomes, as microscopic, insoluble aggregates of protonated CFZ hydrochloride [29]. While the soluble form of CFZ is cytotoxic *in vitro* [28], the insoluble, protonated hydrochloride salt form is significantly less toxic to cells. Importantly, the drug is well tolerated by patients and is relatively nontoxic in animal models [30, 31]. Thus, we decided to further explore the drug's effect on the liver, especially in regards to its pronounced ability to induce granuloma formation.

8.3 Materials and Methods

Drug Administration to Mice. Animal care was provided by the University of Michigan's Unit for Laboratory Animal Medicine (ULAM), and the experimental protocol was approved by the Committee on Use and Care of Animals (Protocol PRO00005542). Mice (4 week old, male C57B16) were purchased from the Jackson Laboratory (Bar Harbor, ME) and acclimatized for 1 week in a specific-pathogen-free animal facility. CFZ (C8895; Sigma, St. Louis, MO) was dissolved in sesame oil (Shirakiku, Japan) to achieve a concentration of 3 mg/ml, which was mixed with Powdered Lab Diet 5001 (PMI International, Inc., St. Louis, MO) to produce a 0.03% drug to powdered feed mix, which was orally administered ad libitum for up to eight weeks. A corresponding amount of sesame oil was mixed with chow for vehicle treatment (control). Mice were euthanized via carbon dioxide asphyxiation and exsanguination at the time of organ harvesting.

Kupffer Cell Isolation. Kupffer cells were isolated from the livers of untreated mice as follows. After euthanasia, the heart was perfused with 10 mL of pre-cooled Hank's buffered salt solution (HBSS) without magnesium or calcium, with 0.5 mM EGTA and 25 mM HEPES, pH adjusted to 7.4. The portal vein was then injected with 10 mL of 1 mg/mL collagenase D (Worthington

Biochemical Corporation, Lakewood, NJ) in DMEM-low glucose (Life Technologies) with 15 mM HEPES (Life Technologies). The liver was then removed, placed in a sterile petri dish, and minced into small (2-4 mm) pieces using a sterile scalpel blade. Collagenase solution (15 mL) was added, and the tissue was incubated (40 min, 37°C), with occasional pipetting to dissociate tissue. The suspension was then filtered through a 100 µm cell strainer (Fisher Scientific, Waltham, MA) and centrifuged (200 x g, 5 min). The supernatant was discarded, and the cells were resuspended in DMEM-low glucose (15 mL) with 15 mM HEPES, and centrifuged (200 x g, 5 min). This was repeated for two additional washes. After the final wash, macrophages were suspended in DMEM:F/12 (1:1) (Life Technologies) with 10% FBS and penicillin/streptomycin, were counted, and plated onto 12-well collagen-coated tissue culture plates and allowed to attach overnight (37°C). The next day, cells were washed with DMEM:F/12 and immunofluorescent staining of F4/80 was performed to identify macrophages [32] from other cell types.

Granuloma Isolation. Granulomas and granuloma macrophages were isolated from eight-week, CFZ-treated mice as follows. After euthanasia, the heart was perfused with 10 mL of pre-cooled Hank's buffered salt solution (HBSS) without magnesium or calcium, with 0.5 mM EGTA and 25 mM HEPES, pH adjusted to 7.4. The portal vein was then injected with 10 mL of 1 mg/mL collagenase D (Worthington Biochemical Corporation, Lakewood, NJ) in DMEM-low glucose (Life Technologies) with 15 mM HEPES (Life Technologies). The liver was then removed, placed in a sterile petri dish, and minced into small (2-4 mm) pieces using a sterile scalpel blade. Collagenase solution (15 mL) was added, and the tissue was incubated (40 min, 37°C), with occasional pipetting to dissociate tissue. Following tissue digestion, the granulomas remained intact and suspended within the Collagenase solution. The granulomas were then removed from suspension, imaged microscopically to confirm that they were granulomas (due to Cy5 fluorescence, drug content, cellularity, and fibrous superstructure). The remaining suspension was then filtered through a 100 µm cell strainer (Fisher Scientific, Waltham, MA) and centrifuged (200 x g, 5 min). The supernatant was discarded, and the remaining granuloma macrophages were resuspended in DMEM-low glucose (15 mL) with 15 mM HEPES, and centrifuged (200 x g, 5 min). This was repeated for two additional washes. After the final wash, macrophages were suspended in DMEM:F/12 (1:1) (Life Technologies) with 10% FBS and penicillin/streptomycin, were counted, and plated onto 12-well collagen-coated tissue culture

plates and allowed to attach overnight (37°C). The next day, cells were washed with DMEM:F/12 and immunofluorescent staining of F4/80 was performed to identify macrophages [32] from other cell types.

Sample Preparation for Microscopy. Cryosectioning was carried out using a Leica 3050S Cryostat (Leica Biosystems Inc., Buffalo Grove, IL). Samples were sectioned to 5 µm. In preparation for cryosectioning, portions of the liver were removed, immediately submerged in OCT (Tissue-Tek catalog no. 4583; Sakura), and frozen (-80°C), or stored in 10% formalin and sent off for staining at the University of Michigan In-Vivo Animal Core for H&E, Picro-Sirius red, and Ki67 staining.

Cell Staining. Following isolation and plating, Kupffer, granuloma macrophages and liver sections were stained for TFEB (Bethyl Laboratories, Montgomery, TX) LAMP1 (ThermoFisher Scientific, Waltham, MA), and LC3 (Sigma-Aldrich, St. Louis, MO) at dilutions of 1:5000, 1:500, and 1:200, respectively, following manufacturers immunofluorescence histochemistry protocols. Immunohistochemistry of F4/80 (Abcam, Cambridge, UK) was performed at a 1:500 dilution. The secondary antibody was Alexa-Fluor 488 (1:500 dilution) (Abcam, Cambridge, UK). Immunohistochemistry of TUNEL (R&D Systems, Minneapolis, MN) was performed using manufacturer's protocol for tissue cryosections. After staining, cells or tissues were imaged using a Nikon Eclipse Ti inverted microscope (Nikon Instruments, Melville, NY) and Nikon DS-U3 camera (Nikon Instruments) and Photometrics CoolSnap MYO camera system (Photometrics, Tucson, AZ), under control of Nikon NIS-Elements AR Software (Nikon Instruments). Illumination for fluorescence imaging is generated using the X-Cite 120Q Widefield Fluorescence Microscope Excitation Light Source (Excelitas Technology, Waltham, MA).

TUNEL Quantification. Following staining, liver cryosections were analyzed using a previously described fluorescence imaging set-up [33]. Using the nuclear (DAPI) signal to generate a mask in ImageJ [34] the mean fluorescence intensity of each nucleus was measured, and any nucleus that showed a mean fluorescence intensity above background fluorescence as determined using a negative control was classified as TUNEL (+). Granulomatous regions were

identified and analyzed separately because of of increased cellular granularity and nuclear content.

Quantification of TFEB Activation. After staining, coverslips containing cell samples were mounted onto glass slides and imaged using the previously described imaging system [33]. To determine the ratio of nuclear to cytoplasmic TFEB staining, images masks were generated using the DAPI staining for the nucleus and a brightness adjusted TFEB staining to capture the entirety of the cytoplasm. The cytoplasmic fluorescence intensity was corrected by removing the fluorescence of the nucleus, and the ratio of total fluorescence signal between the nucleus and cytoplasm was then determined. Cells were classified as either xenobiotic sequestering or not on the basis of mean Cy5 fluorescence intensity using K-Means clustering, with clusters set to two using IBM SPSS Statistics version 24.0 (IBM Software, Armonk, New York).

LC3 Quantification. After staining, coverslips containing cells were mounted onto glass slides and imaged using the previously described imaging system [33]. Cell area was measured by generating a region of interest (ROI) comprising the entirety of the cell. LC (+) inclusions were counted manually within the cell, and reported as LC3 (+) inclusions/cell area. Because the sample preparation resulted in dissolution of drug inclusions from within the cell, cells were classified as xenobiotic sequestering based on the presence of a drug cavity that the insoluble drug aggregates previously occupied.

LAMP1 Quantification. After staining, coverslips containing cells were mounted onto glass slides and imaged using the previously described imaging system [33]. Cellular masks were generated using a brightness adjusted LAMP1 fluorescence image, and classified as xenobiotic sequestering based on the presence of the cavity previously occupied by the insoluble drug precipitates that accumulated within the cell. Mean LAMP1 fluorescence intensity per cell was reported.

Ki67 Quantification. Sections stained for Ki67 were imaged using the brightfield imaging setup previously described [33]. For the CFZ-treated livers, granulomatous and non-granulomatous areas were determined based on the extent of cellular granularity, and analyzed separately. The

number of Ki67 nuclei was counted manually, and is reported as Ki67 (+) nuclei per tissue area following imaging across the tissue section at 10x magnification.

TLR Staining Quantification. Using the imaging method described by Lin et al [35], the intensity of DAB staining in granulomatous and non-granulomatous areas was compared using a previously described brightfield microscopy set-up [33]. To quantify DAB stained images, a red filter (655 ± 30 nm), corresponding to the absorbance of the background tissue staining, and a blue filter (480 ± 30 nm), corresponding to the absorbance peak of DAB, were used. The density of DAB staining indicates TLR staining intensity. The DAB staining density was quantified using ImageJ, and is reported as % Tissue Area TLR2 (+).

Analysis of Drug Distribution. Three livers from mice treated for 0, 2, 4, and 8 weeks were sectioned, and one section per liver was stained for F4/80 (Alexa 488; FITC channel). Ten (10x) magnification images were taken per section to capture the entirety of the liver section. The total F4/80 staining intensity captured by the FITC channel and the protonated, drug fluorescence intensity captured by the Cy5 channel was determined for each image. In sections with granulomas, the granuloma region was outlined based on the high-density pattern of nuclear granularity, and the total fluorescence intensities within the granuloma were measured in the various fluorescence channels. The relative percentage of signal intensity from the granulomas over the ten images was measured, and the percentage of total measured F4/80 and protonated drug fluorescence contributed from the granuloma was determined. Results are reported as the mean \pm S.D of each of the three sections analyzed.

Transmission Electron Microscopy. Organs were submerged in fixative and cut into small (<1 mm) pieces. The organs were preserved in a glass vial with fixative and stored at 4°C. After three rinses with Sorensen's buffer (0.1 M), tissues were stained with 1% osmium tetroxide in Sorensen's buffer and washed three times in Sorensen's buffer. Dehydration was carried out with a graded ethanol-water series (50, 70, and 90% and two changes of 100%) for 15 min each. After washing with three changes of propylene oxide, the tissues were treated with Epon resin (Electron Microscopy Sciences) and polymerized at 60°C for 24 hours. The blocks were then sectioned to 70 nm using an ultramicrotome and mounted on a copper EM grid (Electron

Microscopy Sciences), which was then stained with uranyl acetate and lead citrate before imaging. Samples were imaged and analyzed at the National Center for Microscopy and Imaging Research (NCMIR) at the University of California, San Diego.

Synthesis and Testing of CFZ Derivatives. A small library of R-iminophenazine analogs of CFZ was synthesized, as previously described [36]. For *in vivo* experiments, animal care was provided by the University of Michigan's Unit for Laboratory Animal Medicine (ULAM), and the experimental protocol was approved by the Committee on Use and Care of Animals (Protocol PRO00005542). Mice (4 week old, male C57Bl6) were purchased from the Jackson Laboratory (Bar Harbor, ME) and acclimatized for 1 week in a specific-pathogen-free animal facility. The compound was dissolved in sesame oil (Shirakiku, Japan) to achieve a concentration of 3 mg/ml, which was mixed with Powdered Lab Diet 5001 (PMI International, Inc., St. Louis, MO) to produce a 0.03% drug to powdered feed mix, and orally administered ad libitum for 4 weeks. Following feeding, mice were euthanized via carbon dioxide asphyxiation and exsanguination.

Macrophage Depletion Experiments. To deplete tissue macrophages, mice (n=3-4 per treatment group) were treated with liposomes containing either 7 mg/mL of clodronate or phosphate-buffered saline (PBS) (FormuMax Scientific Inc., Sunnyvale, CA). Liposomes were injected intraperitoneally, as previously described [37]. Mice were initially treated with 200 μ L of liposomes followed by 100 μ L injections twice per week to ensure continual macrophage depletion. Mice were fed CFZ (CFZ) or vehicle diet (untreated) continuously for a four week period. Following two weeks of feeding, liposome administration began for two weeks. The body temperature and weight of each mouse was measured daily, prior to injections. After completing four weeks of feeding and two weeks of liposome treatment, mice were euthanized and tissues were collected. For histological analysis, formalin fixed tissue sections from the clodronate depletion experiments were stained for H&E and analyzed by a pathologist blinded to the experimental conditions at the University of Michigan In-Vitro Animal Core and scored for signs of inflammation and necrosis on a scale of 1-4.

Biochemical Analysis of CFZ in Tissues. Following treatment with CFZ for four weeks, mice were euthanized via CO₂ asphyxiation, and organs removed and weighed. Tissue (20-30 mg) was homogenized in 500 µL of radioimmunoprecipitation assay buffer (Sigma) with added protease inhibitors (Halt protease and phosphatase inhibitor cocktail and 0.5 M EDTA; Thermo Pierce, Rockford, IL), and CFZ was extracted from tissue homogenate (350 µL) with three passes of 1 mL of xylenes. The drug was then extracted from the xylene with three 1 mL passes of 9M sulfuric acid. The recovery yield was determined by spiking samples with a known concentration of CFZ. The concentration of CFZ or phenazine derivative present in the tissue was then determined using the plate reader assay (Biotek Synergy 2, Winooksi, VT) at wavelength 450 nm, and background corrected at wavelength 750 nm, with the aid of a standard curve made with solutions of known concentration.

Biochemical Analysis of Plasma Drug Concentrations. Blood was collected and centrifuged (7,000 × g, 5 min). The resulting serum was extracted with acetonitrile (90% extraction efficiency) for 10 min at 4°C with vortexing. After centrifugation (14,000 x g, 4°C, 10 min), the supernatant was injected into a Waters Acquity UPLC H-Class (Waters, Milford, MA) equipped with an Acquity UPLC BEH C18 column (1.7 µm, 2.1 mm [inner diameter] by 100 mm; Waters, Milford, MA). Mobile phase A was 5 mM ammonium acetate, adjusted to pH 9.9 with ammonium hydroxide, and mobile phase B was acetonitrile. The flow rate was 0.35 ml/min, with a linear gradient from 50 to 100% phase B over 1.5 min, followed by holding at 100% for 1.5 min, a return to 50% phase B, and then re-equilibration for 2.5 min. Standards were prepared by spiking untreated plasma samples with known amounts of CFZ, ranging from 0 to 15 µM. Peak area was determined using Empower 3 Software (Waters, Milford, MA).

Cytokine Measurements. Following euthanasia, sections of liver or isolated granuloma were snap frozen and stored at -80°C. Tissue (20-30 mg) or whole granuloma was homogenized in 500 µL of radioimmunoprecipitation assay buffer (Sigma) with added protease inhibitors (Halt protease and phosphatase inhibitor cocktail and 0.5 M EDTA; Thermo Pierce, Rockford, IL). Protein concentration was determined using BCA assay (ThermoScientific), and samples were loaded using equivalent protein. The supernatants were assayed for IL-1RA by enzyme-linked immunosorbent assay (ELISA; Duoset; R&D Systems, Minneapolis, MN) in triplicate wells

according to the manufacturer's instructions. The cytokine concentrations were expressed nanograms per milligram of protein.

Statistical Analysis. All data are expressed as means \pm the standard deviations (SD). For multiple comparisons, statistical analyses were performed with one-way analysis of variance (ANOVA) and Tukey's post hoc comparisons. All statistical analyses were performed using IBM SPSS Statistics version 24.0 (IBM Software, Armonk, New York). P values less than 0.05 were considered statistically significant.

8.4 Results

8.4.1 Prolonged oral CFZ administration induces extensive liver remodeling

First, we established the time course of granuloma formation in CFZ fed mice. Following short term treatment (<4 weeks), no granulomas or other signs of inflammation were observed in the livers (Figure 1a, 2 wk CFZ). However, as treatment progressed, drug aggregates began to form paralleling granuloma formation, with visible signs of local inflammation (Figure 1a, 8 wk CFZ). The granulomas were primarily localized to areas near the portal vein, and were mainly comprised of immune cells, primarily macrophages (Figure 1a, Inset), surrounded by extensive collagen infiltration and fibrosis. Biochemical analysis of total drug concentration in granulomas revealed the extent of accumulation was comparable to that measured in the whole organ homogenates (30.3 ± 5.4 mg CFZ/ mg protein vs. 42.9 ± 23.0 mg CFZ/ mg protein, respectively; $n=3$ whole organ homogenates or isolated granulomas, $p=0.36$).

Previously, CFZ was used as a probe of the mechanisms driving weak base protonation and precipitation inside cells [24, 26, 27]. CFZ undergoes a fluorescence shift as it forms an insoluble hydrochloride salt inside cells, emitting a distinct signal in the far-red, fluorescence wavelength [38]. In protonated form, it self-assembles into ordered aggregates (Crystal-Like Drug Inclusions, or “CLDIs”), which are also detectable based on their pronounced dichroism properties when illuminated with linearly polarized light [33]. This ability to microscopically monitor the distinct protonation and ordered states of the drug prompted us to ask whether CFZ differentially accumulated in granuloma-associated macrophages versus resting Kupffer cells, and whether the sequestration of the drug in granulomas had any relevance to the health status of

the liver. Remarkably, the preferential accumulation of the protonated form of the drug in granulomas was readily apparent, evidenced by the red shifted fluorescence of the protonated form of the drug which can be observed through the standard Cy5 filter set of the epifluorescence microscope (640 nm excitation/670 nm emission) [38] (Figure 1b).

Within these granulomas, the dramatically greater expression of markers of cellular proliferation and cell death provides evidence of extensive tissue remodeling (Figure 1c). Quantitative analysis revealed a significant increase in Ki67 (+) nuclei per tissue area within the granuloma when compared to the rest of the liver and the livers in untreated animals, with no difference observed between untreated and non-granulomatous regions ($p < 0.01$, ANOVA, Tukey's HSD; Figure SI. 18). Additionally, within the granulomas, there was a significant increase in the percentage of apoptotic cells per tissue area when compared to both non-granulomatous tissue and untreated tissue, as detected by the TUNEL assay ($p < 0.01$, ANOVA, Tukey's HSD; Figure SI. 19). As expected from their role in immune surveillance, granulomas exhibited greater TLR9 staining as compared to both untreated livers and non-granulomatous regions (Figure 1e; Figure SI. 20).

Proceeding to quantify the distribution of protonated drug in relation to granuloma-associated macrophages and non-aggregated resting state Kupffer cells, tissue cryosections from three different animals fed 0, 2, 4, and 8 weeks were stained for the macrophage marker F4/80, and the percentage of F4/80 and Cy5 signal within non-granulomatous and granulomatous regions of the liver was determined from microscopic images. In both the untreated and 2 week CFZ fed animals, there was no indication of granuloma formation, and minimal signs of drug accumulation (Figure 2a,b), resulting in 100% of both the Cy5 and F4/80 signal being localized to non-granulomatous regions of the organ (Figure 2e). After 4 weeks of treatment, protonated drug (Cy5 signal) began to co-localize with F4/80 positive cells (Figure 2c). With increased drug loading, granulomas began to form and trap a greater fraction of the protonated drug (Figure 2c, yellow arrows) in relation to the fraction trapped by the Kupffer cells (Figure 2c, white arrow). At this stage, 10% of the total F4/80 signal within the liver was localized within the granuloma regions, accounting for nearly 10% of the total Cy5 signal (Figure 2e). As drug loading further increased between four to eight weeks of treatment, there was a significant increase in protonated drug (Cy5 signal) ($p < 0.01$, ANOVA, Tukey's HSD) and macrophages ($p < 0.001$, ANOVA, Tukey's HSD) within the granuloma. Since the far-red fluorescence is specific to the protonated,

hydrochloride form of CFZ [39], granuloma-associated macrophages preferentially sequestered the protonated form of the drug, while the unprotonated form of the drug is distributed mostly in non-aggregated resting state Kupffer cells and hepatocytes.

8.4.2 Macrophages incorporated within granulomas exhibit elevated phagolysosomal activity

Next, we determined how aggregation of macrophages as granulomas resulted in a differing macrophage phenotype from resting Kupffer cells. Due to the fact that CFZ becomes protonated in lysosomes, its lysosomal accumulation may result in activation of the transcription factor TFEB, which controls lysosomal biogenesis and is the master regulator of lysosomal proton pump (V-ATPase) expression [40]. Kupffer cells were isolated from the livers of untreated animals, and granulomas and granuloma-associated macrophages were isolated from the livers of 8-week CFZ treated animals, plated, and stained for TFEB, as well as LAMP1 and LC3, markers for lysosomes [41] and autophagic flux [42], respectively (Figure 3a). Significantly greater TFEB activation occurred within the Cy5-positive, granuloma-associated macrophage population, as compared to the Cy5-negative macrophage population, both obtained from the same drug treated animals (n=30 cells per group) ($p < 0.05$, ANOVA, Tukey's HSD) (Figure 3b). However, the level of TFEB activation did not significantly differ from the general population of Kupffer cells obtained from untreated animals. Nevertheless, granuloma-associated (Cy5-positive) macrophages also were significantly larger in size as compared to the general population of (Cy5-negative) drug-treated macrophages, and as compared to resting state Kupffer cells from untreated mice ($p < 0.05$, ANOVA, Tukey's HSD) (Figure 3c). Similarly, granuloma-associated macrophages also showed increased lysosomal-associated membrane protein (LAMP1) (n=25-30 cells per group) ($p < 0.05$, ANOVA, Tukey's HSD) (Figure 3d) as well as an increase in LC3 (+) inclusions which is a marker of autophagy ($p < 0.05$, ANOVA, Tukey's HSD) (n=30 cells per group) (Figure 3e).

8.4.3 Accumulation of insoluble hydrochloride salt precipitates induced granuloma formation

To determine if granuloma formation was a general property of phenazine compounds, or specifically induced by the propensity of CFZ to precipitate out in the lysosomal

microenvironment, we tested Compound 568 (Figure 4a-d), a previously characterized derivative of CFZ that is less prone to precipitate in lysosomal pH and chloride concentrations [43]. Compound 568 has the same phenazine backbone as the CFZ molecule (Figure 4a), but it has an ethyl alcohol group instead of the isopropyl group of CFZ (Figure 4e). This compound has been previously studied side-by-side with CFZ, in terms of solubility [36], intracellular accumulation [36], hydrochloride salt formation [43], and skin pigmentation [43]. Through the small alterations in chemical structure, the solubility of the derivative in the presence of serum proteins is also greatly increased relative to CFZ [36]. Thus, following oral treatment of mice with Compound 568, the livers were analyzed (Figure 4b-d) and compared to those of their CFZ-treated counterparts (Figure 4f-h).

Remarkably, within the livers of mice treated with Compound 568, no granuloma formation was detected (Figure 4c). In the corresponding, CFZ-treated mice, granulomas were found throughout the organ, replete with CLDIs (Figure 4f, g, h). Rather than accumulating as insoluble aggregates, the fluorescence from Compound 568 was mostly localized within the bile canaliculi of the liver (Figure 4d). This indicated that the hepatocytes are able to actively eliminate Compound 568 from the organism by hepatobiliary clearance. Consistent with the reduced liver accumulation and increased hepatobiliary clearance, the measured liver concentrations of Compound 568 were 10-fold lower as compared to those of CFZ (0.27 ± 0.05 mg/g tissue vs. 2 mg/g tissue [43]). Mice treated with compound 568 also had 10-fold lower serum concentrations (0.77 ± 0.12 μ M), compared those treated with CFZ [26].

8.4.4 Drug sequestration in granulomas reduces toxic effects of CFZ

To obtain additional insights into the organization of granulomas, livers of CFZ treated mice were subjected to electron microscopy (Figure 5, Supplemental Figure 4). Upon close examination (Figure SI. 21, GM) the membrane-bound, CLDIs can be observed (Supplemental Figure 4a, CLDI). In a region proximal to the macrophage described in supplemental figure 4, a neutrophil (Supplemental Figure 4, N) is present. While these cells are among the so-called “professional phagocytes” within the body, no CLDIs are observed in this particular cell, and tend to be found within tissue macrophages, lending credence to the hypothesis that CLDI stabilization is a macrophage-specific phenomenon. The collagen fibers (Figure SI. 21, CF) that make up the extracellular space of the granuloma are also visible, wrapping around the cell. One

striking feature of the granuloma-associated macrophages was that there are numerous, dark deformed inclusions throughout the cytoplasm that resemble damaged or depolarized mitochondria (Figure SI. 21, M). Previously, CFZ has been shown to directly damage mitochondria via depolarization of the mitochondrial membrane, resulting in the accumulation of similar structures throughout the cytoplasm [27, 44].

Nevertheless, hepatocytes surrounded the granulomas, and the differences between the two cell types were quite striking. In the region between a small granuloma and the surrounding non-granulomatous region of the liver (Figure 5), it was evident that hepatocytes (HC) possessed intact mitochondria with no signs of drug induced alterations (Figure 5a). The border region between the granuloma and surrounding hepatocytes highlighted the differences between the two cell types (Figure 5b), with granuloma-associated macrophages containing numerous damaged mitochondria (Figure 5b, M). The region in between the granuloma and hepatocyte was also comprised of numerous membrane-bound extracellular vesicles (Figure 5b, V), typical of hepatocyte-monocyte and hepatocyte-hepatocyte communication within the liver.

Proceeding to probe the role of granulomas in relation to drug accumulation and associated toxicity, we chemically depleted the liver macrophages of mice following two weeks of treatment with CFZ, and continuously depleted the macrophages for an additional two weeks of CFZ treatment. The clodronate liposome-injected, CFZ-treated mice weighed an average of nearly 5 grams less than the other treatment groups ($p < 0.001$, ANOVA, Tukey's HSD) (Figure 6a) and had a significantly lower body temperature (Figure 6b) ($p < 0.05$, ANOVA, Tukey's HSD) (Table 1) during the last week of liposome treatment. On the final day of the experiment, the clodronate liposome-injected, CFZ-treated mice also weighed significantly less (Figure 6c) and had a significantly reduced body temperature (Figure 6d) ($p < 0.001$, ANOVA, Tukey's HSD) compared to all other treatment groups, with no significant difference in body mass or body temperature among the other experimental groups ($p > 0.05$, ANOVA, Tukey's HSD). Taken together, this points to a deleterious and synergistic combination of macrophage reduction and drug therapy, resulting in systemic toxicity [45]. Upon gross examination, (Figure 6e) the livers of the PBS liposome-injected, untreated mice showed little external signs of inflammation, and appeared normal. Similarly, the livers of PBS liposome-injected, CFZ-treated mice displayed the characteristic deep red pigmentation typical of CFZ accumulation [26] with no outward signs of tissue damage. In the livers of clodronate liposome-injected, untreated mice there were some

minor sites of necrosis and inflammation noted on the liver due to clodronate treatment, but overall, did not appear significantly affected. In contrast to this, the livers from the clodronate liposome-injected, CFZ-treated did not exhibit signs of extensive protonated CFZ accumulation, and showed signs of pronounced inflammation and tissue necrosis (Figure 6e). There were minor increases in inflammation within the PBS liposome-CFZ treatment group detected upon H&E staining, localized to the site of granulomas, while the clodronate liposome-CFZ treatment groups showed signs of tissue necrosis and increased inflammation, primarily localized to areas surrounding the central vein (Figure 6f), which is typically surrounded by perivascular granulomas.

Macrophage depletion by clodronate in the liver was quantified using F4/80 staining, revealing a mean (\pm S.D.) 42 (\pm 15)% reduction in macrophages in livers of CFZ-treated mice, as compared to the PBS liposome-injected, CFZ-treated mice ($p < 0.05$, ANOVA, Tukey's HSD) (Figure SI. 24). This reduction in macrophages was accompanied by a mean (\pm S.D.) reduction of 32 (\pm 6) % in the amount of protonated drug (Cy5 signal) compared to that of the PBS liposome injected animals of the CFZ-treated group ($p < 0.05$, ANOVA, Tukey's HSD; Figure SI. 25). Due to the reduction in macrophages, less CFZ is able to become trapped within macrophages and granulomas in its relatively more tolerated protonated form, resulting in increased exposure to the cytotoxic soluble form of CFZ, harming the liver and leading to systemic drug-induced toxicity.

In addition to the 30% reduction in granuloma size relative to the PBS liposome-injected counterparts ($p < 0.05$, Student's unpaired two-tailed t-test) the cellular turnover within clodronate liposome-injected granulomas was also significantly reduced. The frequency of apoptotic cells in the granulomas of the liposomal clodronate treated animals was also reduced ($p < 0.05$, ANOVA, Tukey's HSD; Figure 6g; Figure SI. 22). However, some of the cells surrounding the granulomas displayed increased frequency of apoptotic cells, which may correspond to regions of acute necrosis observed in the H&E staining (Figure 6f). Indicating that the reduced size and drug sequestering capacity associated with clodronate treatment also led to a less differentiated granuloma phenotype, the reduction in apoptosis in the clodronate-treated granulomas was paralleled by a reduction in the number of cells undergoing DNA synthesis (detected through Ki67 staining) as compared to control, PBS liposome-injected animals. The PBS-liposome injected mice that were also CFZ-treated showed significantly higher Ki67 (+) nuclei/tissue area

compared to all other non-granulomatous regions ($p < 0.001$, ANOVA, Tukey's HSD; Figure 6h, Figure SI. 23). While the granulomas of the clodronate liposome-injected, CFZ-treated mice also showed elevated Ki67 nuclei/tissue area compared to all other non-granulomatous regions, there was reduced Ki67 staining when compared to the granulomas of the PBS liposome injected, CFZ-treated mice. These results are consistent with a greater rate of cellular turnover over in drug sequestering, "functional" granulomas, as compared to the smaller granulomas of the clodronate-treated livers.

Lastly, we determined how clodronate liposomes influenced the levels of the anti-inflammatory cytokine IL-1RA [24], which was found to be upregulated following a prolonged (8 week) treatment with CFZ. Consistent with the previously reported study, the livers of the PBS liposome-injected, CFZ-treated mice showed significantly elevated levels of IL-1RA (Figure 7b; $p < 0.05$, ANOVA, Tukey's HSD). However, in the clodronate liposome-injected, CFZ-treated group, IL-1RA levels were similar to that of the untreated control groups ($p > 0.05$, ANOVA, Tukey's HSD). To further determine if the granuloma macrophages themselves were responsible for the increased IL-1RA production in CFZ-treated mice, granulomas were isolated from 8 week-CFZ fed livers and compared with whole-tissue homogenates of 8-week CFZ fed livers. The levels of IL-1RA production between the granulomas and whole-organ homogenates were both significantly higher as compared to the livers of control, untreated mice ($p < 0.05$, ANOVA, Tukey's HSD) (Figure 7c), although within treated mice, the levels of IL-1RA present in whole-organ tissue homogenates were not significantly different from that present in the granulomas ($p = 0.963$, ANOVA, Tukey's HSD).

8.5 Discussion

Many adverse drug reactions (ADRs) are associated with hepatotoxicity [46], which is generally thought to be related to the degradation or metabolic activation of drug molecules into reactive intermediates. For example, acetaminophen overdose depletes glucuronide, leading to a secondary metabolism pathway which produces a hepatotoxic acetaminophen metabolite that causes liver damage [47]. Because the liver is the primary site of drug metabolism within the body, a multitude of drugs exert idiosyncratic, hepatotoxic side effects. We therefore postulated that drug-induced liver granulomas may be a toxicity mechanism, downstream of immune cell-

mediated inflammatory reactions that have the potential to interfere with liver structure and function.

Normally, liver granulomas are triggered by bacteria or other pathogens and they are typically thought of as sites of active infection [9]. This made us wonder about how drugs may trigger granuloma formation, and the relationship between drug-induced granulomas and hepatotoxicity. Using CFZ as a model drug, we discovered that granulomas specifically sequester large amounts of CFZ in a protonated, insoluble form that is membrane impermeant and is therefore more readily compartmentalized and isolated from the rest of the liver as compared to the unprotonated free base form of the drug [28]. Additional studies with a closely related phenazine derivative of CFZ that is less prone to precipitating out in the lysosomal pH and chloride microenvironment supports the active role of granulomas in weak base ion trapping and sequestration of insoluble hydrochloride salt form of drugs. Furthermore, chemical depletion of macrophages confirmed the ability of granuloma-associated macrophages to protonate CFZ and sequester it from hepatocytes, serving as a toxicity-reducing mechanism within the liver and systemically.

Interestingly, there are many other drugs on the market, such as methyldopa [48] and phenylbutazone [49], that are known to induce the formation of hepatic granulomas. Based on our observations with CFZ, we hypothesize that granulomas act as integrated, dynamic “super-structures” or “organoids” comprised of specialized macrophages which effectively respond to xenobiotics that form insoluble complexes within the liver. Granuloma-associated macrophages were distinctively different from the non-aggregated, resting state Kupffer cells of the liver, based on their expression of various phenotypic markers associated with an expanded endolysosomal compartment, as well as their high rates of apoptosis and expression of Ki67, and activation of lysosomal biogenesis pathways. Xenobiotic sequestering granuloma-associated macrophages are embedded in a collagenous matrix, effectively isolating the drug from the neighboring hepatocytes. Conversely, non-aggregated, resting state Kupffer cells are primarily surrounded by hepatocytes or endothelial cells, and are localized to the sinusoidal regions of the organ.

Of noteworthy significance, granuloma formation appeared as a highly specific response of macrophages to the formation of insoluble precipitates by the protonated form of CFZ in the presence of high chloride concentrations like that which occur in lysosomes. By slightly altering

the chemical structure of CFZ, the formation of granulomas was inhibited, leading to increased biliary excretion (Figure 4d), and therefore enhancing clearance and reducing net accumulation within the liver, as well as reducing overall exposure.

Macrophage depletion experiments provided additional evidence for the active role of granuloma-associated macrophages in CFZ sequestration and hepatoprotection. Treatment with liposomal clodronate on its own induced some signs of liver damage upon gross examination, and more apparent necrosis and inflammation was observed within the liposome-treated and drug-fed mouse group, resulting in necrosis in entire sections of liver lobes, originating at the periphery of the liver. Additionally, liposomal clodronate treatment, combined with drug therapy led to a reduction in body weight and temperature that was not observed in the clodronate-untreated group, eliminating the possibility that this necrosis was a clodronate-specific phenomenon, and may be a drug-induced toxicity phenomenon. Treatment of mice with liposomal clodronate reduced CFZ-induced granuloma size as well as the sequestration of the protonated, insoluble (membrane-impermeant) form of the drug. The larger granulomas within the PBS-CFZ treated livers also showed higher cellular turnover than the clodronate-CFZ livers (Supplemental Figure 6). This increased turnover and apoptosis within the functional granuloma further delineates the differences between the granuloma-associated macrophages and non-aggregated resting state Kupffer cells within the liver, which is reflected in the changes in the cellular and molecular architecture of the granulomas, clearly observed in the TEMs (Figure 5, Supplemental Figure 4). Lastly, treatment with liposomal clodronate completely inhibited IL-1RA production to levels of untreated animals, suggesting granulomas are actively producing large amounts of IL-1RA, which is a key anti-inflammatory mediator.

As a transcriptional regulatory mechanism mediating the observed phenotypic changes, TFEB activation emerged as a likely candidate (Figure 3b). TFEB activation can explain the expanded endolysosomal compartment of granuloma-associated macrophages, as compared to both drug-exposed and untreated resting state Kupffer cells. It can also explain the increased LAMP1 and LC-3 staining (Figure 3e). The activation of TFEB can promote lysosomal and membrane biogenesis, as well as increases expression of the lysosomal acidification mechanism, namely vacuolar-type proton ATP-ase [50, 51]. Of noteworthy significance, elevated TFEB activation within the xenobiotic sequestering granuloma-associated macrophages, but not within

the drug-treated non-aggregated Kupffer cells also implicates TFEB as a hepatoprotective, xenobiotic response pathway.

Of noteworthy significance, TFEB activation and its role in cell survival has been mostly studied as it relates to cancer cells, where it is negatively associated with the survival of the organism [52, 53]. TFEB's role in cancer cell survival may be related to the increase in lysosomal and autophagic activity within the cell. Many chemotherapeutics are weakly basic, amphiphilic lysosomotropic compounds such as doxorubicin, which has reduced efficacy in human cancer cells following TFEB activation and increased autophagy [54]. In a study performed using different hydrophobic, weakly basic anti-cancer agents, these drugs became trapped within lysosomes, and thus, induced TFEB activation. This led to increased lysosomal exocytosis as a cytoprotective mechanism to remove the drug from the cell, which may be a mechanism of chemoresistance to cancer drugs [55]. Similarly, the extent to which granuloma formation protects the liver from drug induced toxicity, our results point to a natural, protective role of TFEB activation in the protection of the organ and ultimately to the survival of the host.

8.6 Conclusions

To summarize, accompanying the massive bioaccumulation of weakly basic drug, the liver undergoes extensive remodeling through the development of large granulomas comprised of macrophages with distinctly different properties from neighboring non-aggregated macrophages. Granulomas were structurally and functionally distinct structures from the surrounding tissue, and effectively function as an organ within an organ – an “organoid”- helping to limit the exposure of soluble drug to hepatocytes, reducing hepatic damage. Granuloma-associated macrophages restricted the cytotoxic activity of the drug by sequestering the drug as membrane-impermeant insoluble aggregates, while shielding hepatocytes from the free base form of the drug by forming multiple layers of membranes and collagenous matrices around themselves. As a potential master regulator of xenobiotic sequestering macrophages of drug induced granulomas, TFEB activation can explain the expanded lysosomal compartment, membrane turnover and acidification mechanisms that are involved in stabilizing the insoluble, intracellular aggregates formed by the protonated, hydrochloride salt form of the drug. Confirming the protective role of hepatic granulomas, inhibition of granuloma formation reduced

hepatic IL-1RA production, and led to acute necrosis within the liver and systemic indications of drug-toxicity.

8.7 Acknowledgements

The authors thank Eric Bushong and Mark Ellisman for sample analysis with the electron microscopes at the National Center for Microscopy and Imaging Research, University of California San Diego. This work was supported by NIH grant R01GM078200 to GRR.

8.8 Figures

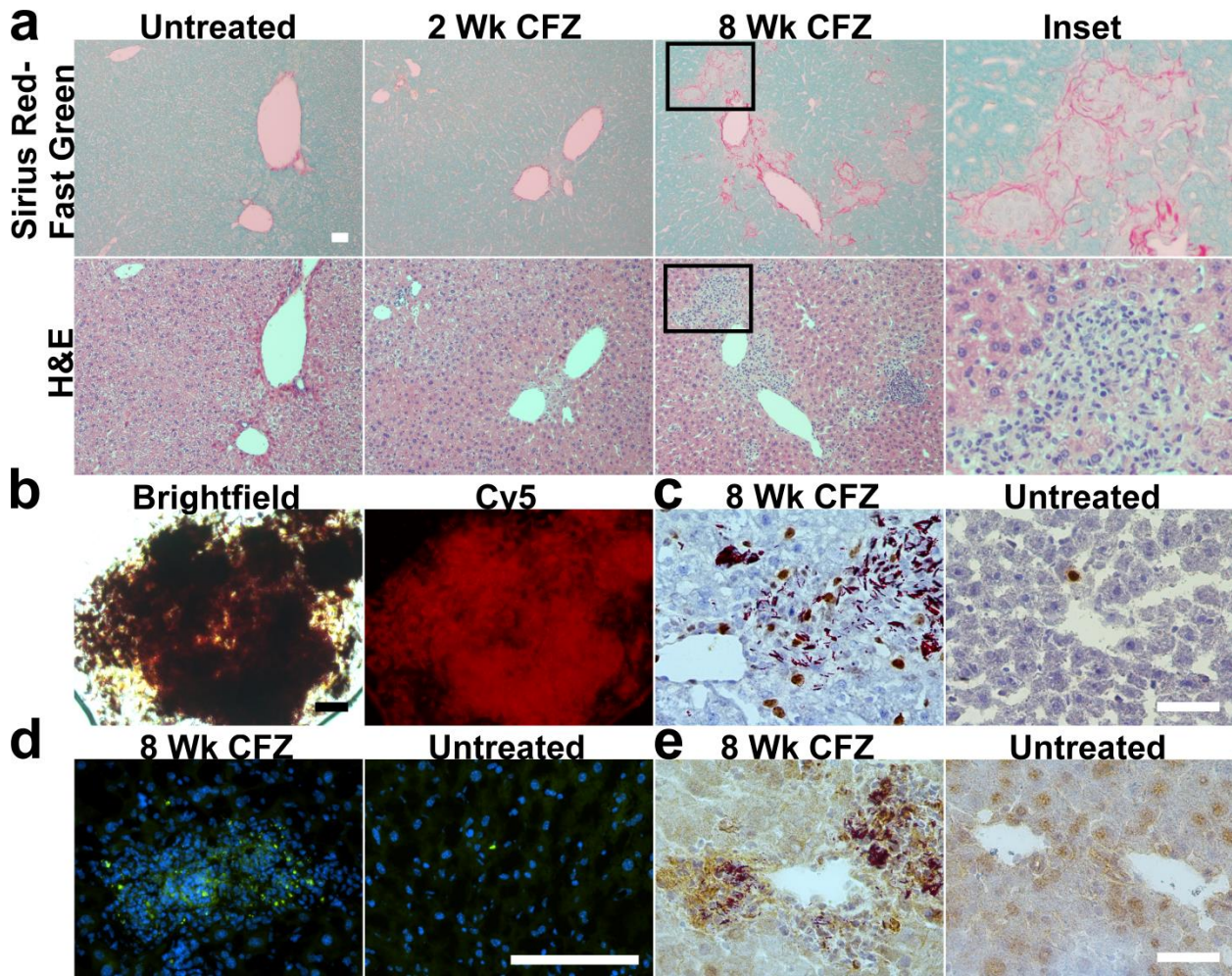


Figure 8-1 CFZ treatment remodels the liver through granuloma formation

A) Increased CFZ treatment results in formation of large granulomas throughout the organ comprised of immune cells. B) CLDIs accumulate extensively within the granuloma, and retain their intrinsic Cy5 fluorescence. C) Granulomatous areas of the liver exhibit higher Ki67 activation when compared to both non-granulomatous areas and untreated livers. D) Granulomatous areas of CFZ treated livers show elevated apoptotic nuclei detected via TUNEL assay when compared to both non-granulomatous areas and untreated livers. E) CLDI accumulation in granulomas results in elevated TLR2 expression within the granuloma, but not the surrounding tissue. Scale bar is 50 μm

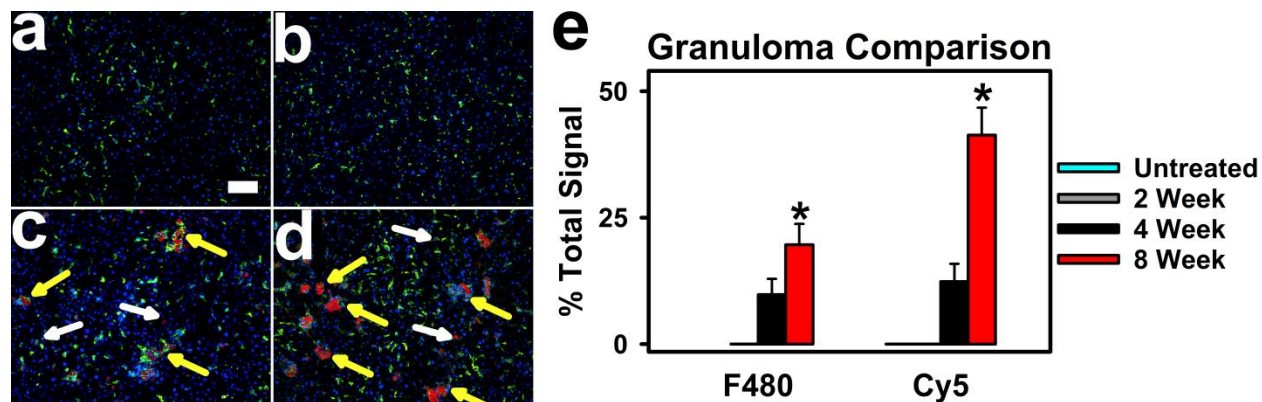


Figure 8-2 Increased drug loading results in macrophages becoming concentrated within granulomas, and increased drug accumulation mainly within the granuloma.

A-D) Untreated, 2, 4 and 8 week immunofluorescence images of liver cryosections stained for the macrophage marker F4/80 (green) and CLDI fluorescence (red). E) The total percentage of F4/80 or Cy5 fluorescence signal coming from the granuloma compared to the non-granulomatous tissue area was determined, revealing a significant increase from four to eight weeks of treatment. Yellow arrows point to granuloma macrophages loaded with CLDIs, while white arrows point to Kupffer cells with CLDIs. (n=3 animals per time point, 10 images per liver cryosections) (*=p<0.01, ANOVA, Tukey's HSD, #=p<0.001, ANOVA, Tukey's HSD).

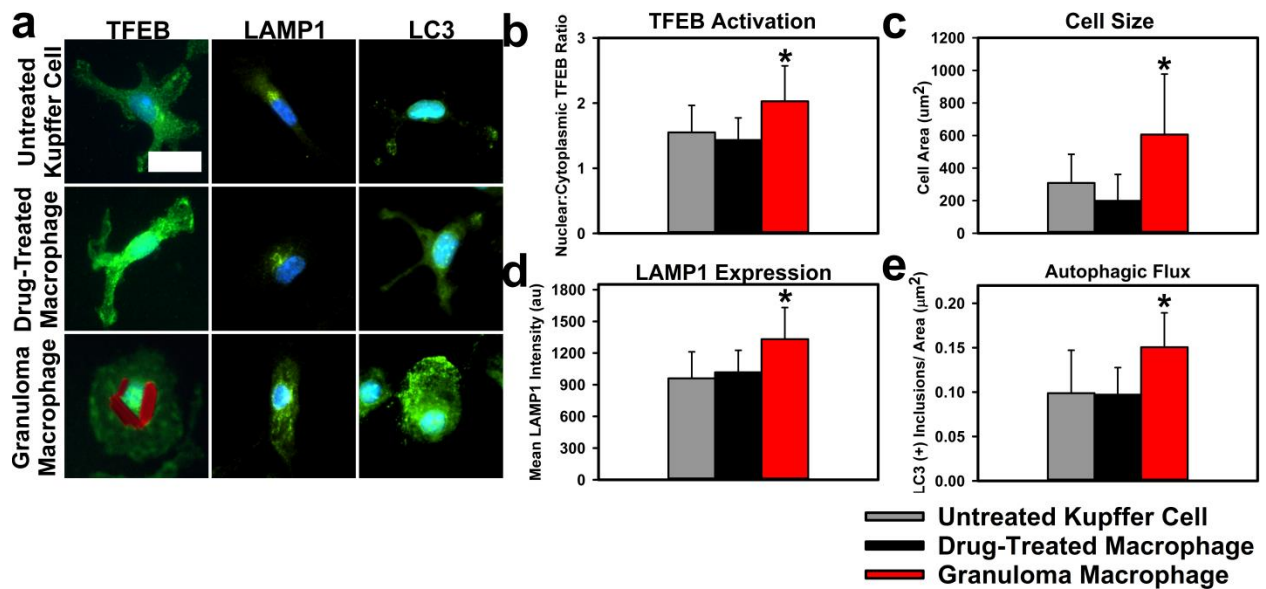


Figure 8-3 Granuloma macrophages are phenotypically different from both untreated and drug treated macrophages

A) Images showing untreated Kupffer cells, drug-treated macrophages and granuloma macrophages isolated from 8 week CFZ-treated liver stained for TFEB, LAMP1 and LC3. B) Granuloma macrophages show significantly elevated TFEB translocation to nucleus compared to untreated and drug-treated macrophages. C) Granuloma macrophages are significantly larger than their untreated and drug-treated macrophage counterparts. D) Granuloma macrophages show significantly elevated expression of LAMP1 within the cell, indicating increased lysosomal content within the cell. E) Granuloma macrophages show increased punctate LC3 staining within the cytoplasm of the cell compared to untreated and drug-treated macrophages, indicating increased autophagic flux within the cell, which may be necessary to form new membranes to trap the CLDI. Scale bar is 15 μm . (n=30-35 cells per group, *= $p < 0.05$, ANOVA, Tukey's HSD).

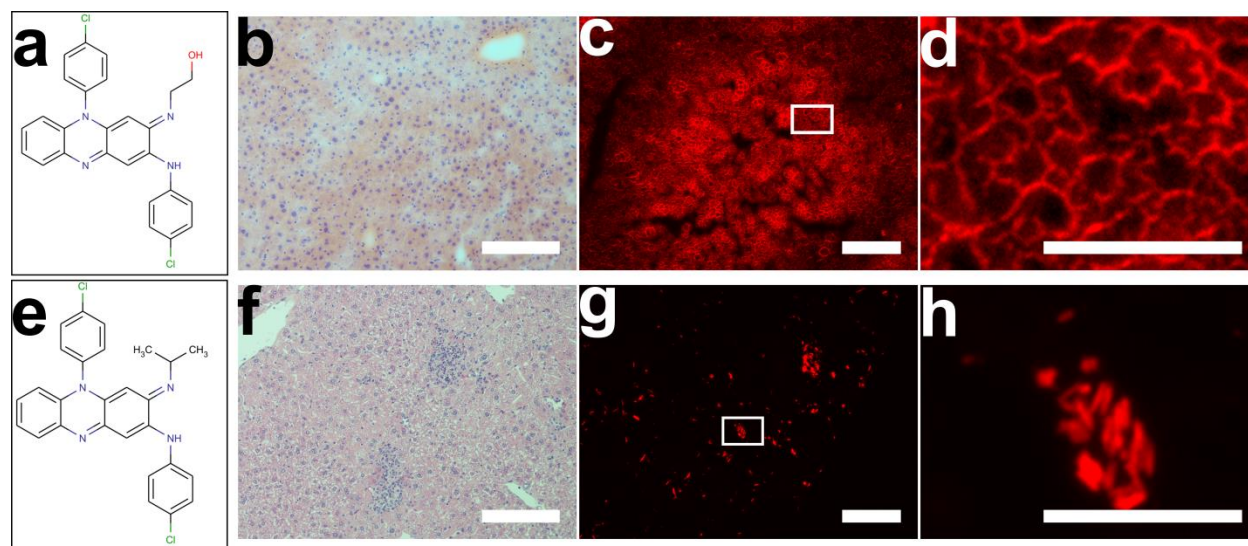


Figure 8-4: The accumulation of insoluble aggregates and granuloma formation is dependent on the isopropyl group in the CFZ molecule

A) The derivative 568 replaces the isopropyl group with an ethyl alcohol, limiting its ability to form insoluble aggregates within the liver and does not induce granulomas as is seen in CFZ. B) H&E staining of a liver from a mouse treated with 568 shows no signs of granuloma formation. Scale bar is 200 μm. C) The fluorescence of derivative 568 can be detected in the bile canaliculi of the liver, showing that the liver may be actively removing the chemical and eliminating it from the body. Scale bar is 200 μm. D) Zoomed in region of the bile canaliculi showing the fluorescence of derivative 568. Scale bar is 50 μm. E) Chemical structure of CFZ. F) H&E staining of CFZ treated liver shows extensive granuloma formation. G) CFZ treatment leads to insoluble aggregate and hydrochloride salt accumulation. H) Zoomed in region of CLDIs within the liver. Scale bar is 50 μm. Note: Brightness for derivative 568 fluorescence images have been elevated to show biliary localization of drug.

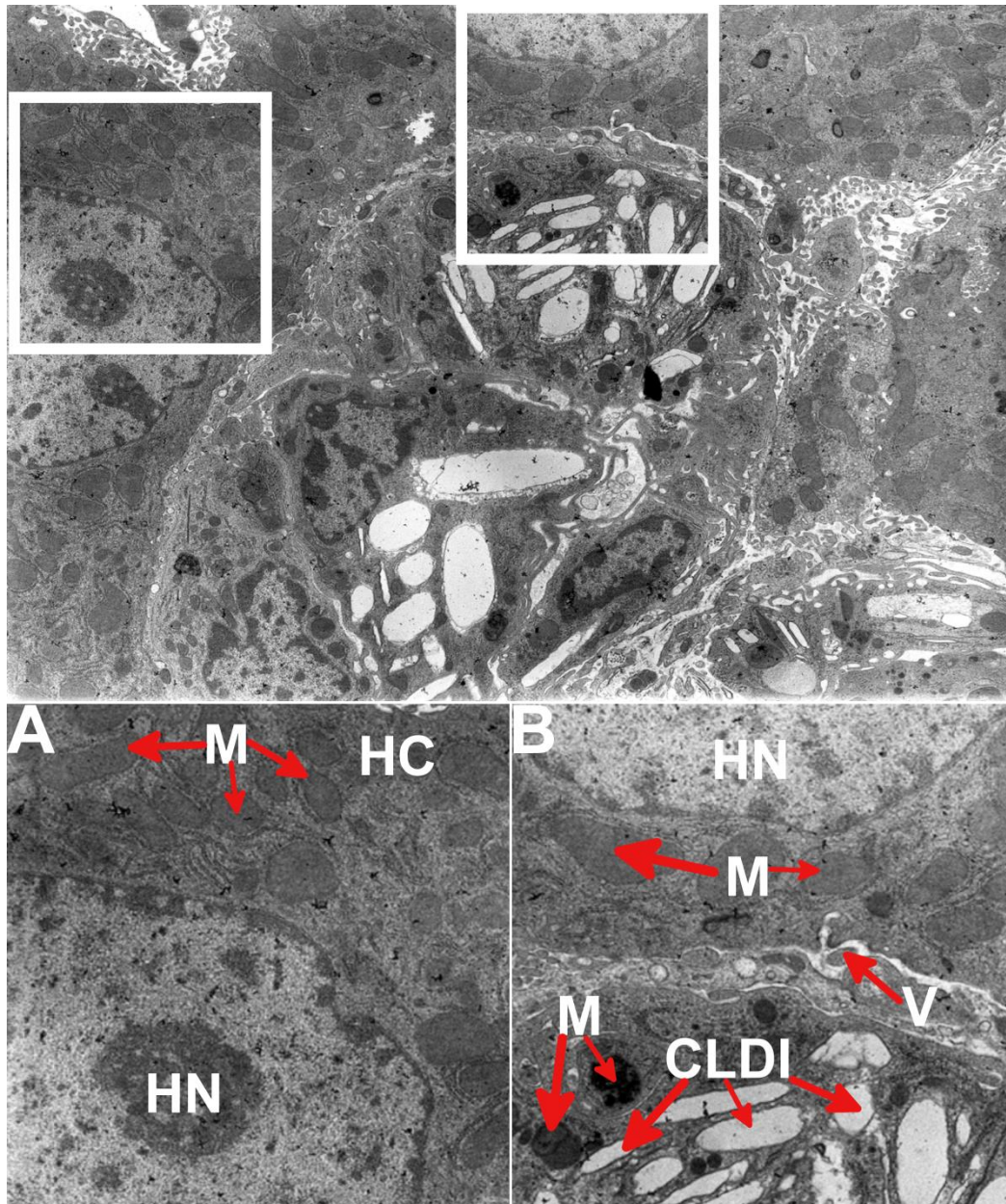


Figure 8-5 TEM of 8-week CFZ treated liver showing granuloma surrounded by hepatocytes

A) A healthy hepatocyte located on the periphery of the granuloma shows normal mitochondria unaffected by the drug. B) Border region between the granuloma and healthy liver tissue. The granuloma macrophage is loaded with CLDIs, and as a result, shows damaged mitochondria. In between the granuloma macrophage is region of cellular debris, which may limit exposure of toxic drug to the tissue. The neighboring hepatocyte shows healthy mitochondria. (M: Mitochondria, HN: Hepatocyte nucleus, HC: Hepatocyte, D: Debris, CLDI: Crystal-Like Drug Inclusion)

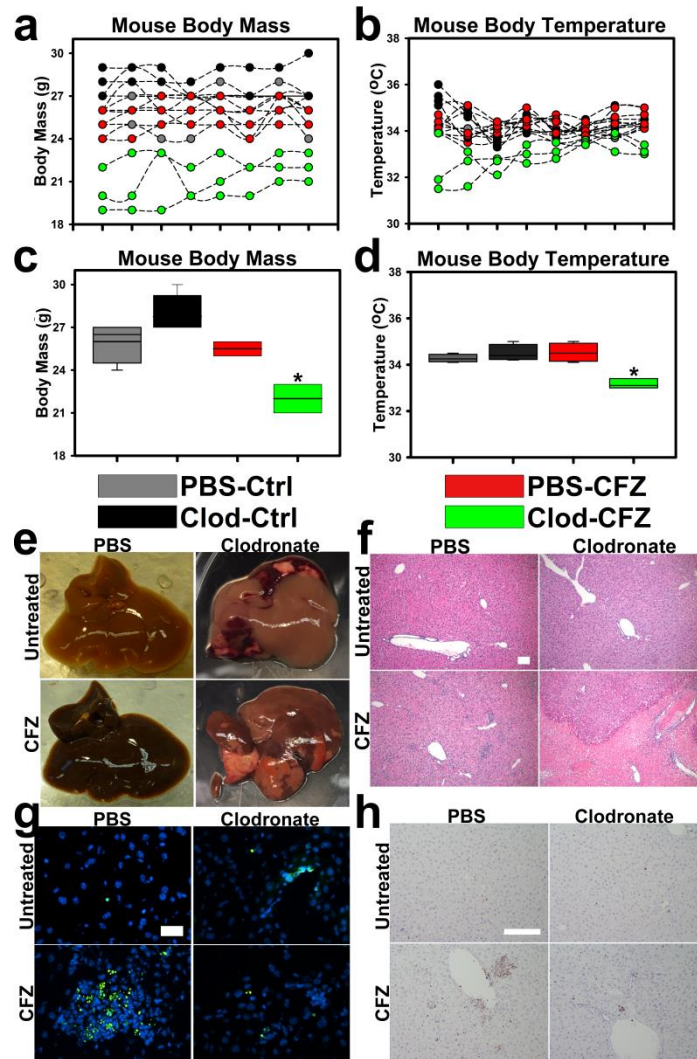


Figure 8-6 Chemical depletion of macrophages leads to signs of toxicity in animals fed CFZ. A, B) Daily mouse body mass and temperature taken during final week of liposome injection. C, D) Box plot of mouse body weight and temperature taken on final day of experiment. (*= $p < 0.001$, ANOVA, Tukey's HSD). E) Macroscopic images of livers removed from mice treated with PBS or clodronate liposomes, fed either a control or supplemented diet. The clodronate CFZ fed livers showed signs of necrosis upon gross examination. F) H&E staining of liver sections from macrophage-depleted and healthy animals. The clodronate-CFZ treated livers showed signs of necrosis radiating outward from the hepatic portal vein, while the PBS-CFZ treated mice only showed minor inflammation localized to the granulomatous areas. Scale bar is 100 μm . G) TUNEL staining of liver cryosections from clodronate experiments. Apoptosis in the PBS-CFZ treated groups was localized primarily to the granulomatous regions, while the necrotic, clodronate-CFZ livers showed reduced apoptosis within the granuloma and elevated apoptosis in small, localized regions of the liver, consistent with the previously observed necrosis. Scale bar is 25 μm . H) Immuno-histochemical staining for cellular replication marker Ki67 within liver sections. Granulomatous regions of PBS-CFZ treated livers showed significantly elevated cellular replication compared to the granulomas of the clodronate-CFZ treated livers. Scale bar is 200 μm .

Treatment	Average Body Mass (g) (n=3-4 mice per group)	Average Body Temperature (°C) (n=3-4 mice per group)
PBS + Control Diet	26.3 ± 1.4	34.2 ± 0.5
PBS + CFZ Diet	25.7 ± 0.8	34.3 ± 0.3
Clodronate + Control Diet	27.4 ± 1.1	34.4 ± 0.6
Clodronate + CFZ Diet	21.2 ± 1.4*	33.1 ± 0.9*

Table 8-1 Chemical depletion of macrophages and drug treatment leads to indications of failing health

Mice treated with clodronate and fed a CFZ-supplemented diet showed significantly reduced body weight and body temperature, two classic markers of drug toxicity. (*= $p < 0.05$, ANOVA, Tukey's HSD).

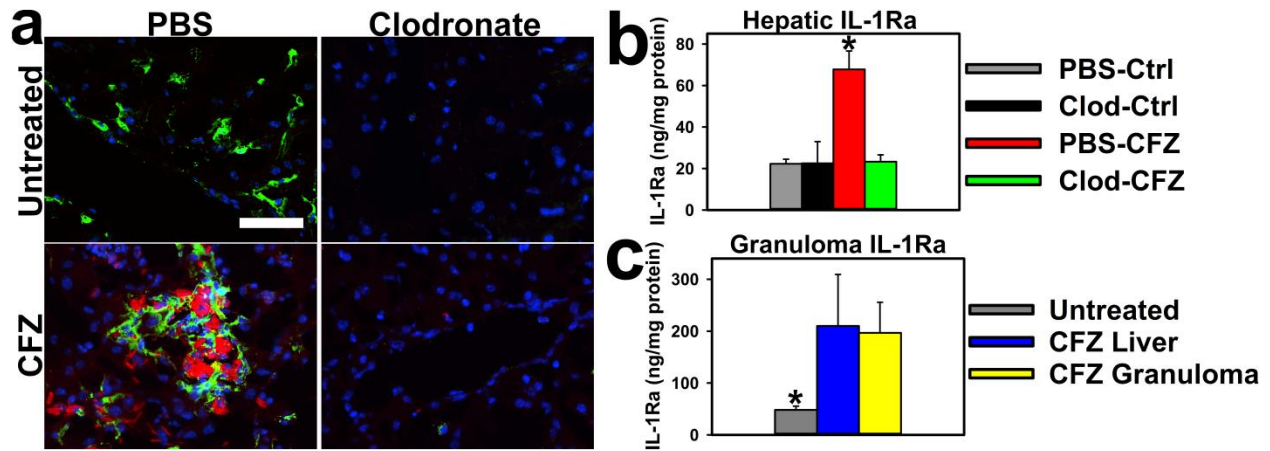


Figure 8-7 Formation of granulomas is necessary for the increased IL-1RA production within the liver of CFZ-treated mice

A) Liver cryosections of PBS or clodronate treated mice fed a control diet or CFZ-supplemented diet stained for F4/80 (green) and showing CLDI fluorescence. Treatment with clodronate reduces hepatic macrophages, resulting in reduced granuloma size and CLDI accumulation within the granuloma. B) IL-1RA production is inhibited within clodronate-CFZ treated mice, while it is significantly elevated in the PBS-CFZ treatment group. C) The granulomas which form ultimately are responsible for the production of IL-1RA, producing similar levels of IL-1RA to whole-organ homogenates. Scale bar is 50 μ m. (*= $p < 0.05$, ANOVA, Tukey's HSD).

8.9 Supporting Information

This manuscript is currently in preparation, and supplemental figures are available in Appendix E.

8.10 References

1. A. S. Greenberg and M. S. Obin, "Obesity and the role of adipose tissue in inflammation and metabolism," *The American Journal of Clinical Nutrition* 83, 461S-465S (2006).
2. R. Monteiro and I. Azevedo, "Chronic Inflammation in Obesity and the Metabolic Syndrome," *Mediators of Inflammation* 2010(2010).
3. S. M. Crusz and F. R. Balkwill, "Inflammation and cancer: advances and new agents," *Nat Rev Clin Oncol* 12, 584-596 (2015).
4. L. M. Coussens and Z. Werb, "Inflammation and cancer," *Nature* 420, 860-867 (2002).
5. M. Coash, F. Forouhar, C. H. Wu, and G. Y. Wu, "Granulomatous liver diseases: A review," *Journal of the Formosan Medical Association* 111, 3-13 (2012).
6. T. d. Brito and M. F. Franco, "Granulomatous inflammation," *Revista do Instituto de Medicina Tropical de São Paulo* 36, 185-192 (1994).
7. A. Zumla and D. G. James, "Granulomatous infections: etiology and classification," *Clinical infectious diseases : an official publication of the Infectious Diseases Society of America* 23, 146-158 (1996).
8. R. M. Bhat and C. Prakash, "Leprosy: An Overview of Pathophysiology," *Interdisciplinary Perspectives on Infectious Diseases* 2012, 6 (2012).
9. M. Silva Miranda, A. Breiman, S. Allain, F. Deknuydt, and F. Altare, "The Tuberculous Granuloma: An Unsuccessful Host Defence Mechanism Providing a Safety Shelter for the Bacteria?," *Clinical and Developmental Immunology* 2012, 14 (2012).
10. H. J. Freeman, "Granuloma-positive Crohn's disease," *Canadian Journal of Gastroenterology* 21, 583-587 (2007).
11. L. Henry, B. Wagner, M. K. Faulkner, D. N. Slater, and I. D. Ansell, "Metal deposition in post-surgical granulomas of the urinary tract," *Histopathology* 22, 457-465 (1993).

12. E. L. Culver, J. Watkins, and R. H. Westbrook, "Granulomas of the liver," *Clinical Liver Disease* 7, 92-96 (2016).
13. C. R. Espiritu, T. S. Kim, and R. A. Levine, "Granulomatous hepatitis associated with sulfadimethoxine hypersensitivity," *JAMA* 202, 985-988 (1967).
14. D. A. Bramlet, Z. Posalaky, and R. Olson, "Granulomatous hepatitis as a manifestation of quinidine hypersensitivity," *Archives of internal medicine* 140, 395-397 (1980).
15. A. T. Nguyen-Lefebvre and A. Horuzsko, "Kupffer Cell Metabolism and Function," *Journal of enzymology and metabolism* 1(2015).
16. N. Milosevic, H. Schawalder, and P. Maier, "Kupffer cell-mediated differential down-regulation of cytochrome P450 metabolism in rat hepatocytes," *European journal of pharmacology* 368, 75-87 (1999).
17. H. Ding, J. Tong, S. C. Wu, D. K. Yin, X. F. Yuan, J. Y. Wu, J. Chen, and G. G. Shi, "Modulation of Kupffer cells on hepatic drug metabolism," *World Journal of Gastroenterology* 10, 1325-1328 (2004).
18. D. L. Laskin, "Parenchymal and nonparenchymal cell interactions in hepatotoxicity," *Advances in experimental medicine and biology* 283, 499-505 (1991).
19. R. A. Roberts, P. E. Ganey, C. Ju, L. M. Kamendulis, I. Rusyn, and J. E. Klaunig, "Role of the Kupffer cell in mediating hepatic toxicity and carcinogenesis," *Toxicological sciences : an official journal of the Society of Toxicology* 96, 2-15 (2007).
20. V. Kegel, E. Pfeiffer, B. Burkhardt, J. L. Liu, K. Zeilinger, #xfc, A. K. ssler, D. Seehofer, and G. Damm, "Subtoxic Concentrations of Hepatotoxic Drugs Lead to Kupffer Cell Activation in a Human In Vitro Liver Model: An Approach to Study DILI," *Mediators of Inflammation* 2015, 14 (2015).
21. M. Cholo, H. Steel, P. Fourie, W. Germishuizen, and R. Anderson, "Clofazimine: current status and future prospects," *Journal of Antimicrobial Chemotherapy* (2011).
22. S. Tyagi, N. C. Ammerman, S. Y. Li, J. Adamson, P. J. Converse, R. V. Swanson, D. V. Almeida, and J. H. Grosset, "Clofazimine shortens the duration of the first-line treatment regimen for experimental chemotherapy of tuberculosis," *Proc Natl Acad Sci U S A* 112, 869-874 (2015).

23. DrugBank, "Clofazimine," (drugbank.ca, 2013).
24. G. S. Yoon, R. K. Keswani, S. Sud, P. M. Rzczycki, M. D. Murashov, T. A. Koehn, T. J. Standiford, K. A. Stringer, and G. R. Rosania, "Clofazimine Biocrystal Accumulation in Macrophages Upregulates Interleukin 1 Receptor Antagonist Production To Induce a Systemic Anti-Inflammatory State," *Antimicrob Agents Chemother* 60, 3470-3479 (2016).
25. J. Trexel, G. S. Yoon, R. K. Keswani, C. McHugh, L. Yeomans, V. Vitvitsky, R. Banerjee, S. Sud, Y. Sun, G. R. Rosania, and K. A. Stringer, "Macrophage-Mediated Clofazimine Sequestration Is Accompanied by a Shift in Host Energy Metabolism," *J Pharm Sci* 106, 1162-1174 (2017).
26. J. Baik, K. A. Stringer, G. Mane, and G. R. Rosania, "Multiscale Distribution and Bioaccumulation Analysis of Clofazimine Reveals a Massive Immune System-Mediated Xenobiotic Sequestration Response," *Antimicrob. Agents. Chemother.* 57, 1218-1230 (2013).
27. J. Baik and G. R. Rosania, "Macrophages Sequester Clofazimine in an Intracellular Liquid Crystal-Like Supramolecular Organization," *PLoS ONE* 7, e47494 (2012).
28. G. Yoon, S. Sud, R. Keswani, J. Baik, T. Standiford, K. Stringer, and G. Rosania, "Phagocytosed Clofazimine Biocrystals can Modulate Innate Immune Signaling by Inhibiting TNF Alpha and Boosting IL-1RA Secretion," *Mol. Pharmaceutics* (2015).
29. R. Keswani, J. Baik, L. Yeomans, C. Hitzman, A. Johnson, A. Pawate, P. Kenis, N. Rodriguez-Hornedo, K. Stringer, and G. Rosania, "Chemical Analysis of Drug Biocrystals: A Role for Counterion Transport Pathways in Intracellular Drug Disposition," *Molecular Pharmaceutics* (2015).
30. S. I. Kaluarachchi, B. M. Fernandopulle, and B. P. Gunawardane, "Hepatic and haematological adverse reactions associated with the use of multidrug therapy in leprosy--a five year retrospective study," *Indian journal of leprosy* 73, 121-129 (2001).
31. H. Singh, B. Nel, V. Dey, P. Tiwari, and N. Dulhani, "Adverse effects of multi-drug therapy in leprosy, a two years' experience (2006-2008) in tertiary health care centre in the tribal region of Chhattisgarh State (Bastar, Jagdalpur)," *Leprosy review* 82, 17-24 (2011).
32. P. J. Murray and T. A. Wynn, "Protective and pathogenic functions of macrophage subsets," *Nat Rev Immunol* 11, 723-737 (2011).

33. P. Rzeczycki, G. S. Yoon, R. K. Keswani, S. Sud, K. A. Stringer, and G. R. Rosania, "Detecting ordered small molecule drug aggregates in live macrophages: a multi-parameter microscope image data acquisition and analysis strategy," *Biomed. Opt. Express* 8, 860-872 (2017).
34. C. A. Schneider, W. S. Rasband, and K. W. Eliceiri, "NIH Image to ImageJ: 25 years of image analysis," *Nat Meth* 9, 671-675 (2012).
35. S. Lin, J. Racz, M. Tai, K. Brooks, P. Rzeczycki, L. Heath, M. Newstead, T. Standiford, G. Rosania, and K. Stringer, "A Role for Low Density Lipoprotein Receptor-Related Protein 1 in the Cellular Uptake of Tissue Plasminogen Activator in the Lungs," *Pharm Res*, 1-11 (2015).
36. K. A. Min, W. G. Rajeswaran, R. Oldenbourg, G. Harris, R. K. Keswani, M. Chiang, P. Rzeczycki, A. Talattof, M. Hafeez, R. W. Horobin, S. D. Larsen, K. A. Stringer, and G. R. Rosania, "Massive Bioaccumulation and Self-Assembly of Phenazine Compounds in Live Cells," *Advanced Science* 2(2015).
37. N. van Rooijen and E. Hendriks, "Liposomes for Specific Depletion of Macrophages from Organs and Tissues," in *Liposomes*, V. Weissig, ed. (Humana Press, 2010), pp. 189-203.
38. R. Keswani, G. Yoon, S. Sud, K. Stringer, and G. Rosania, "A Far-Red Fluorescent Probe For Flow Cytometric Xenobiotic-Sequestering Cell Functional Studies," *Cytometry Part A* (2015).
39. R. Latini, G. Tognoni, and R. E. Kates, "Clinical pharmacokinetics of amiodarone," *Clinical pharmacokinetics* 9, 136-156 (1984).
40. B. Zhitomirsky and Y. G. Assaraf, "Lysosomal sequestration of hydrophobic weak base chemotherapeutics triggers lysosomal biogenesis and lysosome-dependent cancer multidrug resistance," *Oncotarget* 6, 1143-1156 (2015).
41. N. Andrejewski, E.-L. Punnonen, G. Guhde, Y. Tanaka, R. Lüllmann-Rauch, D. Hartmann, K. von Figura, and P. Saftig, "Normal Lysosomal Morphology and Function in LAMP-1-deficient Mice," *Journal of Biological Chemistry* 274, 12692-12701 (1999).
42. I. Tanida, T. Ueno, and E. Kominami, "LC3 and Autophagy," *Methods in molecular biology* (Clifton, N.J.) 445, 77-88 (2008).

43. M. D. Murashov, V. LaLone, P. M. Rzeczycki, R. K. Keswani, G. S. Yoon, S. Sud, W. Rajeswaran, S. Larsen, K. A. Stringer, and G. R. Rosania, "The Physicochemical Basis of Clofazimine-Induced Skin Pigmentation," *Journal of Investigative Dermatology* (2017).
44. R. M. Sri-Pathmanathan, J. A. Plumb, and K. C. Fearon, "Clofazimine alters the energy metabolism and inhibits the growth rate of a human lung-cancer cell line in vitro and in vivo," *Int J Cancer* 56, 900-905 (1994).
45. W. S. Stokes, "Humane Endpoints for Laboratory Animals Used in Regulatory Testing," *ILAR Journal* 43, S31-S38 (2002).
46. W. M. Lee "Drug-Induced Hepatotoxicity," *New England Journal of Medicine* 349, 474-485 (2003).
47. M. J. Hodgman and A. R. Garrard, "A review of acetaminophen poisoning," *Critical care clinics* 28, 499-516 (2012).
48. A. C. Miller, Jr. and W. M. Reid, "Methyldopa-induced granulomatous hepatitis," *Jama* 235, 2001-2002 (1976).
49. K. G. Ishak, J. P. Kirchner, and J. K. Dhar, "Granulomas and cholestatic--hepatocellular injury associated with phenylbutazone. Report of two cases," *The American journal of digestive diseases* 22, 611-617 (1977).
50. A. Rocznik-Ferguson, C. S. Petit, F. Froehlich, S. Qian, J. Ky, B. Angarola, T. C. Walther, and S. M. Ferguson, "The Transcription Factor TFEB Links mTORC1 Signaling to Transcriptional Control of Lysosome Homeostasis," *Science Signaling* 5, ra42-ra42 (2012).
51. S. Peña-Llopis, S. Vega-Rubin-de-Celis, J. C. Schwartz, N. C. Wolff, T. A. T. Tran, L. Zou, X. J. Xie, D. R. Corey, and J. Brugarolas, "Regulation of TFEB and V-ATPases by mTORC1," *Embo j* 30, 3242-3258 (2011).
52. A. Giatromanolaki, D. Kalamida, E. Sivridis, I. V. Karagounis, K. C. Gatter, A. L. Harris, and M. I. Koukourakis, "Increased expression of transcription factor EB (TFEB) is associated with autophagy, migratory phenotype and poor prognosis in non-small cell lung cancer," *Lung Cancer* 90, 98-105 (2015).
53. R. M. Perera, S. Stoykova, B. N. Nicolay, K. N. Ross, J. Fitamant, M. Boukhali, J. Lengrand, V. Deshpande, M. K. Selig, C. R. Ferrone, J. Settleman, G. Stephanopoulos, N. J.

Dyson, R. Zoncu, S. Ramaswamy, W. Haas, and N. Bardeesy, "Transcriptional control of autophagy-lysosome function drives pancreatic cancer metabolism," *Nature* 524, 361-365 (2015).

54. L. M. Fang, B. Li, J. J. Guan, H. D. Xu, G. H. Shen, Q. G. Gao, and Z. H. Qin, "Transcription factor EB is involved in autophagy-mediated chemoresistance to doxorubicin in human cancer cells," *Acta pharmacologica Sinica* 38, 1305-1316 (2017).

55. B. Zhitomirsky and Y. G. Assaraf, "Lysosomal accumulation of anticancer drugs triggers lysosomal exocytosis," *Oncotarget* 8, 45117-45132 (2017).

Chapter 9

Conclusions

9.1 Macrophages Actively Stabilize Crystal-Like Drug Inclusions

The macrophage has unique properties that allow it to both accumulate and stabilize the crystal-like drug inclusions (CLDIs) that result from prolonged clofazimine administration. The active stabilization of CLDIs by the macrophage was discovered after revealing the changes that the cell and organs both undergo to increased drug treatment and the subsequent increase in CLDI accumulation. As the length of treatment progresses, the macrophage population within the lung, liver, and spleen expands significantly. This larger macrophage population increases the amount of drug that can be sequestered and stabilized as a CLDI within these organs. As a result of the increased macrophage population, the amount of drug found in the liver, lung, and spleen increasing massively from weeks 3 to 8, when the drug shifts from being primarily found in its soluble form to its insoluble form [1, 2]. During this time, the macrophage also actively altered its internal membrane to maximize drug loading, while at the same time, minimizing the total required surface area of membrane necessary to stabilize the crystal. This was observed in alveolar macrophages, which acquired the drug in the form of small volume, spherical vesicles at early stages of treatment (<4 weeks) [3]. As this is not energy efficient [4], the cell forms larger, polyhedral crystals, occupying more cellular volume but allowing for increased intracellular drug loading.

The alteration in membrane arrangement the macrophage undergoes does not come without a cost to the cell. Due to the stress put upon the lysosome brought about by drug trapping [5, 6], the macrophage activates a key nuclear transcription factor, TFEB. Upon instances of lysosomal or nutrient stress, TFEB translocates from the cytosol to the nucleus, where it increases the expression of a variety of genes, those most critical for CLDI stabilization being

related to lysosomal biogenesis and membrane formation [7, 8]. Activation of TFEB within CLDI-containing macrophages resulted in increased cell size, lysosomal content, and autophagic flux, all pointing to cellular adaptations brought about to stabilize the CLDI. Increasing autophagic flux allows for degradation of cellular material, increasing the ability to form lysosomal membranes which trap and stabilize CLDIs, all within a cell that has increased in size to trap and stabilize more drug. As more lysosomes form, increased soluble drug can potentially become ion-trapped [9], leading to increased drug accumulation and subsequent CLDI stabilization. The increased membrane production also allows these cells to increase in size, increasing their capacity for CLDI accumulation.

Additionally, the specificity of the macrophage as the active stabilizer of clofazimine biocrystals was confirmed following the chemical depletion of these cells in the liver, spleen, and peritoneal cavity. Without macrophages in the liver and spleen, CLDI accumulation (detected as a reduced ratio between the intrinsic far-red fluorescence of the CLDI [10] and the nuclear signal) was significantly reduced. The inability to actively stabilize the CLDI within the macrophage reduced the total drug that became trapped within those organs, indicating that both CLDI stabilization and the accumulation of drug in general is a macrophage-specific phenomenon. Finally, when macrophages of the peritoneal cavity were removed and isolated biocrystals were introduced, there was a significant reduction in the estimated half-life of the CLDI within the peritoneum when compared to the group with a healthy peritoneal macrophage population. Macrophages are not the only cell present in the peritoneum, with B- and T-cells also residing within the cavity [11]. The depletion method used only affects highly phagocytic cells, and since these cells are not one of the so-called “professional phagocytes” of the body like the macrophage [12], they remain within the cavity. However, their endolysosomal system is not equipped to phagocytose the CLDI and stabilize it within the endolysosomal compartment, leading to the CLDI remaining in the relatively more basic extracellular environment, inducing solubilization and CLDI degradation; this points to an active and specific role that the macrophage plays in CLDI accumulation and stabilization.

9.2 Multi-parameter Microscopy and Drug Analysis

The development and refinement of a multi-parameter microscopy imaging and acquisition strategy as it relates to intracellular drug accumulation has the potential to be a useful

tool in drug discovery and development, especially in the early stages. Here, we applied this technique to link changes in the protonation state (far-red fluorescence [10]), cellular accumulation (absorbance), and the organization of drug (linear diattenuation/dichroism) within the cell. As it relates to general drug development, microscopic analysis, and more specifically, polarized light microscopy, is a commonly used high throughput technique to study solubilization and precipitation of compounds *in vitro* [13]. However, multi-parameter imaging that combines two or more types of imaging modalities is becoming more and more common in drug development. For instance, flow cytometry to study phenotypic changes to individual cells, rather than to entire populations of cells within a cell culture vessel can be used to elucidate specific effects to a certain cell type following drug treatment [14].

The multi-parameter imaging and acquisition strategy that was developed can be used to study both *in vitro* accumulation and precipitation of drugs in cultured cells, and to study changes to specific populations of live cells following *in vivo* drug treatment. To this end, studying the cellular pharmacokinetics of a therapeutic is becoming increasingly important in pre-clinical drug development and lead selection [15]. Since the efficacy of a drug is highly dependent on its ability to concentrate itself at the proper site of action [16], be it a cellular receptor or organelle, it is vital in the early stages of drug development to determine exactly where a drug molecule is concentrating once it enters a cell at a precise level. Currently, single-cell pharmacokinetic studies are performed using fluorescence [17] and fluorescence anisotropy [18] microscopy to study the localization of drug molecules within subcellular compartments at the early stages of drug development to aid in deciding which target compounds to further develop. Combining linear diattenuation anisotropy and absorbance microscopy with more commonly applied techniques (i.e. fluorescence and fluorescence anisotropy) has the potential to improve the power of these analyses. For example, linear diattenuation anisotropy is highly specific to even the most minor changes in molecular order present in a sample [19]. Given this, certain drugs, particularly those that are lipophilic, will intercalate within lipid membranes intracellularly, resulting in an altered membrane structure and phospholipidosis [20, 21], which can potentially be detected as an increased intracellular linear diattenuation signal.

One other powerful application of this analytical polarization imaging method involves the ability to rapidly distinguish one polymorphic form of a chemical entity from another.

Simply put, polymorphism occurs when a compound has multiple possible molecular arrangements of molecules in a solid phase [22], resulting in different crystal structures. In the case of clofazimine, the drug undergoes a polymorphic change during bioaccumulation, changing its underlying crystal structure, which is detectable as both a marked increase in far-red fluorescence and linear diattenuation [3, 10]. Many drugs that are currently being brought to the market are poorly soluble chemical entities [23], and one method used to improve solubility is formulating the proper crystal polymorph of the drug [24]. It is estimated that over 50% of therapeutic agents show some form of polymorphism [25] and ensuring that the formulation that is being delivered to the patient contains the proper crystal form of the drug is vital in ensuring that the drug product works as intended.

The dissolution rate and solubility of a formulation can be significantly affected if the active pharmaceutical ingredient is not in the proper polymorphic form, or if the polymorph changes during formulation, manufacturing, storage, and administration; the bioavailability and efficacy of the drug product can be altered significantly following a change in the polymorph in the formulation, resulting in reduced therapeutic benefits [22, 24-26]. To this end, ensuring that the patient is receiving the correct form of the active pharmaceutical ingredient when taking their medications is vital. Currently, a variety of techniques are utilized to study the polymorphic form present in drug formulations, including infrared spectroscopy, nuclear magnetic resonance, and x-ray diffraction [22]. The “gold-standard” for analysis of polymorphs is single crystal x-ray diffraction, but preparation of a crystal that is appropriate for analysis can be difficult [27], making it challenging to study polymorph stability in real-time. Multi-parameter microscopy combining polarization microscopy with other imaging modalities such as fluorescence can potentially be utilized to analyze polymorph stability *in vitro* under a variety of conditions. Nonlinear optical stokes ellipsometric microscopy has been previously used to differentiate between two polymorphic forms of d-mannitol (orthorhombic and monoclinic), a common excipient in pharmaceutical formulations [28]. Similarly, using the multi-parameter imaging system developed here, the two polymorphic forms of clofazimine can be readily discriminated. Using quantitative multi-parameter imaging, stability of polymorphic forms of drug within a formulation can be studied in real-time under a variety of conditions. Additionally, insoluble polymorphs can be directly incubated with cells and their stability under intracellular conditions can be monitored in real time.

9.3 Macrophage Stabilization of Intracellular Drug Biocrystals and Potential for Therapeutic Development

Development of poorly soluble, acidic and basic drugs into a workable drug product presents a number of challenges to formulation scientists, leading to novel strategies such as salt formation and taking advantage of the acid-base chemistry [29-31]. Instead of attempting to deliver the drug as a form that must solubilize to reach the site of action, why not formulate crystalline forms of the drug and use that as a drug product that can deliver the therapeutic to a specific site of action? Specific targeting of macrophages is a hot topic in drug design currently, in particular, for cancer therapeutics and other immunomodulatory therapies [32-35] as a strategy to minimize off-target effects and toxicity. In the work presented in the previous chapters, it was shown that macrophages actively promote the stabilization and accumulation of drug biocrystals, due in large part to their increased activation of TFEB, a master regulator of lysosome biogenesis, among other critical cellular functions related to the endolysosomal system [7]. Due to the macrophage's increased expression of lysosomal acidification mechanisms, particularly the vacuolar-type proton ATP-ase (V-ATPase) [36], these cells are also equipped to stabilize biocrystals introduced to the body. Interestingly, phagocytosis of extracellular CLDIs *in vitro* resulted in increased production of the anti-inflammatory cytokine IL-1RA and reduced production of the pro-inflammatory TNF- α [37]. While it is not known if this occurs *in vivo*, biocrystal accumulation within the liver resulted in IL-1RA upregulation [38], so it is not unreasonable to believe that formulations of insoluble clofazimine biocrystals show the same immunomodulatory effects.

Additionally, the discovery of the particular subset of liver macrophages, the xenobiotic sequestering macrophage and the adaptations that they undergo shows the potential for why these cells may be a future avenue for insoluble drug targeted therapies. Following loading with biocrystals, the macrophage adjusted its internal membrane arrangement to maximize loading while minimizing the volume that the drug cargo occupied. By loading the cell with an insoluble aggregate, rather than just through exposure to the soluble form of the drug, the cell also alters its endolysosomal system through activation of TFEB. This induces production of lysosomes within the cell [7], and subsequently, expression of lysosomal acidification mechanisms increases [39], actively promoting the stability of these crystals within this subset of cells. The macrophages'

ability to actively adapt its cargo carrying capacity to an external cargo loading stimulus makes the macrophage the prime candidate for targeting and loading with insoluble drug aggregates, serving as a long term cellular drug depot, slowly releasing drug directly at the site of action, be it in a tumor-associated macrophage within the tumor micro-environment or at a locally inflamed area where immunomodulation is necessary.

It is not unreasonable to believe that other poorly soluble, weakly basic drug molecules can be reformulated into stable, hydrochloride salts forms which can target macrophages where they can stably reside and slowly release drug to the surrounding tissue environment. As it stands currently, more than 78% of drugs currently in use contain at least one ionizable moiety within the molecule [30]. For weakly basic drugs, around 20% have a pKa in the range of lysosomal pH ($4 < \text{pKa} < 6.5$) [30], meaning that these drug molecules should be explored for potential salt formation and lysosomal targeting. As a delivery strategy, formulating hydrochloride salt forms of drug poses several challenges. Firstly, the salt crystals need to remain in an environment containing the proper pH and salt content to prevent conversion from to the free base form of the drug and solubilization. To accomplish this, the drug would need to be delivered in a solution that is at or below the pH_{max} of the salt form of the drug. When the pH is at or below the pH_{max} (i.e. is more acidic), the solid, salt form of the drug will be most stable form of the drug, while at pH values above the pH_{max} (i.e. a more basic solution), the solid, free base form of the drug will be more thermodynamically stable, resulting in conversion and destabilization of the solid dosage form [40, 41]. The solution would also need to have the proper counter-ion concentration to prevent dissolution of the salt as well; mimicking the lysosomal environment (pH of approximately 4.5 and chloride concentration of above 80 mM[42, 43]) should allow for the stabilization of a wide variety of hydrochloride salt drugs.

Once a proper solution for delivery has been designed, formulating a vehicle to deliver the stable crystal to the tissue or cell of interest must be developed. Currently, liposomal formulations are extensively used in cancer therapeutics due to the ability to modify the surface of the liposome with targeting ligands or antibody surface modifications [44]. By modifying the surface of the liposome, cancerous tissues or cells can be specifically targeted, reducing off-target effects and limiting toxicity [45]. Aside from delivering drug in solution, liposomal formulations have been used to deliver insoluble drug formulations as well. For example, the

anti-cancer therapeutic Doxil, a liposomal formulation of doxorubicin hydrochloride, is comprised of liposomes loaded with a crystalline precipitate of drug [46]. Doxorubicin has a risk for cardiotoxicity, but formulations of Doxil show significantly reduced instances of cardiotoxicity due to the specific targeting of the tumor [47]. Using the remote loading approach that is used to formulate Doxil [48], other weakly basic drugs can potentially be explored as candidates for development into liposomal formulations which can specifically target sites of interest and limit systemic toxic events.

By targeting the site of interest, either through formulating a liposome of size that will undergo phagocytosis by macrophages, or through addition of targeting moieties to the surface of the liposome, lower doses of drug would be needed, reducing possibilities for off-target reactions and toxicity. Additionally, if properly formulated, these crystalline formulations can act as a cellular drug depot similar to the CLDIs that are found within macrophages. Even following cessation of treatment, CLDIs remain within macrophages of the liver and spleen [1], where they act as a cell-assembled drug depot and help keep plasma concentrations of clofazimine at levels above the minimum inhibitory concentration for *Mycobacterium tuberculosis* and *Mycobacterium leprae* [49]. Sustained or continuous release depot-type formulations have been utilized extensively since the 1970s [50] to deliver poorly soluble drugs over the course of months or years. These types of formulations increase patient compliance, as they eliminate the need to take a pill daily or weekly, reducing missed dosages. In all, formulations of insoluble, weakly basic crystalline drugs should be considered for development in the future as a method for site-specific drug delivery and loading.

9.4 References

1. J. Baik, K. A. Stringer, G. Mane, and G. R. Rosania, "Multiscale Distribution and Bioaccumulation Analysis of Clofazimine Reveals a Massive Immune System-Mediated Xenobiotic Sequestration Response," *Antimicrob. Agents. Chemother.* **57**, 1218-1230 (2013).
2. J. Baik and G. R. Rosania, "Macrophages Sequester Clofazimine in an Intracellular Liquid Crystal-Like Supramolecular Organization," *PLoS ONE* **7**, e47494 (2012).
3. P. Rzczycki, G. S. Yoon, R. K. Keswani, S. Sud, K. A. Stringer, and G. R. Rosania, "Detecting ordered small molecule drug aggregates in live macrophages: a multi-parameter microscope image data acquisition and analysis strategy," *Biomed. Opt. Express* **8**, 860-872 (2017).
4. J. C. Stachowiak, F. M. Brodsky, and E. A. Miller, "A cost-benefit analysis of the physical mechanisms of membrane curvature," *Nat Cell Biol* **15**, 1019-1027 (2013).
5. J. A. Martina, H. I. Diab, O. A. Brady, and R. Puertollano, "TFEB and TFE3 are novel components of the integrated stress response," *Embo j* **35**, 479-495 (2016).
6. N. Raben and R. Puertollano, "TFEB and TFE3: Linking Lysosomes to Cellular Adaptation to Stress," *Annual review of cell and developmental biology* **32**, 255-278 (2016).
7. G. Napolitano and A. Ballabio, "TFEB at a glance," *Journal of Cell Science* (2016).
8. A. Rocznik-Ferguson, C. S. Petit, F. Froehlich, S. Qian, J. Ky, B. Angarola, T. C. Walther, and S. M. Ferguson, "The Transcription Factor TFEB Links mTORC1 Signaling to Transcriptional Control of Lysosome Homeostasis," *Science Signaling* **5**, ra42-ra42 (2012).
9. R. Logan, A. C. Kong, E. Axcell, and J. P. Krise, "Amine-Containing Molecules and the Induction of an Expanded Lysosomal Volume Phenotype: A Structure–Activity Relationship Study," *Journal of Pharmaceutical Sciences* **103**, 1572-1580 (2014).
10. R. Keswani, G. Yoon, S. Sud, K. Stringer, and G. Rosania, "A Far-Red Fluorescent Probe For Flow Cytometric Xenobiotic-Sequestering Cell Functional Studies," *Cytometry Part A* (2015).

11. K. Abe, S. Honma, and T. Ito, "Peritoneal cells in mice: Quantitative and qualitative cell morphology," *American Journal of Anatomy* **156**, 37-50 (1979).
12. M. Rabinovitch, "Professional and non-professional phagocytes: an introduction," *Trends in Cell Biology* **5**, 85-87 (1995).
13. K. Sugano, T. Kato, K. Suzuki, K. Keiko, T. Sujaku, and T. Mano, "High throughput solubility measurement with automated polarized light microscopy analysis," *Journal of Pharmaceutical Sciences* **95**, 2115-2122 (2006).
14. A. Bullen, "Microscopic imaging techniques for drug discovery," **7**, 54 (2008).
15. N. Zheng, H. N. Tsai, X. Zhang, and G. R. Rosania, "The subcellular distribution of small molecules: from pharmacokinetics to synthetic biology," *Mol Pharm* **8**, 1619-1628 (2011).
16. F. Zhou, J. Zhang, P. Li, F. Niu, X. Wu, G. Wang, and M. S. Roberts, "Toward a new age of cellular pharmacokinetics in drug discovery," *Drug metabolism reviews* **43**, 335-345 (2011).
17. C. Vinegoni, J. M. Dubach, G. M. Thurber, M. A. Miller, R. Mazitschek, and R. Weissleder, "Advances in measuring single-cell pharmacokinetics and pharmacology in vivo," *Drug discovery today* **20**, 1087-1092 (2015).
18. J. M. Dubach, C. Vinegoni, R. Mazitschek, P. Fumene Feruglio, L. A. Cameron, and R. Weissleder, "In vivo imaging of specific drug-target binding at subcellular resolution," *Nature communications* **5**, 3946 (2014).
19. S. B. Mehta, M. Shribak, and R. Oldenbourg, "Polarized light imaging of birefringence and diattenuation at high resolution and high sensitivity," *Journal of Optics* **15**, 094007 (2013).
20. N. Anderson and J. Borlak, "Drug-induced phospholipidosis," *FEBS Lett* **580**, 5533-5540 (2006).
21. M. J. Reasor, C. L. Ogle, E. R. Walker, and S. Kacew, "Amiodarone-induced Phospholipidosis in Rat Alveolar Macrophages," *American Review of Respiratory Disease* **137**, 510-518 (1988).
22. J. Halebian and W. McCrone, "Pharmaceutical applications of polymorphism," *J Pharm Sci* **58**, 911-929 (1969).

23. K. Savjani, A. Gajjar, and J. Savjani, "Drug Solubility: Importance and Enhancement Techniques," *ISRN Pharmaceutics* **2012**, 10 (2012).
24. R. Censi and P. Di Martino, "Polymorph Impact on the Bioavailability and Stability of Poorly Soluble Drugs," *Molecules (Basel, Switzerland)* **20**, 18759-18776 (2015).
25. K. Raza, P. Kumar, S. Ratan, R. Malik, and S. Arora, "Polymorphism: The Phenomenon Affecting the Performance of Drugs," *SOJ Pharmacy and Pharmaceutical Sciences* **1**, 10 (2014).
26. D. Singhal and W. Curatolo, "Drug polymorphism and dosage form design: a practical perspective," *Adv Drug Deliv Rev* **56**, 335-347 (2004).
27. E. H. Lee, "A practical guide to pharmaceutical polymorph screening & selection," *Asian Journal of Pharmaceutical Sciences* **9**, 163-175 (2014).
28. P. D. Schmitt, E. L. DeWalt, X. Y. Dow, and G. J. Simpson, "Rapid Discrimination of Polymorphic Crystal Forms by Nonlinear Optical Stokes Ellipsometric Microscopy," *Analytical Chemistry* **88**, 5760-5768 (2016).
29. H. Williams, N. Trevaskis, S. Charman, R. Shanker, W. Charman, C. Pouton, and C. Porter, "Strategies to Address Low Drug Solubility in Discovery and Development," *Pharmacological Reviews* **65**, 315-499 (2013).
30. D. T. Manallack, R. J. Prankerd, E. Yuriev, T. I. Oprea, and D. K. Chalmers, "The Significance of Acid/Base Properties in Drug Discovery," *Chemical Society reviews* **42**, 485-496 (2013).
31. A. Serajuddin, "Salt formation to improve drug solubility," *Advanced Drug Delivery Reviews* **59**, 603-616 (2007).
32. S. K. Patel and J. M. Janjic, "Macrophage Targeted Theranostics as Personalized Nanomedicine Strategies for Inflammatory Diseases," *Theranostics* **5**, 150-172 (2015).
33. N. K. Jain, V. Mishra, and N. K. Mehra, "Targeted drug delivery to macrophages," *Expert opinion on drug delivery* **10**, 353-367 (2013).
34. L. A. Needham, A. H. Davidson, L. J. Bawden, A. Belfield, E. A. Bone, D. H. Brotherton, S. Bryant, M. H. Charlton, V. L. Clark, S. J. Davies, A. Donald, F. A. Day, D. Krige,

V. Legris, J. McDermott, Y. McGovern, J. Owen, S. R. Patel, S. Pintat, R. J. Testar, G. M. A. Wells, D. Moffat, and A. H. Drummond, "Drug Targeting to Monocytes and Macrophages Using Esterase-Sensitive Chemical Motifs," *Journal of Pharmacology and Experimental Therapeutics* **339**, 132-142 (2011).

35. A. Kaur, S. Jain, and A. K. Tiwary, "Mannan-coated gelatin nanoparticles for sustained and targeted delivery of didanosine: in vitro and in vivo evaluation," *Acta pharmaceutica (Zagreb, Croatia)* **58**, 61-74 (2008).

36. S.-P. Wang, I. Krits, S. Bai, and B. S. Lee, "Regulation of Enhanced Vacuolar H⁺-ATPase Expression in Macrophages," *Journal of Biological Chemistry* **277**, 8827-8834 (2002).

37. G. Yoon, S. Sud, R. Keswani, J. Baik, T. Standiford, K. Stringer, and G. Rosania, "Phagocytosed Clofazimine Biocrystals can Modulate Innate Immune Signaling by Inhibiting TNF Alpha and Boosting IL-1RA Secretion," *Mol. Pharmaceutics* (2015).

38. G. S. Yoon, R. K. Keswani, S. Sud, P. M. Rzczycki, M. D. Murashov, T. A. Koehn, T. J. Standiford, K. A. Stringer, and G. R. Rosania, "Clofazimine Biocrystal Accumulation in Macrophages Upregulates Interleukin 1 Receptor Antagonist Production To Induce a Systemic Anti-Inflammatory State," *Antimicrob Agents Chemother* **60**, 3470-3479 (2016).

39. S. Peña-Llopis, S. Vega-Rubin-de-Celis, J. C. Schwartz, N. C. Wolff, T. A. T. Tran, L. Zou, X. J. Xie, D. R. Corey, and J. Brugarolas, "Regulation of TFEB and V-ATPases by mTORC1," *Embo j* **30**, 3242-3258 (2011).

40. Y.-L. Hsieh, J. M. Merritt, W. Yu, and L. S. Taylor, "Salt Stability – The Effect of pH_{max} on Salt to Free Base Conversion," *Pharm Res* **32**, 3110-3118 (2015).

41. T. B. Hansen and H. Qu, "Mechanism of Process-Induced Salt-to-Free Base Transformation of Pharmaceutical Products," *Chemical Engineering & Technology* **37**, 1347-1352 (2014).

42. H. Xu and D. Ren, "Lysosomal physiology," *Annu Rev Physiol* **77**, 57-80 (2015).

43. J. A. Mindell, "Lysosomal Acidification Mechanisms," *Annual Review of Physiology* **74**, 69-86 (2012).

44. B. S. Pattni, V. V. Chupin, and V. P. Torchilin, "New Developments in Liposomal Drug Delivery," *Chem Rev* **115**, 10938-10966 (2015).

45. P. P. Deshpande, S. Biswas, and V. P. Torchilin, "Current trends in the use of liposomes for tumor targeting," *Nanomedicine (London, England)* **8**(2013).
46. U. Bulbake, S. Doppalapudi, N. Kommineni, and W. Khan, "Liposomal Formulations in Clinical Use: An Updated Review," *Pharmaceutics* **9**(2017).
47. G. Batist, "Cardiac safety of liposomal anthracyclines," *Cardiovascular toxicology* **7**, 72-74 (2007).
48. Y. Barenholz, "Doxil® — The first FDA-approved nano-drug: Lessons learned," *Journal of Controlled Release* **160**, 117-134 (2012).
49. R. V. Swanson, J. Adamson, C. Moodley, B. Ngcobo, N. C. Ammerman, A. Dorasamy, S. Moodley, Z. Mgaga, A. Tapley, L. A. Bester, S. Singh, J. H. Grosset, and D. V. Almeida, "Pharmacokinetics and Pharmacodynamics of Clofazimine in a Mouse Model of Tuberculosis," *Antimicrob Agents Chemother* **59**, 3042-3051 (2015).
50. J. C. Wright and A. S. Hoffman, "Historical Overview of Long Acting Injections and Implants," in *Long Acting Injections and Implants*, J. C. Wright and D. J. Burgess, eds. (Springer US, Boston, MA, 2012), pp. 11-24.

Appendix A

Supporting Information in Chapter 2

Figure SI. 1- Degradation of human tPA.

Western blot of human tPA (htPA) that was added to homogenized mouse lung and shows the rapid degradation of the parent protein (MW ~68kDa; lane 2). This is further illustrated by the increased signal intensities of smaller molecular degradation products. This is apparent as early as 5 min after the addition of htPA (5 μ g) to lung homogenate (lane 1) and continues to be evident at 15 (lane 3) and 30 min (lane 4). MWM= molecular weight marker.

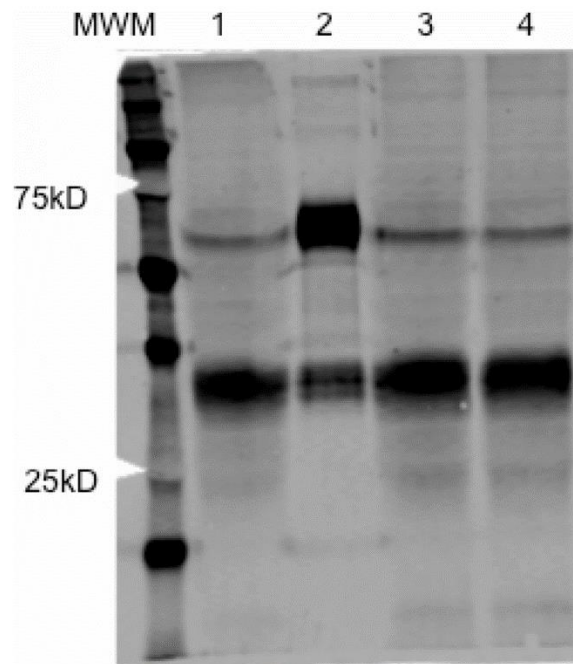


Figure SI. 2- Brightfield images of LRP1 stained lung through different filters.

Bright field images with blue filter show greater intensity of staining than red filter images. A representative image of an LRP1 stained mouse lung (40X) section in the (A) bright field; (B) with the red filter; and (C) the blue filter. Scale bar is 50 μ m.

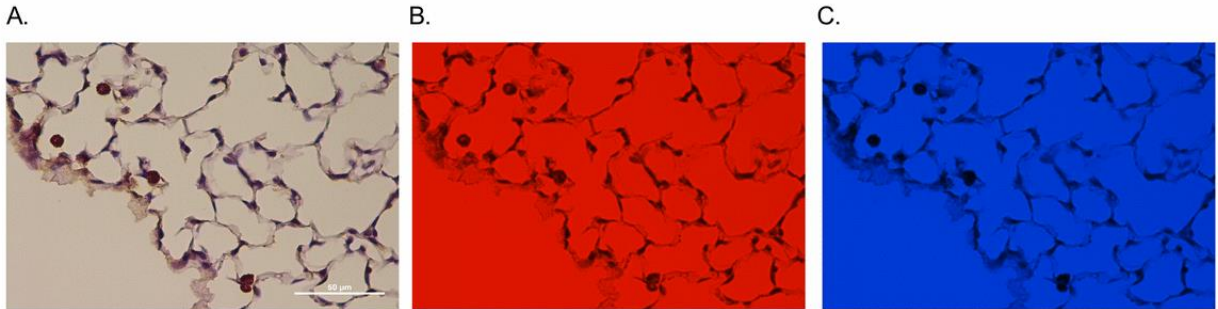


Figure SI. 3- Thresholding of tissue section.

Threshold applied images from bright field red and blue filters. The red filtered image captures all tissue positive areas on the slide. The blue filtered image captures only stained area on the tissue. A representative bright field image (A) of stained mouse lung section (40X) with the threshold-applied red filter image (B) and the threshold-applied blue filter image (C). Scale bar is 50 μ m.

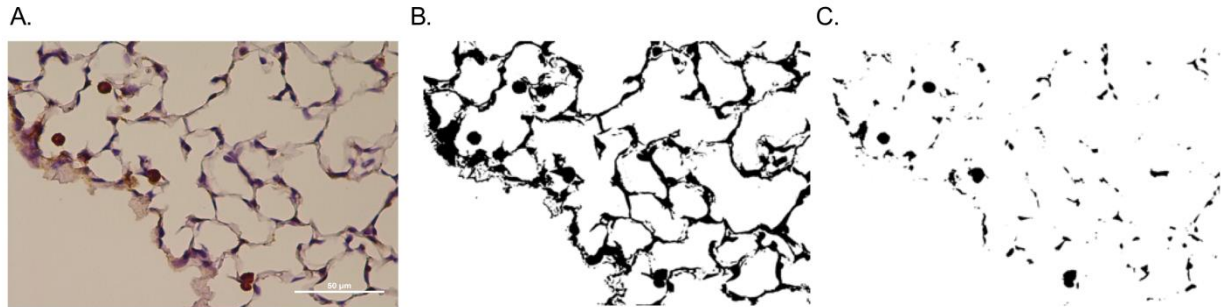


Figure SI. 4- Mouse liver and lung sections stained for LRP1.

Sections of LRP1 stained and unstained sections of mouse liver and lung (40X). Representative (A) LRP1 stained liver; (B) unstained liver; (C) LRP1 stained lung and (D) unstained lung. Scale bar is 50µm.

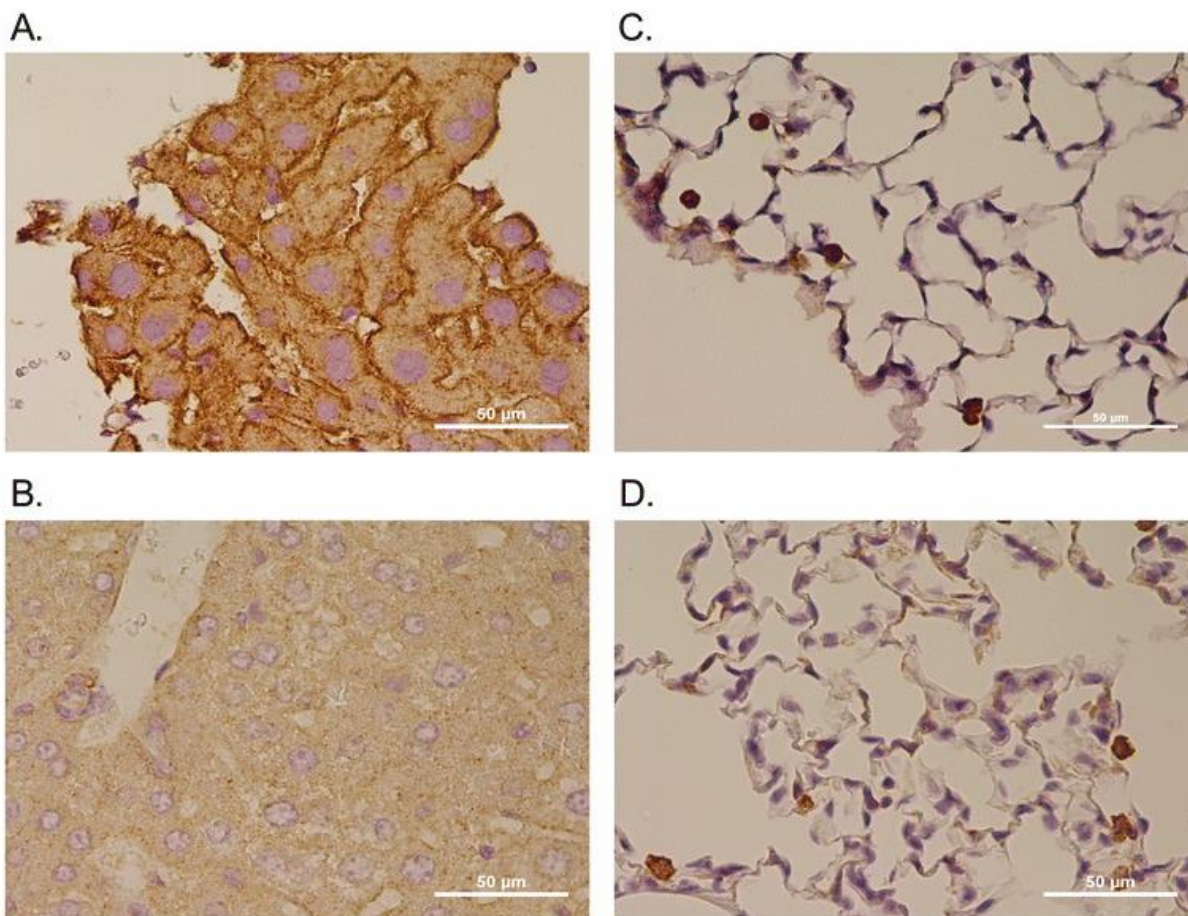
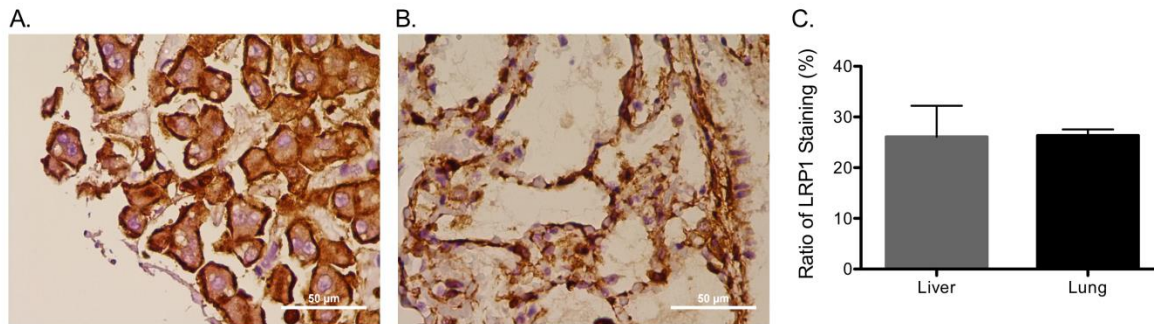


Figure SI. 5- Ratio of LRP1 staining in liver and lung.

As in the mouse, the ratio of LRP1 staining in macaque monkey liver and lung sections were similar. Representative color light micrographs of (A) liver and (B) lung sections (40X) stained for LRP1 and 3'3'-diaminozenidene (DAB) that is depicted by the brown staining. (C) Quantitation of the ratio of LRP1 staining in liver and lung sections was not different between the two groups ($p=0.969$ by unpaired Student's t-test). Data are mean (\pm S.E.M.) of 7 sections/group. Scale bar is $50\mu\text{m}$.



Methods

Western Blot of Human tPA in Mouse Lung Homogenate

The lungs of a post-mortem C56Bl/6 male mouse were perfused blood-free and homogenized in the absence of protease inhibitors as previously described (1). Briefly, the sample was homogenized (Tissuemiser, Fisher Scientific, Pittsburg, PA) on ice in the presence of tissue extraction reagent (Pierce, Rockford, IL). Residual red blood cells were lysed by the addition of red blood cell lysing buffer (1 mL; Sigma, St. Louis, MO). Homogenate was transferred to a microcentrifuge tube and clarified by centrifugation ($13,000 \times g$, 4°C) for 20 min. A known amount of htPA (5 μg) was added to the homogenate (1 mL) and it was incubated (37°C). Over time, aliquots (50 μL) were removed from the primary sample and transferred to the freezer (-80°C). Upon completion of the experiment, an equal volume (30 μL) of each sample was subjected to 12.5% SDS-PAGE. Following electrophoresis, proteins were transferred to PVDF and the membrane was probed for human tPA (1:10,000 dilution of a rabbit anti-human tPA antibody; Molecular Innovations). Protein was detected using a secondary fluorescent antibody (goat anti-rabbit IgG cy5, 1:5000 dilution) and an image of the blot was acquired using a Typhoon Variable Mode Imager (GE Healthcare).

Image Acquisition and Analysis Workflow

Digital images of stained and unstained lung and liver sections at 40X magnification were acquired on a Ti Eclipse inverted microscope (Nikon Instruments, Inc., Melville, NY, USA) using bright field optics under Kohler illumination. To acquire and quantify DAB stained images, a red filter ($655 \pm 30 \text{ nm}$), which corresponds to the absorbance peak of the background staining, and a blue filter ($480 \pm 30 \text{ nm}$), which corresponds to the absorbance peak of DAB, were used (Figure S1). The density of DAB staining is indicative of LRP1 receptor density. To quantify DAB staining density all images were analyzed with ImageJ. The red filter image was first converted to grey scale (Figure S2). Then, a threshold was applied to this image to select the pixels corresponding to the tissue region. This threshold was based on a visual inspection of the tissue sample, capturing pixel intensities that corresponded to the tissue itself. This was performed on five control lung and liver images, allowing for an average background tissue signal to be determined for each organ. The average threshold value, as determined from the

untreated tissue samples, was applied to the corresponding blue image, selecting the pixels corresponding to the darkly stained DAB positive regions. The selected pixels for the red image was used as a measure of the total area of the tissue region, and the selected pixels for the blue were used as a measure of the tissue area with DAB signal. Dividing the pixel area of DAB signal by the total tissue area was then used to calculate the % area stained measurement. For the comparative analysis of lung and liver LRP1, the area and area fraction (%area) measurements were acquired. The area captures the total image in square pixels while the %area measures the percentage of pixels that fall within the set threshold over the total area. The ratio of LRP1 positive staining was determined by dividing the pixel area of DAB signal by the total tissue area which was used to calculate the % area stained measurement. Any nonspecific background staining removed from the true LRP1 signal, by subtracting the background % tissue area with LRP1 staining measured with a negative control (unstained) set of images from the % tissue area with LRP1 staining from the experimental (DAB stained) set of images (Figure S3).

Appendix B

Supporting Information in Chapter 3

1. Synthesis of **3** (N-(4-Aryl)-2-nitroaniline).

General Procedure A: K₂CO₃ (1.76 g, 12.8 mmole) and KF (0.49 g, 12.8 mmole) was mixed well by grinding in a mortar. This mixture was added to the 20 mL microwave reaction vial. Then aniline **1** (15.3 mmole, 1.2 equivalents), followed by fluoronitrobenzene **2** (1.35 mL, 12.8 mmole) were added and the reaction mixture was irradiated under a microwave at 180°C for a total of about 16 h and monitored by TLC at regular intervals. The solid mixture was extracted with DCM (4 × 20 mL), washed with 1N HCl (2 × 30 mL), water (2 × 50 mL), dried (Na₂SO₄) and the solvent was removed under reduced pressure to yield the crude product. It was purified using flash chromatography.

General Procedure B: To a solution of aniline **1** (10 mmole) and powdered KOH (2.81g, 50 mmole) in DMSO (10 mL) was added slowly fluoronitrobenzene (1.32 mL, 12.5 mmole) over a period of 0.5h. It was stirred at room temperature for 3h. The content was poured over ice and neutralized with 2N HCl. The precipitated orange solid was filtered, washed with water (200 mL), dried under suction and then under high vacuum overnight.

2. Synthesis of **4** (N-Arylbenzene-1,2-diamine).

General Procedure C: A 250-mL round bottom flask was flushed with N₂ and then charged with the nitro compound, **3**, MeCN (60 mL) and 10% Pd/C (0.11g). It was flushed again with N₂ and sealed with rubber septum. The evacuated flask was filled with H₂ and it was stirred at RT in a H₂ atmosphere using a balloon overnight. TLC results after overnight stirring indicated completion of reaction. The solution was filtered with the aid of celite. The solvent was removed under reduced pressure to yield the compound **4**. It was purified if necessary.

3. Synthesis of **5** (3-Imino-N,5-bis(aryl)-3,5-dihydrophenazin-2-amine hydrochloride).

General Procedure D: To a solution of the diamino compound (2.9 mmole) in glacial AcOH

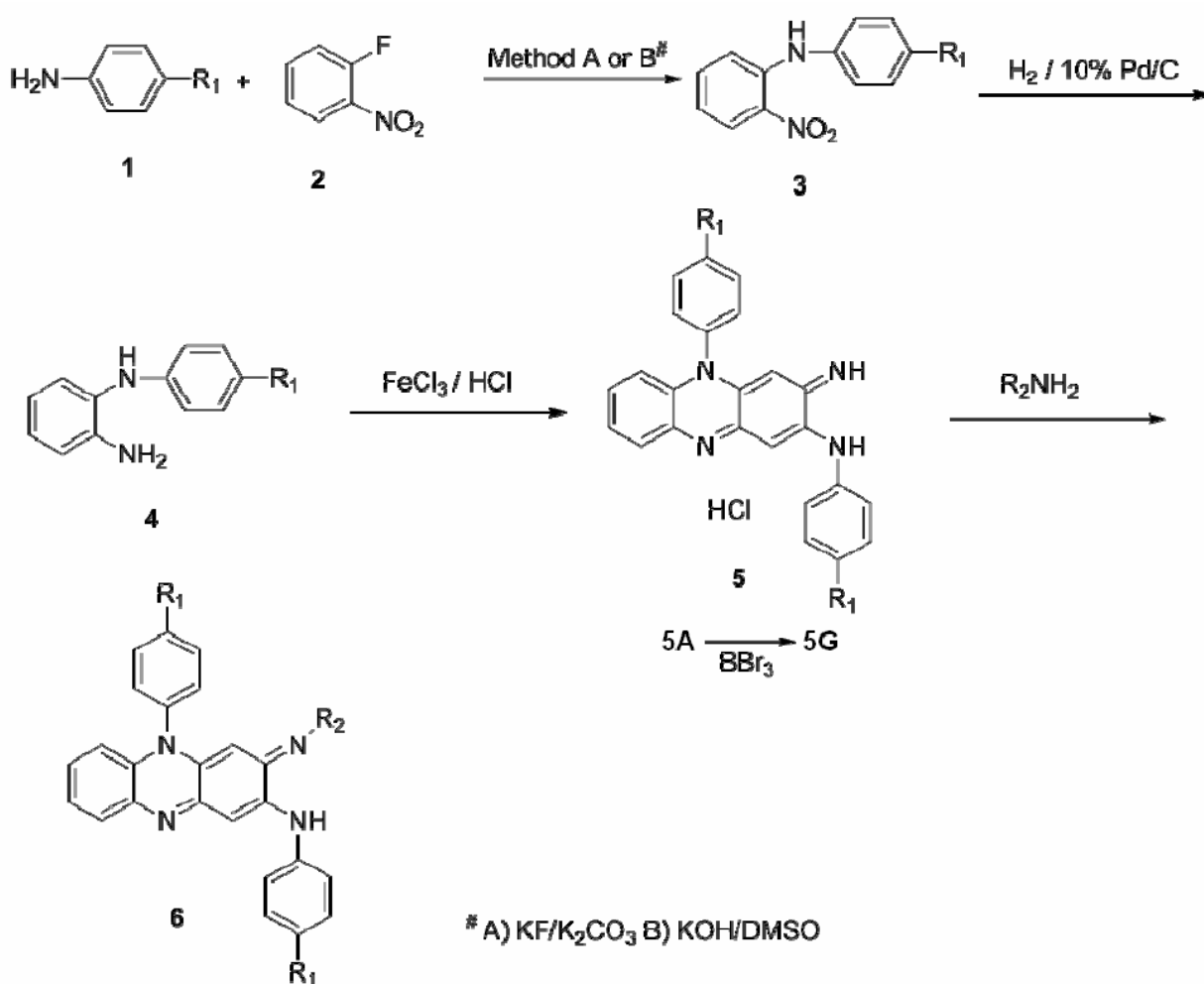
(4.5 mL) was added a solution of $\text{FeCl}_3 \cdot 6\text{H}_2\text{O}$ (8.7 mmole, 3 equivalent) in water (15 mL) and 12 N HCl (0.4 mL, 4.5 equivalent). The reaction was left stirring at room temperature overnight after dilution with 7 mL of H_2O . The reaction was further diluted with 10 mL of H_2O . After 1h, the precipitate was filtered, washed with excess water, dried under suction and then inside a vacuum desiccator.

4. Synthesis of **6** ((E)-3-(Isopropylimino)-N,5-bis(aryl)-3,5-dihydrophenazin-2-amine).

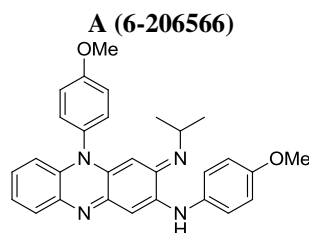
General Procedure E: The phenazine hydrochloride (0.1g) was suspended in dioxane or EtOH (1 mL). To this suspension was added isopropylamine (0.2 mL) and the mixture was heated in a sealed tube for 5 h. The solution was filtered and the flask was washed with EtOH (1 mL). The filtrate was diluted with H_2O until it becomes slightly turbid. The compound was crystallized and then recrystallized from aqueous EtOH or purified by the flash chromatography.

Figure SI 6- Synthesis scheme for phenazine compounds.

Treatment of aniline derivatives 1 with 2-fluoronitrobenzene 2 following the published procedure [12] (Method A using KF/K₂CO₃ or B using KOH/DMSO) gave the secondary amine derivatives 3 in 22 - 63% yield. Reduction of the nitro group was carried out using 10% Pd/C catalyst under hydrogen atmosphere to yield the diamine 4 in 55 - 99% yield. Then the diamine 4 was oxidised[3, 5] in aqueous ferric chloride solution to give the corresponding phenazine salts 5 in 70 - 96%. The dimethoxyphenazine salt 5A was demethylated using borontribromide in dichloromethane to give the hydroxyphenazine hydrobromide 5G in 67% yield. The phenazine salts 5 on treatment with variety of primary amines gave the corresponding phenazine derivatives 6 in 10 - 85% yield.



General procedures and characterization data of riminophenazine derivative compounds

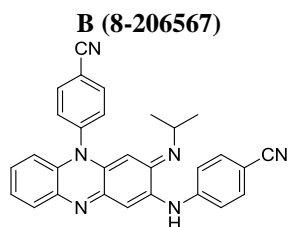


N-(4-Methoxyphenyl)-2-nitroaniline, **3A** (General Procedure A): Purified by the flash chromatography using 5-40% EtOAc/hexanes. Yield: 1.25g (63%); $^1\text{H NMR}$ (500 MHz, CDCl_3) δ 9.41 (s, 1H), 8.21 (d, $J = 8.5$ Hz, 1H), 7.35 – 7.31 (m, 1H), 7.23 – 7.19 (m, 2H), 7.03 – 7.00 (m, 1H), 6.99 – 6.95 (m, 2H), 6.75 – 6.70 (m, 1H), 3.86 (s, 3H).

N-(4-Methoxyphenyl)benzene-1,2-diamine, **4A** (General Procedure C): Purified using 5-40% EtOAc/Hexanes gradient Yield: 0.62g (59%); $^1\text{H NMR}$ (500 MHz, CDCl_3) δ 7.06 – 7.00 (m, 2H), 6.82 – 6.78 (m, 2H), 6.76 – 6.70 (m, 3H), 6.67 (td, $J = 7.5, 1.4$ Hz, 1H), 3.77 (s, 3H), 3.17 (q, $J = 7.2$ Hz, 2H) & 1.24 (t, $J = 7.2$ Hz, 3H).

3-Imino-*N*,5-bis(4-methoxyphenyl)-3,5-dihydrophenazin-2-amine hydrochloride, **5A** (General Procedure D): Yield: 1.2g (90%); MS (ESI^+), m/z : 423.2 (M+1); $^1\text{H NMR}$ (500 MHz, CD_3OD) δ 8.21 – 8.16 (m, 1H), 7.81 – 7.72 (m, 3H), 7.56 (d, $J = 1.1$ Hz, 1H), 7.44 – 7.38 (m, 2H), 7.25 – 7.21 (m, 2H), 7.18 – 7.14 (m, 1H), 7.03 – 7.00 (m, 1H), 6.98 – 6.95 (m, 1H), 6.86 – 6.83 (m, 1H), 6.39 (s, 1H), 3.91 (s, 3H) & 3.85 (s, 3H).

(*E*)-3-(Isopropylimino)-*N*,5-bis(4-methoxyphenyl)-3,5-dihydrophenazin-2-amine.[1, 2] **6A** (General Procedure E): Yield: 67 mg (66%); MS (ESI^+), m/z : 465.2 (M+1); $^1\text{H NMR}$ (400 MHz, CDCl_3) δ 7.67 (d, $J = 7.6$ Hz, 1H), 7.60 (t, $J = 8.1$ Hz, 1H), 7.23 (d, $J = 6.7$ Hz, 1H), 7.17 – 7.07 (m, 3H), 6.98 (d, $J = 7.9$ Hz, 1H), 6.93 – 6.81 (m, 4H), 6.62 (d, $J = 8.2, 2.4$ Hz, 1H), 6.52 (d, $J = 8.3$ Hz, 1H), 5.33 (s, 1H), 3.83 (d, $J = 11.8$ Hz, 6H), 3.44 (h, $J = 6.3$ Hz, 1H) & 1.07 (t, $J = 6.5$ Hz, 6H).

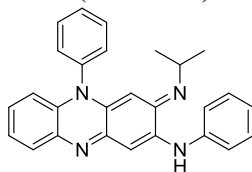


4-((2-Nitrophenyl)amino)benzonitrile, **3B** (General Procedure A): Purified by the flash chromatography using 5-40% EtOAc/hexanes. Yield: 0.84g (28%); $^1\text{H NMR}$ (500 MHz, CDCl_3) δ 9.43 (s, 1H), 8.23 (dd, $J = 8.6, 1.5$ Hz, 1H), 7.66 (d, $J = 8.2$ Hz, 2H), 7.54 – 7.44 (m, 2H), 7.33 (d, $J = 8.7$ Hz, 2H), 7.02 – 6.95 (m, 1H).

4-((2-Aminophenyl)amino)benzonitrile, **4B** (General Procedure C): Yield: 0.38g (99%); $^1\text{H NMR}$ (500 MHz, CDCl_3) δ 7.45 (d, $J = 8.5$ Hz, 2H), 7.17 – 7.07 (m, 2H), 6.84 (d, $J = 7.8$ Hz, 1H), 6.82 – 6.78 (m, 1H), 6.68 (d, $J = 8.5$ Hz, 2H), 5.62 (s, 1H) & 3.79 (s, 2H).

4-((5-(4-Cyanophenyl)-3-imino-3,5-dihydrophenazin-2-yl)amino)benzonitrile hydrochloride, **5B** (General Procedure D): Yield: 0.33g (85%); MS (ESI^+), m/z : 413 (M+1); $^1\text{H NMR}$ (500 MHz, $(\text{CD}_3)_2\text{SO}$) δ 10.13 (s, 1H), 9.56 – 9.37 (m, 2H), 8.45 (d, $J = 8.1$ Hz, 2H), 8.30 – 8.23 (m, 1H), 7.99 (d, $J = 8.0$ Hz, 2H), 7.88 (d, $J = 8.3$ Hz, 2H), 7.82 – 7.77 (m, 2H), 7.71 (s, 1H), 7.62 (d, $J = 8.3$ Hz, 2H), 7.10 – 7.05 (m, 1H), 6.18 (s, 1H).

(*E*)-4-((5-(4-Cyanophenyl)-3-(isopropylimino)-3,5-dihydrophenazin-2-yl)amino)benzonitrile, **6B** (General Procedure E): Yield: 49 mg (48%); MS (ESI^+), m/z : 455.2 (M+1); $^1\text{H NMR}$ (400 MHz, CDCl_3) δ 8.06 (d, $J = 8.1$ Hz, 2H), 7.73 (d, $J = 7.8$ Hz, 1H), 7.63 (d, $J = 8.3$ Hz, 2H), 7.53 (d, $J = 8.1$ Hz, 2H), 7.41 (d, $J = 8.4$ Hz, 2H), 7.24 – 7.14 (m, 2H), 7.03 (s, 1H), 6.37 (d, $J = 8.1$ Hz, 1H), 5.18 (s, 1H), 3.41 (p, $J = 6.1$ Hz, 1H), 1.08 (d, $J = 6.2$ Hz, 6H).

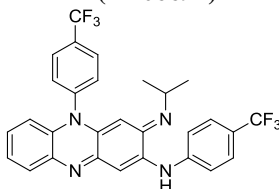
C (12-206693)

2-Nitro-N-phenylaniline, **3C** (General Procedure A): Purified by the flash chromatography using 3% EtOAc/hexanes. Yield: 0.52g (23%); $^1\text{H NMR}$ (400 MHz, CDCl_3) δ 9.49 (s, 1H), 8.20 (dd, $J = 8.6, 1.7$ Hz, 1H), 7.44 – 7.34 (m, 3H), 7.30 – 7.20 (m, 4H), 6.77 (ddd, $J = 8.4, 6.9, 1.4$ Hz, 1H).

N-Phenylbenzene-1,2-diamine, **4C** (General Procedure C): Yield: 0.41g (97%); $^1\text{H NMR}$ (400 MHz, CDCl_3) δ 7.26 – 7.17 (m, 2H), 7.12 (dd, $J = 7.8, 1.5$ Hz, 1H), 7.06 – 6.97 (m, 1H), 6.86 – 6.71 (m, 5H), 5.17 (s, 1H), 3.76 (s, 2H).

3-Imino-N,5-diphenyl-3,5-dihydrophenazin-2-amine hydrochloride, **5C** (General Procedure D): Yield: 0.32g (74%); $^1\text{H NMR}$ (400 MHz, $(\text{CD}_3)_2\text{SO}$) δ 9.67 (s, 1H), 9.38 (s, 2H), 8.21 – 8.14 (m, 1H), 7.95 – 7.83 (m, 3H), 7.77 – 7.70 (m, 4H), 7.55 – 7.46 (m, 4H), 7.34 (s, 1H), 7.29 – 7.24 (m, 1H), 7.02 – 6.95 (m, 1H), 6.21 (s, 1H).

(E)-3-(Isopropylimino)-N,5-diphenyl-3,5-dihydrophenazin-2-amine, [1] **6C** (General Procedure E): Yield: 65 mg (85%); $^1\text{H NMR}$ (400 MHz, CDCl_3) δ 7.76 – 7.59 (m, 4H), 7.49 – 7.25 (m, 7H), 7.17 – 7.04 (m, 3H), 6.89 (s, 1H), 6.45 (d, $J = 8.1$ Hz, 1H), 5.25 (s, 1H), 3.39 (d, $J = 6.2$ Hz, 1H), 1.04 (d, $J = 6.2$ Hz, 6H).

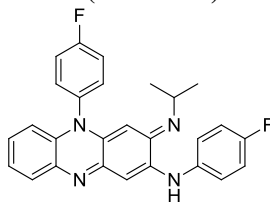
D (4-206694)

2-Nitro-N-(4-(trifluoromethyl)phenyl)aniline, **3D** (General Procedure A): Purified by the flash chromatography using 15-65% EtOAc/hexanes. Yield: 0.15g (7%); $^1\text{H NMR}$ (400 MHz, CDCl_3) δ 9.47 (s, 1H), 8.23 (d, $J = 8.5$ Hz, 1H), 7.65 (d, $J = 8.3$ Hz, 2H), 7.48 – 7.43 (m, 1H), 7.40 – 7.34 (m, 3H), 6.93 – 6.87 (m, 1H).

N-(4-(Trifluoromethyl)phenyl)benzene-1,2-diamine, **4D** (General Procedure C): Yield: 0.13g (99%); $^1\text{H NMR}$ (400 MHz, CDCl_3) δ 7.41 (d, $J = 8.6$ Hz, 2H), 7.14 – 7.03 (m, 2H), 6.85 – 6.72 (m, 2H), 6.70 (d, $J = 8.6$ Hz, 2H), 5.41 (s, 1H), 3.76 (s, 2H).

3-Imino-N,5-bis(4-(trifluoromethyl)phenyl)-3,5-dihydrophenazin-2-amine hydrochloride, **5D** (General Procedure D): Yield: 0.12g (94%); $^1\text{H NMR}$ (400 MHz, $(\text{CD}_3)_2\text{SO}$) δ 9.75 (s, 1H), 9.40 – 9.22 (m, 2H), 8.34 (d, $J = 8.1$ Hz, 2H), 8.27 – 8.23 (m, 1H), 8.22 – 8.17 (m, 1H), 8.01 (d, $J = 8.1$ Hz, 2H), 7.96 – 7.90 (m, 1H), 7.85 – 7.77 (m, 4H), 7.73 – 7.68 (m, 1H), 7.66 – 7.62 (m, 3H), 7.47 (t, $J = 8.1$ Hz, 1H), 7.28 (s, 1H), 7.05 (dd, $J = 7.0, 3.0$ Hz, 1H), 6.18 (s, 1H).

(E)-3-(Isopropylimino)-N,5-bis(4-(trifluoromethyl)phenyl)-3,5-dihydrophenazin-2-amine, **6D** (General Procedure E): Yield: 52 mg (52%); MS (ESI^+), m/z : 541.1 ($\text{M}+1$); $^1\text{H NMR}$ (400 MHz, CDCl_3) δ 8.02 (d, $J = 8.2$ Hz, 2H), 7.72 (dd, $J = 7.8, 1.3$ Hz, 1H), 7.61 (d, $J = 8.4$ Hz, 2H), 7.53 (d, $J = 8.1$ Hz, 2H), 7.44 (d, $J = 8.4$ Hz, 2H), 7.23 – 7.12 (m, 2H), 7.00 (s, 1H), 6.39 (d, $J = 7.9$ Hz, 1H), 5.22 (s, 1H), 3.42 (hept, $J = 6.3$ Hz, 1H), 1.08 (d, $J = 6.2$ Hz, 6H), 9.07 – 8.48 (m, 1H).

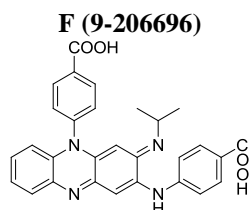
E (11-206695)

N-(4-Fluorophenyl)-2-nitroaniline, **3E** (General Procedure B): Yield: 0.52g (22%); ¹H NMR (400 MHz, CDCl₃) δ 9.40 (s, 1H), 8.21 (dd, *J* = 8.6, 1.6 Hz, 1H), 7.40 – 7.33 (m, 1H), 7.25 (dd, *J* = 9.8, 3.8 Hz, 2H), 7.12 (t, *J* = 8.5 Hz, 2H), 7.05 (dd, *J* = 8.6, 1.3 Hz, 1H), 6.81 – 6.74 (m, 1H).

N-(4-Fluorophenyl)benzene-1,2-diamine, **4E** (General Procedure C): Purified using 12-15% EtOAc/Hexanes gradient. Yield: 0.36g (79%); ¹H NMR (400 MHz, CDCl₃) δ 7.05 (dd, *J* = 7.8, 1.5 Hz, 1H), 7.02 – 6.97 (m, 1H), 6.95 – 6.87 (m, 2H), 6.83 – 6.64 (m, 4H), 5.06 (s, 1H), 3.74 (s, 2H).

3-Imino-*N*,5-bis(4-fluorophenyl)-3,5-dihydrophenazin-2-amine hydrochloride, **5E** (General Procedure D): Yield: 0.36g (96%); ¹H NMR (500 MHz, (CD₃)₂SO) δ 9.56 (s, 1H), 9.41 – 9.17 (m, 2H), 8.18 (d, *J* = 7.3 Hz, 1H), 7.84 – 7.71 (m, 6H), 7.52 – 7.47 (m, 2H), 7.41 – 7.34 (m, 2H), 7.25 – 7.17 (m, 1H), 7.07 (d, *J* = 7.6 Hz, 1H), 6.24 – 6.19 (m, 1H).

(*E*)-*N*,5-bis(4-Fluorophenyl)-3-(isopropylimino)-3,5-dihydrophenazin-2-amine.[2] **6E** (General Procedure E): Yield: 90 mg (59%); MS (ESI⁺), *m/z*: 441.1 (M+1); ¹H NMR (400 MHz, CDCl₃) δ 7.67 (dd, *J* = 7.8, 1.7 Hz, 1H), 7.45 – 7.38 (m, 2H), 7.36 – 7.29 (m, 4H), 7.20 – 7.02 (m, 5H), 6.71 (s, 1H), 6.45 (d, *J* = 8.0 Hz, 1H), 5.26 (s, 1H), 3.45 (hept, *J* = 6.4 Hz, 1H), 1.08 (d, *J* = 6.3 Hz, 6H).

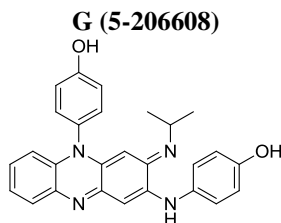


4-((2-Nitrophenyl)amino)benzoic acid, **3F** (General Procedure B): Yield: 1.55g (60%) (It's a mixture of about 1:3 ester/carboxylic acid and used in subsequent transformation as such without further purification); ¹H NMR (500 MHz, (CD₃)₂SO) δ 12.64 (s, 1H), 9.31 (s, 1H), 8.16 – 8.04 (m, 1H), 7.93 – 7.84 (m, 2H), 7.63 – 7.44 (m, 2H), 7.38 – 7.26 (m, 2H), 7.13 – 7.00 (m, 1H).

4-((2-Aminophenyl)amino)benzoic acid, **4F** (General Procedure C): Crystallized from aqueous Methanol. Yield: 0.24g (55%); ¹H NMR (500 MHz, (CD₃)₂SO) δ 12.17 (s, 1H), 7.86 (d, *J* = 28.3 Hz, 1H), 7.69 (d, *J* = 8.7 Hz, 2H), 7.01 (d, *J* = 7.8 Hz, 1H), 6.96 – 6.89 (m, 1H), 6.79 – 6.74 (m, 1H), 6.65 (d, *J* = 8.7 Hz, 2H), 4.95 – 4.69 (m, 2H), 6.61 – 6.53 (m, 1H).

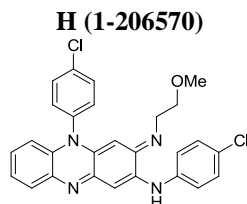
4-((5-(4-Carboxyphenyl)-3-imino-3,5-dihydrophenazin-2-yl)amino)benzoic acid hydrochloride, **5F** (General Procedure D): Yield: 0.17g (70%); ¹H NMR (400 MHz, (CD₃)₂SO) δ 13.05 (s, 2H), 9.76 (s, 1H), 9.33 (s, 2H), 8.45 – 8.40 (m, 2H), 8.28 – 8.23 (m, 1H), 8.03 (d, *J* = 8.5 Hz, 2H), 7.87 (d, *J* = 8.4 Hz, 2H), 7.82 – 7.74 (m, 2H), 7.68 – 7.64 (m, 1H), 7.55 (d, *J* = 8.1 Hz, 2H), 7.11 – 7.03 (m, 1H), 6.23 – 6.19 (m, 1H).

(*E*)-4-((5-(4-Carboxyphenyl)-3-(isopropylimino)-3,5-dihydrophenazin-2-yl)amino)benzoic acid, **6F** (General Procedure E): Yield: 90 mg (59%); MS(ESI⁺), *m/z*: 494.1 (M+1); ¹H NMR (400 MHz, CD₃OD) δ 8.38 (d, *J* = 8.0 Hz, 2H), 8.27 – 8.19 (m, 1H), 8.07 (d, *J* = 8.2 Hz, 2H), 7.81 – 7.72 (m, 2H), 7.69 (s, 1H), 7.59 (d, *J* = 7.9 Hz, 2H), 7.40 (d, *J* = 8.2 Hz, 2H), 7.26 – 7.16 (m, 1H), 6.34 (s, 1H), 1.28 (d, *J* = 6.6 Hz, 6H).

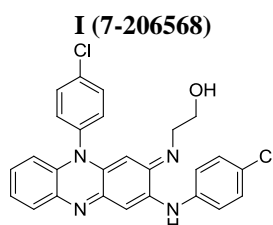


Method for chemical synthesis of 4-((5-(4-Hydroxyphenyl)-3-imino-3,5-dihydrophenazin-2-yl)amino)phenol hydrobromide, **5G**: To the solution of the phenazine **5A** (56 mg) in DCM (3 mL) was added BBr₃ in DCM (1 mL) and the solution was stirred at RT for 4 days. Water (4 mL) was added to quench the reaction, the precipitate was filtered, washed with water (15 mL) and dried under vacuum desiccator for 2 days. Yield: 39 mg (67%); MS (ESI⁺), *m/z*: 395.1 (M+1); ¹H NMR (400 MHz, (CD₃)₂SO) δ 10.38 (s, 1H), 9.74 (s, 1H), 9.27 (s, 1H), 8.70 (s, 1H), 8.20 (s, 1H), 7.81 – 7.64 (m, 3H), 7.42 (s, 1H), 7.34 – 7.19 (m, 2H), 7.16 – 7.05 (m, 3H), 6.85 (s, 2H), 6.73 – 6.60 (m, 1H), 6.31 (s, 1H).

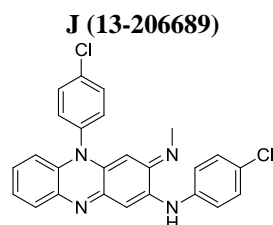
(*E*)-4-((5-(4-Hydroxyphenyl)-3-(isopropylimino)-3,5-dihydrophenazin-2-yl)amino)phenol, **6G** (General Procedure E): Purified using 40-100% EtOAc/Hexanes gradient. Yield: 19 mg (65%); MS (ESI⁺), *m/z*: 437.2 (M+1); ¹H NMR (400 MHz, (CD₃)₂SO) δ 10.03 (s, 1H), 9.50 (s, 1H), 7.60 (d, *J* = 7.5 Hz, 1H), 7.57 – 7.51 (m, 1H), 7.21 – 7.00 (m, 5H), 6.84 (d, *J* = 7.9 Hz, 1H), 6.82 – 6.80 (m, 1H), 6.78 – 6.74 (m, 2H), 6.72 – 6.69 (m, 1H), 6.49 (t, *J* = 8.3 Hz, 2H), 5.26 (s, 1H), 3.33 (q, *J* = 6.8 Hz, 1H), 1.03 – 0.98 (m, 6H).



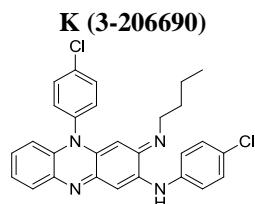
(*E*)-*N*,5-bis(4-chlorophenyl)-3-((2-methoxyethyl)imino)-3,5-dihydrophenazin-2-amine,[1] **6H** (General Procedure E): Purified using 10-50% EtOAc/Hexanes gradient. Yield: 18 mg (17%); MS (ESI⁺), *m/z*: 490.1 & 492.1 (M+1); ¹H NMR (400 MHz, CDCl₃) δ 7.74 – 7.67 (m, 3H), 7.38 – 7.26 (m, 7H), 7.24 – 7.09 (m, 3H), 6.84 (s, 1H), 6.50 – 6.44 (m, 1H), 5.28 (s, 1H), 3.72 (t, *J* = 6.2 Hz, 2H), 3.40 (s, 3H), 3.31 (t, *J* = 6.2 Hz, 2H).



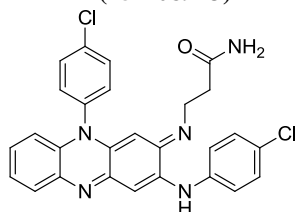
(*E*)-2-((10-(4-Chlorophenyl)-3-((4-chlorophenyl)amino)phenazin-2(10H)-ylidene)amino)ethanol, [3] **6I** (General Procedure E): Yield: 41 mg (40%); MS (ESI⁺), *m/z*: 475.1 & 477.1 (M+1); ¹H NMR (400 MHz, CDCl₃) δ 7.74 – 7.65 (m, 3H), 7.33 – 7.28 (m, 2H), 7.27 – 7.21 (m, 5H), 7.21 – 7.07 (m, 3H), 6.83 (s, 1H), 6.47 (d, *J* = 7.7 Hz, 1H), 5.25 (s, 1H), 3.88 (t, *J* = 5.3 Hz, 2H), 3.23 (t, *J* = 5.3 Hz, 2H).



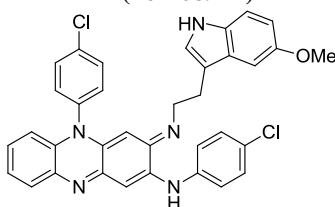
(*E*)-*N*,5-Bis(4-chlorophenyl)-3-(methylimino)-3,5-dihydrophenazin-2-amine,[3] **6J** (General Procedure E): Purified using 15 - 60% EtOAc/Hexanes gradient. Yield: 28 mg (29%); MS (ESI⁺), *m/z*: 446.1 & 448.1 (M+1); ¹H NMR (400 MHz, CDCl₃) δ 7.69 (d, *J* = 8.6 Hz, 3H), 7.35 – 7.24 (m, 7H), 7.20 – 7.11 (m, 2H), 6.83 (s, 1H), 6.46 (d, *J* = 8.1 Hz, 1H), 5.27 (s, 1H), 3.06 (s, 3H).



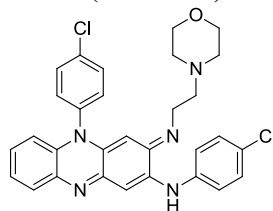
(*E*)-3-(Butylimino)-*N*,5-bis(4-chlorophenyl)-3,5-dihydrophenazin-2-amine,[3] **6K** (General Procedure E): Purified using 35 - 45% EtOAc/Hexanes gradient. Yield: 38 mg (37%); MS (ESI⁺), *m/z*: 487.1 & 489.1 (M+1); ¹H NMR (400 MHz, CDCl₃) δ 7.72 – 7.64 (m, 3H), 7.32 – 7.25 (m, 6H), 7.19 – 7.08 (m, 3H), 6.81 (s, 1H), 6.44 (d, *J* = 8.0 Hz, 1H), 5.24 (s, 1H), 3.14 (t, *J* = 6.9 Hz, 2H), 1.61 – 1.55 (m, 2H), 1.38 – 1.31 (m, 2H), 0.87 (t, *J* = 7.3 Hz, 3H).

L (15-208923)

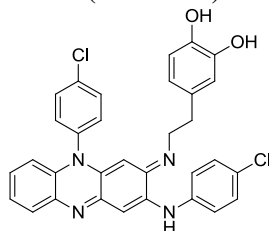
(*E*)-3-((10-(4-Chlorophenyl)-3-((4-chlorophenyl)amino)phenazin-2(10*H*)-ylidene)amino)-propanamide, **6L**
 (General Procedure E): Yield: 18 mg (24%); MS(ESI⁺), *m/z*: 502.0 & 504.0 (M+1); ¹H NMR (400 MHz, CDCl₃) δ 7.77 (d, *J* = 7.9 Hz, 1H), 7.71 (d, *J* = 8.6 Hz, 2H), 7.34 – 7.25 (m, 8H), 7.23 – 7.18 (m, 2H), 6.91 (s, 1H), 6.54 (d, *J* = 8.3 Hz, 1H), 5.32 (s, 2H), 3.38 (t, *J* = 6.2 Hz, 2H), 2.65 (t, *J* = 6.2 Hz, 2H).

M (16-208922)

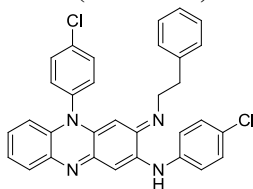
(*E*)-*N*,5-Bis(4-chlorophenyl)-3-((2-(5-methoxy-1*H*-indol-3-yl)ethyl)imino)-3,5-dihydrophenazin-2-amine, **6M**
 (General Procedure E): Yield: 26 mg (20%); MS(ESI⁺), *m/z*: 604.0 & 606.0 (M+1); ¹H NMR (400 MHz, CDCl₃) δ 7.84 (s, 1H), 7.69 (d, *J* = 8.1 Hz, 1H), 7.62 (d, *J* = 8.4 Hz, 2H), 7.32 (d, *J* = 8.7 Hz, 2H), 7.25 – 7.21 (m, 3H), 7.20 – 7.09 (m, 5H), 7.06 – 7.04 (m, 1H), 6.90 – 6.83 (m, 3H), 6.41 (d, *J* = 8.1 Hz, 1H), 5.19 (s, 1H), 3.82 (s, 3H), 3.49 (t, *J* = 7.0 Hz, 2H), 3.07 (t, *J* = 7.0 Hz, 2H).

N (17-208921)

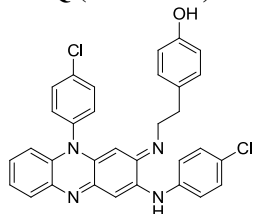
(*E*)-*N*,5-Bis(4-chlorophenyl)-3-((2-morpholinoethyl)imino)-3,5-dihydrophenazin-2-amine,[4] **6N** (General Procedure E): Yield: 38 mg (33%); MS(ESI⁺), *m/z*: 544.0 & 546.0 (M+1); ¹H NMR (400 MHz, CDCl₃) δ 7.72 – 7.66 (m, 2H), 7.36 – 7.24 (m, 7H), 7.23 – 7.06 (m, 3H), 6.84 (s, 1H), 6.45 (d, *J* = 8.2 Hz, 1H), 5.24 (s, 1H), 3.74 – 3.65 (m, 4H), 3.33 (t, *J* = 7.3 Hz, 2H), 2.68 (t, *J* = 7.3 Hz, 2H), 2.50 – 2.40 (m, 4H).

O (19-209042)

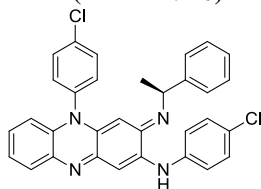
(*E*)-4-(2-((10-(4-Chlorophenyl)-3-((4-chlorophenyl)amino)phenazin-2(10*H*)-ylidene)amino)-ethyl)benzene-1,2-diol, **6O** (General Procedure E): Yield: 13 mg (17%); MS(ESI⁺), *m/z*: 567.0 & 569.0 (M+1); ¹H NMR (400 MHz, CD₃OD) δ 8.22 – 8.17 (m, 1H), 7.98 – 7.92 (m, 2H), 7.78 – 7.73 (m, 2H), 7.59 – 7.55 (m, 2H), 7.51 (s, 1H), 7.48 – 7.45 (m, 2H), 7.36 – 7.32 (m, 2H), 7.17 – 7.13 (m, 1H), 6.67 (d, *J* = 7.9 Hz, 1H), 6.55 – 6.52 (m, 1H), 6.28 – 6.22 (m, 1H), 5.89 (s, 1H), 3.47 (d, *J* = 7.3 Hz, 2H), 2.72 (t, *J* = 7.3 Hz, 2H).

P (10-206691)

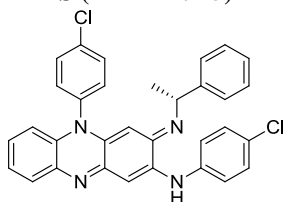
(*E*)-*N*,5-Bis(4-chlorophenyl)-3-(phenethylimino)-3,5-dihydrophenazin-2-amine,[2, 5] **6P** (General Procedure E): Yield: 53 mg (46%); MS (ESI⁺), *m/z*: 535.0 & 537.0 (M+1); ¹H NMR (400 MHz, CDCl₃) δ 7.75 – 7.65 (m, 3H), 7.37 – 7.26 (m, 8H), 7.23 – 7.16 (m, 3H), 7.15 – 7.09 (m, 3H), 6.86 (s, 1H), 6.46 (d, *J* = 8.3 Hz, 1H), 5.28 (s, 1H), 3.44 (t, *J* = 7.7 Hz, 2H), 2.88 (t, *J* = 7.7 Hz, 2H).

Q (14-206571)

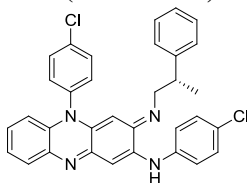
(*E*)-4-(2-((10-(4-chlorophenyl)-3-((4-chlorophenyl)amino)phenazin-2(10*H*)-ylidene)amino)-ethyl)phenol, **6Q** (General Procedure E): Purified using 12 - 60% EtOAc/Hexanes gradient. Yield: 12 mg (10%); MS (ESI⁺), *m/z*: 551.1 & 553.1 (M+1); ¹H NMR (400 MHz, (CD₃)₂SO) δ 7.92 (dd, *J* = 8.7, 2.2 Hz, 2H), 7.70 (s, 1H), 7.60 – 7.53 (m, 2H), 7.53 – 7.45 (m, 2H), 7.44 – 7.39 (m, 2H), 7.30 (s, 2H), 6.87 – 6.77 (m, 3H), 6.72 – 6.67 (m, 2H), 6.55 (s, 1H), 5.28 (s, 1H), 3.32 (t, *J* = 7.9 Hz, 2H), 2.59 (t, *J* = 7.8 Hz, 2H).

R (21L-211916)

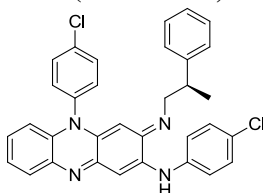
(*S,E*)-*N*,5-Bis(4-chlorophenyl)-3-((1-phenylethyl)imino)-3,5-dihydrophenazin-2-amine,[6] **6R** (General Procedure E): Yield: 15 mg (18%); MS(ESI⁺), *m/z*: 535.0 & 537.0 (M+1); ¹H NMR (400 MHz, CDCl₃) δ 7.77 – 7.66 (m, 2H), 7.58 (d, *J* = 8.6 Hz, 1H), 7.34 – 7.27 (m, 5H), 7.23 (d, *J* = 7.3 Hz, 2H), 7.20 – 7.05 (m, 6H), 6.97 (d, *J* = 8.5 Hz, 1H), 6.85 (s, 1H), 6.47 (d, *J* = 8.2 Hz, 1H), 5.22 (s, 1H), 4.34 (q, *J* = 6.6 Hz, 1H), 1.50 (d, *J* = 6.6 Hz, 3H).

S (21R-211915)

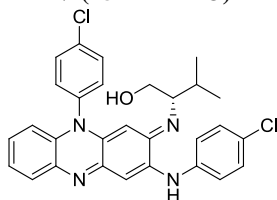
(*R,E*)-*N*,5-Bis(4-chlorophenyl)-3-((1-phenylethyl)imino)-3,5-dihydrophenazin-2-amine,[6] **6S** (General Procedure E): Yield: 15 mg (18%); MS(ESI⁺), *m/z*: 535.0 & 537.0 (M+1); ¹H NMR (500 MHz, CDCl₃) δ 7.74 (d, *J* = 7.9 Hz, 1H), 7.71 (d, *J* = 7.9 Hz, 1H), 7.60 (d, *J* = 8.3 Hz, 1H), 7.38 – 7.29 (m, 6H), 7.26 – 7.23 (m, 2H), 7.21 – 7.17 (m, 2H), 7.16 – 7.12 (m, 1H), 7.10 – 7.06 (m, 2H), 7.01 – 6.97 (m, 1H), 6.87 (s, 1H), 6.49 (d, *J* = 8.3 Hz, 1H), 5.23 (s, 1H), 4.35 (q, *J* = 6.6 Hz, 1H), 1.51 (d, *J* = 6.5 Hz, 3H).

T (22L-212016)

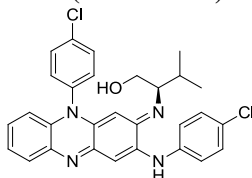
(*S,E*)-*N*,5-Bis(4-chlorophenyl)-3-((2-phenylpropyl)imino)-3,5-dihydrophenazin-2-amine, **6T** (General Procedure E): Yield: 35 mg (60%); MS (ESI⁺), *m/z*: 549.1 & 551.1 (M+1); ¹H NMR (500 MHz, CDCl₃) δ 7.76 – 7.68 (m, 3H), 7.36 – 7.28 (m, 6H), 7.27 – 7.12 (m, 8H), 6.86 (s, 1H), 6.45 (d, *J* = 8.2 Hz, 1H), 5.25 (s, 1H), 3.33 (d, *J* = 6.4 Hz, 2H), 3.08 (h, *J* = 6.8 Hz, 1H), 1.35 (d, *J* = 6.9 Hz, 3H).

U (22R-212017)

(*R,E*)-*N*,5-Bis(4-chlorophenyl)-3-((2-phenylpropyl)imino)-3,5-dihydrophenazin-2-amine, **6U** (General Procedure E): Yield: 35 mg (60%); MS (ESI⁺), *m/z*: 549.1 & 551.1 (M+1); ¹H NMR (500 MHz, CDCl₃) δ 7.75 – 7.69 (m, 3H), 7.36 – 7.28 (m, 6H), 7.26 – 7.13 (m, 8H), 6.86 (s, 1H), 6.45 (d, *J* = 8.2 Hz, 1H), 5.25 (s, 1H), 3.32 (d, *J* = 6.8 Hz, 2H), 3.08 (h, *J* = 6.8 Hz, 1H), 1.34 (d, *J* = 6.8 Hz, 3H).

V (25L-212173)

(*S,E*)-2-((10-(4-Chlorophenyl)-3-((4-chlorophenyl)amino)phenazin-2(10*H*)-ylidene)amino)-3-methylbutan-1-ol, **6V** (General Procedure E): Purified using 15 - 50% EtOAc/Hexanes gradient. Yield: 54 mg (49%); MS (ESI⁺), *m/z*: 517.13 & 519.13 (M+1); ¹H NMR (400 MHz, CDCl₃) δ 7.77 – 7.65 (m, 3H), 7.42 – 7.08 (m, 10H), 6.87 (s, 1H), 6.48 (d, *J* = 7.9 Hz, 1H), 5.37 (s, 1H), 3.77 – 3.64 (m, 2H), 3.24 – 3.14 (m, 1H), 1.89 – 1.72 (m, 1H), 0.88 – 0.73 (m, 6H).

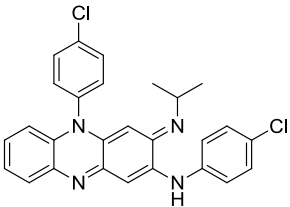
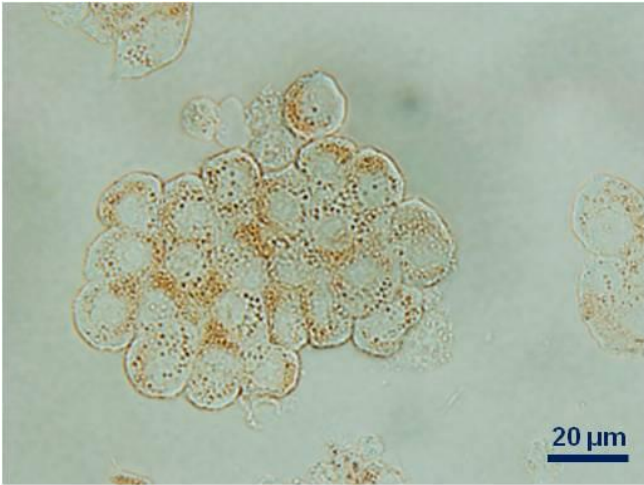
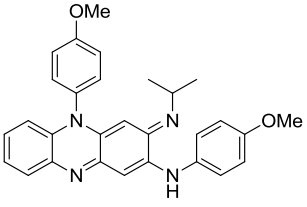
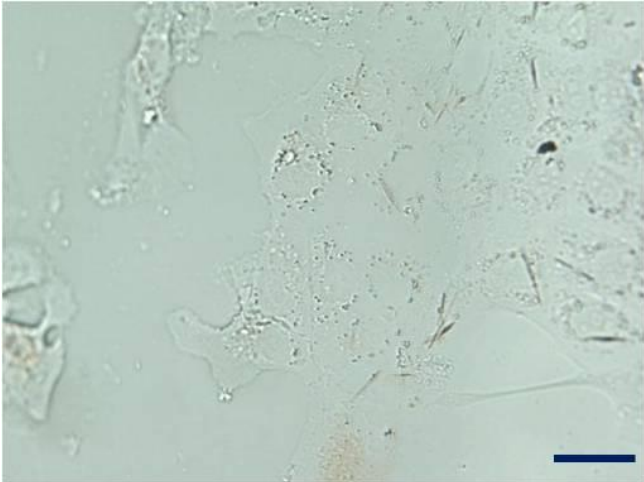
W (25R-212172)

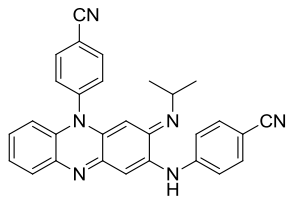
(*R,E*)-2-((10-(4-Chlorophenyl)-3-((4-chlorophenyl)amino)phenazin-2(10*H*)-ylidene)amino)-3-methylbutan-1-ol, **6W** (General Procedure E): Purified using 25 - 50% EtOAc/Hexanes gradient. Yield: 46 mg (42%); MS (ESI⁺), *m/z*: 517.16 & 519.17 (M+1); ¹H NMR (400 MHz, CDCl₃) δ 7.74 – 7.65 (m, 3H), 7.36 – 7.12 (m, 10H), 6.87 (s, 1H), 6.48 (d, *J* = 8.1 Hz, 1H), 5.37 (s, 1H), 3.75 – 3.65 (m, 2H), 3.24 – 3.13 (m, 1H), 1.88 – 1.72 (m, 1H), 0.87 – 0.74 (m, 6H).

Table S1- Calculated physicochemical properties, predicted cell uptake and subcellular localization properties of clofazimine and related phenazine analogs with chlorophenyl substitutions.

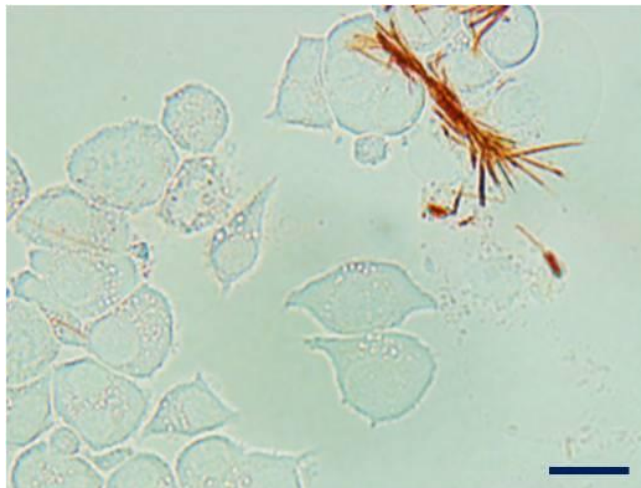
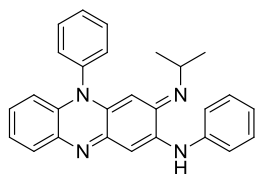
Chemical ID	R ₁	R ₂	Mol.wt	pKa	logP	Predicted ease of cell entry	Predicted intracellular localization
CFZ	Cl	-CH(Me) ₂	473.4	pK _{a1} = 9.29 pK _{a2} = 2.31	7.30	Poor-Moderate <i>Free base trapped in plasma membrane</i>	E G L M P
A	OMe	-CH(Me) ₂	464.6	pK _{a1} = 9.68 pK _{a2} = 2.35	5.78	Moderate <i>Free base membrane bound</i>	E G L M
B	CN	-CH(Me) ₂	454.5	pK _{a1} = 9.35 pK _{a2} = 2.30	5.81	Moderate <i>Free base membrane bound</i>	E G L M
C	H	-CH(Me) ₂	404.5	pK _{a1} = 10.06 pK _{a2} = 2.31	6.10	Moderate? <i>Free base membrane bound</i>	E G L M
D	CF ₃	-CH(Me) ₂	540.5	pK _{a1} = 8.88 pK _{a2} = 2.32	7.85	Poor <i>Free base trapped in plasma membrane</i>	E G L M P
E	F	-CH(Me) ₂	440.5	pK _{a1} = 9.30 pK _{a2} = 2.31	6.38	Moderate <i>Free base membrane bound</i>	E G L M
F	COOH	-CH(Me) ₂	492.5	pK _{a1} = 9.77 pK _{a2} = 2.29	5.41	Poor <i>A dianionic species is membrane impermeable</i>	Cytosol
G	OH	-CH(Me) ₂	436.5	pK _{a1} = 9.49 pK _{a2} = 2.35	5.49	Moderate-good <i>Free base near bound/permeable boundary</i>	E G L M

Table S2- Observed cellular staining pattern following 72 hour incubation with clofazimine and related phenazine analogs with chlorophenyl substitutions. Scale bar is 20 μm .

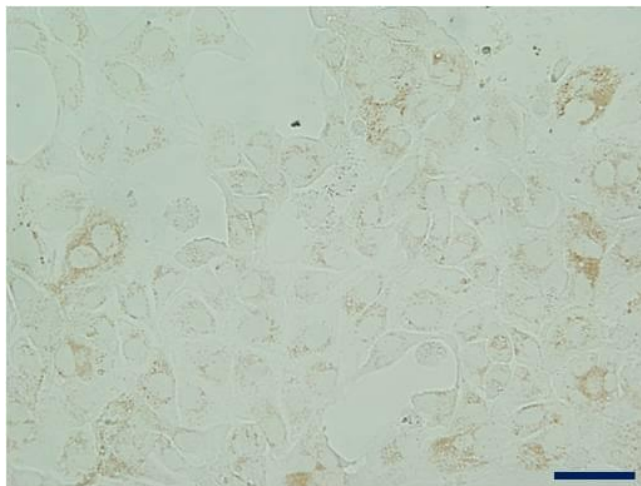
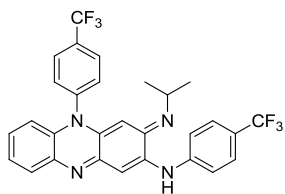
ID	Notes	Transmitted microscopy images
CFZ	<div data-bbox="305 411 592 615"></div> <p data-bbox="302 621 630 772">Orange-brown staining pattern associated with perinuclear cytoplasmic vesicles. Cells were homogeneously stained. Inferred uptake: Moderate.</p>	
A	<div data-bbox="305 915 609 1119"></div> <p data-bbox="302 1119 630 1207">Compound did not exhibit any intracellular staining pattern. Inferred uptake: Slow.</p>	

B

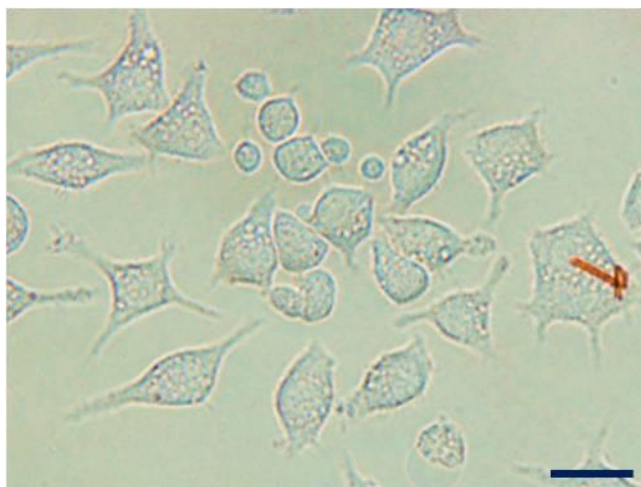
Compound formed large extracellular crystals. No intracellular staining pattern. Inferred uptake: Very slow.

**C**

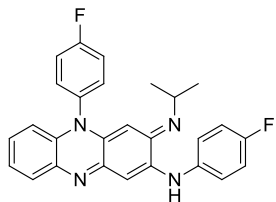
Very faint, brown perinuclear staining pattern observed across all cells. Inferred uptake: Slow.

**D**

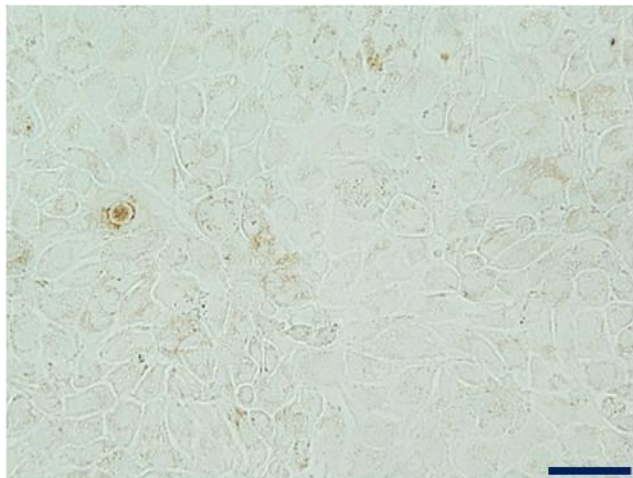
No intracellular staining pattern observed. Small percentage of cells with orange crystals. Inferred uptake: Very slow.



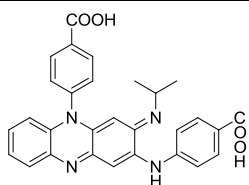
E



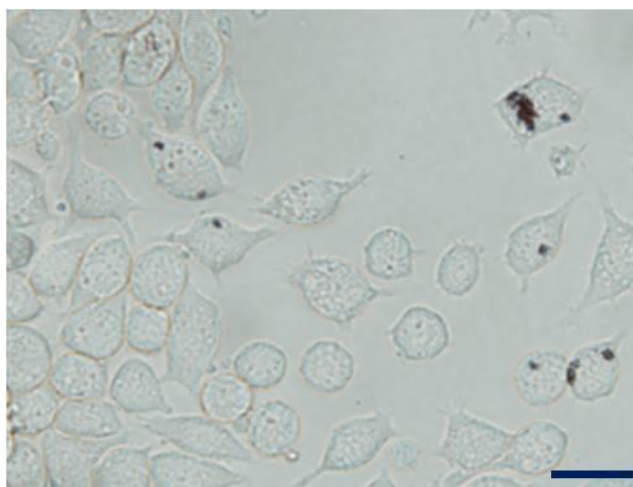
Very faint, brown perinuclear staining pattern observed across all cells.
Inferred uptake: Slow.



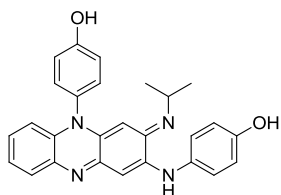
F



Most cells did not exhibit any staining. A few cells with associated black precipitates, likely derived extracellularly.
Inferred uptake: Very slow.



G



Dark brown perinuclear staining pattern associated with cytoplasmic vesicles.
Inferred uptake: Good.

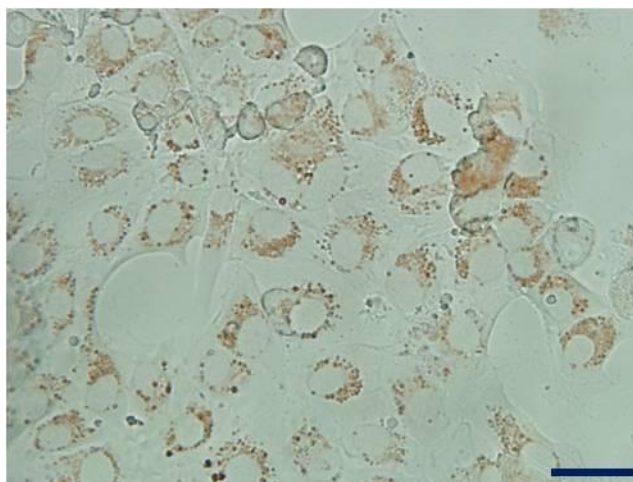
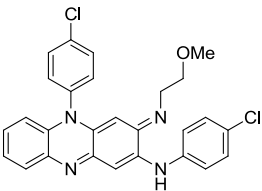
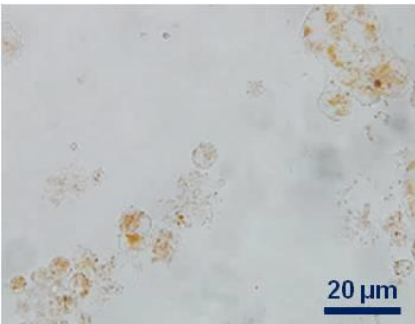
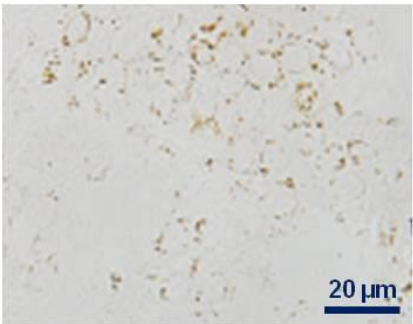
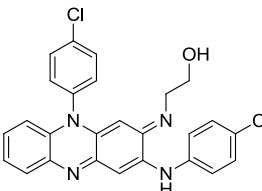
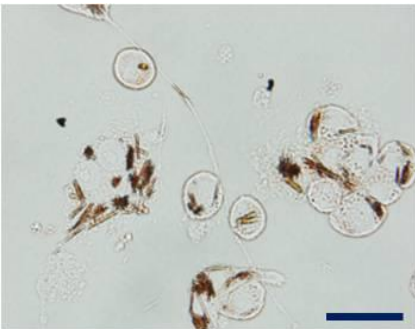
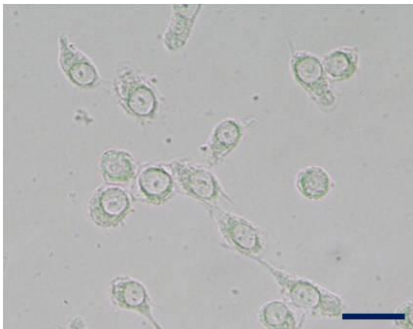
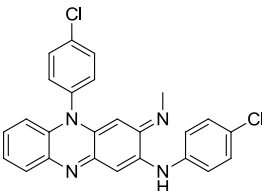
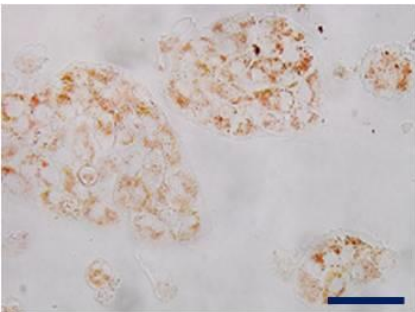
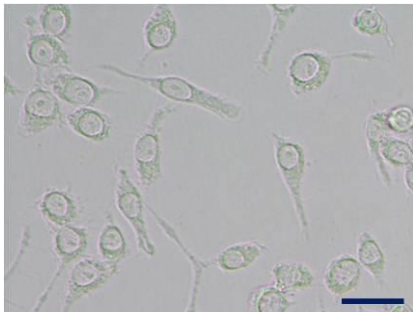
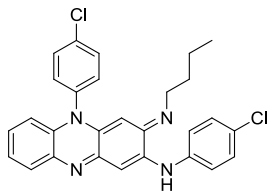


Table S3- Calculated physicochemical properties, predicted cell uptake and subcellular localization properties of clofazimine and related phenazine analogs with different R-imino substitutions.

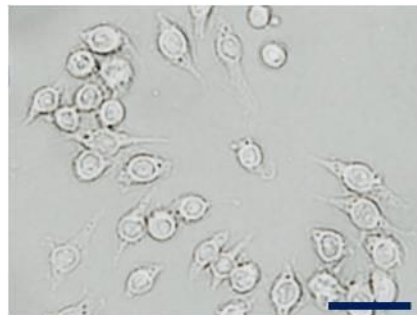
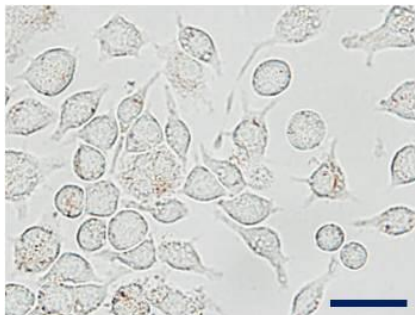
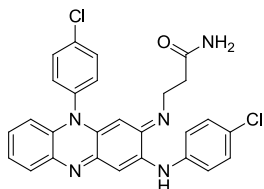
Chemical ID	R ₁	R ₂	Mol.wt	pKa	logP	Predicted ease of cell entry	Predicted intracellular localization
H	Cl	2-methoxyethyl	489.4	pK _{a1} = 8.70 pK _{a2} = 2.31	6.48	Moderate <i>Free base</i> <i>membrane bound</i>	E G L M
I	Cl	2-hydroxyethyl	475.4	pK _{a1} = 8.65 pK _{a2} = 2.31	5.84	Moderate <i>Free base</i> <i>membrane bound</i>	E G L M
J	Cl	Methyl	445.3	pK _{a1} = 9.88 pK _{a2} = 2.33	6.53	Moderate <i>Free base</i> <i>membrane bound</i>	E G L M
K	Cl	n-butyl	487.4	pK _{a1} = 9.59 pK _{a2} = 2.32	7.85	Poor-Moderate <i>Free base trapped in</i> <i>plasma membrane</i>	E G L M P
L	Cl	3-amino-3-oxopropyl	502.4	pK _{a1} = 9.20 pK _{a2} = 2.32	5.44	Moderate <i>Free base</i> <i>membrane bound</i>	E G L M
M	Cl	2-(5-methoxy-1H-indol-3-yl)ethyl	604.5	pK _{a1} = 9.51 pK _{a2} = 2.33	8.49	Poor- <i>Free base trapped in</i> <i>plasma membrane</i>	E G L M P
N	Cl	2-morpholinoethyl	544.7	pK _{a1} = 9.16 pK _{a2} = 4.94 pK _{a3} = 2.32	6.33	Moderate <i>Free base</i> <i>Membrane bound</i>	E G L M
O	Cl	2-(3,4-dihydroxyphenyl)ethyl	567.5	pK _{a1} = 9.00 pK _{a2} = 2.33	7.94	Poor- <i>Free base trapped in</i> <i>plasma membrane</i>	E G L M P

Table S4. Observed cellular staining pattern following 72 hour incubation with clofazimine and related phenazine analogs possessing R-imino group substitutions. Scale bar is 20 μm .

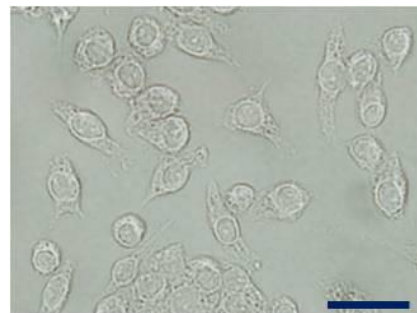
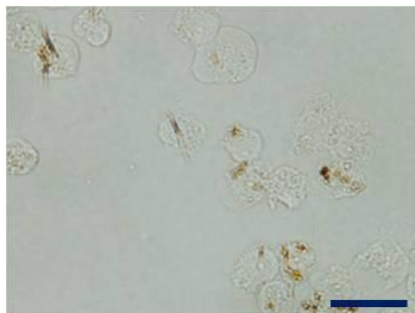
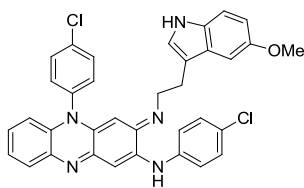
ID	Notes	Live Cells	Fixed Cells
H	 <p>Brown staining associated with vesicles/membranes. Fixed cells also exhibited staining, suggesting nonspecific partitioning. Inferred uptake: Moderate</p>		
I	 <p>Dark brown, crystal-like inclusions present in live cells but absent in fixed cells. Inferred uptake: Excellent.</p>		
J	 <p>Orange perinuclear staining pattern associated with cytoplasmic membranes. Staining not observed in fixed cells. Inferred uptake: Good.</p>		

K

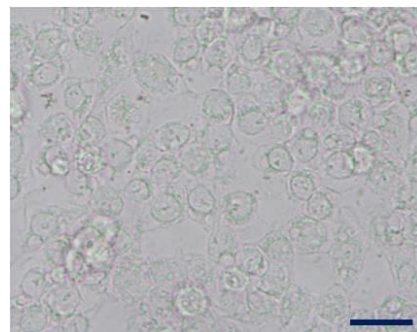
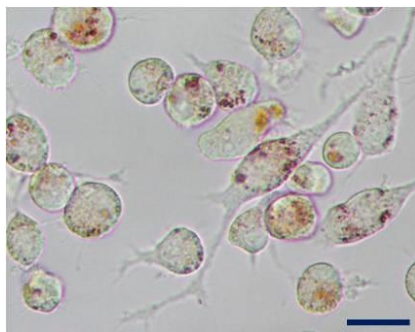
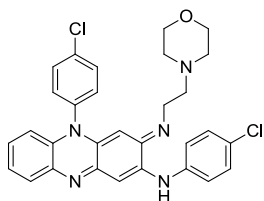
Very faint, brown perinuclear staining pattern. Inferred uptake: Slow.

**L**

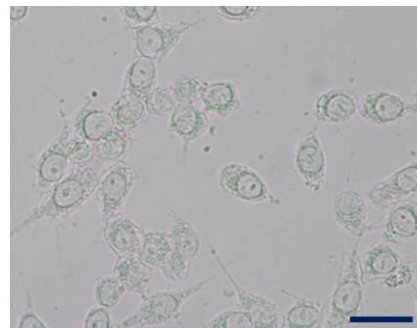
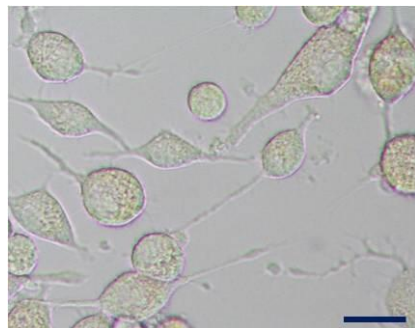
Small brown inclusions present in live cells but absent in fixed cells. Inferred uptake: Good.

**M**

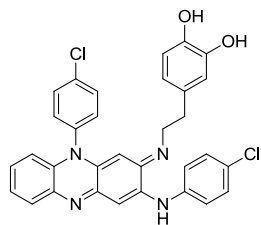
Orange-brown or purple inclusions present in live cells. Staining not observed in fixed cells. Inferred uptake: Good.

**N**

Faint orange staining pattern associated with perinuclear cytoplasmic vesicles. Cells were homogeneously stained. Staining not observed in fixed cells. Inferred uptake: Moderate.



O



Most of cells have shown faint orange colored vesicles. Some cells contained orange-brown perinuclear staining patterns. Staining not observed in fixed cells. Inferred uptake: Good.

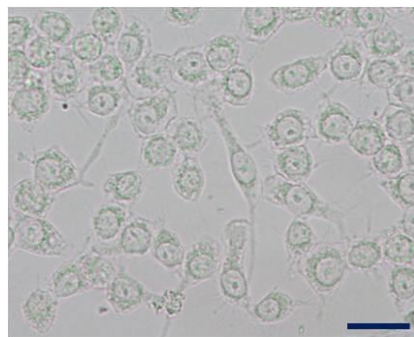
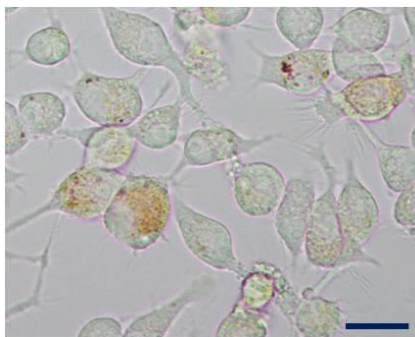
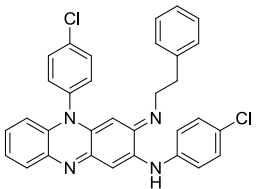
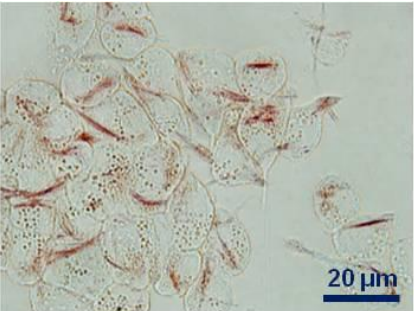
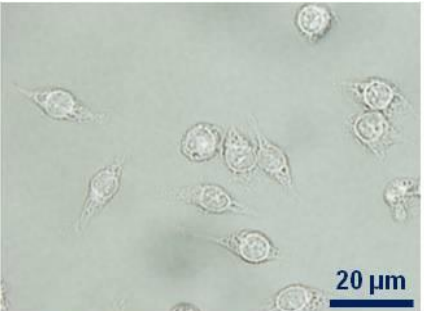
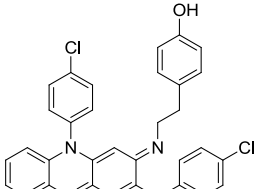
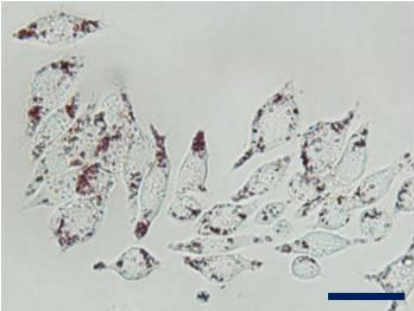
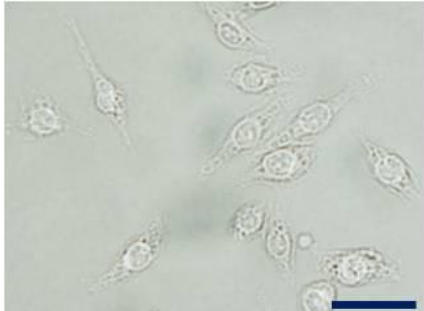
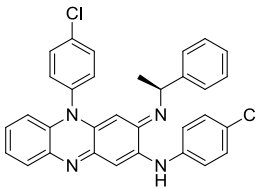
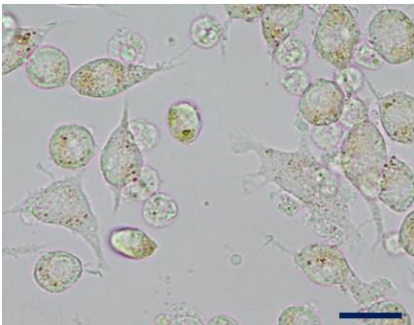
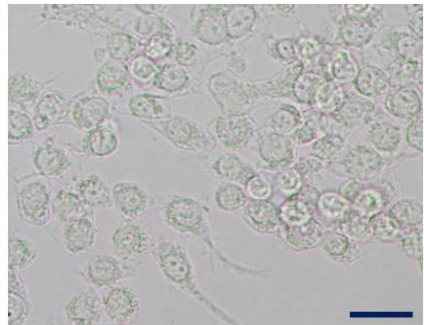
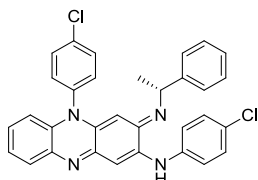


Table S5- Calculated physicochemical properties, predicted cell uptake and subcellular localization properties of clofazimine and related phenazine analogs with additional R-imino substitutions.

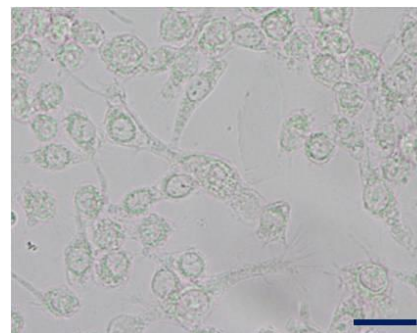
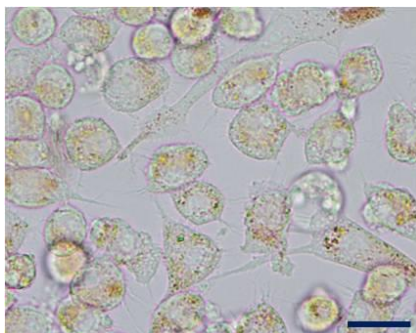
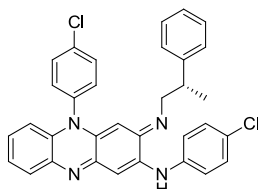
Chemical ID	R ₁	R ₂	Mol.wt	pKa	logP	Predicted ease of cell entry	Predicted intracellular localization
P	Cl	2-phenylethyl	535.5	pK _{a1} = 9.51 pK _{a2} = 2.32	8.54	Poor <i>Free base trapped in plasma membrane</i>	G L P
Q	Cl	2-(4-hydroxyphenyl) ethyl	551.5	pK _{a1} = 9.32 pK _{a2} = 2.33	8.24	Poor <i>Free base trapped in plasma membrane</i>	G L P
R	Cl	(S)-1-phenylethyl	535.5	pK _{a1} = 8.35 pK _{a2} = 2.30	8.67	Poor- <i>Free base trapped in plasma membrane</i>	E G L M P
S	Cl	(R)-1-phenylethyl	535.5	pK _{a1} = 8.35 pK _{a2} = 2.30	8.67	Poor- <i>Free base trapped in plasma membrane</i>	E G L M P
T	Cl	(S)-2-phenylpropyl	549.5	pK _{a1} = 9.46 pK _{a2} = 2.32	8.91	Poor- <i>Free base trapped in plasma membrane</i>	E G L M P
U	Cl	(R)-2-phenylpropyl	549.5	pK _{a1} = 9.46 pK _{a2} = 2.32	8.91	Poor- <i>Free base trapped in plasma membrane</i>	E G L M P
V	Cl	(S)-1-hydroxy-3-methylbut-2-yl	517.5	pK _{a1} = 8.28 pK _{a2} = 2.30	7.14	Poor-Moderate <i>Free base trapped in plasma membrane</i>	E G L M P
W	Cl	(R)-1-hydroxy-3-methylbut-2-yl	517.5	pK _{a1} = 8.28 pK _{a2} = 2.30	7.14	Poor-Moderate <i>Free base trapped in plasma membrane</i>	E G L M P

Table S6- Observed cellular staining pattern following 72 hour incubation with clofazimine and related phenazine analogs possessing R-imino group substitutions. Scale bar is 20 μm .

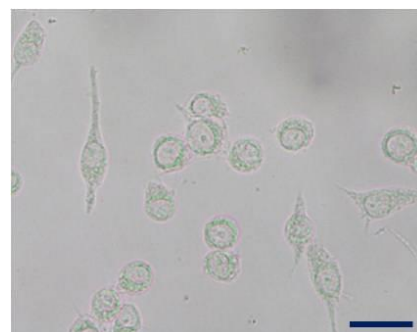
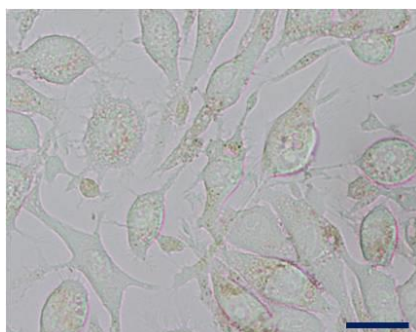
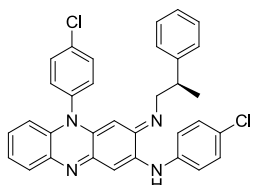
ID	Notes	Live Cells	Fixed Cells
P	 <p data-bbox="240 615 540 762">Large fibrous/crystal-like brown inclusions present in live cells but absent in fixed cells. Inferred uptake: Excellent.</p>		
Q	 <p data-bbox="240 1020 540 1171">Purple-black dense cytoplasmic inclusions in live cells but absent in fixed cells. Inferred uptake: Excellent.</p>		
R	 <p data-bbox="240 1381 540 1568">Orange-brown staining pattern associated with perinuclear cytoplasmic vesicles in live cells. No staining found in Fixed cells. Inferred uptake: Good.</p>		

S

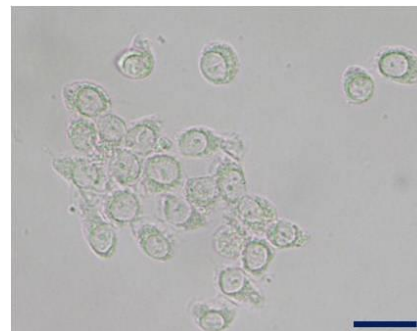
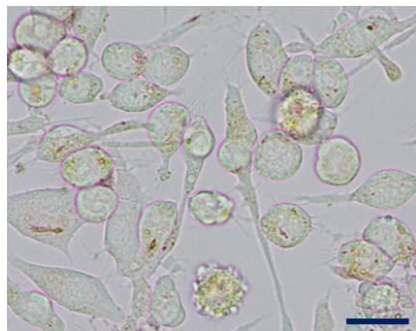
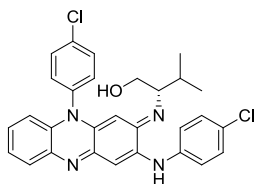
Orange-brown staining pattern associated with perinuclear cytoplasmic vesicles in live cells. Fixed cells do not show any staining. Inferred uptake: Good.

**T**

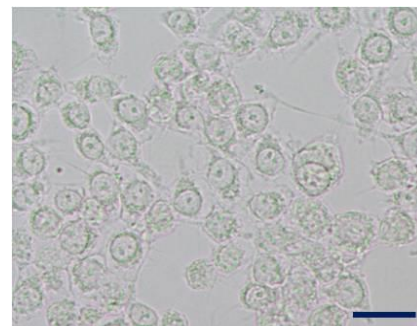
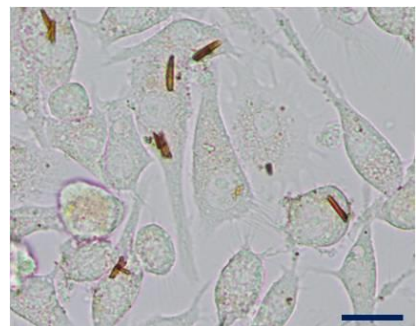
Faint orange perinuclear vesicles are present in live cells. Staining not observed in fixed cells. Inferred uptake: Moderate.

**U**

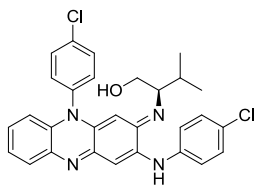
Fibrous/crystal-like brown inclusions with orange perinuclear vesicles are present in live cells but absent in fixed cells. Inferred uptake: Good.

**V**

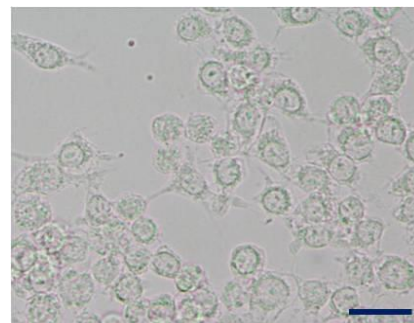
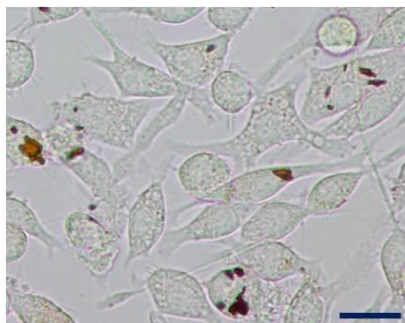
Brown crystal-like inclusions appeared in live cells. Staining not observed in fixed cells. Inferred uptake: Good.



W



Brown crystal-like inclusions are shown in live cells but absent in fixed cells. Inferred uptake: Good.



References

1. a)V. C. Barry, M. L. Conalty, *Am. Rev. Tuberc.* 1958, 78, 62-73; b)J. Belton, M. Conalty, C. O'Callaghan, J. O'Sullivan, D. Twomey, in *Proceedings of the Royal Irish Academy. Section B: Biological, Geological, and Chemical Science*, JSTOR, Ireland, 1961, pp. 15-22.
2. J. O'Sullivan, *J. Chem. Soc.* 1958, 859-863.
3. J. F. O'Sullivan, M. L. Conalty, N. E. Morrison, *J. Med. Chem.* 1988, 31, 567-572.
4. A. C.-G. G.-A. JORI, H. ZEVIO, *Farmaco. Edizione scientifica.* 1962, 17, 308-319.
5. J. F. O'Sullivan, *J. Chem. Res., Miniprint*, 1984, 52.
6. C. Hansch, A. Leo, Wiley, New York, 1979, pp. 18-43.
7. a)R. W. Horobin, F. Rashid-Doubell, J. D. Pediani, G. Milligan, *Biotech. Histochem.* 2013, 88, 440-460; b)R. W. Horobin, F. Rashid-Doubell, *Biotech. Histochem.* 2013, 88, 461-476.
8. J. Baik, G. R. Rosania, *Mol. Pharm.* 2011, 8, 1742-1749.
9. a)R. Oldenbourg, *Nature* 1996, 381, 811-812; b)R. Oldenbourg, G. Mei, *J. Microsc.* 1995, 180, 140-147; c)M. Shribak, R. Oldenbourg, *Appl. Opt.* 2003, 42, 3009-3017.
10. a)S. B. Mehta, M. Shribak, R. Oldenbourg, *J. Opt.* 2013, 15, 094007-094020; b)B. S. DeMay, N. Noda, A. S. Gladfelter, R. Oldenbourg, *Biophys. J.* 2011, 101, 985-994.
11. H. Abdi, L. J. Williams, *Wiley Interdisciplinary Reviews: Computational Statistics.* 2010, 2, 433-459.
12. a)Z.-B. Xu, Y. Lu, Z.-R. Guo, *Synlett.* 2003, 4, 564-566; b)P. Kirsch, A. SchonlebenJanas, R. H. Schirmer, *Liebigs Annalen* 1995, 1995, 1275-1281.

Appendix C

Supporting Information for Chapter 4

Supplemental Materials and Methods

Mouse bronchoalveolar lavage (BAL) harvest. PBS/LPS-instilled and CFZ-treated or control mice were euthanized by exsanguination while deeply anesthetized with an intraperitoneal injection of ketamine/xylazine (100 mg/kg, 10 mg/kg). The trachea was surgically exposed and cannulated with an 18G needle and the lungs were lavaged by instilling 1 ml DPBS (Life Technologies, Carlsbad, CA) containing 0.5 mM EDTA (Sigma, St. Louis, MO). The retrieved BAL was then centrifuged (10 min at 400 x g, 4°C), and the supernatant was frozen (-80 °C), while the cell pellets were resuspended in 1 ml RPMI 1640 media (Life Technologies). To count total cells, the cells were stained with Trypan blue and counted using a hemocytometer.

Immunohistochemistry and imaging. After euthanasia with ketamine/xylazine and exsanguination, the liver, spleen and kidneys were removed *en bloc* and the lungs were inflated with 0.8 ml (50% OCT, 15% sucrose in PBS) and frozen in Tissue-Plus OCT compound (Fisher HealthCare, Houston, TX). Tissue blocks were sectioned at a thickness 6 µm, using Leica 3050S cryostat. For immunohistochemistry, sections were fixed in 4% paraformaldehyde for 10 min, blocked for 2 h and incubated with primary antibody at 1 µg/ml overnight (4°C) followed by HRP-conjugated secondary antibody for 1 h, DAB substrate incubation (intelliPATH FLX DAB chromogen kit, Biocare Medical, Concord, CA) and hematoxylin counterstain. For fluorescence immunostaining, FITC-conjugated secondary antibody (Sigma) was incubated for 1 h, and Hoechst 33342 (Life Technologies) was used for nuclear detection. Non-fluorescence staining was performed by the Pathology Core for Animal Research (PCAR) in the Unit for Laboratory Animal Medicine (ULAM) at the University of Michigan. Sections were mounted on glass slides with ProlongGold (Life Technologies). Brightfield and fluorescence (DAPI, FITC and Cy5) images were acquired using the Nikon Eclipse Ti (Japan) inverted microscope equipped with a

Nikon Digital Sight DS-Fi2 camera (Japan) for brightfield and Photometrics Coolsnap Myo camera (Tucson, AZ) for fluorescence.

SDS-PAGE and Western Blot. Harvested organs were washed in ice-cold DPBS and homogenized by sonication in radioimmunoprecipitation assay (RIPA) buffer (Sigma). Halt protease and phosphatase inhibitor cocktail and 0.5 M EDTA (Thermo Pierce) were added to the RIPA buffer (1:100 dilutions) before use. The protein concentration in homogenates was determined with a BCA assay (Thermo Pierce) and equal amounts of total protein were suspended in 4x sample buffer (Bio-Rad, Hercules, CA) and heated (4 min at 94°C). Proteins were separated by SDS-PAGE in 4-15% or 4-20% bis-acrylamide gels (Bio-Rad) and electroblotted onto PVDF membranes (Millipore, Billerica, MA) using the Criterion system (Bio-Rad). After blocking for 1 h in Tris-buffered saline/Tween (TBST, pH 7.6; 20 mM Tris-HCl, 150 mM NaCl, and 0.05% Tween20) containing 5% nonfat milk (Meijer), the blots were probed with primary antibodies diluted in 5% BSA or 5% nonfat milk overnight at 4°C. The membranes were washed with TBST and incubated with a 1:2000 dilution of HRP-conjugated anti-rabbit secondary antibodies (Millipore) for 1 h at room temperature. Protein bands were visualized on X-ray film (Thermo) using chemiluminescence (Supersignal reagents; Pierce).

Equation for Mouse Terminal Endpoint Assessment.

$$D_{LPS-\overline{PBS}} = \sqrt{(o_{LPS} - \bar{o}_{PBS})^2 + (w_{LPS} - \bar{w}_{PBS})^2 + (t_{LPS} - \bar{t}_{PBS})^2}$$

$D_{LPS-\overline{PBS}}$: total distance between LPS-instilled mouse and mean of PBS-instilled mice

\bar{o}_{PBS} : mean oxygen saturation change of PBS-instilled mice

o_{LPS} : oxygen saturation change of LPS-instilled mouse

\bar{w}_{PBS} : mean weight change of PBS-instilled mice

w_{LPS} : weight change of LPS-instilled mouse

\bar{t}_{PBS} : mean temperature change of PBS-instilled mice

t_{LPS} : temperature change of LPS-instilled mouse

- ❖ All changes represent percent changes from day 0 baseline measurement

Figure SI. 7- CFZ accumulation in lung macrophages.

Clofazimine (CFZ) bioaccumulation and crystal formation in the lung occurs after 2 weeks in CD68 (+) macrophages. Representative brightfield and fluorescence (FITC for CD68 and Cy5 for CFZ) images of lung sections from control mice and mice treated with CFZ for 2 and 8 weeks. In the lung, CFZ can be seen accumulating inside macrophages after 2 week CFZ treatment with no crystallization. At 8 weeks, CFZ crystals can be seen located inside macrophages. Scale bar 10 μ m.

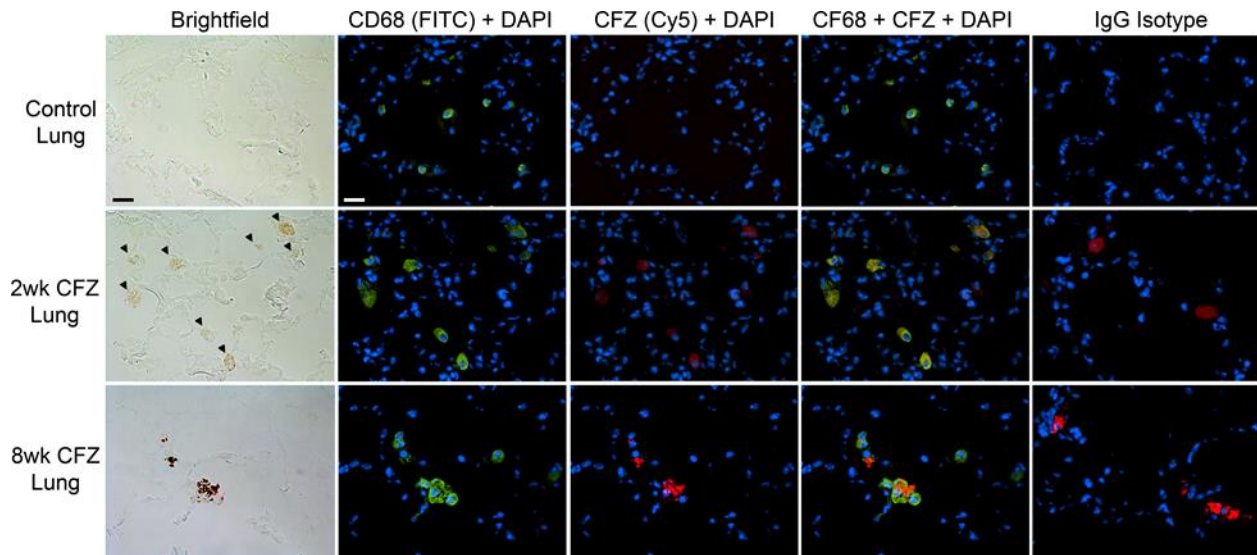


Figure SI. 8- IL-1 β cleavage in spleen, lung, and kidney.

Clofazimine (CFZ) bioaccumulation does not affect IL-1 β cleavage in the spleen, lung or kidney. Western blots of spleen, lung and kidney homogenates showing that IL-1 β cleavage was not altered after 8 weeks of CFZ treatment.

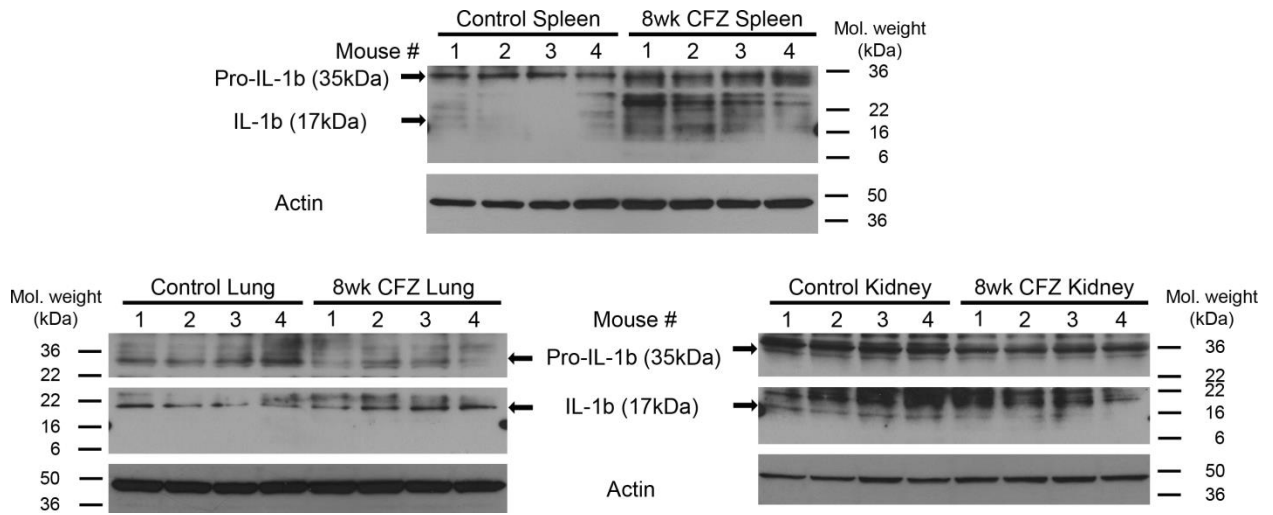


Figure SI. 9- CFZ accumulation within IL-1RA knockout mice.

(A) 6 week CFZ-treated IL-1RA knockout (KO) mice show reduced body weight compared to control diet treated littermates and wildtype (WT) mice. (B) IL-1RA KO mice display reduced liver weight compared to WT, but spleen are comparable. (C) Representative brightfield and fluorescence (Cy5 for crystalline CFZ) images of liver sections from WT and IL-1RA KO mice treated with CFZ for 6 weeks. Scale bar = 100 μ m. (D) Cy5 fluorescence intensity values of liver sections from WT and IL-1RA KO and CFZ-treated mice. Data are the mean \pm S.D. of 4 images. Scale bar = 100 μ m.

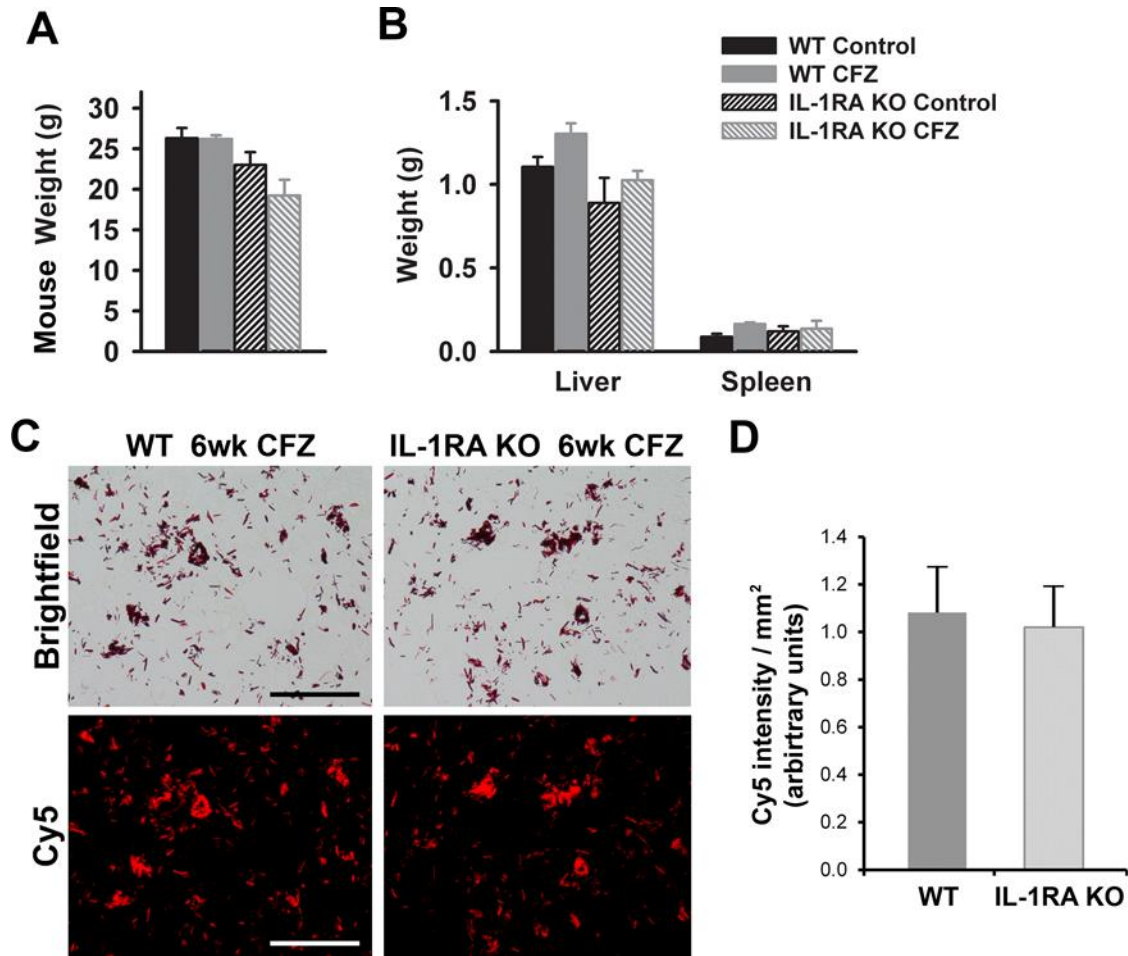


Figure SI. 10- Vital signs of mice following LPS or PBS injection.

Daily monitoring of changes in arterial oxygen saturation (A), body weight (B), temperature (C), heart rate (D), respiratory rate (E), and pulse distention (F) in 8 week CFZ-treated and control mice after PBS (white circle) or LPS (grey circle)-induced acute lung injury. Control mice lung function progressively deteriorated at a higher rate than CFZ-treated mice as CFZ-treated mice displayed higher arterial oxygen levels at day 5 and day 6 (A). Control mice injected with LPS lost weight more rapidly compared to CFZ-treated mice (B). CFZ-treated mice were more resistant to hypothermia (C), drop in heart rate (D) and respiratory rate (E) after the second LPS injection compared to control-mice (day 4). Data is the compilation of two separate experiments and presented as mean \pm S.D. (PBS n=4, LPS n=12). Black dots represent mice that reached terminal endpoint and were euthanized. One-way ANOVA was used to compare changes in parameters between control vs CFZ-treated mice with PBS or LPS injections per timepoint and $p \leq 0.05$ was considered statistically significant. * $p \leq 0.05$, ** $p \leq 0.01$.

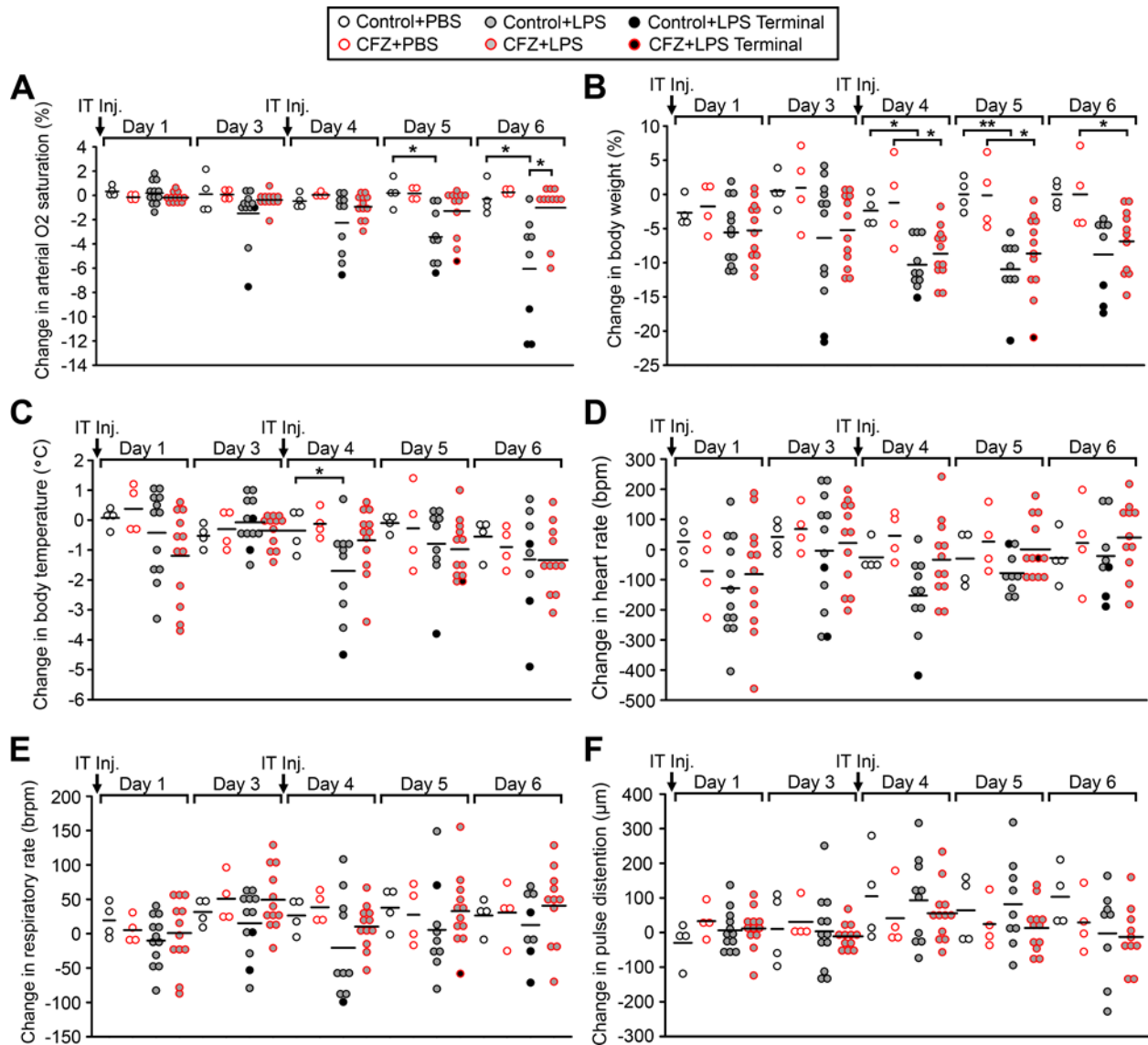


Table S7- Vital signs of control and clofazimine-treated mice (8 week treatment). P values were calculated using Student's t-test (two-way, unpaired)

Vital signs	Control diet treated (n=16)	CFZ treated (n=16)	P value
Weight (g ± S.D.)	26.13 ± 1.49	24.39 ± 1.92	0.008
Body Temperature (°C ± S.D.)	35.30 ± 0.54	35.52 ± 0.76	0.35
Arterial O ₂ Saturation (% ± S.D.)	97.52 ± 0.76	99.01 ± 0.24	0.00000064
Respiratory rate (brpm ± S.D.)	172.85 ± 18.25	154.29 ± 19.43	0.009
Heart rate (bpm ± S.D.)	632.91 ± 89.55	573.94 ± 85.28	0.066
Pulse distention (µm ± S.D)	512.22 ± 60.35	425.57 ± 52.32	0.00015

Appendix D

Supporting Information for Chapter 5

Supplemental Materials and Methods

Mouse Model for Generating Biocrystals. Macrophages containing biocrystals were generated as published before [23,25,37]. Mice (4 week old, male C57Bl/6) were purchased from the Jackson Laboratory (Bar Harbor, ME) and acclimatized for 1 week in a specific-pathogen-free animal facility. Animal care was provided by the University of Michigan's Unit for Laboratory Animal Medicine (ULAM). The experimental protocol was approved by the Committee on Use and Care of Animals and all procedures were carried out in accordance with the approved protocol. Clofazimine (CFZ) (C8895; Sigma-Aldrich, St. Louis, MO) was dissolved in sesame oil (Roland, China, or Shirakiku, Japan) to achieve a concentration of 3 mg/ml, which was mixed with Powdered Lab Diet 5001 (PMI International, Inc., St. Louis, MO) to produce a 0.03% drug to powdered chow feed.

Peritoneal Lavage to obtain Peritoneal Macrophages. Peritoneal lavage was done 8 weeks after the initiation of CFZ treatment. Mice were euthanized by exsanguination while deeply anesthetized by an intraperitoneal injection of ketamine (100 mg/kg)/xylazine (10 mg/kg) followed by sterilization of the outer skin with 70% of ethanol. A small incision was made along the midline of the abdomen followed by abdominal skin retraction up to the thoracic boundary and the animal extremities to expose the intact peritoneal wall. A smaller incision was then made on the peritoneal wall to expose the cavity. The entire peritoneal cavity was washed with ice-cold sterile Phosphate Buffered Saline (PBS) + 5% of Fetal Bovine Serum (FBS) (5–10 ml) and collected as peritoneal exudate. The exudate was then centrifuged (100 x g for 5 min, 4 °C) and resuspended in 1.5 ml of PBS + 5% of FBS. Cells were counted using a hemocytometer for viable cells using Trypan Blue and for biocrystal-containing cells. For preparation of microscopy slides, a 20 µl drop of cell suspension was placed on a glass slide and allowed to dry overnight in

the dark. The following day, a single drop of Prolong® Gold (Life Technologies, Carlsbad, CA) was added to the dry slide and a cover slip was applied prior to imaging.

Alveolar Lavage to obtain Alveolar Macrophages. Mice were euthanized as described above and the trachea was surgically exposed and cannulated with an 18G luer stub and the lungs were lavaged to obtain alveolar exudate by instilling PBS containing 0.5 mM of EDTA in 1 ml aliquots for a total of 6 ml. The alveolar exudate fluid was centrifuged (400 x g, 10 min, 4 °C) and resuspended in RPMI 1640 media. Viable (using Trypan Blue staining method) and biocrystal containing cells were counted using a hemocytometer followed by preparation of microscope slides as mentioned above.

Isolation of Biocrystals. At 8 weeks post-drug feeding, mice were euthanized as described above and spleens were harvested and cut open to prepare tissue homogenate in phosphate-buffered saline (PBS). The tissue homogenate was sonicated for 30 min and centrifuged (100 x g for 1 min) to remove large cell debris. A solution of 10% sucrose in PBS was added to the acquired supernatant and the mixture was centrifuged (100 x g). The resulting supernatant was centrifuged (3200 x g for 20 min) to pellet drug inclusions which were then resuspended in 2 ml of 10% sucrose in water (w/v). CLDIs were further purified using a three-layer discontinuous gradient (50, 30, and 10% sucrose (w/v) in PBS) centrifugation method (3200 x g for 30 min, no brakes)[37].

Brightfield and Polarization Microscopy. The combination brightfield and diattenuation LC-Pol-Scope microscope set-up is a custom built microscopic imaging system similar to the birefringence LC-PolScope designed by Oldenbourg et al[34], but without the polarization analyzer. Our LC-PolScope is built on the Nikon Eclipse Ti inverted microscope (Nikon Instruments, Melville, New York), with the computer-controlled universal compensator (Hinds Instrumentation, Hillsboro, Oregon) placed between the interference filter (623±22 nm, Semrock Optics, Rochester, New York) and condenser lens. Illuminating light is narrowed to 623 nm by the interference filter, and the light is linearly polarized by passing it through a universal compensator, allowing for the diattenuation of the sample to be measured. The LC in the universal compensator is controlled by Image J “Micro-manager” software (Vale Laboratory, UCSF) and is automatically rotated to produce polarized light at 0°, 45°, 90° and 135° angles, respective to the horizontal, during image acquisition. The image maps of diattenuation, mean transmittance, and angle of high transmittance are generated by image analysis algorithms

followed by calibration and have been published before[32,34]. Brightfield and fluorescence images were captured using the Nikon DS-U3 camera (Nikon Instruments) and Photometrics CoolSnap MYO camera system (Photometrics, Tucson, Arizona), respectively, under the control of Nikon NIS-Elements AR software (Nikon Instruments). Microscopy slides of samples were prepared as mentioned before.

Measuring Curvature of Crystals. The diattenuation images obtained using Polarization microscopy were used to quantify for curvature of biocrystals using a ThreePointROI plugin for ImageJ, as used elsewhere[44]. Briefly, three points were marked along the maximum Feret's length of the high diattenuation signal of the crystal which was used by the plugin to draw a circle through the three points and accordingly provide a radius of the circle (r). Curvature for this circle is then defined as $\kappa = 1/r$. Co-linear points that define an impossible circle resulted in a circle with $r = "-1"$ or "2147483647" pixels and were marked as $\kappa=0$. A line was then drawn through the three points used to generate the circle to generate a chord of length (x) for that circle. Using the length of the chord and the radius, the angle formed by the biocrystal arc through that circle was then computed using the formula $\theta = 2\sin^{-1}(x/2r)$. The arc length of the biocrystal was then computed as $L = \theta \times r$ where θ is in radians. Linear curvature density was computed as κ/L .

Synthesis of CFZ-HCl Crystals. To grow the biomimetic crystals (CFZ-HCl) in bulk, HCl was added to a 2mM CFZ in methanol solution until the HCl concentration was 0.1M. After the solution sat for 5 minutes, water is added to the solution to double the solution volume. Within minutes, thin dark red crystals are observed. To grow diffraction quality crystals of CFZ-HCl, 2mM CFZ was dissolved in benzene and 0.1M HCl was added to the solution. The solution was allowed to slowly evaporate and red, rectangular plate-like crystals were observed.

Qualitative Bending/Flexibility Analysis. Crystals that were about 2 mm long and $\sim 20 \mu\text{m}$ thick were isolated from the crystallization solution and manipulated to demonstrate the crystal's elasticity. Crystals were placed on a microscope slide in a small amount of water to prevent the crystal from moving off the slide. A pair of tweezers and a crystallization probe were used to manipulate the crystals. Video of this procedure was taken with a Leica M205 C stereo microscope. See Movies 1 and 2. For analysis of bent crystals via polarization or Raman microscopy, bent crystals were snap-frozen over dry ice and imaged either on a glass microscopy slide (Polarization) or a silicon wafer (Raman).

Powder X-Ray Diffraction (p-XRD). Powder XRD of isolated biocrystals was carried out as published before[25] with Bruker D8 Advance: Cu K α radiation ($\lambda = 1.5406 \text{ \AA}$), tube voltage = 40kV, and tube current = 40 mA. Data were collected at $2\theta = 4^\circ$ to 40° at a continuous scan rate of $2.5^\circ/\text{min}$. For CFZ-HCl crystals - data was collected on a Rigaku Miniflex 600 in the Bragg-Brentano geometry. The data was collected from $5^\circ - 40^\circ$, 2θ with 0.02° steps and a 1.00 s detection time. Data was background subtracted using Origin® (Origin Labs, Northampton, MA)

Single Crystal X-Ray Diffraction. Single crystal X-ray data was collected on a Bruker D8 Venture equipped with a four-circle kappa diffractometer and Photon 100 detector with Cu source that supplied the multi-mirror monochromated incident beam. A combination of Phi and Omega scans were used to collect the necessary data. A single crystal was picked and mounted on a 0.3mm loop using paratone oil then cooled to 100 K in a nitrogen supplied Oxford 700 Cryostream. Data was integrated using SAINT and absorption corrected using SAINT/SADABS v2014/4. The final structure was solved using SHELX-2014-6.

Raman Microscopy. Confocal Raman microscopy was performed using a WITec alpha300 R equipped with a near-IR 785 nm to minimize clofazimine's fluorescence signal. Samples were positioned on the stage for spectral data acquisition and were observed using the reflectance illumination mode of the microscope. Once positioned, the 4 μm diameter 785 nm laser illumination spot was directed to the sample, and the Raman spectrum was acquired. Raw data were background subtracted from the signal obtained from pure silicon wafers and further baseline-corrected using Origin® (Origin Labs, Northampton, MA).

Differential Scanning Calorimetry (DSC). Samples were analyzed using a TA Instruments 2910 MDSC system equipped with a refrigerated cooling unit. All experiments were performed by heating the pre-weighed samples at a rate of $10^\circ\text{C}/\text{min}$ under a dry nitrogen atmosphere. Temperature and enthalpy of the instrument were calibrated using high purity indium standard.

Figure SI. 11- Curvature of drug biocrystals.

Curvature (κ) of biocrystals measured from two different macrophage populations (peritoneal and alveolar) and isolated biocrystals from the spleen plotted as a function of their arc length (L).

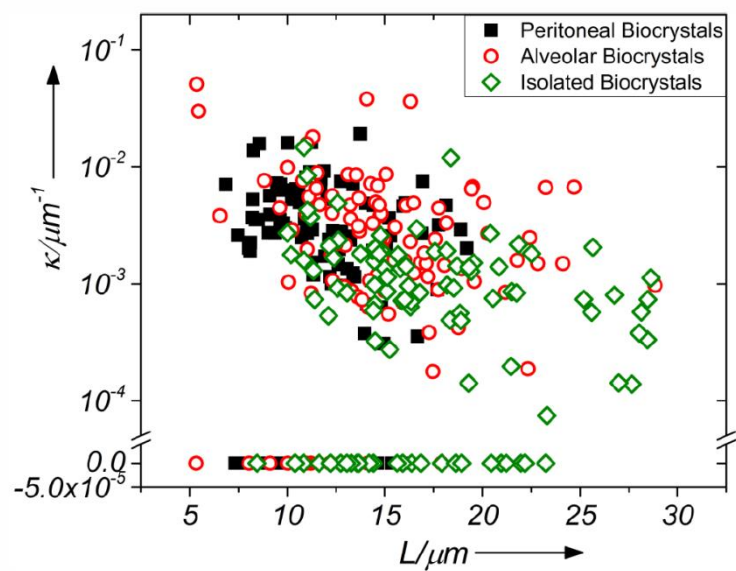


Figure SI. 12- Face indexed image of CFZ-HCl crystal that was used for single crystals X-ray diffraction.

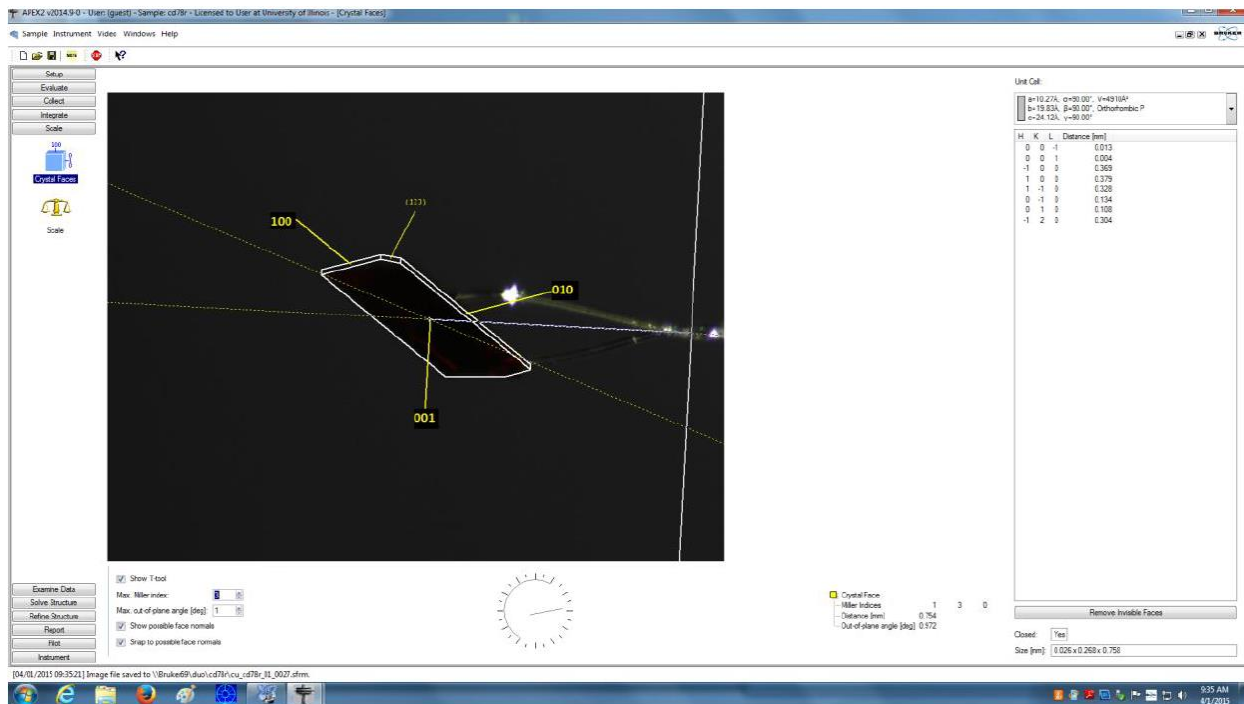


Figure SI. 13- Asymmetric unit of CFZ-HCl.

Asymmetric unit of CFZ-HCl including the position of the water molecule and the disorder in the propyl group showed as a transparent overlay. The water has ~13% occupancy and the presence of water is likely due to the solvent used in the crystallization solution or HCl.

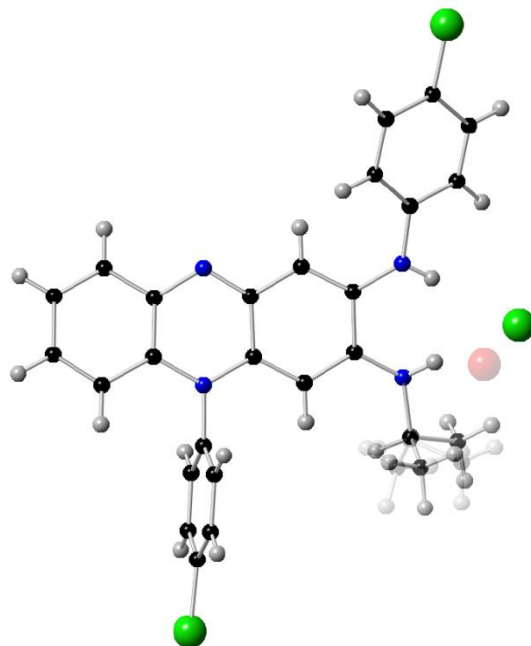


Figure SI. 14- Cl1 interaction with C5-H5 viewed along the b-axis to form a chain of CFZ-HCl molecules and along the c-axis to show the position of the Cl1 interaction within the zig-zag.

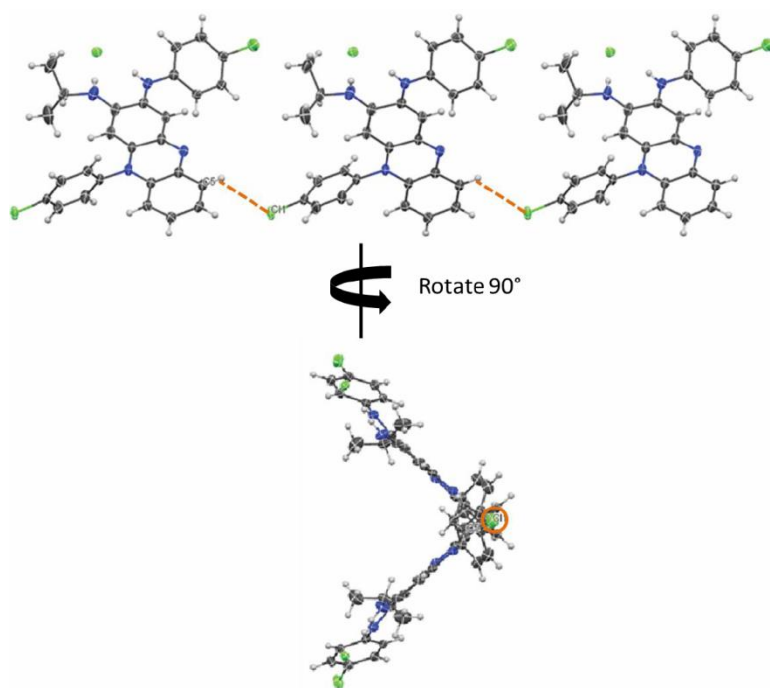


Figure SI. 15- Crystallographic projection of the major faces of the CFZ-HCl crystal. The rows of corrugated structure along the (001) face are colored blue and orange to help visualize the crystal packing. The projections show a stacking of 2 x 2 x 2 (a x b x c) unit cells.

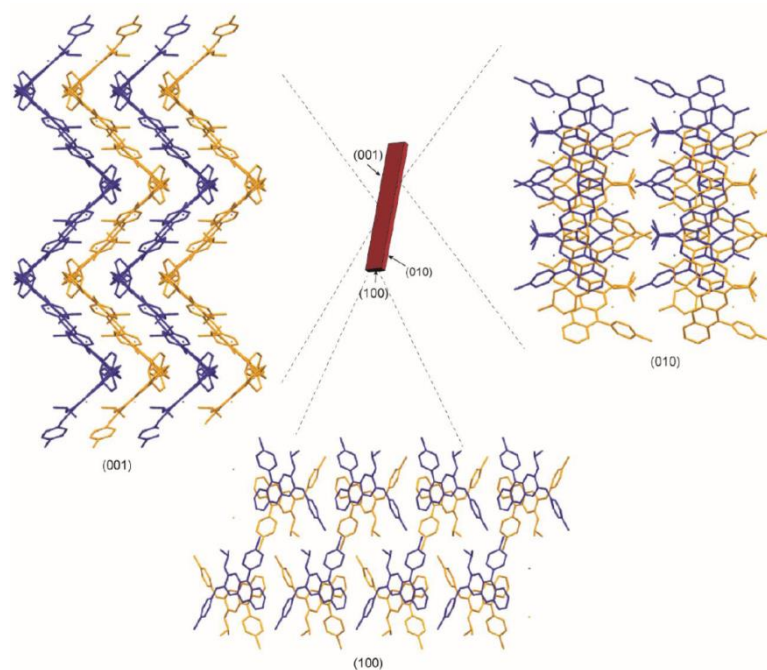


Figure SI. 16- Raman spectra of CFZ-HCl crystal pre- and post-bending.
(A) Raman Reflectance Brightfield images of (*top*) short CFZ-HCl crystals and (*bottom*) at the bent point of a long CFZ-HCl elastic crystal. Blue arrows indicate moving away from the confocal plane used to obtain the point spectra of CFZ-HCl; (B) Raman Spectra of CFZ-HCl reference crystals (*top*) with crystals that were subjected to mechanical bending (before and after) (*second and third from top*) and crystals that had an inherent curvature (*bottom*).

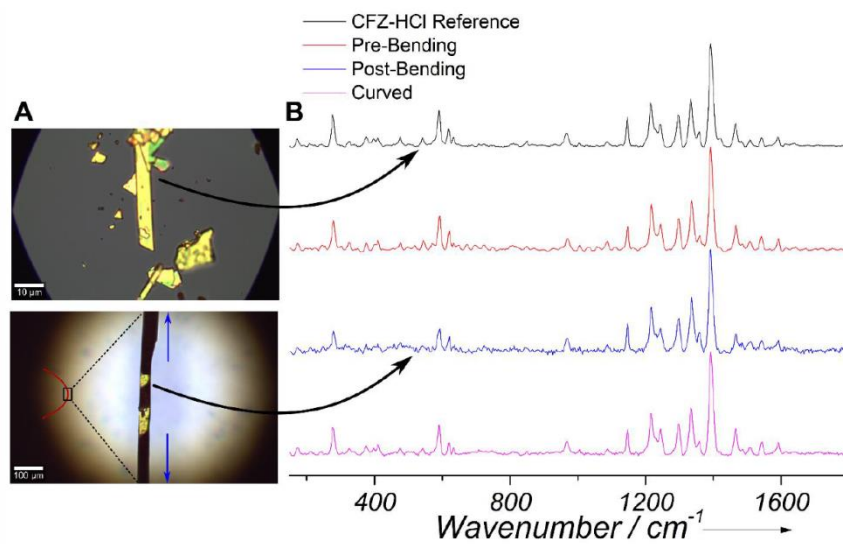


Figure SI. 17- Melting point of CFZ-HCl determined via DSC.
Differential Scanning Calorimetry of CFZ-HCl. Melting Point indicated with curved arrow – 275.80 °C.

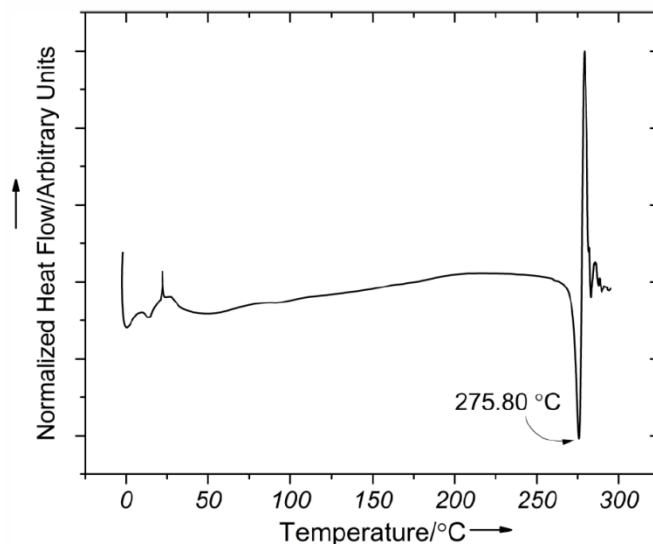


Table S8- Crystallographic data for CFZ-HCl.

Empirical formula	C ₂₇ H _{23.26} Cl ₃ N ₄ O _{0.13}
Formula weight (mg/ml)	512.18
Temperature (K)	100
Wavelength (Å)	1.54178
Crystal system	Orthorhombic
Space group	Pbca
a (Å)	10.266
b (Å)	19.828
c (Å)	24.156
α (°)	90
β (°)	90
γ (°)	90
Volume (Å ³)	4917.1
Z	8
Density (calc., mg/m ³)	1.384
Absorption coefficient (mm ⁻¹)	3.562
F(000)	2122
Crystal size (mm ³)	0.758 x 0.269 x 0.014
Theta range for data collection (°)	3.659 to 68.333
Index ranges	-12<=h<=12 -23<=k<=21 -29<=l<=29
Reflections collected	28160
Independent reflections	4500 [R(int) = 0.0352]
Completeness to theta max	99.8 %
Absorption correction	Integration
Max. and min. transmission	0.9615 and 0.3840
Refinement method	Full-matrix least-squares on F ²
Data / restraints / parameters	4500 / 134 / 365
Goodness-of-fit on F ²	1.069
Final R indices [I>2σ(I)]	R1 = 0.0392, wR2 = 0.0982
R indices (all data)	R1 = 0.0422, wR2 = 0.1010
Extinction coefficient	0.00261
Largest diff. peak and hole (e.Å ⁻³)	0.685 and -0.415

Table S9- Molecular interactions within the CFZ-HCl crystal structure.

	D-H...A	D	d	theta
N-H...Cl	N3-H3A...Cl3	3.172	2.376	166.45
	N4-H4A...Cl3	3.104	2.243	174.51
C-H...Cl	C5-H5...Cl1	3.516	2.937	120.48
	C14-H14...Cl3	3.503	2.724	139.72
	C24-H24...Cl3	3.457	2.757	131.19
	C25_a-H25_a...Cl1	3.891	2.972	153.33
	C27_a-H27A_a...Cl3	3.671	2.899	136.36
π ... π	C1-C6...C7-C12	3.573		
	C1-C6...C1-N1-C12-C7-N2-C6	3.888		
	C19-C24...C7-C12	4.117		
H... π	C3-H3...C19-C24	3.153		
	C21-H21...C1-C6	3.313		
with water present new interactions are formed				
	D-H...A	D	d	theta
C-H...O	C17-H17...O1_b	3.076	2.583	112.62
	C18-H18...O1_b	3.005	2.442	117.82
C-H...Cl	C26B_b-H26E_b...Cl2	3.641	2.676	168.28
	C26B_b-H26F_b...Cl3	3.607	2.985	122.52
	C27B_b-H27F_b...Cl2	3.643	2.672	170.96

Appendix E

Supporting Information for Chapter 8

Figure SI. 18- Comparison of cellular proliferation within untreated, CFZ-treated, and granulomatous regions of CFZ-treated livers.

Increased Cell Proliferation within granulomatous regions of CFZ treated livers. (n=30 images per group)

(*= $p < 0.05$, ANOVA, Tukey's HSD).

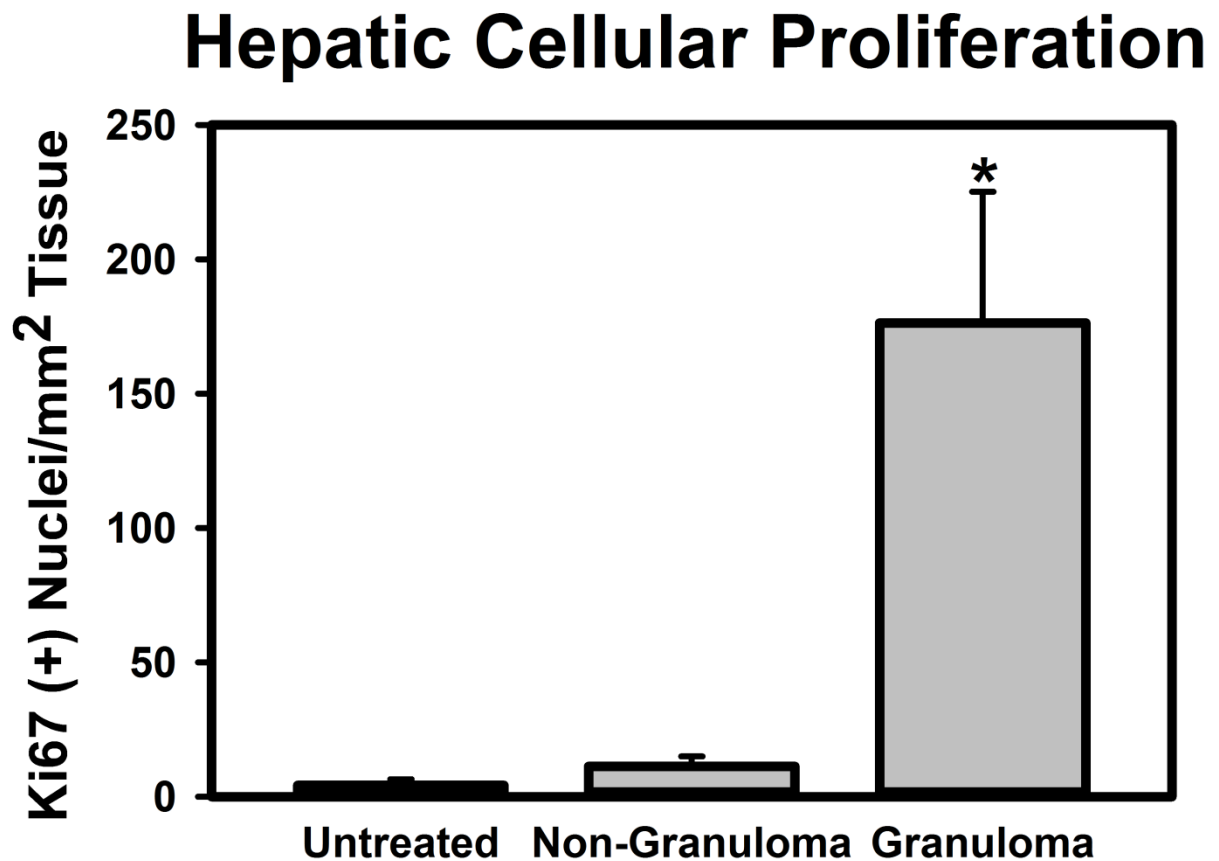


Figure SI. 19- TUNEL assay in untreated, 2 week, 4 week, and 8 week CFZ treated-livers.

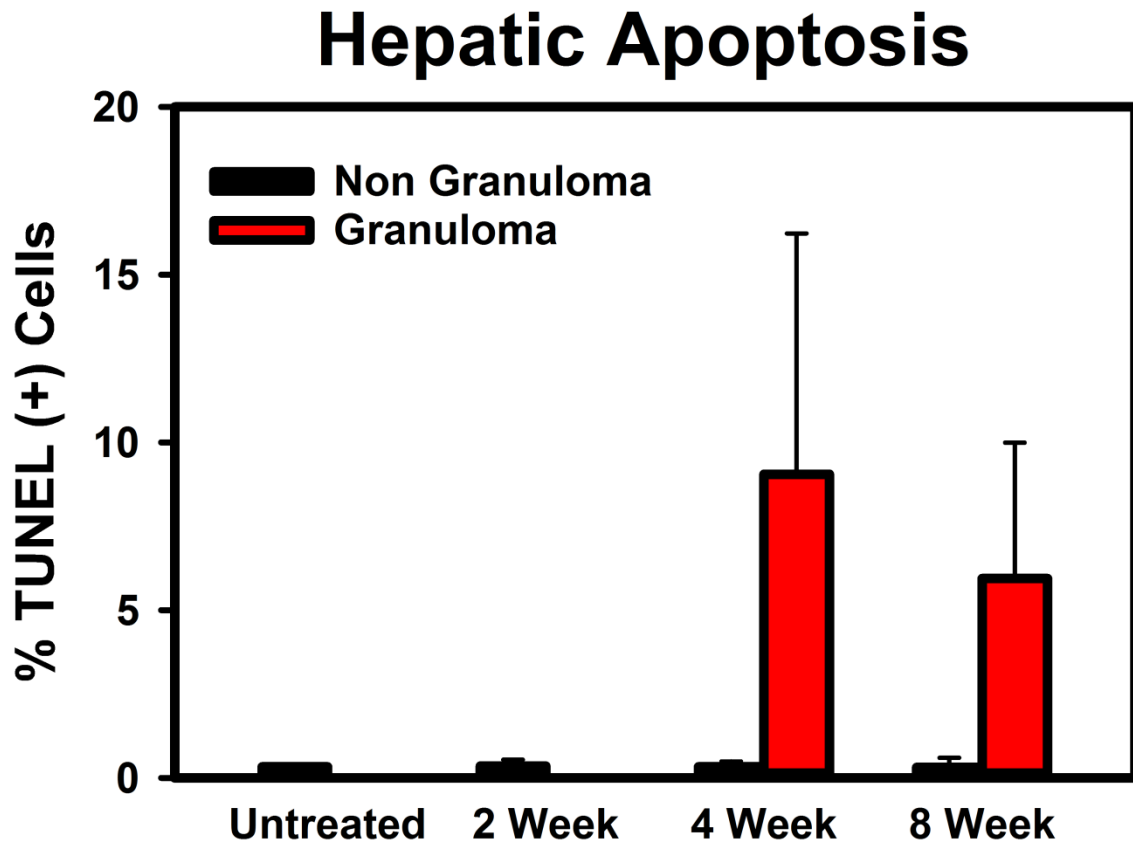


Figure SI. 20- Hepatic TLR2 expression measurement. (n=10 untreated and non-granulomatous regions at 10x, n=10 granulomas) (*=p<0.05, ANOVA, Tukey's HSD)

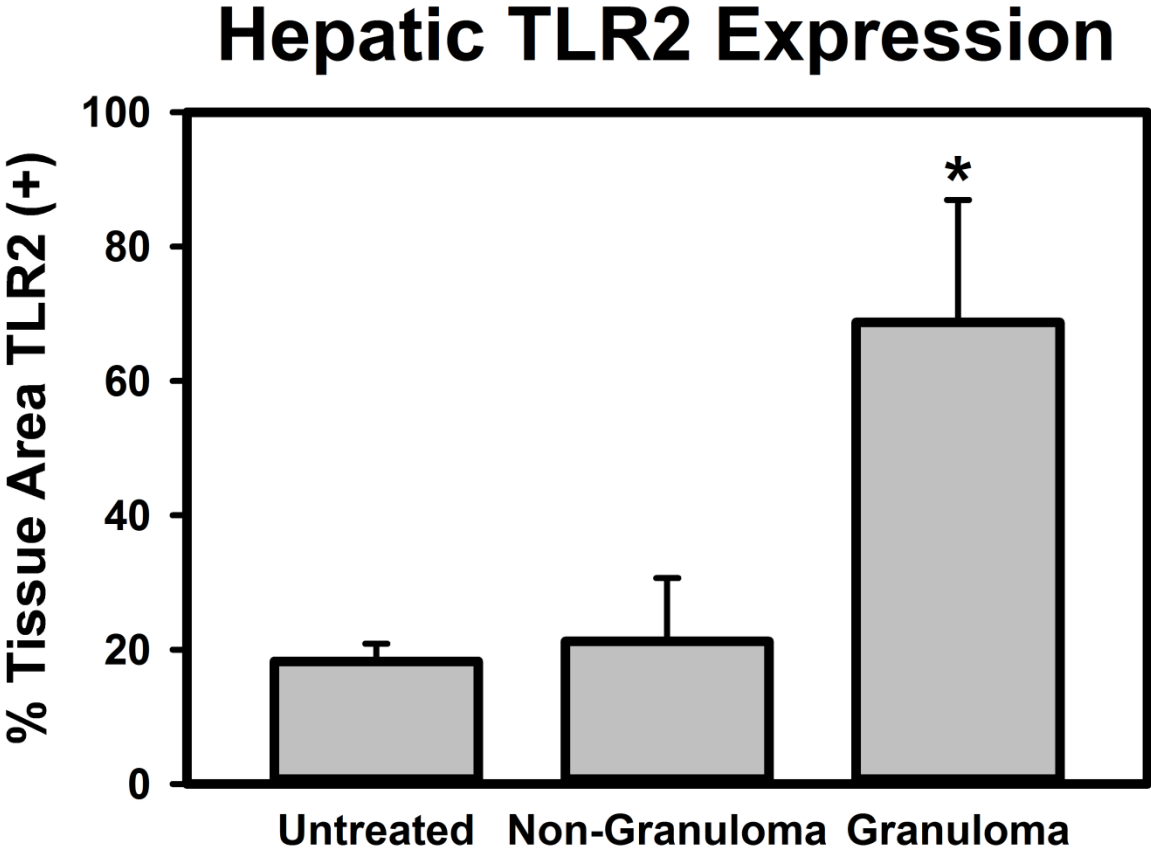


Figure SI. 21- TEM image of granuloma within liver of 8-week CFZ treated mouse.

Granuloma-associated macrophages containing CLDIs show damaged mitochondria and formation of collagen fibers surrounding the cell. A neighboring neutrophil, while exposed to drug, does not contain CLDIs, indicating that CLDI stabilization and sequestration may be macrophage specific.

(M: Mitochondria, GM: Granuloma-associated macrophage, CLDI: Crystal-like Drug Inclusion, CF: Collagen Fibers, N: Neutrophil)

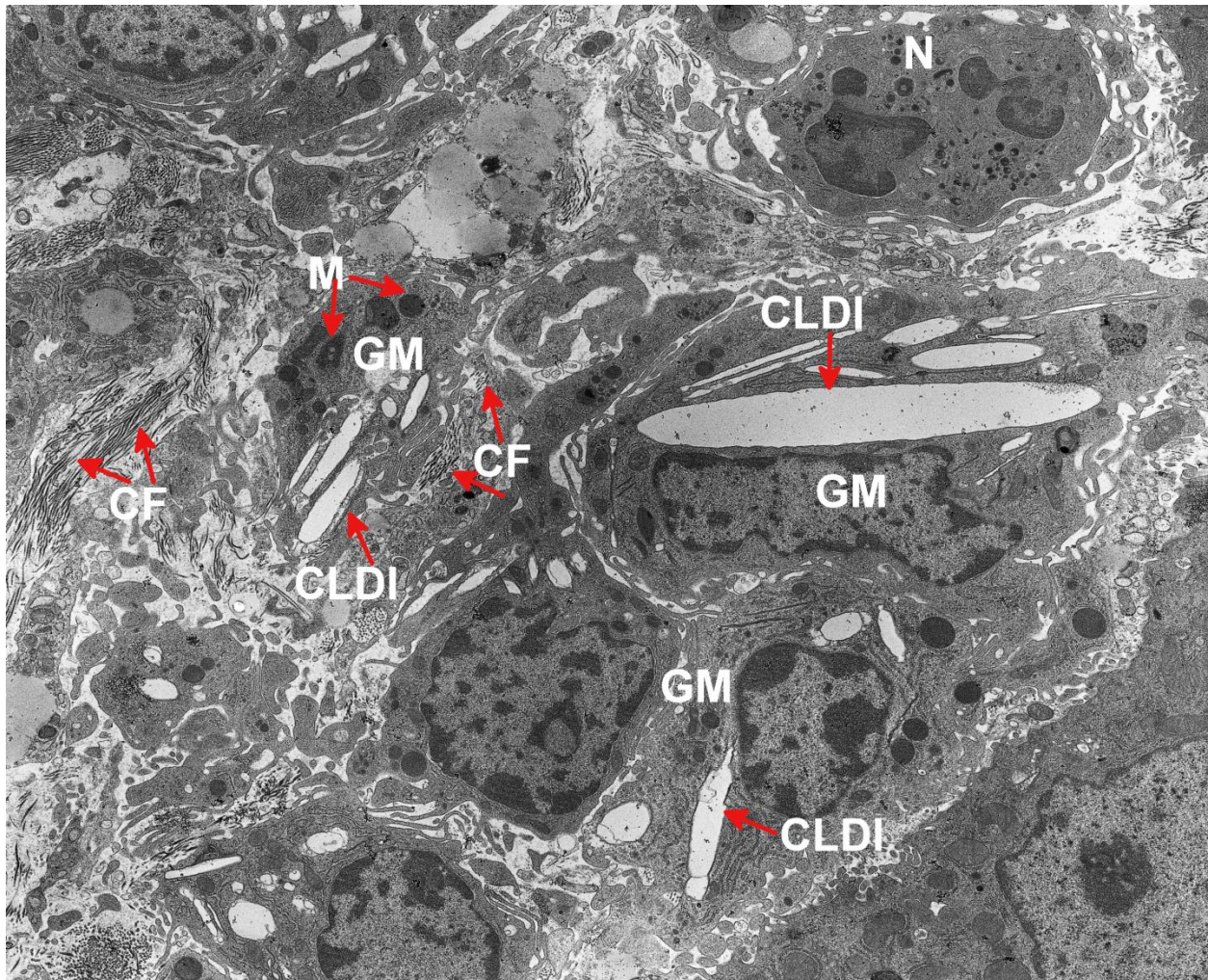


Figure SI. 22- Hepatic apoptosis in clodronate and PBS-treated mice.

Hepatic granulomas of PBS-CFZ treated mice show significantly higher rates of apoptosis compared to the clodronate-CFZ treated granulomas. (*= $p < 0.001$, ANOVA, Tukey's HSD).

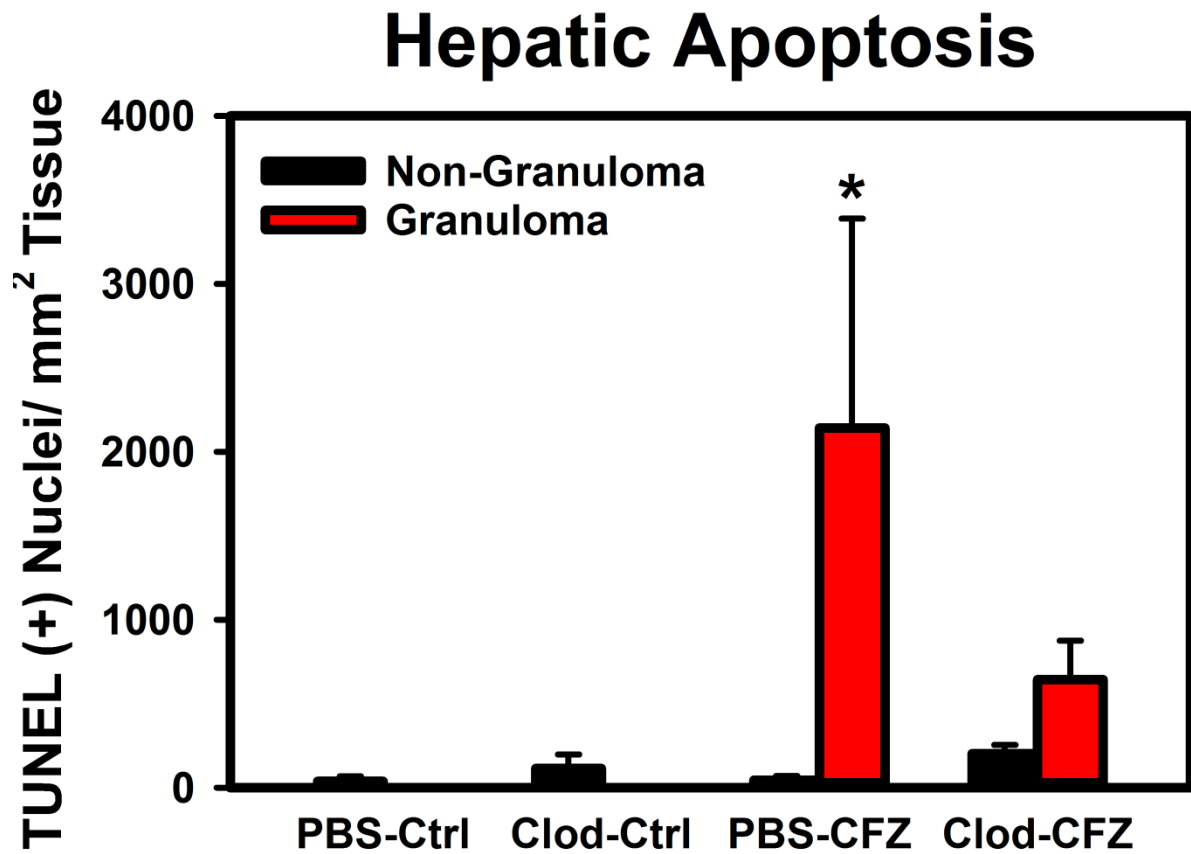


Figure SI. 23- Cellular proliferation in clodronate- and PBS-treated mice.

Clodronate treatment reduces cellular proliferation within CFZ-induced granulomas. The number of Ki67 (+) nuclei within granulomas is significantly reduced in clodronate-CFZ treated mice. (n=30 images per treatment group, n=30 granulomas, *=p<0.001, ANOVA, Tukey's HSD).

Hepatic Cellular Proliferation

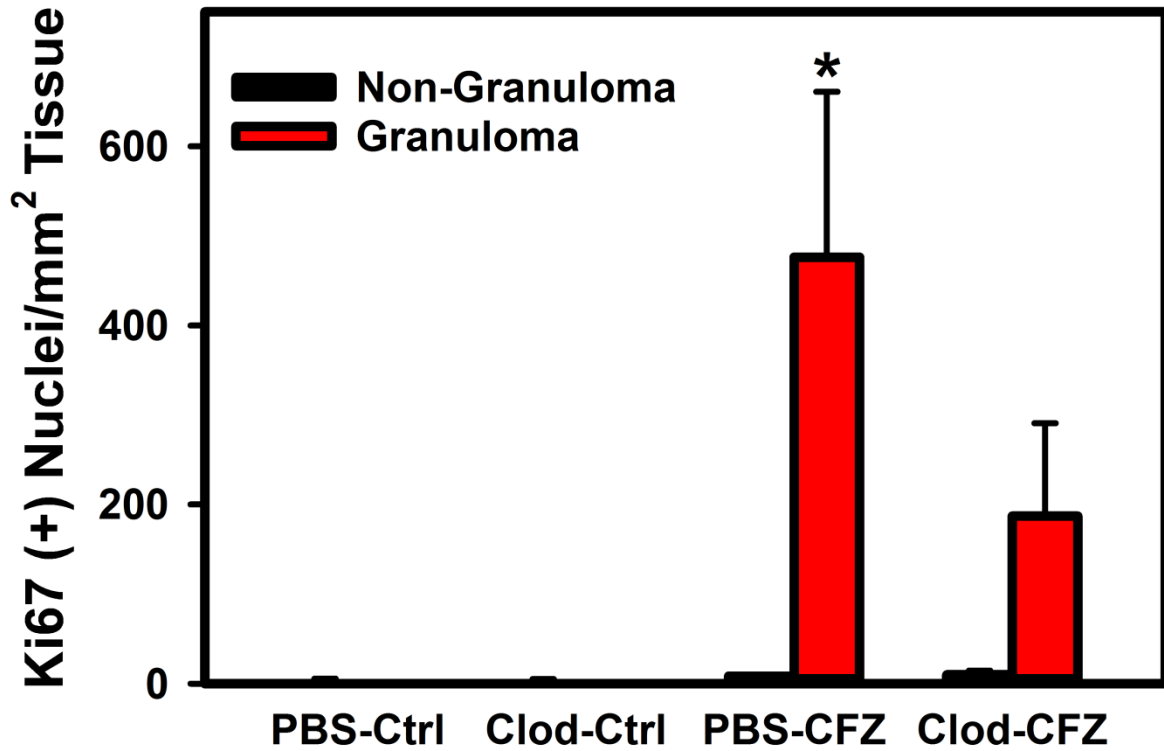


Figure SI. 24- Hepatic macrophage quantification in clodronate- and PBS-treated mice.

F4/80: DAPI ratio analysis reveals significant reduction in liver macrophages following clodronate depletion. (n=10 images per liver, n=3 organs per group) (*=p<0.05, ANOVA, Tukey's HSD).

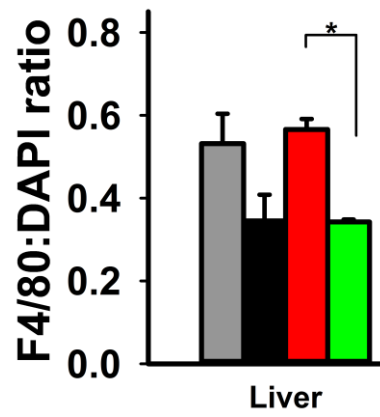


Figure SI. 25- Quantification of protonated CFZ within livers of clodronate- and PBS-treated mice.

Cy5: DAPI ratio analysis reveals significant reduction in liver CLDI accumulation following clodronate depletion.

(n=10 images per liver, n=3 organs per group) (*= $p < 0.05$, ANOVA, Tukey's HSD).

